

OPTICAL PROPERTIES OF GaAs-Al<sub>x</sub>Ga<sub>1-x</sub>As  
SUPERLATTICES INVESTIGATED  
BY TUNABLE LASER  
SPECTROSCOPY

By

PAN SANG JUNG

Bachelor of Science  
in Engineering  
Seoul National University  
Seoul, Korea  
1977

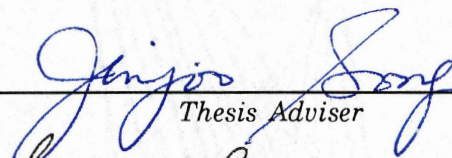
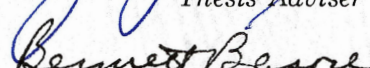
Master of Science  
Korea Advanced Institute of  
Science and Technology  
Seoul, Korea  
1980

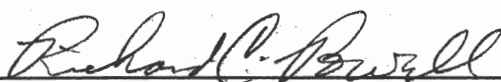
Submitted to the Faculty of the  
Graduate College of the  
Oklahoma State University  
in partial fulfillment of  
the requirement of  
the Degree of  
DOCTOR OF PHILOSOPHY  
December, 1989

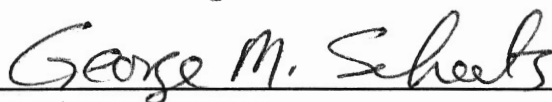
Thesis  
1989D  
J950  
cop.2

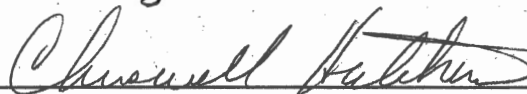
OPTICAL PROPERTIES OF GaAs-Al<sub>x</sub>Ga<sub>1-x</sub>As  
SUPERLATTICES INVESTIGATED  
BY TUNABLE LASER  
SPECTROSCOPY

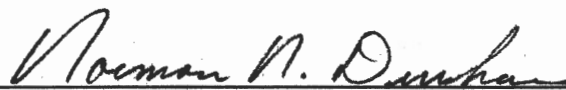
Thesis Approved:

  
\_\_\_\_\_  
*Thesis Adviser*  


  
\_\_\_\_\_

  
\_\_\_\_\_

  
\_\_\_\_\_

  
\_\_\_\_\_  
*Dean of the Graduate College*

## PREFACE

Optical properties of GaAs-Al<sub>x</sub>Ga<sub>1-x</sub>As superlattices (SLs) are investigated by tunable dye-laser spectroscopy. We observed several new effects, including excitonic effects associated with miniband dispersions and multi-phonon Raman scattering in thin-barrier superlattices. Those observations are consistent with theoretical results. The scope of the work covers the first unconfined states above the potential barrier and the ground state near the band gap of the potential well in SL structures.

I wish to express my sincere gratitude to individuals who assisted me for this work, both at Oklahoma State University and at University of Southern California, where a part of the work was done. My special gratitude goes to my thesis advisor, Dr. J. J. Song, for her intelligent guidance, inspirations, devotions and invaluable aid. I am also grateful to other committee members: Dr. Bennett L. Basore, for serving the chairman of the committee, Dr. Chriswell G. Hutchens, for many helpful guidances, Dr. George Sheets and Dr. Richard C. Powell for their advisement during the course of this thesis. I am indebted to the courtesy of Dr. Y. C. Chang at University of Illinois, and Dr. J. N. Schulman at Hughes Research Laboratories for their computer programs. Precision samples are from Dr. C. W. Tu at University of California, San Diego. A part of the work is

supported by Office of Naval Research and Air Force Office of Scientific Research. The deepest gratitude goes to my family, especially, my wife, Mansook, who have been patient and supporting all the times. This thesis is dedicated to the memory of my father, Soon Chang Jung.

## TABLE OF CONTENTS

Chapter	Page
<b>I. INTRODUCTION .....</b>	<b>1</b>
Superlattices and Microstructures .....	2
GaAs and Al <sub>x</sub> Ga <sub>1-x</sub> As Crystals .....	4
Parameters in Superlattices .....	11
Heavy Holes and Light Holes .....	14
Excitons .....	17
Mini zones, Critical Points, and Optical Resonances...	24
Critical Points of Optical Transitions in Crystal Band .....	24
Minibands in Superlattices .....	26
<b>II. EXPERIMENTAL METHODS .....</b>	<b>30</b>
Photoluminescence and Excitation Spectroscopy .....	32
Raman Scattering .....	33
Phonon Modes in GaAs-Al <sub>x</sub> Ga <sub>1-x</sub> As .....	35
Loudon's Selection Rules .....	36
Raman Scattering Spectra .....	42
Determining Axes of Samples .....	45
<b>III. EXPERIMENTAL SETUP .....</b>	<b>47</b>
Optics .....	47
Programs .....	59
<b>IV. SAMPLES FOR EXPERIMENTS .....</b>	<b>70</b>
<b>V. EXCITONIC RESONANCE IN FIRST UNCONFINED STATES .....</b>	<b>78</b>
Doublet Above Potential Barrier .....	78
Resonant Raman Scattering .....	91
Phonon Interactions in Resonance .....	91

Chapter	Page
Deformation Potential (DP) .....	92
Fröhlich Interactions (F) .....	93
Interface Modes (IF) .....	94
Impurity Assisted Processes .....	94
Incoming and Outgoing Resonances: Double Resonances .....	95
Resonant Raman Spectra .....	95
RRS in the First Unconfined State .....	97
 <b>VI. EXCITONIC RESONANCES AT THE GROUND STATES....</b>	 <b>118</b>
Dispersion Associated Resonance in Superlattices .....	118
Multiple Resonance and Phonon Scattering .....	132
 <b>VII. EXCITONS IN THIN BARRIER SUPERLATTICES .....</b>	 <b>153</b>
Excitonic Line Widths .....	154
Intensities and Energies .....	165
 <b>VIII. SUMMARY AND CONCLUSION .....</b>	 <b>173</b>
 REFERENCES .....	 176
 APPENDIX .....	 184

## LIST OF TABLES

Table		Page
I.	Physical parameters of GaAs, $\text{Al}_x\text{Ga}_{1-x}\text{As}$ , and AlAs. ....	10
II.	Critical points and the density of state functions. ....	25
III.	Raman tensors for crystal symmetry groups. ....	40
IV.	Raman tensors for processes in GaAs, and GaAs- $\text{Al}_x\text{Ga}_{1-x}\text{As}$ quantum-wells and superlattices. ....	41
V.	Ranges and power output of dye used. ....	49
VI.	The comparison of sample parameters.- An example. ....	74
VII.	The list of the samples used in experiments. ....	77
VIII.	The parameters used in calculations of resonant Raman scattering. ....	111
IX.	Intensities, full-width-half-maximum, positions, and polarizations of various Raman modes. ....	135
X.	Examples of calculation of excitonic life times of superlattice minibands. ....	151
XI.	Exciton binding energy. ....	167



## LIST OF FIGURES

Figure	Page
1. Types of superlattices. ....	5
2. The unit cell and crystal structure of GaAs and AlAs. ....	7
3. Various symmetry points and the energy band structure of GaAs. ....	8
4. Schematic parameters of a superlattice. ....	12
5. Changes of energy levels and minibands in superlattices and quantum wells. ....	13
6. Optical transitions between energy levels in a parabolic quantum well. ....	15
7. Density of state functions with excitonic effects. ....	23
8. Brillouin zones of superlattices. ....	27
9. A typical PLE spectrum from GaAs-Al <sub>x</sub> Ga <sub>1-x</sub> As superlattices. ....	34
10. Phonon dispersion relations of GaAs. ....	37
11. Raman spectra from GaAs-Al <sub>x</sub> Ga <sub>1-x</sub> As. ....	43
12. Schematic diagrams of experiment. ....	48
13. The dye laser beam path in the cavity. ....	55
14. Basic block flow chart of software. ....	62
15. The APL-component file structure for the experimental environment. ....	66

Figure	Page
16. A simple Molecular-Beam-Epitaxy growth chamber. ....	71
17. The relative determination x from Raman spectra. ....	75
18. A simplified energy band diagram. ....	80
19. PLE spectra taken from GaAs/Al <sub>0.22</sub> Ga <sub>0.78</sub> As superlattices..	82
20. Comparison of wavefunctions of first unconfined states. ....	84
21. The energy splitting of doublets and dispersions. ....	87
22. Unconfined transitions from another set of samples. ....	89
23. Resonant Raman spectra. ....	96
24. A typical RRS spectrum. ....	103
25. RRS spectra from Sample A to D. ....	109
26. Effective lifetimes obtained from fitting process. ....	112
27. The range of the dispersion designed for samples. ....	119
28. Calculated photoabsorption lineshape changes of 1HH. ....	121
29. PLE spectra taken from a series of GaAs-Al <sub>0.18</sub> Ga <sub>0.82</sub> As SL. ....	123
30. PLE spectra from a series of GaAs-Al <sub>x</sub> Ga <sub>1-x</sub> As SL samples. ....	125
31. The portion of the spectra for H and L. ....	126
32. Calculated absorption coefficient for excitonic states. ....	129
33. n = 2 Heavy hole miniband excitonic effects. ....	131
34. Multi-phonon Raman Spectra. ....	137
35. Photoluminescence and resonated Raman peak. ....	138

Figure	Page
36. Relative intensity of the overtones and combinations. ....	144
37. Energy dispersion diagram SL sample. ....	146
38. Change of FWHM of phonon modes. ....	149
39. Two types of width fluctuations and resulting energy levels in QWs. ....	156
40. PLE data SET I showing narrowing in the line-width. ....	158
41. Two mechanisms of line-width narrowing. ....	163
42. Comparison between positions of L and H peaks with calculated bandedges by TBA. ....	169
43. Comparison of PLE intensities and the CPA calculation...	171

## LIST OF SYMBOLS

$\Gamma_1$	PLE excitonic line width obtained by CPA.
$\gamma_1, \gamma_2, \gamma_3$	Luttinger constants
$\Gamma_b, \Gamma_c, \Gamma_a$	Energy broadening given by the effective lifetimes of states
$\gamma_b, \gamma_z$	EFMD in barrier width, and well width, respectively
$\Gamma_f$	Total EFMD
$\Delta_0$	Split-off at $E_0$
$\Delta_1$	Split-off at $E_1$
$\Delta E$	Sum of the miniband dispersions at CB and VB
$\delta v$	Incremental width per phonon mode number
$\epsilon$	dielectric constant
$\eta$	A coefficient
$\mu$	reduced mass
$\rho$	Retaining ratio
$\sigma$	Raman scattering cross section
$\Phi$	Wavefunctions in real space
$\phi$	Wavefunctions in $\mathbf{K}$ space.
$\omega$	Optical frequency
$\omega_p$	Phonon frequency
0D	Zero dimension, zero dimensional

1D	One dimension, one dimensional
1e, 1hh, 1lh	n=1 CB state, n=1 heavy hole state, n=1 light hole state, respectively
1HH	Optical transition between n=1 heavy hole and n=1 of CB
1LH	Optical transition between n=1 light hole and n=1 of CB
2D	Two dimension, two dimensional
2HH	Optical transition between n=2 heavy hole and n=2 of CB
3D	Three dimension, three dimensional
a	Crystal lattice constant
$a_B$	Bohr radius of excitons
$a_H$	Bohr radius of a hydrogen atom
AlAs	Aluminum Arsenide
$Al_xGa_{1-x}As$	Aluminum Gallium Arsenide
APL	A computer programming language
BZ	Brillouin zone
CB	Conduction band
CPA	Coherent potential approximation
CW	Continuous wave
d	Period of SL
D(E), DOS	Density of state function
$D_1, D_2$	Diameters of lenses
e	electron charge
E(K)	Energy dispersion relation
$E_0$	Fundamental bandgap

$E_1$	Bulk $M_1$ -type bandgap along $\Lambda$ direction
$E_B$	Bandgap of GaAs
EFMD	Energy fluctuation due to the monolayer difference
$E_{xb}$	Exciton binding energy
F	F number of lenses and spectrometers
$f_1, f_2$	Focal length of lenses
FWHM	Full width at half maximum
GaAs	Gallium Arsenide
$\hbar$	Plank's constant
H, $H_{ep}$	Hamiltonian, electron-phonon interaction Hamiltonian
HH	Heavy hole
H, L	2s-combination peaks of HH and LH
INTER-F	Inter-layer fluctuation
INTRA-F	Intra-layer fluctuation
$I_{\perp}, I_{\parallel}$	Intensities of light in two orthogonal polarizations
J	Total angular momentum
$J_{eh}$	Joint density of state function
$\mathbf{K}$	Momentum vector of exciton
$\mathbf{k}, \mathbf{k}_i$	Photon wavevector
$k_z$	Electron / hole wavevector in the z-direction
$L_1, L_2$	Lenses
$L_b$	Barrier width
LH	Light hole

LHe	Liquid helium
LO	Longitudinal optical (phonon)
$L_z$	Well width
M	Matrix element
m	Order of a phonon mode
$m^*$	Effective mass, a general notation
$m_{hh}, m_{lh}, m_e$	Effective masses of heavy holes, light holes, and electrons, in semiconductor.
$m_{  }, m_z$	Effective masses in parallel to the SL layer, or the z-axis.
$M_1, M_2, M_0$	The critical point types
MBE	Molecular-Beam-Epitaxy
MQW	Multiple quantum well
n	Quantum state principal quantum number
N	Exciton quantum number
PL	Photoluminescence (Spectroscopy)
PLE	Photoluminescence excitation (Spectroscopy)
q	Momentum of phonons
$q_z$	z-component of q
QSE	Quantum size effects
QW	Quantum well
$r_h, r_e$	Real coordinate of holes and electrons
$R_{ij}$	Raman tensor
RRS	Resonant Raman Scattering
RS	Raman scattering

$R_y$	Rydberg constant
SL	Superlattice
$T_{2d}$ , $D_{2d}$ , $\Gamma$	Crystal point symmetry notations
TBA	Tight-binding approximation
$t_{LO}$ , $t_R$	Lifetimes of LO phonon and excitons
TO	Transverse optical (phonon)
$\mathbf{u}$ , $\mathbf{v}$	The unit vectors of light polarizations
VB	Valence band
$x$	Aluminum concentration of the barrier
$x$ , $y$ , $z$	crystal axes
$X_{ij}$	Dielectric susceptibility tensor
ZB	BZ boundary
ZC	BZ center
$\mathfrak{R}$	Optical transition rate



# CHAPTER I

## INTRODUCTION

In this Chapter, we introduce briefly a few basic aspects of superlattice structures, i.e., the materials, the energy bands, and the properties of electrons and hole as well as excitons. In particular, we explain definitions of the bandedge critical point and the notion of minibands. We will concentrate on properties related to GaAs and  $\text{Al}_x\text{Ga}_{1-x}\text{As}$ , which is the materials of superlattices (SLs) and quantum wells (QWs) in this thesis. Fundamental physical parameters of GaAs and  $\text{Al}_x\text{Ga}_{1-x}\text{As}$  are well established and they are readily available such that high quality samples are routinely fabricated with these materials. As result, we are able to observe new optical effects which can be weakened by non-ideal crystalline conditions. The purpose of this thesis is to investigate specifically optical resonance effects of excitons at edges of minibands in superlattices as we vary one of parameters of superlattices. The organization of remainders of the thesis is in the following.

Chapters II to IV are introductory providing a general background for chapters V to VII, where main topics are discussed. In Chapter II, we review two experimental methods we use, i.e., photoluminescence-excitation and Raman spectroscopy with an introduction to phonons in semiconductors. Chapter III is devoted to details of experimental apparatus and procedures

covering the software and optics. In Chapter IV, we describe samples used in this work, with a brief discussion about a few characterization methods of sample parameters. From Chapter V to VII, we present observation of several excitonic resonance phenomena and describe behaviors depending on a sample parameter, the barrier width ( $L_b$ ). First, we discuss that the bandedge resonance produces a doublet at the first unconfined states in Chapter V. Excitonic effects at the ground state of superlattices show characteristic spectra and multiple-resonance phonon peaks, which are topics discussed in Chapter VI. In Chapter VII, general trends are discussed in terms of the linewidth, the strength, and the binding energy of ground-state excitons as barrier widths become thinner, and thus SLs are closer to bulk crystals. Finally, we summarize and conclude results of this thesis in Chapter VIII.

## Superlattices and Microstructures

In crystalline solids, periodic layers of atoms in a lattice produce a band structure of states. If there exist other periodic variations of potentials over the same lattice, the crystal structure is called a superlattice (SL). Due to such a periodic potential structure, energy bands are divided into smaller bands, called minibands. Suppose we can artificially add such potentials onto a semiconductor. Then, we can imagine possibilities of *engineering* [1] the energy band structure of a crystal by using various types of potential structures. These concepts have become more practical recently as we can fabricate a structure with a precision control in atomic scales (a few Å).

Generally, those superstructures can be made to be periodic in one, two or three axis-directions. We call it, then, a two-dimensional (2D) multiple quantum well (MQW), an one-dimensional (1D) quantum wire or a zero-dimensional (0D) quantum dot, respectively, after the *degree of freedom* in the motion of carriers in those structures. In this thesis, we are concerned with cases from strictly 2D to almost 3D, which is covered by SLs with the periodicity in the one crystal axis (the z-axis) direction and with various structure parameters. This knowledge can be extended to those of more-reduced dimensionality. The energy dispersion of minibands can vary from virtually zero at discrete levels to the continuum-like case, depending on the detailed shape of super-potentials. It has been well known quantum mechanically that electrons confined in a potential well with a size comparable to De Broglie wavelength exhibit *quantum size effects* (QSE) [2,20] resulting in quantized energy levels of zero width. A superlattice is formed when those quantum-wells (QWs) are periodically repeated close to one another so that there can be a finite possibility of electron coupling from one well to the next. Discrete levels of energy states, then, are broadened and form minibands. Minibands become broader as those wells are brought closer or potential barriers between them get lower. The discussion in this thesis are on SLs which have more significant miniband widths than MQWs. MQWs have been studied extensively so far.

Historically, before semiconductor SLs become available, the investigations on QSE were on a narrow channel of carriers formed in metal-

semiconductor interfaces, surface induced layers, or doped heterojunctions [15], all of which are not very controllable and those results showed rather indirect verifications of QSE. Nonetheless, the scientific interest on QSE accompanies the advance of the technology. The technology of manufacturing semiconductor materials progresses so rapidly that such a quantum-size can be artificially fabricated routinely just in two decades (1960s-1980s). Molecular-Beam-Epitaxy (MBE) [3] and Metal Organic Chemical Vapor Deposition (MOCVD) [4] (or similar Organometallic Vapor Phase Epitaxy (OMVPE) [5]) are two main technologies for SL fabrication. SLs and MQWs are fabricated by alternating two or more different kinds of atomic layers (Type I superlattices) or by planting alternatively donors and acceptors in one crystal (Type II superlattices). See Figure 1. Shaded areas stand for the bandgap of materials. In the drawing, the upper boundary corresponds to the conduction band (CB) edge, and lower one to the valence band (VB) edge of a semiconductor.

### GaAs and $\text{Al}_x\text{Ga}_{1-x}\text{As}$ Crystals

GaAs is a binary alloy crystal with Ga and As in a two overlapping face-centered-cubic lattices like diamonds, i.e., the zincblende structure. In AlAs crystals, aluminum atoms substitute for gallium atoms. Gallium and aluminum atoms have three valence electrons each and an arsenic atom has five valence electrons. Bonds are denoted by  $sp^3$  which results in a tetrahedral cell formed of one atom at the center and four atoms at peaks.

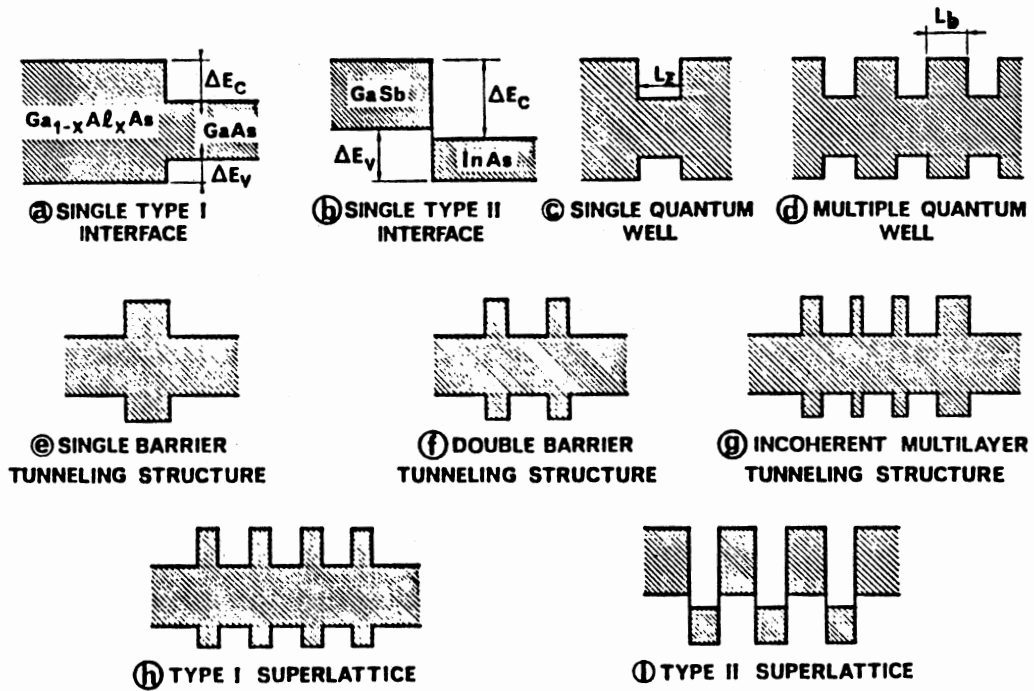


Figure 1. Types of superlattices. [After 13].

Each atom is surrounded by four other atoms. The angle between bonds is  $109.47^\circ$ . The ionicity is given  $f_i = 0.31$  [7]. The unit cell is shown in Figure 2. Integers in brackets,  $[m\ n\ l]$ , denote directions in a crystal lattice in Miller notation [6]. Those in parentheses,  $(m\ n\ l)$ , refers to a family of planes parallel to one which intersects the principal axis at  $x=a/m$ ,  $y=a/n$ , and  $z=a/l$ , where  $a$  is the lattice constant, i.e., the length of one side of the unit cell.  $\{m\ n\ l\}$  is a group of  $(m\ n\ l)$  planes where  $m$ ,  $n$ , and  $l$  are interchanged including negative numbers which is indicated by an upper bar according to this notation. The lattice constant of GaAs at 300K is [7]

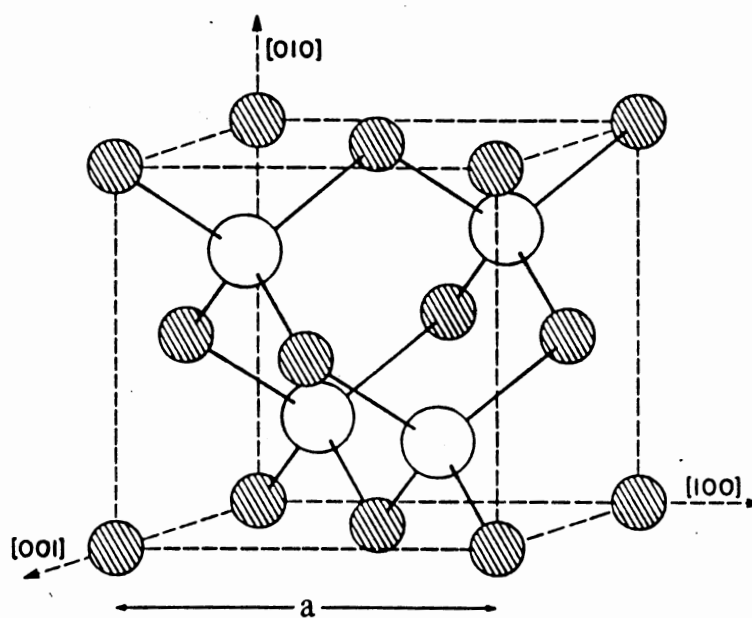
$$a = 5.65325 \pm 0.00002 \text{ \AA}. \quad (1)$$

If we look along  $[001]$  direction, we see alternating layers of Ga atoms and As atoms. The distance between layers of a pair of Ga-As is  $a/2 \approx 2.83\text{\AA}$ . We will use this value in the remainder of the thesis. The lattice constant for AlAs is very close to that of GaAs. The mismatch is less than 0.15% at 300K [9]. This is one of reasons why a GaAs- $\text{Al}_x\text{Ga}_{1-x}\text{As}$  system was the first combination which is widely used for high quality superlattices and quantum wells. The bandgap of AlAs crystal is much larger than that of GaAs. Therefore, using an alloy of  $\text{Al}_x\text{Ga}_{1-x}\text{As}$  with varying  $x$ -value, we can obtain an alloy with any values of bandgap between those of GaAs and AlAs. The bandgap is, according to Reference 12,

$$E_g^\Gamma = 1.424 + 1.247x, \text{ for } 0 \leq x \leq 0.45. \quad (2)$$

$\Gamma$  is the notation for the highest symmetry point at the center of Brillouin zone (BZ) of bulk GaAs. Those symmetry points in GaAs crystals

(a)



(b)

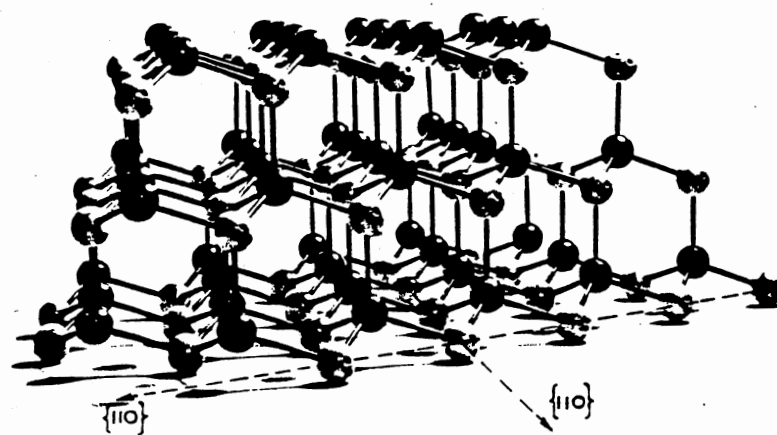


Figure 2. The unit cell (a) and crystal structure (b) of GaAs and AlAs.

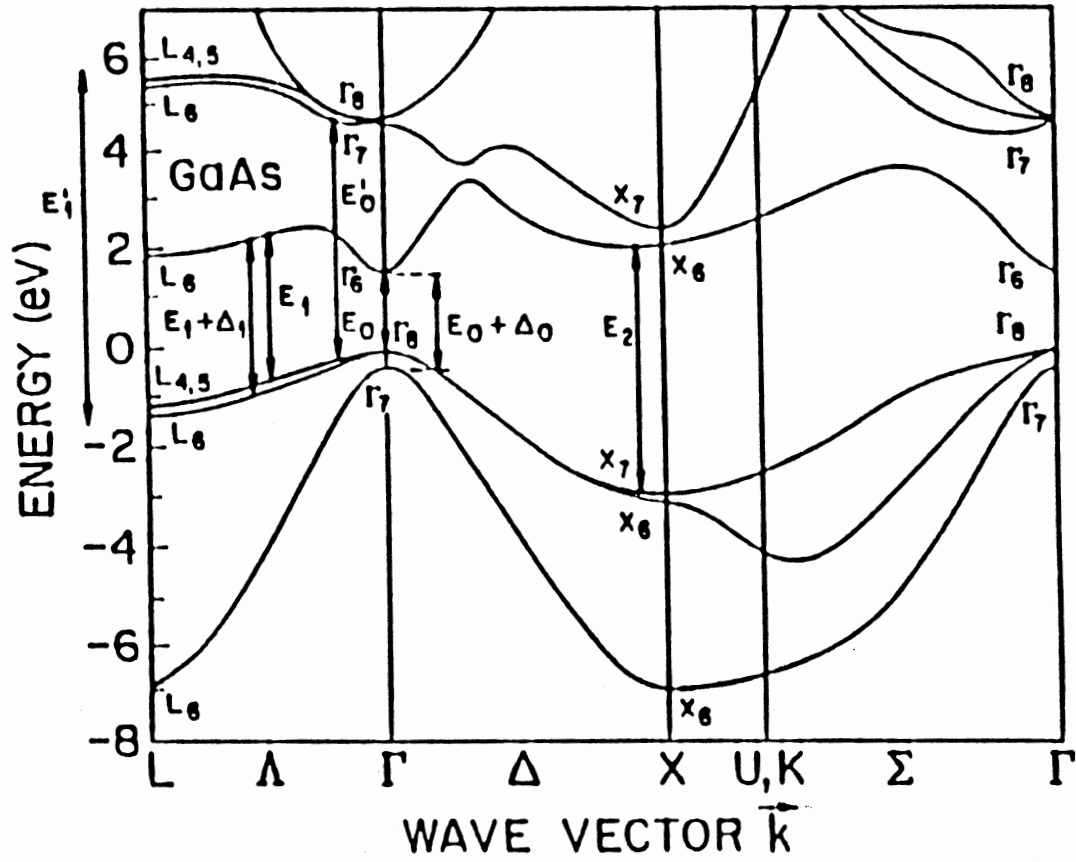


Figure 3. Various symmetry points and the energy band structure of GaAs.



are shown in Figure 3. Both the minimum of CB and the maximum of VB are located at  $\Gamma$  point for GaAs. This kind of a bandgap is called a *direct gap*. In other crystals, the minimum of CB can be other symmetry points. Such a bandgap is then called an *indirect gap* as that of an AlAs crystal where CB at X point is lower than CB at the  $\Gamma$  point. Accordingly, for their alloy  $\text{Al}_x\text{Ga}_{1-x}\text{As}$ , the direct gap becomes indirect for  $x \geq 0.45$ . The bandgap also varies with the temperature. Near 0 K, the bandgap of GaAs is 1.5192 eV. Various parameters of GaAs, AlAs, and  $\text{Al}_x\text{Ga}_{1-x}\text{As}$  are summarized in Table I. In Figure 3, the gap between  $\Gamma_8$  and  $\Gamma_6$  is the fundamental gap of GaAs, denoted by  $E_0$ .  $\Gamma_7$  point is referred to as the spin-orbital-split band. The gap between  $\Gamma_6$  and  $\Gamma_7$  is denoted by  $E_0 + \Delta_0$ .  $\Delta_0$  is the amount of the split. The near-parallel section off  $\Gamma$ -point, along  $\Lambda$  to [111] direction, is  $E_1$  gap, and its split-off is called  $E_1 + \Delta_1$ . These two received much attention due to their rare  $M_1$ -type critical point.

The band diagram of AlAs is considered similar to that of GaAs except for the ordering (relative positions in energy) of bandedges.  $\text{Al}_x\text{Ga}_{1-x}\text{As}$  is somewhat different in a sense that it is a ternary alloy. Sites of Ga are replaced by Al atoms in a random manner so that  $x$  can have any value between 0 and 1. Properties such as band structures are often theoretically calculated by an interpolation scheme [9] where known parameters of GaAs and AlAs are used. Equation (2) is one of results of such an approach. In interpolation schemes, the higher-order terms in the relation is important when we need precise values.

TABLE I

PHYSICAL PARAMETERS OF GaAs, Al<sub>x</sub>Ga<sub>1-x</sub>As, AND AlAs [9]

Parameter	GaAs	AlAs	Al <sub>x</sub> Ga <sub>1-x</sub> As
Space group	$F\bar{4}3m^a$	$F\bar{4}3m^a$	$F\bar{4}3m$
Lattice constant $a$ (Å)	5.6533 <sup>b</sup>	5.6611 <sup>c</sup>	5.6533 + 0.0078x
Crystal density $\rho$ (g/cm <sup>3</sup> )	5.360 <sup>d</sup>	3.760 <sup>e</sup>	5.36 - 1.6x
Melting point (°C)	1238 <sup>f</sup>	1740 <sup>g</sup>	1238 - 58x + 560x <sup>2</sup> <sup>i</sup> 1238 + 1082x - 560x <sup>2</sup> <sup>u</sup>
Thermal expansion coefficient $\alpha_{th}$ ( $\times 10^{-6}$ °C)	6.4 <sup>h</sup>	5.2 <sup>i</sup>	6.4 - 1.2x
Elastic stiffness constant $C_{ij}$ ( $\times 10^{11}$ dyn/cm <sup>2</sup> )			
LO-phonon energy $\hbar\omega_{LO}$ (meV)			
GaAs-type	36.25 <sup>m</sup>	...	36.25 - 6.55x + 1.79x <sup>2</sup>
AlAs-type	...	50.09 <sup>m</sup>	44.63 + 8.78x - 3.32x <sup>2</sup>
TO-phonon energy $\hbar\omega_{LO}$ (meV)			
GaAs-type	33.29 <sup>m</sup>	...	33.29 - 0.64x - 1.16x <sup>2</sup>
AlAs-type	...	44.88 <sup>m</sup>	44.63 + 0.55x - 0.30x <sup>2</sup>
Specific heat $C_p$ (cal/g deg)	0.08 <sup>n</sup>	0.11 <sup>o</sup>	0.08 + 0.03x
Debye temperature $\theta_D$ (K)	370 <sup>p</sup>	446 <sup>q</sup>	370 + 54x + 22x <sup>2</sup>
Lattice thermal resistivity $W$ (deg cm/W)	2.27 <sup>r</sup>	1.10 <sup>r</sup>	2.27 + 28.83x - 30x <sup>2</sup>
Temperature coefficient of $E_g^c$ ( $\times 10^{-4}$ eV/deg)			
$dE_g^c/dT$	-3.95 <sup>j</sup>	-5.1 <sup>k</sup>	-3.95 - 1.15x
$dE_g^c/dT$	-3.6 <sup>l</sup>	-3.6 <sup>k</sup>	-3.6
Conduction-band effective mass			
$\Gamma$ valley $m_e^c$	0.067 <sup>a</sup>	0.150 <sup>a</sup>	...
$X$ valley $m_{ix}$	0.23 <sup>m</sup>	0.19 <sup>n</sup>	...
$m_{ix}$	1.3 <sup>o</sup>	1.1 <sup>n</sup>	...
$L$ valley $m_{iL}$	0.0754 <sup>p</sup>	0.0964 <sup>q</sup>	...
$m_{iL}$	1.9 <sup>r</sup>	1.9 <sup>r</sup>	...
Density-of-states electron mass $m_e^d$			
$\Gamma$ valley $m_e^d$	0.067	0.150	0.067 + 0.083x
$X$ valley $m_e^d$	0.85 <sup>i</sup>	0.71 <sup>i</sup>	0.85 - 0.14x
$L$ valley $m_e^d$	0.56 <sup>i</sup>	0.66 <sup>i</sup>	0.56 + 0.1x
Valence-band effective mass			
$m_{ih}$	0.087 <sup>a</sup>	0.150 <sup>v</sup>	0.087 + 0.063x
$m_{hh}$	0.62 <sup>v</sup>	0.76 <sup>v</sup>	0.62 + 0.14x
$m_{so}$	0.15 <sup>v</sup>	0.24 <sup>v</sup>	0.15 + 0.09x
Band-gap energy $E_g^c$ (eV)	1.424 ( $E_g^c$ ) <sup>a</sup>	2.168 ( $E_g^c$ ) <sup>a</sup>	1.424 + 1.247x (0 < x < 0.45) <sup>a</sup> 1.900 + 0.125x + 0.143x <sup>2</sup> (0.45 < x < 1.0) <sup>a</sup>
Critical-point energy (eV)			
$E_0$	1.425 <sup>b</sup>	3.02 <sup>c</sup>	1.425 + 1.155x + 0.37x <sup>2</sup> <sup>w</sup>
$E_0 + \Delta_0$	1.765 <sup>b</sup>	3.32 <sup>c</sup>	1.765 + 1.115x + 0.37x <sup>2</sup>
$E_1(1)$	2.89 <sup>b</sup>	3.82 <sup>c</sup>	2.89 + 0.94x
Electron affinity $\chi_e$ (eV)	4.07 <sup>d</sup>	3.5 <sup>d</sup>	4.07 - 1.1x (0 < x < 0.45) 3.64 - 0.14x (0.45 < x < 1.0)
Ionic $f_i$	0.310 <sup>e</sup>	0.274 <sup>e</sup>	0.310 - 0.036x
$E_1(1) + \Delta_1$	3.12 <sup>b</sup>	4.03 <sup>c</sup>	3.12 + 0.91x
Net charge $Q$ (eV)	0.46 <sup>f</sup>	0.47 <sup>f</sup>	0.46 + 0.01x
Exciton Rydberg energy $G$ (meV)	4.7 <sup>h,k</sup>	17.0 <sup>g</sup>	4.7 + 6.82x + 5.48x <sup>2</sup>
Exciton Bohr radius $a_B$ (Å)	115 <sup>g</sup>	42 <sup>g</sup>	115 - 142x + 61x <sup>2</sup>
Effective mass used in the thesis			
$m_e^c$	0.0671	0.15	0.0671+0.083x
$m_{hh}^c$	0.34	0.53	0.34+0.19x
$m_{ih}^c$	0.094	0.15	0.094+0.056x

## Parameters of Superlattices

Superlattice structures are described schematically with three parameters in this thesis. See Figure 4. Those parameters are, the width of the potential well ( $L_z$ ), that of the barrier ( $L_b$ ), and the concentration of aluminum in the potential barrier ( $x$ ). The bandgap of the barrier material is given by Equation (2). While the sum of the barrier height in CB and that in VB are given by the difference between the bandgaps of GaAs and  $\text{Al}_x\text{Ga}_{1-x}\text{As}$ , the bandgap discontinuity, ( $\Delta E_c$  for CB;  $\Delta E_v$  for VB) is usually given by a ratio of partition. Generally,  $\Delta E_c:\Delta E_v$  is assumed with a value between 85:15 [20] to 60:40 [14]. Exact values used are slightly different from one author to another even until recently [11,16], such as, 65:35 [17], 57:43 [18], and so on. We use here 60:40 following the previous work in Reference 66.

If  $L_b$  is large, the structure can be called as a multiple quantum-well. The distinction between SLs and MQWs is due to the extent of coupling between electrons or holes in adjacent wells. The criterion is rather flexible. A higher potential barrier can effectively isolate wells so that a structure can be a MQW even with smaller  $L_b$ . The period,  $d$ , of a SL is given by the sum of  $L_z$  and  $L_b$ . It determines the width of mini-Brillouin zones as we discuss later. Edges of a miniband (the minimum and the maximum energy) vary depending on  $L_z$ ,  $L_b$ , and  $x$ . Roughly speaking, for square potential wells,  $L_z$  changes the energy level higher or lower,  $L_b$  and  $x$  change the width of minibands. This is illustrated in Figure 5, where minibands and levels are compared for a specific case of symmetric wells ( $L_z = L_b$ ), with a fixed

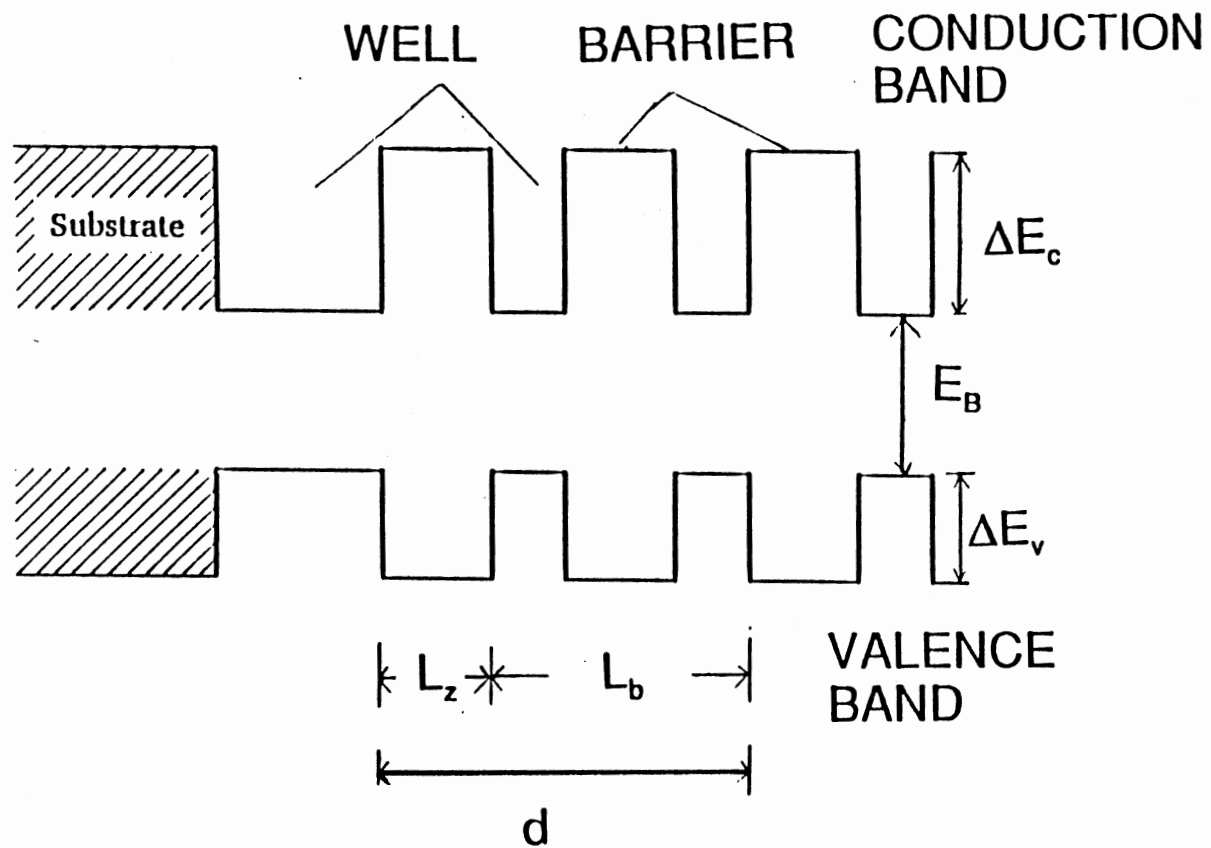


Figure 4. Schematic parameters of a superlattice.

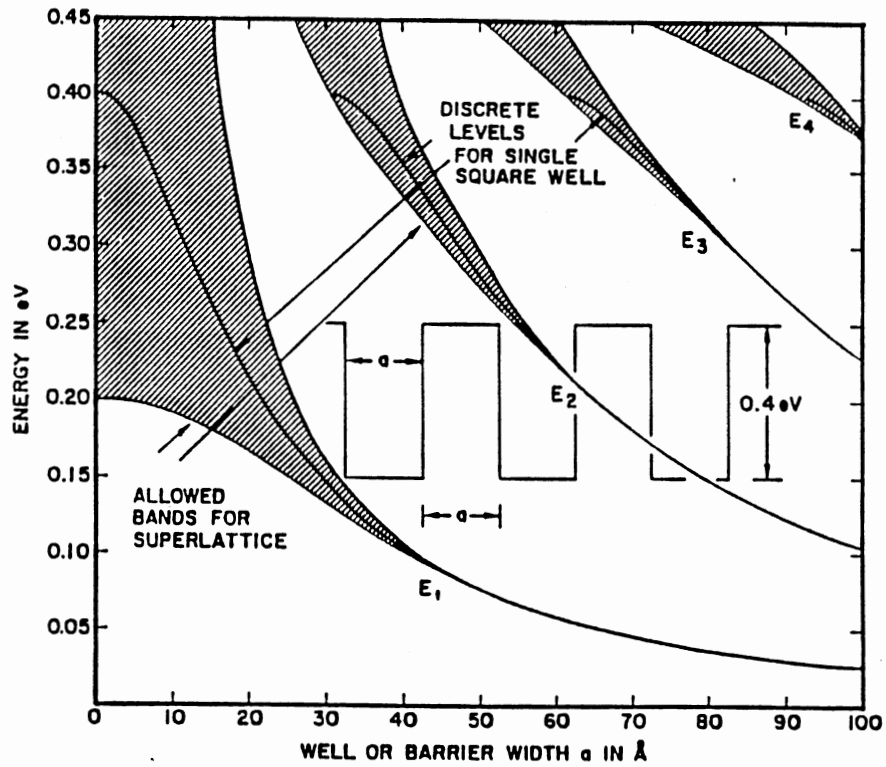


Figure 5. Changes of energy levels and minibands in superlattices and quantum wells, for a specific case of  $L_z = L_b = a$ , with a fixed barrier height. [After 13]

barrier height of 0.4eV.  $E_1$  to  $E_4$  are lower four levels of the SL. Shaded areas are minibands. As  $L_b$  decreases, the width of minibands becomes larger. Also, as  $L_z$  decreases, levels move higher in energy. For cases of arbitrarily different  $L_z$  and  $L_b$ , these trends are followed approximately. In general, the minimum and the maximum energy of minibands may vary at different rates.

For one other aspect, note that the spacing between  $E_1 - E_2$  and  $E_2 - E_3$  are different, which is true for a square-well case. In parabolic potential wells, the spacing becomes equal. Peaks in Figure 6 are from transitions between quantum levels in a parabolic QW. Equal spacing is obviously observed.

## Heavy Holes and Light Holes

For free electrons, the energy dispersion relation is

$$E(\mathbf{K}) = \hbar^2 |\mathbf{K}|^2 / 2m_0, \quad (3)$$

where  $\mathbf{K}$  is the 3D electron wavevector and  $m_0$  is the electron mass. In the bulk GaAs crystal near crystal symmetry points, the energy of electrons is given approximately by a parabolic function in  $\mathbf{K}$ , similar to free electrons.

Thus, effective masses of electrons are defined as

$$m_i^* = \hbar^2 / (\partial^2 E / \partial K_i^2), \quad (4)$$

where  $i$  is for different directions of  $\mathbf{K}$ . Near the  $\Gamma$  point of VB of GaAs, there are two kinds of hole states, heavy-hole and light-hole states. At  $\mathbf{K}=0$ , the band has 4-fold degeneracy as indicated by the total angular momentum

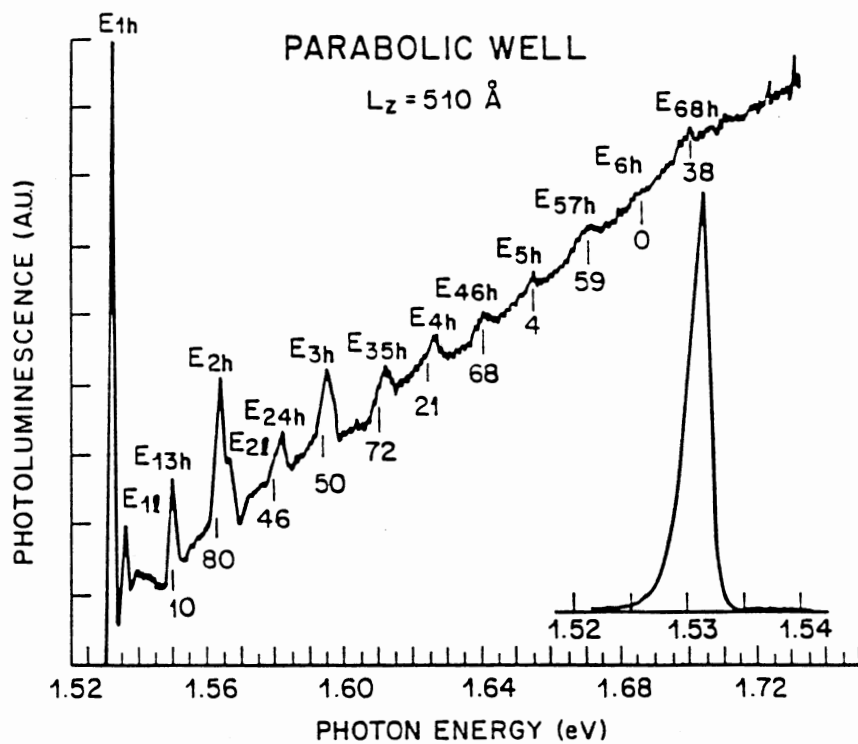


Figure 6. Optical transitions between energy levels in a parabolic quantum well. [After 13].

$J=3/2$ . The origin of this degeneracy is basis wavefunctions which are from valence electrons of Ga and As atoms, according to Kane model [8].

For a bulk crystal effective masses are usually considered not different depending on the direction of  $\mathbf{K}$  since the energy dispersion is almost isotropic. For 2D SLs and QWs, it is necessary to differentiate those effective masses in two different directions, i.e., one in the parallel direction ( $m_{\parallel}^*$ ) and one in the perpendicular direction ( $m_z^*$ ) (z-axis direction; the growth direction; the normal to SL layers). Taking z axis as [001], the energy of holes is approximately given as follows. Including Luttinger interactions[10] where quantum potentials are treated as a perturbation on the crystal lattice potential [13], we obtain

$$E_{\text{hh}}(J_z=\pm 3/2) = (\hbar^2 k_{\parallel}^2/2m_0)(\gamma_1+\gamma_2) + (\hbar^2 k_z^2/2m_0)(\gamma_1-2\gamma_2), \quad (5)$$

$$E_{\text{lh}}(J_z=\pm 1/2) = (\hbar^2 k_{\parallel}^2/2m_0)(\gamma_1-\gamma_2) + (\hbar^2 k_z^2/2m_0)(\gamma_1+2\gamma_2), \quad (6)$$

where  $\gamma_1, \gamma_2$  are Luttinger parameters [19], and  $J_z$  is the z-component of  $\mathbf{J}$ , the angular momentum. The results show us that effective masses are, in comparison with Equation (3),

$$m_{\text{llh}}^* = m_0/(\gamma_1+\gamma_2) \text{ and } m_{\text{zhh}}^* = m_0/(\gamma_1-2\gamma_2) \quad (\text{for heavy holes}), \quad (7)$$

$$m_{\text{llh}}^* = m_0/(\gamma_1-\gamma_2) \text{ and } m_{\text{zlh}}^* = m_0/(\gamma_1+2\gamma_2) \quad (\text{for light holes}). \quad (8)$$

According to Equations (7) and (8), the z-components of the masses are  $m_{\text{lh}}^* = 0.08m_0$ , and  $m_{\text{hh}}^* = 0.45m_0$  [10]. However, the results are from simple ideal cases. The real situation is complicated by other effects, such as, nonparabolicity of dispersion, band mixing, effects of finite potential well shapes, etc. [13] We use here for calculations of energy levels,  $m_e =$



$0.0671m_0$ ,  $m_{hh} = 0.34m_0$ ,  $m_{lh} = 0.094m_0$  for GaAs and  $m_e = 0.0853m_0$ ,  $m_{hh} = 0.382m_0$ ,  $m_{lh} = 0.106m_0$  for  $Al_{0.22}Ga_{0.78}As$  from Reference 66. For other values of  $x$ , the value can be obtained by linear interpolation. The superscripts (\*'s) of effective mass symbols will be omitted in the remainder of this thesis. Effective masses used in this thesis are listed in Table I.

We have seen in Equations (5) and (6) that heavy hole and light hole bands have different angular momenta. This results in different circular polarizations in photoluminescence signals from them. This fact was utilized for a positive identification of heavy-hole and light-hole peaks in a photoluminescence spectrum [28].

## Excitons

A hole refers to an unoccupied electron state in VB [21]. It behaves just like a particle with a positive charge in the crystal lattice. Excitons are particles formed with electrons and holes which are bonded by Coulomb forces. Excitons are usually formed where there is optical excitation of semiconductors [21]. Excitonic effects are effects due to Coulomb interaction between electrons and holes in contrast to the cases of uncorrelated electrons and holes [21]. Excitonic effects are possible because the energy of an exciton is lower than that of uncorrelated holes and electrons. R. J. Elliot provided a simple picture of an exciton by considering it as a hydrogen-like atom with a reduced mass  $\mu$  [22].

Excitons can be described in two limiting approximations. One is Frenkel exciton if an exciton is small and tightly bound, and the other is Wannier exciton if an exciton is weakly bound with a large electron-hole separation in comparison with a lattice constant [6]. Also, a non-hydrogenic model often used is one with Koster-Slater interaction. Simple theories presented here belong to the case of Wannier-type hydrogenic excitons. The energy of an exciton is discrete as an hydrogen atom, such as,

$$E_N = E_B - E_{xb}/N, \quad N = 1, 2, \dots \quad (9)$$

where  $E_B$  is the continuum energy between electrons and holes which is usually the fundamental bandgap, and  $E_{xb}$  is called the binding energy of the exciton.  $E_{xb}$  is the energy required to annihilate an exciton at the ground state ( $N=1$ ). For the bulk GaAs,  $E_{xb}$  is equal to  $R_y$  based on the hydrogenic model. And we can rewrite that

$$R_y = e^4 \mu / 2 \epsilon^2 \hbar^2 = (\underline{\mu} / \underline{\epsilon}^2) R_{yH}, \quad (10)$$

where  $\epsilon$  is the dielectric constant,  $\underline{\epsilon}$  is the relative dielectric constant,  $\underline{\mu}$  is a normalized mass,  $\mu/m_0$ , and  $R_{yH}$  is Rydberg constant of a hydrogen atom. For GaAs bulk,  $R_y = 4.2$  meV. In QWs and SLs,

$$1/\mu_{\pm} = 1/m_e + (\gamma_1 \pm \gamma_2)/m_0 = 1/m_e + (1 \pm 1/2)/2m_{hh} + (1 \pm 1/2)/2m_{lh}, \quad (11)$$

where  $\mu_{\pm}$  is for light-hole excitons (- sign) and heavy-hole excitons (+ sign). In the second equality, Equations (7) and (8) are substituted for Luttinger constants [10]. We can also define a Bohr radius for an exciton, that is,

$$a_B = (4\pi\epsilon\hbar^2/\mu e^2) = (\underline{\epsilon}/\underline{\mu})a_H, \quad (12)$$

where  $a_H (=0.53\text{\AA})$  is Bohr radius of a hydrogen atom. Again, for a bulk GaAs,  $2a_B \sim 130 \text{\AA}$ . If the width of QWs is smaller than the exciton diameter, exciton wavefunctions are expected to be distorted, or to be squeezed [10]. In such cases, more exact calculations are needed since the hydrogenic model no longer applies. Still, in SLs with low or thin barriers, excitons still retain its sphericity, at the least, in part. Thus, we can utilize the hydrogenic model as a guideline in many cases.

As mentioned previously, excitons result from optical excitations. That is, the absorbed light generates pairs of electrons in CB and holes in VB. The rate,  $\mathfrak{R}$ , of the *optical transition* is proportional to a dipole-transition matrix-element  $M$  in such a way,

$$\mathfrak{R}(\hbar\omega) = 2\pi/\hbar |M|^2 \delta(E_e - E_h - \hbar\omega), \quad M = \langle elph \rangle, \quad (13)$$

where  $\langle el$  and  $\langle hl$  are states with energy  $E_e$  and  $E_h$ , respectively.  $p$  is a dipole moment operator. Equation (13) is called Fermi's *Golden Rule*. The expression shows a sharp peak in  $\mathfrak{R}$  for two discrete levels  $\langle el$  and  $\langle hl$ . In general, there are many states both in CB and VB. Nonetheless, it has been shown that excitonic optical transitions can be described by the transition between only two states [23]. When states have an energy dispersion in  $\mathbf{K}$ , there is a selection rule about  $\mathbf{K}$  of an exciton. From the fundamental theory of excitons [21],  $M$  can be written as

$$A_p \langle \Phi_e(\mathbf{r}_e) | e^{i\mathbf{k}\cdot\mathbf{r}} \mathbf{e} \cdot \mathbf{p} | \Phi_h(\mathbf{r}_h) \rangle, \quad (14)$$

where  $A_p$  is a constant,  $\Phi_e(\mathbf{r}_e)$  is the wavefunction of the electron state at the position  $\mathbf{r}_e$ ,  $\Phi_h(\mathbf{r}_h)$  is for the hole state,  $\mathbf{e}$  is the incident photon polarization

vector,  $\mathbf{p}$  is the momentum operator, and  $\mathbf{k}$  is the photon wavevector.

Again, we can write  $\Phi(\mathbf{r})$  as  $\int d\mathbf{K} \phi(\mathbf{K})e^{i\mathbf{K}\cdot\mathbf{r}}$ , then, by changing the order of integration, we will have

$$A_p' \int d\mathbf{K} \langle \phi_e(\mathbf{K}_e) | e \cdot \mathbf{p} | \phi_h(\mathbf{K}_h) \rangle \delta(\mathbf{K}_h - \mathbf{K}_e + \mathbf{k}), \quad (15)$$

where  $A_p'$  is another constant. These results tell us that the optical transition occurs only between electron and hole states with

$$\mathbf{K}_e - \mathbf{K}_h = \mathbf{k} \approx 0 \Rightarrow \mathbf{K}_h \approx \mathbf{K}_e. \quad (16)$$

where  $|\mathbf{k}| \ll |\mathbf{K}_e|$  or  $|\mathbf{K}_h|$  is used in the optical frequency. Such an optical transition is called the *direct transition*, since the transition occurs between same momenta of electrons and holes. Thus main excitonic transitions occur between states with same momenta. However, there can be another kind of the transition called the *indirect transition*. It only can occur with the help of a lattice phonon in the process. A phonon is a collective excitation representing the vibration of the lattice. In such cases, the above expression is modified with  $\mathbf{q}$ , the momentum of a phonon, thus

$$\mathbf{K}_e - \mathbf{K}_h \approx \mathbf{q}. \quad (17)$$

Indirect transitions often occur across an indirect bandgap. It is usually weaker than a direct one and shows very strong temperature dependence partly because the population of phonons is temperature dependent at low temperatures.

The selection rule is caused by Bloch-type function of  $e^{i\mathbf{K}\cdot\mathbf{r}}$ . In QWs, the wavefunction in the z-direction becomes different from that in the x,y direction. If the incident polarization is in the x,y direction, which is true in

most reported experiments, the integral contains only the quantized envelope wavefunction in the z-coordinate. In the x-y direction, it contains the usual Bloch functions. Therefore, in an infinitely deep QW, the integral of quantized wavefunction determines the selection rule, that is, [24]

$$\Delta n = 0, \quad (18)$$

where  $n$  is the quantum number for the discrete levels. Thus, transitions are allowed between electrons and hole levels with the same quantum number, such as,  $n=1$  electron level to  $n=1$  heavy hole level, or  $n=1$  light hole level, and so on. The assumption of an infinite height often breaks down in real QWs and SLs. Still forbidden ( $\Delta n \neq 0$ ) transitions are usually weaker than allowed transitions.

The strength of optical transitions is often measured by the absorption coefficient which is given by Equation (15). It is considered quite convenient, if we define a joint density of states (DOS) such that

$$J_{eh}(\hbar\omega) = [1/(2\pi)^3] \int 2d\mathbf{K} \delta\{E_e(\mathbf{K}) - E_h(\mathbf{K}) - \hbar\omega\}, \quad (19)$$

where the integral is over the entire BZ. Then the absorption coefficient  $\alpha(\hbar\omega)$  is

$$\alpha(\hbar\omega) \approx A_0 \sum \langle \phi_e(\mathbf{K}_e) | \mathbf{e} \cdot \mathbf{p} | \phi_h(\mathbf{K}_h) \rangle J_{eh}(\hbar\omega), \quad (20)$$

where matrix elements are assumed constant and their contributions are summed up over all the states of  $\langle e|$  and  $\langle h|$  in the BZ. DOS functions can be derived entirely from energy dispersion relations which varies according to the dimensionality of the crystal. In 3D case, it is proportional to  $(\hbar\omega - E_B)^{1/2}$ . For 2D case, such as QWs, it is a step function. Excitonic effects can

change the DOS function shape [25]. Those effects are theoretically calculated using a Hamiltonian of a form (See Reference 21, p276),

$$H_{\text{ex}} = H_0 - e^2/\epsilon|r_e - r_h|, \quad (21)$$

where  $H_0$  is Hamiltonian for uncorrelated electron-hole pairs. Important changes can be two-fold [10,13,25]. One is at the bandedge, where DOS has an additional enhancement factor so that the resultant function of 3D is more or less a step-function. This contribution is called *Sommerfeld factor* due to Coulomb interaction given by Equation (21). See Figure 7. A similar shape of an absorption spectrum is observed experimentally in GaAs [26]. For 2D-DOS, the original step function has a decaying slope in the higher energy continuum. The other effect is like a hydrogen atom. An exciton has discrete excited states below the fundamental gap as mentioned in Equation (9). Experimentally, those peaks are observed for  $N=1$ , the ground state of an exciton. The  $N=2$  peak, from the second excited state of an exciton, also called *2s-state*, is rarely resolved in bulk GaAs, and appeared at the rising-slope of 2D DOS in the QW case [27]. To determine the binding energy of exciton  $E_{\text{xb}}$ , we have to know precisely the relative location of  $E_{\text{b}}$ . Or, alternatively, if we can identify the 2s-state peak, we can deduce  $E_{\text{xb}}$  from the difference between 1s-, and 2s-state positions.  $E_{\text{xb}}$  is expected to vary depending on parameters of specific SLs and QWs due to the difference in the degree of confinement. The precise experimental determination has been difficult particularly due to the ambiguous location of  $E_{\text{b}}$ . When the dispersion of a miniband is significant, we have found that 2s-state related

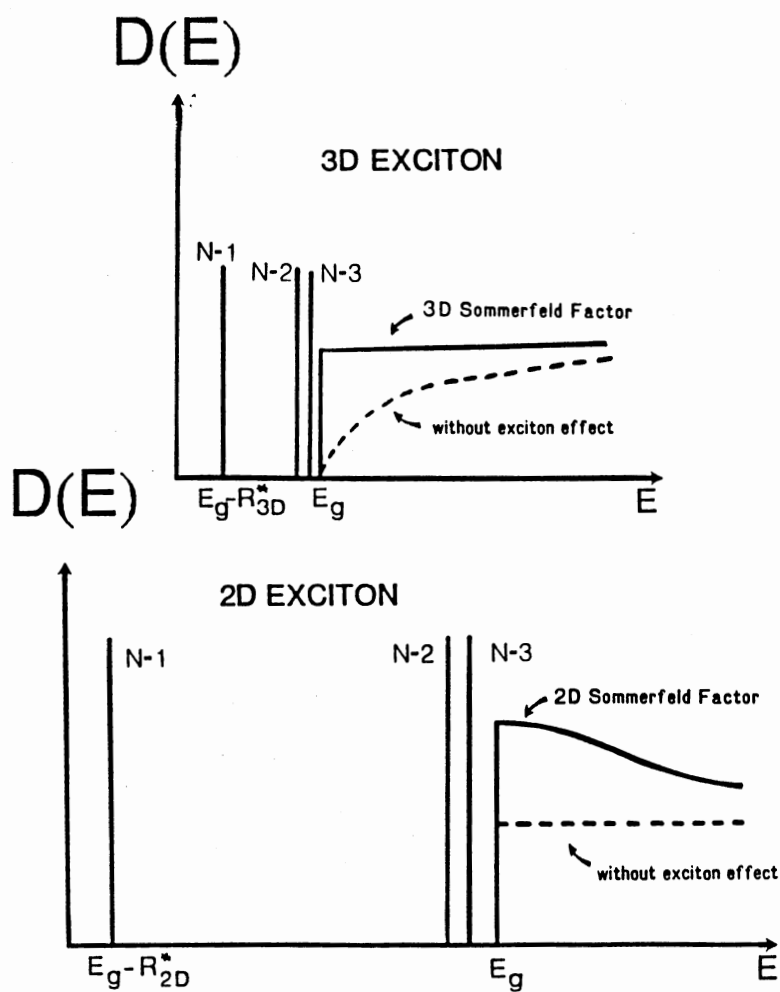


Figure 7. Density of state functions with excitonic effects.  $E_g$  is the energy of the optical transitions at the band gap.  $R_{3D}^*$ ,  $R_{2D}^*$  are Rydberg constants in 3D, 2D, respectively. [After 13]

peaks appear more profoundly. The 2s-state locates at a sharply rising slope. The details will be discussed in Chapter VI. The exact knowledge of the excitonic binding energy can allow us to estimate the possibility of excitonic effects in comparison with external perturbations.

## Mini Zones, Critical Points, and Optical Resonances

### Critical Points of Optical Transitions in Crystal Band

The density-of-states function given in Equation (19) can be rewritten in a more general form using the identity relation for delta functions as

$$J_{cv}(E) = \frac{2}{(2\pi)^3} \int_{E_c(\mathbf{K}) - E_v(\mathbf{K}) = E} \frac{dS}{|\nabla_{\mathbf{K}} [E_c(\mathbf{K}) - E_v(\mathbf{K})]|}, \quad (22)$$

where c, v represents CB and VB, respectively, S is the surface where  $E_c(\mathbf{K}) - E_v(\mathbf{K}) = E$ . The denominator determines a singularity when

$$\nabla_{\mathbf{K}} E_c(\mathbf{K}) - \nabla_{\mathbf{K}} E_v(\mathbf{K}) = 0. \quad (23)$$

These points are called critical points.  $E_c(\mathbf{K})$  and  $E_v(\mathbf{K})$  are dispersion relations of CB and VB. The density of states function is not analytic at those points. At high symmetry points, such as  $\Gamma$ , each term in Equation (23) becomes zero. The function  $E(\mathbf{K}) = E_c(\mathbf{K}) - E_v(\mathbf{K})$  can be four types at the critical point. They are  $M_0$ ,  $M_1$ ,  $M_2$ , and  $M_3$ .  $M_0$  is most often encountered and it is at direct fundamental band gaps.  $E(\mathbf{K})$  is minimum at that point;



TABLE II  
CRITICAL POINTS AND DENSITY OF STATE FUNCTIONS

Critical Point	Joint density of states	Schematic representation
$M_0$ Minimum	$J(E) = \begin{cases} B + O(E - E_0) & \text{when } E < E_0 \\ B + A(E - E_0)^{1/2} + O(E - E_0) & \text{when } E > E_0 \end{cases}$	
$M_1$ Saddle point	$J(E) = \begin{cases} B - A(E_0 - E)^{1/2} + O(E - E_0) & \text{when } E < E_0 \\ B + O(E - E_0) & \text{when } E > E_0 \end{cases}$	
$M_2$ Saddle Point	$J(E) = \begin{cases} B + O(E - E_0) & \text{when } E < E_0 \\ B - A(E - E_0)^{1/2} + O(E - E_0) & \text{when } E > E_0 \end{cases}$	
$M_3$ Maximum	$J(E) = \begin{cases} B + A(E_0 - E)^{1/2} + O(E - E_0) & \text{when } E < E_0 \\ B + O(E - E_0) & \text{when } E > E_0 \end{cases}$	

thus effective masses in three directions are all positive.  $M_1$  is called a saddle point since the functional shape looks like a saddle which can have the minimum in one direction and the maximum in others. Definitions and corresponding DOS functions are summarized in Table II [23]. Excitons at those critical points show resonances. J. C. Phillips [29] discussed those resonances including those at  $M_1$ -type critical points. The most successful experimental verification of the  $M_1$ -type point is at  $E_1$ -gap of GaAs or InSb. M. Cardona [31] explained that observed structures are due to excitonic effects at the  $M_1$  critical point. Other types of critical points are rarely observed in GaAs. Specially, the  $E_1$  gap is 2D-type as in QWs and SLs since  $\nabla_{\mathbf{K}}E(\mathbf{K}) = 0$  (constant) to  $\Lambda$  direction, and in others, the parabolic minimum. Therefore, one can imagine  $M_1$ -type (saddle point) excitons can be also observable in SLs. In this thesis, excitonic resonances are observed at both  $M_0$ -type and  $M_1$ -type critical points in the first unconfined states of a series of SLs. See Chapter V, for more discussions.

### Minibands in Superlattices

A miniband formed in SLs will have a dispersion relation. Minibands with different quantum numbers will have different widths. The dispersion relation  $E(\mathbf{K})$  can be illustrated as shown in Figure 8. In SLs, the period  $d$  is  $N_b$  times of atomic layers. As the width of BZ is  $\pi/a$  in a bulk crystal, the width of the minizone is  $1/N_b$ , i.e.,

$$\pi/d = (1/N_b) \pi/a. \quad (24)$$

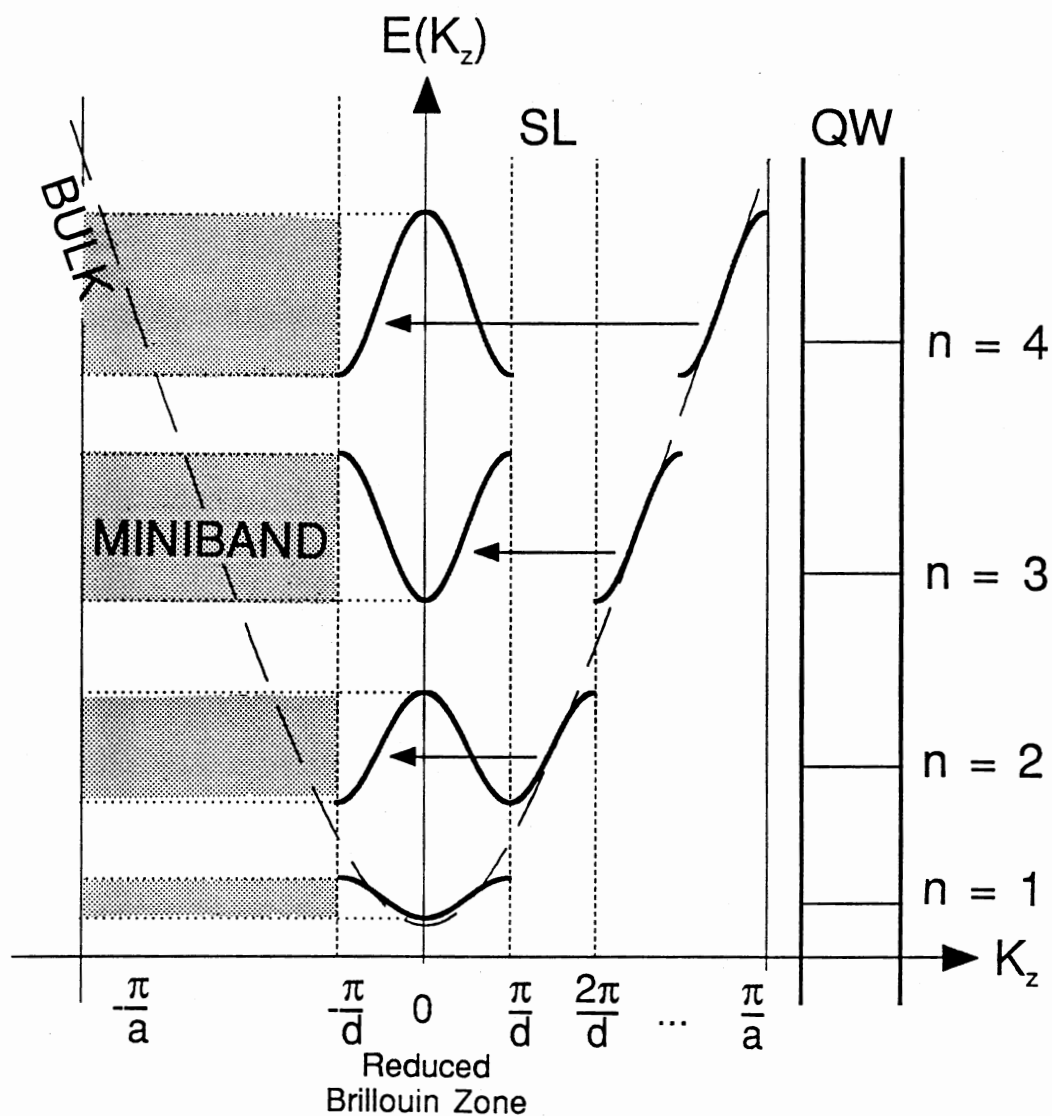


Figure 8. Brillouin zones of superlattices. Minizones are formed from the bulk dispersion relation by division due to the period of a SL,  $d$ . With larger  $d$ , the energy dispersion at each minizone is reduced approaching a zero width, a multiple quantum well case.

For MQWs, where  $L_b$  is large, the miniband width is negligible (very small dispersion) at the ground state. On the other hand, if  $d$  is smaller, the width of the miniband increases. Compare the solid curves with the dotted one in the same figure which represents a bulk dispersion relation. At each crossing point at  $K_z = n\pi/d$ , there is an energy gap. The magnitude of the gap is determined by the individual well shape given by  $L_b$ ,  $L_z$ , and  $x$ , the height of the barrier. It is because the shape determines the degree of well-to-well coupling. If the coupling is large, the gap narrows down towards to a bulk-like case. Conversely, it will approach an isolated MQW case with a small coupling. Just like in the bulk crystal BZ, minizones are often shown folded into the first zone, as shown at the range of  $-\pi/d < K_z < \pi/d$ , in Figure 8. This is called a reduced BZ scheme.

Note that at edges of each miniband, curvatures are close to zero. This will make critical points. Particularly, at the top of each band, the maximum point is formed if we look only in the quantized  $z$ -direction. This point can be a  $M_1$  critical point because in the other directions ( $x$ - $y$  directions), the energy is the minimum. In other words, different kinds of critical points are readily realized in SLs. We should be cautioned, however, that Figure 8 is not drawn to show optical transition energies between the hole and electron minibands. Critical points are defined with a joint density function between bands in CB and VB, as shown in Equation (22). In GaAs- $\text{Al}_x\text{Ga}_{1-x}\text{As}$  SLs, hole dispersions are smaller than those of electrons because the effective mass of electrons is much smaller. Thus, a joint DOS is largely determined by CB

miniband dispersion relations. Usually,  $M_1$ -points can be at ZC of even quantum numbers, or ZB of odd numbered, with  $\Delta n = 0$ . Here ZC and ZB are defined at a reduced BZ scheme.

In this introduction, we have explained the possibility of the resonance at critical points of minibands in SLs, as well as a few fundamental aspects. As we have found, the critical points result from an additional periodic potential in superlattices on the crystal lattice. Those critical points and excitonic effects in SLs are bases for the discussion of resonance phenomena throughout this thesis.

## CHAPTER II

### EXPERIMENTAL METHODS

For the investigation of properties of semiconductors, optical methods have been used extensively. With the advent of the strong coherent light of lasers, optical methods have been used more widely to examine the band structure, behaviors of electrons and holes, phonons, and many other collective excitations of semiconductors. Before lasers, there was a limit in the resolution of optical measurement because the slit of the spectrometer had to be reduced and consequently the intensity was decreased if one needed the narrow spectral-width light for a better resolution. In recent decades, however, the wide availability of lasers has greatly enhanced the capability of optical measurement. The intense coherent light of a narrow bandwidth enables us to detect fine structures of spectra much more easily. Even some non-optical constants can be obtained by optical methods. To make optical methods even more useful, combined effects, such as electro-optic, thermo-optic, magneto-optic, and elasto-optic effects are available in many materials for investigations of optical devices. Thus optical methods can provide a large amount of the vital information about the bulk crystal, including QWs and SLs of semiconductors. In this thesis, we utilize two optical method to investigate the excitonic resonances. Advantages are that they are

nondestructive, relatively non-disturbing to original sample conditions, and can be very sensitive. Optical methods, however, can not give directly physical dimensions of the structure, such as well widths and number of layers, etc. Those parameters can be obtained from material characterization techniques, e.g. a transmission electron microscopy (TEM) and X-ray diffractometry [38].

Photoluminescence (PL) and Raman Scattering Spectroscopy (RS) are two of major optical methods to investigate SL structures. One of others we'd like to mention is the absorption spectroscopy. It has been used widely, but the high absorption coefficient of semiconductors in many cases is a draw-back since it requires preparations of thin samples. Reflection spectroscopy also has been used. This method gives large background signals due to the small variation of the dielectric constant. Thus, modulation spectroscopy has been invented [30]. Still, the modulation requires either attachment of electrodes (electro-reflectance: ER), or a strong laser light (photo-reflectance:PR [32]). Another method used in semiconductor research is a magneto-optic method where a magnetic field is applied with variable magnitudes [37]. In this method, zero-field responses are extrapolated from on-field data. On the other hand, PL as well as RS does not need any sample preparation except simple cleaning procedures. More importantly, energy structures and sample conditions can be maintained, if done carefully, as if there were no excitation. From an experimental point of view, an unperturbed measurement is always the best for the direct interpretation of results and, thus, the high accuracy.

## Photoluminescence and Excitation Spectroscopy

Luminescence is the phenomenon where a material emits light as a response to a form of excitation. Their names reflect the kind of excitation. For example, if the excitation is by light, it is photoluminescence. Other types include electroluminescence, thermoluminescence, etc. Usually, the process in PL proceeds as follows:

Absorption of light  $\Rightarrow$  carrier generation  
 $\Rightarrow$  carrier relaxation  $\Rightarrow$  Photon emission.

Since carriers tend to relax to lower allowed energy states, the absorbed light is of a higher energy than light emitted according to a simple picture where there is no higher-order process. Also, light emitted spontaneously is incoherent because the recombination of carriers are a statistically random process. In QWs or SLs, excited carriers relax to the lowest state which is, in most cases,  $n=1$  quantum state or the lower-energy edge of  $n=1$  miniband at low temperatures. Then, when the spectrum of luminescence is analyzed, information can be obtained about the ground-state [33,34]. The position of PL peak gives the size of the bandgap, and the width or the shape gives information about homogeneity of structures [35]. Some additional peaks may represent impurity-, defect-, or interface-related states [36].



The excitation is done by higher energy photons than the energy of the lowest state, as mentioned. PL intensity is proportional to the population of carriers gathered at the ground state. The number of carriers is partly proportional to the number of absorbed photons. If we vary the excitation wavelength, while keeping the detection frequency within the range of PL, we have a photoluminescence excitation (PLE) spectrum. Only if a majority of carriers generated is collected in the ground state where PL is detected, PLE spectra can be close to absorption spectra, which is an absorption coefficient as a function of the wavelength. The difference between PLE and absorption spectra arises because not every carrier generated, of both electron and hole, is captured at the ground state. In Figure 9, we show a typical PLE spectrum including a theoretical calculation of absorption spectra from a SL, without excitonic effects. On the lower energy side, scanning is stopped just before the incident frequency is as same as the detection frequency. Those peaked structures correspond to the excitonic resonance at various quantum states. Note the sharpness decreases near to the barrier height (the bandgap of  $\text{Al}_x\text{Ga}_{1-x}\text{As}$ ,  $\sim 1.76\text{eV}$ ).

## Raman Scattering

Understanding behaviors of phonons is important since phonons are responsible for properties of semiconductors, such as, resistance, recombination of carriers, their temperature-dependence, etc. Raman scattering is often associated with phonons. Raman Scattering was named after C. V. Raman

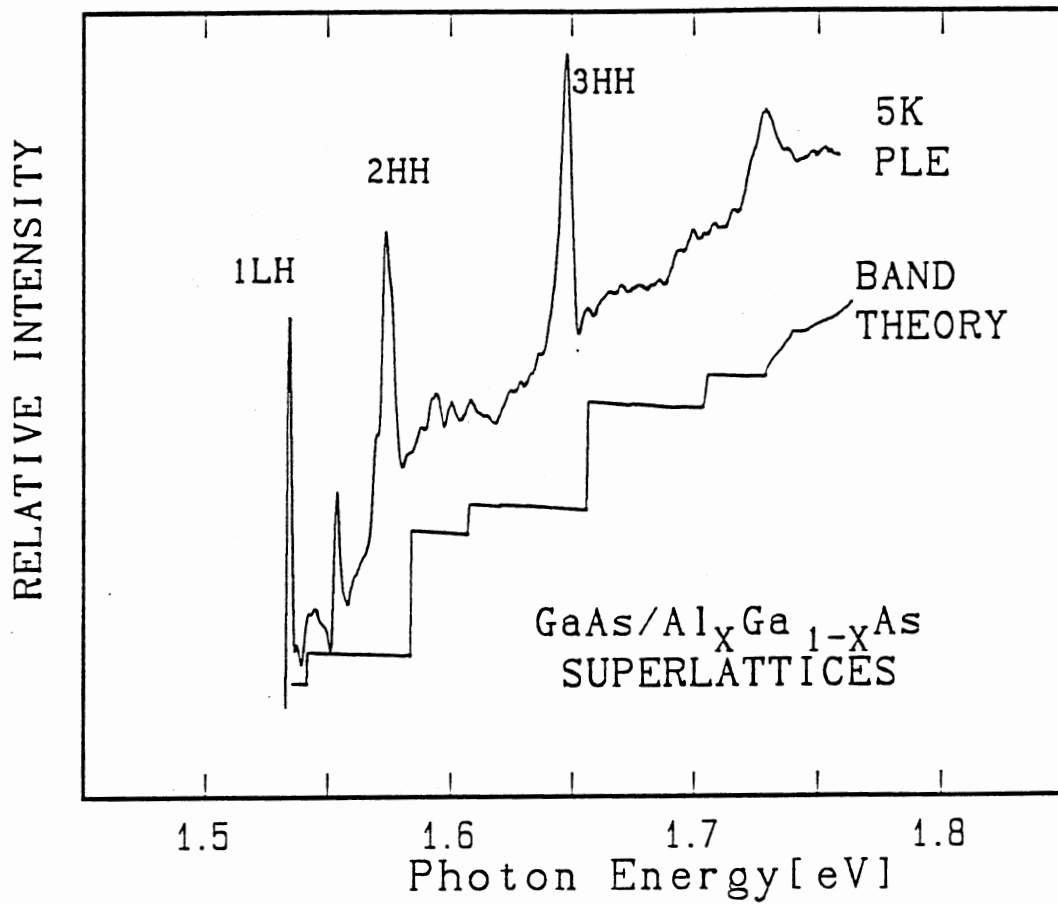


Figure 9. A typical PLE spectrum from GaAs-Al<sub>x</sub>Ga<sub>1-x</sub>As superlattices. A theoretical calculation of absorption spectra from a SL without excitonic effects is also shown by the step-like curve.

who discovered the phenomenon experimentally in 1928, following the prediction of A. Smekal in 1923. Since then, this phenomenon has been used so widely for structures of molecular liquid, gases, and lattice dynamics of crystals that the number of reported works is astronomical. See Reference 39. In this thesis, we emphasize those works on solids, and, more specifically, GaAs,  $\text{Al}_x\text{Ga}_{1-x}\text{As}$ , or other III-V semiconductors when they are related. The process of the first-order Raman scattering is in general:

- a. Photon(incident)  $\Rightarrow$  electron+hole  $\Rightarrow$  Phonon  $\Rightarrow$  electron'+ hole'  $\Rightarrow$  photon'
- b. Photon(incident)  $\Rightarrow$  Phonon + Photon'

Most likely (a) is dominant, because (b) needs an infrared sensitive phonon which is not in homopolar crystals like diamonds, Si, etc. [40] In other words, most Raman processes involve the generation of electron-hole pairs.

### Phonon Modes in GaAs- $\text{Al}_x\text{Ga}_{1-x}\text{As}$

A phonon is a collective vibrational mode of atoms forming the crystal lattice. The lattice consists schematically of a 3-dimensional (3D) mesh of springs with lattice points at each node. There are basically four modes of phonons, that is, LO (longitudinal optical), TO (transverse optical), LA (longitudinal acoustic), and TA (transverse acoustic) modes. Those phonons in longitudinal branches vibrate in parallel displacement to the propagation direction of phonons, and transverse ones in perpendicular displacement. At optical frequencies, due to the high frequency, neighboring lattice points vibrate anti-phase around the center of the mass. At acoustic frequencies, they vibrate in-phase. Raman scattering refers to scattering by optical phonons, while

Brillouin scattering is by acoustic phonons. Figure 10 shows dispersion relations (energy vs. wavevector) of phonon branches of GaAs [45].

### Loudon's Selection Rules

In a transparent medium, the energy and momentum of the process should be conserved. Thus,

$$\omega = \omega_1 - \omega_2 = \pm \omega_p \quad (25)$$

$$\mathbf{k} = \mathbf{k}_1 - \mathbf{k}_2 = \pm \mathbf{q} \quad (26)$$

where  $\omega_p$ ,  $\mathbf{q}$  are the frequency and the momentum vector of phonon, and  $\mathbf{k}_1$ ,  $\mathbf{k}_2$  are incident and scattered wavevectors, respectively. The  $\pm$  sign corresponds to Stoke's and anti-Stoke's scattering. As is manifested in Equation (25), Stoke's scattering is one where the scattered light has a smaller frequency than incident light. Anti-Stokes's refers to the opposite case. In the frequency range of our experiments, that is, in the visible frequency range,  $|\mathbf{k}|$  is less than  $10^5 \text{ cm}^{-1}$ , while the range of  $|\mathbf{q}|$  is comparable to the width of the first Brillouin zone,  $\sim 2\pi/d \approx 10^9 \text{ cm}^{-1}$ , where  $d$  is the period of a superlattice. Hence in most cases,  $|\mathbf{k}| = \mathbf{q} \approx 0$ . If the process involves more than two phonons,

$$\mathbf{k} = \sum_i \mathbf{q}_i \approx 0. \quad (27)$$

In this multi-phonon scattering, each phonon does not have to be of zero-momentum. The efficiency of such a process is much less than that of a single-phonon process unless there is enhancement due to a resonance.

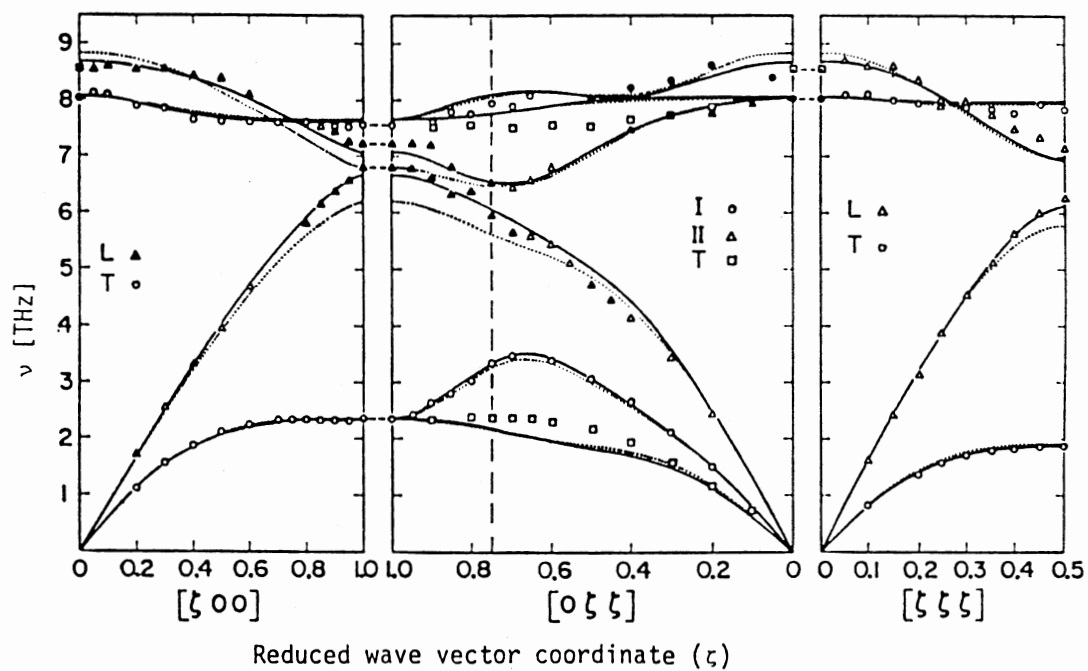


Figure 10. Phonon dispersion relations of GaAs. The horizontal axis is in the wavevector of phonons to several different directions. L is longitudinal phonons, T is transverse mode. The upper two sets of curves are optical branches, while lower ones are acoustic branches.

If the medium is lossy, above conservation rule needs modification. In such cases, it has been shown that there is tolerance in the rule such that [40]

$$\Delta|q| = \text{Im}(\mathbf{k}_1) + \text{Im}(\mathbf{k}_2), \text{ and } \mathbf{q} = \text{Re}(\mathbf{k}_1 - \mathbf{k}_2) \quad (28)$$

Raman scattering efficiency depends on the polarization of the incident and the scattered light. R. Loudon described selection rules deduced from general crystal symmetry groups; if we know that a crystal belongs to a specific symmetry group, we can predict polarization selection rules. In doing so, he assumed that Raman tensors are not a function of  $\mathbf{q}$ . Alternatively, this can also mean cases where  $q \rightarrow 0$  and  $\omega_p \rightarrow 0$ , i.e., the phonon energy and momentum are neglected (dipole approximation). In a certain case when the dipole approximation is true, it is called *allowed scattering*. Otherwise, it is called *forbidden scattering*. In the latter case, selection rules become different from the former case. Forbidden scattering often occurs when Raman scattering is at or close to the resonance of the electronic states in the crystal. In particular, in semiconductors, forbidden LO scattering is often shows stronger resonant behavior to energy states in QWs and SLs than allowed scattering. In some cases, the forbidden two-phonon scattering can be stronger than allowed single-phonon Raman scattering.

Loudon's selection rules state how the efficiency is given depending on polarizations of incident/scattered light in the case of dipole approximation (allowed scattering). According to Loudon, [41] The scattering efficiency  $S$  (per solid angle) is

$$S_{uv} = A \sigma^2 = A [ \mathbf{u}^j \mathbf{R}_{jk} \mathbf{v}_k ]^2 \quad (29)$$

where  $\mathbf{R}_{jk}$  is a 2nd-order Raman tensor, and  $\mathbf{u}$ ,  $\mathbf{v}$  are unit vectors of scattered and incident polarizations of light, respectively. In those equations, repeated indices imply the summation. Remembering that  $\omega_p \rightarrow 0$ , and that the Raman efficiency is proportional to the induced polarization inside of a crystal,  $R$  is related to the macroscopic dielectric susceptibility tensor  $X_{ij}$  in a following manner.

$$\mathbf{u}_j \mathbf{R}_{jk} \mathbf{v}_k = A' \mathbf{u}_i \mathbf{v}_j \mathbf{u}_k \mathbf{v}_l (dX_{ij}/d\omega)(dX_{kl}/d\omega)^*, \quad (30)$$

where  $A'$  is a proper constant. Thus, we see that the Raman efficiency is related to the differential of the dielectric constant [42]. Under the condition of allowed scattering, a phonon symmetry group can be directly linked to a crystal point group. In Table III, the point group pertinent to GaAs-Al<sub>x</sub>Ga<sub>1-x</sub>As superlattices are listed. In backscattering cases from the surface of (100), which is the configuration of this thesis, LO and TO are forbidden according to Loudon's selection rule. As we stated previously, GaAs and Al<sub>x</sub>Ga<sub>1-x</sub>As crystalize in a zincblende structure, which has a  $T_d(\bar{4}3m)$  point group symmetry. When GaAs and Al<sub>x</sub>Ga<sub>1-x</sub>As thin layers are alternatively deposited on a GaAs (100) substrate, the cubic point group of  $T_d$  changes to the trigonal point group  $D_{2d}(\bar{4}2m)$  due to the formation of MQW structures. This change is analogous to the change of symmetry induced by uniaxial stress along [001] direction [43]. Table IV(a) presents allowed Raman tensors for various vibration directions in bulk GaAs. Since lattice displacement (phonons) belong to  $\Gamma_{15}$ , elements are from  $T_d(\bar{4}3m)$  in columns of  $\Gamma_{15}$  in Table III.

TABLE III

## RAMAN TENSORS FOR CRYSTAL SYMMETRY GROUPS

Trigonal											
$\begin{bmatrix} a \\ & a \\ & & b \end{bmatrix} \begin{bmatrix} & c \\ -c & \end{bmatrix} \begin{bmatrix} d \\ & -d \end{bmatrix} \begin{bmatrix} e \\ & e \end{bmatrix} \underbrace{\begin{bmatrix} & f \\ & & g \\ & & & g \end{bmatrix}}_{g} \begin{bmatrix} f \\ & f \end{bmatrix}$											
422	$D_3$										
4mm	$C_{3c}$	$A_1$	$\Gamma_1$	$A_2$	$\Gamma_2$	$B_1$	$\Gamma_3$	$B_2$	$\Gamma_4$	$E$	$\Gamma_5$
42m	$D_{2d}$										
4/mmm	$D_{3h}$	$A_{1g}$	$\Gamma_1^+$	$A_{2g}$	$\Gamma_2^+$	$B_{1g}$	$\Gamma_3^+$	$B_{2g}$	$\Gamma_4^+$	$E_g$	$\Gamma_5^+$
$I_{1111} = a^2 + d^2$ ; $I_{3333} = b^2$ ; $I_{1122} = \frac{1}{2}(a^2 - c^2 + e^2 - d^2)$ $I_{1133} = \frac{1}{2}(ab + fg)$ ; $I_{1212} = e^2 + c^2$ ; $I_{3232} = f^2$ ; $I_{2323} = g^2$											
Cubic											
$\begin{bmatrix} a \\ & a \\ & & a \end{bmatrix} \begin{bmatrix} b \\ & b \\ & & -2b \end{bmatrix} \underbrace{\begin{bmatrix} -3^{1/2}b \\ & 3^{1/2}b \end{bmatrix}}_{3^{1/2}b} \begin{bmatrix} c \\ & c \\ & & d \end{bmatrix} \begin{bmatrix} d \\ & d \end{bmatrix} \begin{bmatrix} c \\ & c \\ & & d \end{bmatrix}$											
23	$T$	$A$	$\Gamma_1$	$E$		$\Gamma_2 + \Gamma_3$	$T$		$\Gamma_4$		
m3	$T_h$	$A_g$	$\Gamma_1^+$	$E_g$		$\Gamma_2^+ + \Gamma_3^+$	$T_g$		$F_4^+$		
$I_{1111} = a^2 + 4b^2$ ; $I_{1122} = \frac{1}{2}(a^2 - 2b^2 + dc)$ ; $I_{2121} = c^2$ $I_{1212} = d^2$											
$\begin{bmatrix} a \\ & a \\ & & a \end{bmatrix} \begin{bmatrix} b \\ & b \\ & & -2b \end{bmatrix} \underbrace{\begin{bmatrix} -3^{1/2}b \\ & 3^{1/2}b \end{bmatrix}}_{3^{1/2}b} \begin{bmatrix} c \\ & c \\ & & -c \end{bmatrix} \begin{bmatrix} c \\ & c \\ & & -c \end{bmatrix} \begin{bmatrix} d \\ & d \\ & & d \end{bmatrix} \begin{bmatrix} d \\ & d \\ & & d \end{bmatrix}$											
432	$O$	$A_1$	$\Gamma_1$	$E$		$\Gamma_3$	$\Gamma_{12}$	$T_1$		$\Gamma_4$	$\Gamma_{15}$
43m	$T_d$										
m3m	$O_h$	$A_{1g}$	$\Gamma_1^+$	$E_g$		$\Gamma_3^+$	$\Gamma_{12}^+$	$T_{1g}$		$\Gamma_4^+$	$\Gamma_{25}^+$
$I_{1111} = a^2 + 4b^2$ ; $I_{1122} = \frac{1}{2}(a^2 - 2b^2 + d^2 - c^2)$ ; $I_{1212} = d^2 + c^2$											

NOTE: Two different notations are given. 422,4/mmm, E,  $A_1$ , etc., are Schoenflies notation;  $D_4$ ,  $D_{2d}$ ,  $\Gamma_5$ ,  $\Gamma_1$ , etc. are Hermann-Mauguin notations. Only Trigonal and Cubic groups are listed.

SOURCE: M. Cardona, *Resonance Phenomena in Light Scattering in Solids II*, edited by M. Cardona and G. Güntherodt, (Springer, Berlin, 1982)



TABLE IV

RAMAN TENSORS FOR PROCESSES IN GaAs, GaAsAl<sub>x</sub>Ga<sub>1-x</sub>As  
QUANTUM-WELLS AND SUPERLATTICES

(a)

$$\bar{R}_{H}(u_x) = \begin{pmatrix} 0 & 0 & 0 \\ 0 & 0 & a \\ 0 & a & 0 \end{pmatrix} \quad \text{for phonon displacements along } \hat{x};$$

$$\bar{R}_{H}(u_y) = \begin{pmatrix} 0 & 0 & a \\ 0 & 0 & 0 \\ a & 0 & 0 \end{pmatrix} \quad \text{for displacements along } \hat{y};$$

$$\text{and } \bar{R}_{H}(u_z) = \begin{pmatrix} 0 & a & 0 \\ a & 0 & 0 \\ 0 & 0 & 0 \end{pmatrix} \quad \text{for displacements along } \hat{z}.$$

(b)

For q along x

$$\bar{R}_{H}(u_x) = \begin{pmatrix} A & 0 & 0 \\ 0 & A & 0 \\ 0 & 0 & A \end{pmatrix}; \quad \bar{R}_{H}(u_y) = \begin{pmatrix} D & E-C & 0 \\ E+C & -D & 0 \\ 0 & 0 & 0 \end{pmatrix}; \quad \bar{R}_{H}(u_z) = \begin{pmatrix} 0 & 0 & -B \\ 0 & 0 & 0 \\ B & 0 & 0 \end{pmatrix}$$

For q along y

$$\bar{R}_{H}(u_x) = \begin{pmatrix} D & E+C & 0 \\ E-C & -D & 0 \\ 0 & 0 & 0 \end{pmatrix}; \quad \bar{R}_{H}(u_y) = \begin{pmatrix} A & 0 & 0 \\ 0 & A & 0 \\ 0 & 0 & A \end{pmatrix}; \quad \bar{R}_{H}(u_z) = \begin{pmatrix} 0 & 0 & 0 \\ 0 & 0 & B \\ 0 & -B & 0 \end{pmatrix}$$

For q along z

$$\bar{R}_{H}(u_x) = \begin{pmatrix} 0 & 0 & -G \\ 0 & 0 & 0 \\ G & 0 & 0 \end{pmatrix}; \quad \bar{R}_{H}(u_y) = \begin{pmatrix} 0 & 0 & 0 \\ 0 & 0 & G \\ 0 & -G & 0 \end{pmatrix}; \quad \bar{R}_{H}(u_z) = \begin{pmatrix} F & 0 & 0 \\ 0 & F & 0 \\ 0 & 0 & F \end{pmatrix}$$

NOTE: (a) Allowed process of bulk GaAs, (b) The forbidden, q-dependent Fröhlich process of GaAs-Al<sub>x</sub>Ga<sub>1-x</sub>As quantum-wells.

SOURCE: J. E. Zucker, Ph. D. Thesis, Columbia University, 1985.

For forbidden scattering cases, Raman tensors depend on  $\mathbf{q}$  so that the rank is now three, viz.,

$$\sigma = \mathbf{u}_i \mathbf{R}_{ijk} v_j \mathbf{q}_k. \quad (31)$$

In QWs, the symmetry group is  $D_{2d}(\bar{4}2m)$  as mentioned. In Reference 44, those tensors are derived for each direction of  $\mathbf{q}$ , by representing each lattice vibrations by a product of symmetry groups given in the  $D_{2d}(\bar{4}2m)$  row of Table III. Results are in Table IV(b). Tensors related to works in this thesis are those with  $\mathbf{q}$  along the z-direction and with  $u_z$  for LO modes, or with  $u_x, u_y$  for TO modes. For example, in a backscattering configuration,  $\mathbf{q}$  has only a z-component since the LO mode vibrates in the z-direction. Then, allowed scattering produces light polarized orthogonally in x-y plane [See Table IV(a)], while the forbidden one is polarized in parallel [See Table IV(b)]. For TO-case, the scattering is not possible without any z-components in both incident and scattering polarizations. It is worth noting that tensors are derived using only the linear term in  $\mathbf{q}$  and there may exist contributions from higher order terms in experimental data. Also, it is based on the symmetry of phonons and the crystal.

### Raman Scattering Spectra

In this section, we present a few typical Raman spectra, as examples. In Figure 11, Raman spectra from various samples are shown. They are taken by experiments carried out in this thesis. (a) is for  $\text{Al}_x\text{Ga}_{1-x}\text{As}$  ( $x=0.18$ ) thin film grown on (100)-GaAs substrate. In (c), the spectra are from a bulk

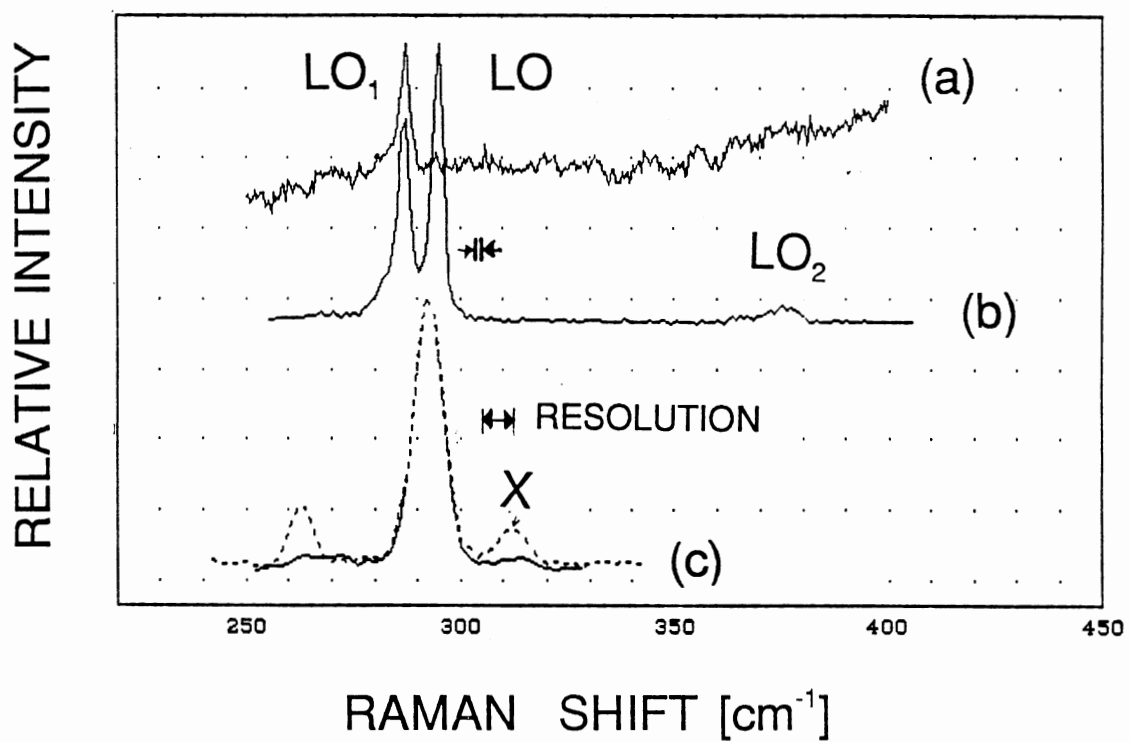


Figure 11. Raman spectra from GaAs- $\text{Al}_x\text{Ga}_{1-x}\text{As}$ . Spectra are from a thin-film of  $\text{Al}_x\text{Ga}_{1-x}\text{As}$  (a), from a superlattice (b), and from a bulk GaAs (c).

GaAs (solid line) and MBE grown GaAs (dotted line). For an example of spectra from superlattices, curve (b) is included. All the spectra are taken with an unpolarized detector at 5K except curves in (c) which are taken at room temperature. Forbidden LO modes have been observed in the backscattering configuration for GaAs and GaAs-Al<sub>x</sub>Ga<sub>1-x</sub>As. They are allowed to the normal to the incident direction (in x or y direction) [77]. On the other hand, allowed TO modes were observed in SLs grown along the [012] direction [48]. It has been known that TO modes also can be observed due to a small angle deviated from normal to the sample z axis. Small TO lines at ~270 cm<sup>-1</sup> have been reported [48]. Also, with certain MBE samples TO modes showed up strong, related to the carbon contents on sample surfaces [49]. Specially, it may be regarded as one indication of the degree of disorientation of samples because TO can be allowed in other than {100} surfaces [50]. For our case, in curve (c) (the dotted curve), TO appears mainly due to this reason, because other samples grown later don't show the same intensity. LO and TO modes are resolved at 293 cm<sup>-1</sup> and 263 cm<sup>-1</sup> in Spectrum (c). The peak X is at 312 cm<sup>-1</sup>, without a clear origin. This may be the interface mode. Also, considering that this spectrum was taken at room temperature in air, this may be some spurious effects due to chemicals left by cleaning procedures, or adsorbed from air. Note that the dotted spectrum is in good contrast with the solid curve which is from bulk GaAs. Here, TO is also much weaker. In the Al<sub>x</sub>Ga<sub>1-x</sub>As thin film, spectra (a), the GaAs-like LO peak appears at 287.79cm<sup>-1</sup>. The AlAs-like LO peak merges

with the background at  $\sim 375 \text{ cm}^{-1}$  and TO is in  $265 \text{ cm}^{-1}$ . The higher background is believed to be the bandedge PL of  $\text{Al}_x\text{Ga}_{1-x}\text{As}$ . For superlattices, or quantum wells, Raman spectra essentially show both GaAs (the well material) phonon peaks at  $294.99 \text{ cm}^{-1}$ ,  $\text{Al}_x\text{Ga}_{1-x}\text{As}$  (the barrier material) phonon peaks at  $287.05 \text{ cm}^{-1}$  (LO, GaAs-like), and  $375 \text{ cm}^{-1}$  ( $\text{LO}_1$ , AlAs-like). See the spectrum (b). This one has resonance enhancements involved. Namely, the strength of each peak may vary differently with respect to the excitation wavelength. This sample is SL I.2 in Table VII. GaAs LO peak is at a slightly different position from that of bulk GaAs [Spectra (c)]. It may be due to either a small calibration difference in spectrometer, or the difference in the temperature [53].

## Determining Axes of Samples

For Raman experiments, it is important to know the actual crystal orientation of samples. According to the convention in Figure 2, Ga atom is at  $a/4 (1,1,1)$ . The surest way to determine the axis of the sample under investigation is preferential etching of (001) surface, with a solution of  $\text{CrO}_3/\text{HF}$  or  $\text{HNO}_3$ . A pyramid form will be formed on the surface. Since the activity of Ga surface is less than the As surface, the plane is Ga-terminated and is  $\{111\}$ . Thus the longest side of a pyramid is parallel to  $[110]$  direction [46]. Another way is to watch cleavage surfaces. The substrate here is on (001). Cleavage planes of zincblende crystals are  $\{110\}$  planes. For GaAs bulk, they are (110) planes and weakly (111) planes [47].

Therefore, a thin sample grown on a (001) GaAs substrate will be cleaved easily to the [110] direction, which is where (110) planes meet (001) surfaces. Perpendicular to [110], the  $[\bar{1}\bar{1}0]$  direction is the other probable cleavage direction on a (001) substrate since it is on (110) planes. When we cleave the sample from a large piece, the easier one should be [110] direction and the other will be  $[\bar{1}\bar{1}0]$ . In practice, it is usually difficult to distinguish them.

For our Raman experiment conditions, the input laser polarization is always parallel to one of edges of cleaved samples. Thus the polarization configurations of experiments are either  $z(x+y,x+y)\bar{z}$  or  $z(x+y,x-y)\bar{z}$  for back scattering experiments.  $z$  is the sample growth direction. The notation is used widely, for example see Reference 49.  $A(B,C)D$  denotes: A,D; the incident, scattered direction vectors, respectively, B,C; the incident, scattered polarization vectors, respectively. The negative direction is indicated by an upper-bar.

In this Chapter, we discussed principles of PLE and Raman scattering in relation to experiments. We have explained why two optical methods are so widely used. For Raman scattering, a few selected topics from the vast amount of underlying physical principles are briefly introduced as they are related to discussions in this thesis. Higher order Raman processes and resonant Raman effects are discussed in the later chapters.

## CHAPTER III

### EXPERIMENTAL SETUP

#### Optics

Optical arrangements are depicted in Figure 12. The laser is a Spectra-Physics dye laser pumped by CW Ar-ion laser operating either at 5145 or 4880 Å wavelength. The kind of dye is chosen to give the required wavelength range for each experiment. In Table V, those used in this thesis are summarized with experimentally obtained maximum wavelength ranges and the peak power as well as a few particular conditions of operation. The sample is mounted on the copper block (cold finger) surface near the optic center of an optical dewar. The dewar is a liquid helium (LHe) refrigerator of a transfer-type (5K, the lowest temperature) or a closed-circle type (15K). In the center of the cold finger surface is a small pass-through hole (2mm $\phi$ ). The spectrometer is either a 0.85-meter double-grating (1408, SPEX Inc., f/6.9) or 0.6-meter Triple-grating (1877, SPEX Inc., f/6.3) with 1200cm<sup>-1</sup> gratings. The scattered light from the sample is collected by the lens L<sub>1</sub>, then focused on the entrance slit of the spectrometer by another lens L<sub>2</sub>. The convergence of light, D<sub>2</sub>/f<sub>2</sub> is usually set to be equal to the numerical aperture of the spectrometer (8, 1403; 4.5, 1877), where D<sub>2</sub> is the diameter and f<sub>2</sub> is

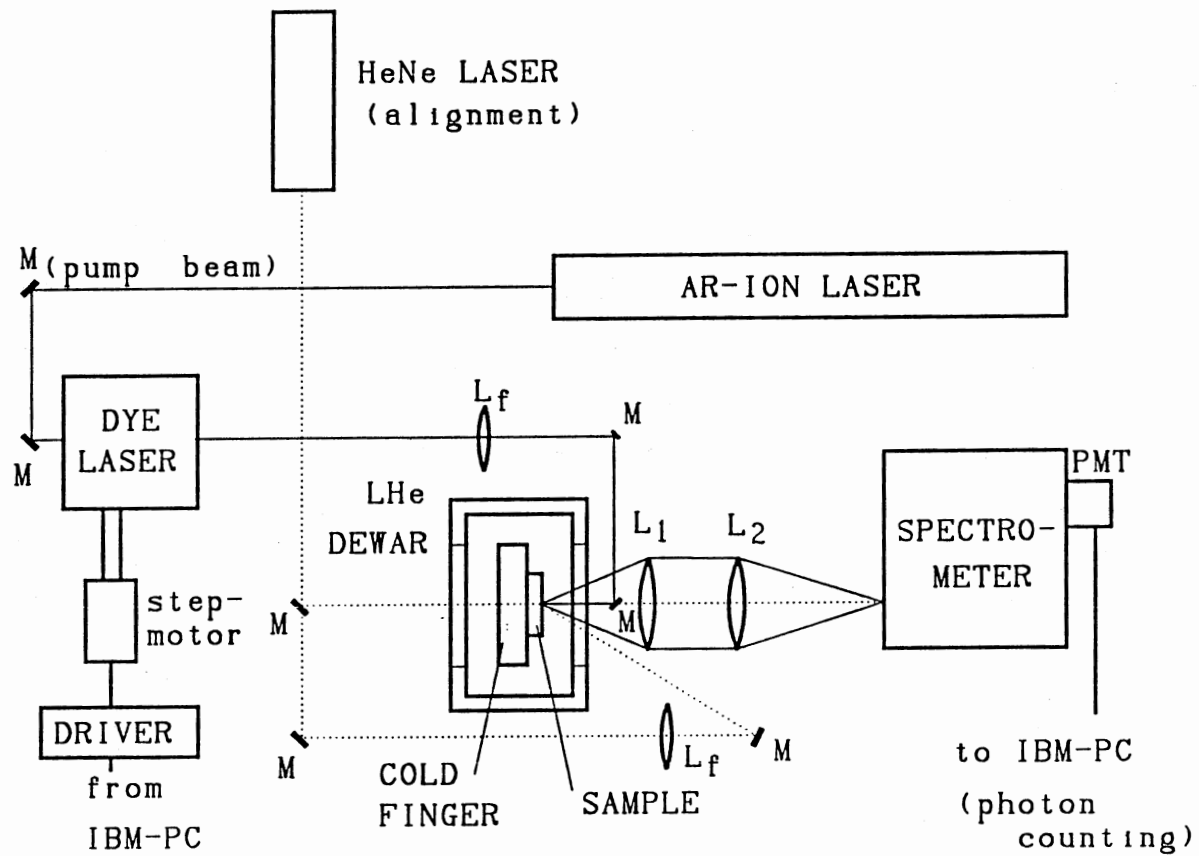
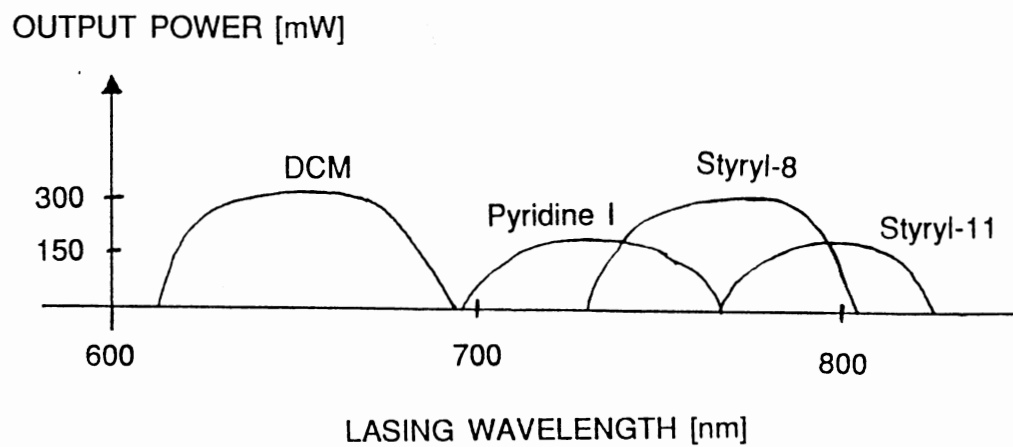


Figure 12. Schematic Diagrams of Experiment.



TABLE V  
RANGES AND POWER OUTPUT OF DYE USED

DYE NAME	Scale <sup>†</sup> (mils)	Range(nm)	Pump power(W) (5145Å)
DCM	145-477	613-692	3.5
Pyridine I (LDS698)	120-330	695-770	2.5
Styryl-8 (LDS751)	226-435	730-806	3.5
Styryl-11 (LDS798)	342-497	768-826	4



<sup>†</sup> The scale depends on the tuning element and the mechanical setting of micrometer.

the focal length of the lens  $L_2$ . This is close to an optimum condition to have full utilization of the spectrometer resolution and minimization of the loss of the signal intensity. However, in reality, the precise location of  $L_2$  is determined through a manual realignment by observing the detected intensity. The alignment to the optic axis is very important in Raman scattering experiments in order to maintain the accuracy of frequency calibration.

In experiments, the optical alignment is done as follows. Lens  $L_1$  should be on a stable 3-axis adjustable translation stage with a micrometer, and  $L_2$  needs a low-precision 3-axis adjustment. In putting lenses in, we make sure that they are perpendicular to the optic axis correctly as possible. One of ways to check this is to observe, on a far target, the motion of the beam as it passes through the lens on the stage. If it is correct, varying the micrometer to two extreme positions should not change the beam position on the target. The axes of the sample holder should be adjusted by the same way. Usually it is a good practice to align the axes of every optical element to directions of mounting holes on a commercial optical table. Following procedures are generally followed in experiments.

- a. Remove all lenses in front of the spectrometer. Set an auxiliary HeNe laser on the optic axis, making sure that the beam passes through centers of entrance-slit, mirrors, mid-slits and the exit-slit of the spectrometer by adjusting the height and the direction of the beam of a HeNe laser which is at a distance of more than a few meters from the spectrometer.

- b. Move the sample holder so that HeNe beam passes through the hole at the center of the cold finger inside of the dewar as precisely as possible. It will be better if we put the tail of dewar together even if the vacuum is not ready.
- c. Use another HeNe beam focused by a long-focal-length lens ( $f \approx 30\text{cm}$ ) to illuminate the center hole of the cold finger. This beam follows on an alternate path outside of the dewar. Using a first surface mirror, make sure that this beam meets the first beam at the center of the hole (the optic axis) of the cold finger. Put a crossed pattern target in front of the entrance slit of the spectrometer. Align the crossing point to the center of the beam. Then, it becomes the location of the optic axis at the entrance of the spectrometer.
- d. Put lens  $L_1$  near its focal point from the sample; then adjust the position so that the first beam passes through the center of  $L_1$ , and hit the center of the cross target. Then, put  $L_2$  so that the beam is approximately focused at the optic axis of the target.
- e. Move the sample holder so that the second HeNe beam hits the copper surface of the cold finger. Then, dim the room light and find a focused spot on the target. Readjust the z-axis of  $L_1$  so that the perimeter of the beam after the lens corresponds approximately to the diameter of  $L_2$ . Then adjust z-axis of  $L_2$  to focus the beam. If you can not get this condition, realign  $L_1$ . Always be familiar with the lens equation of geometric optics [54]. In particular, it is very convenient to remember directions of changes of image positions and magnifications with the change of the distance between the object and the lens.
- f. Now, your lenses are on the optic axis. Therefore, one should be very careful about further adjustments after this point since it is easy to destroy the alignment by varying the micrometer blindly in trying to maximize the signal.

- g. To set the sample on the optic axis, first move the sample holder into a position so that the second beam hits a spot on the sample surface to be examined. Observe the focused target in front of the spectrometer. If it is close to the optimum, one will see a coin-like pattern with a bright spot at the center (diameter  $\sim 10\text{mm}$  or less). If the spot is too dim, move the sample holder to a different point on the sample surface, usually close to the edge. Now, if the spot is not a clear coin-shape, move the z-axis of the **sample-holder**. Do not touch micrometers of the lens stages, yet. If you can not get a coin pattern, the distance between  $L_1$  and  $L_2$  (or their focal lengths) is not correct. Then go back to step e, and repeat. In case that your sample surface is too clean to produce any visible pattern, you can proceed to the next step.
- h. Now remove the target in front of the spectrometer, set the spectrometer to a signal wavelength, and open the shutter. If you do not know the signal position, set the spectrometer at  $6328\text{\AA}$ . It is very easy to over-expose the PMT detector, so be very careful. Put a neutral density filter ( $\sim\text{ND3}$  or more) near HeNe laser, not in front of the spectrometer. Then open the spectrometer shutter. Find the peak, and set the spectrometer.
- i. First maximize the signal by adjusting the position of the second HeNe beam (or any other laser source to use). It can be done just roughly. Then, the fine adjustment of  $L_1$  is in order. First note micrometer readings. They should be near the middle of the micrometer scale. It is not a good idea to adjust  $L_2$  at the same time. First of all, the position of  $L_2$  is not very critical. Thus the small adjustment of  $L_1$  is not only more effective in compensating for the error but the position of  $L_2$  can also be a firm reference. First, adjust **only the x-y axis of  $L_1$** . Then adjust **the z-axis of the sample holder** to maximize the signal. The reason is that the thickness of sample could have changed the focus condition. Remember your focused point was at the bare surface of the

cold-finger. If you have to move  $L_1$  more than 1/4 inch, set the micrometer to the original position, and readjust the position of the second HeNe beam position and the z-axis of the sample holder. Repeat this procedure until you can not improve the signal any more.

- j. Finally, let us emphasize that you should use the adjustment of  $L_1$  only for fine trimming, and use the x-y positions of the secondary beam (or that of the dye laser) plus the z-axis of the sample holder for rough adjustments. One caution is that if you move the z-axis of the sample holder, you will probably have to readjust the x-y position of the beam again since they are not independent of each other in many cases.

To obtain the best signal-to-noise ratio, the performance of lasers is crucial. The dye laser has characteristics as complicated as the molecular structure of dyes. The Ar-ion pump laser also sometimes fails preventing successful carry-out of experiments, particularly, if we run experiments for a long period of time. For resonant Raman scattering experiments, the running time limits the fineness of spectra because of a large number of data points that need to be taken. For example, we have scanned 50 data-point Raman spectra (resolution  $0.2\text{cm}^{-1}$ , increment  $0.5\text{cm}^{-1}$ ) from 680nm to 750 nm excitation with increment of 0.5 nm (1.2 meV), which makes 7000 data-points. This lasted about 4 hours which is practically the limit. Optical multi-channel analyzers are available, but a resolution of better than  $0.5\text{cm}^{-1}$  necessary for resolving Raman peaks in this thesis is still hard to obtain [55].

General properties of dye laser systems are already well known; thus the emphasis here is on documenting particular aspects of lasers which has been

found to affect the quality of data during experiments of this thesis. The first is the intensity stability. The stability of dye laser (Model 375B, Spectra-Physics) was known to depend on the quality of the pump beam and the dye laser alignment. The alignment of the dye laser is not very difficult if one follows detailed procedures given in the equipment manual [56]. See Figure 13. The essence is overlapping three points exactly, i.e., the focal point of the pump beam, the focal point of cavity mirrors, and a uniform spot in the dye jet. From the condition of the factory setup, the focal point of the cavity should be well aligned within the adjustment range of its two external adjustments after we adjust other two focuses. The position of the dye-jet is adjustable independently, first by loosening a knob outside the laser in the pump beam direction and by set/resetting an internal screw at the bottom of the dye jet-assembly. *Too much change may ruin Brewster angle of the dye jet.* In practice, more improvement may be attained if we can improve the jet quality, either by cleaning or by replacing the jet nozzle. It is sometimes necessary to loosen the knob and jiggle the whole jet assembly to have maximum output and fasten it carefully. However, the quality of the jet varies with the dye solution pressure. Too high a pressure may make the dye flow turbulent and overflow (at more than ~100 psi) when we use a low-viscosity dye solution (such as DCM and Styryl 11). The relative position of the cavity focal point is varied by adjusting the end mirror and the output mirror. Two knobs at the outside in the exit direction are for output mirrors. To align the end mirror, we should first identify the proper

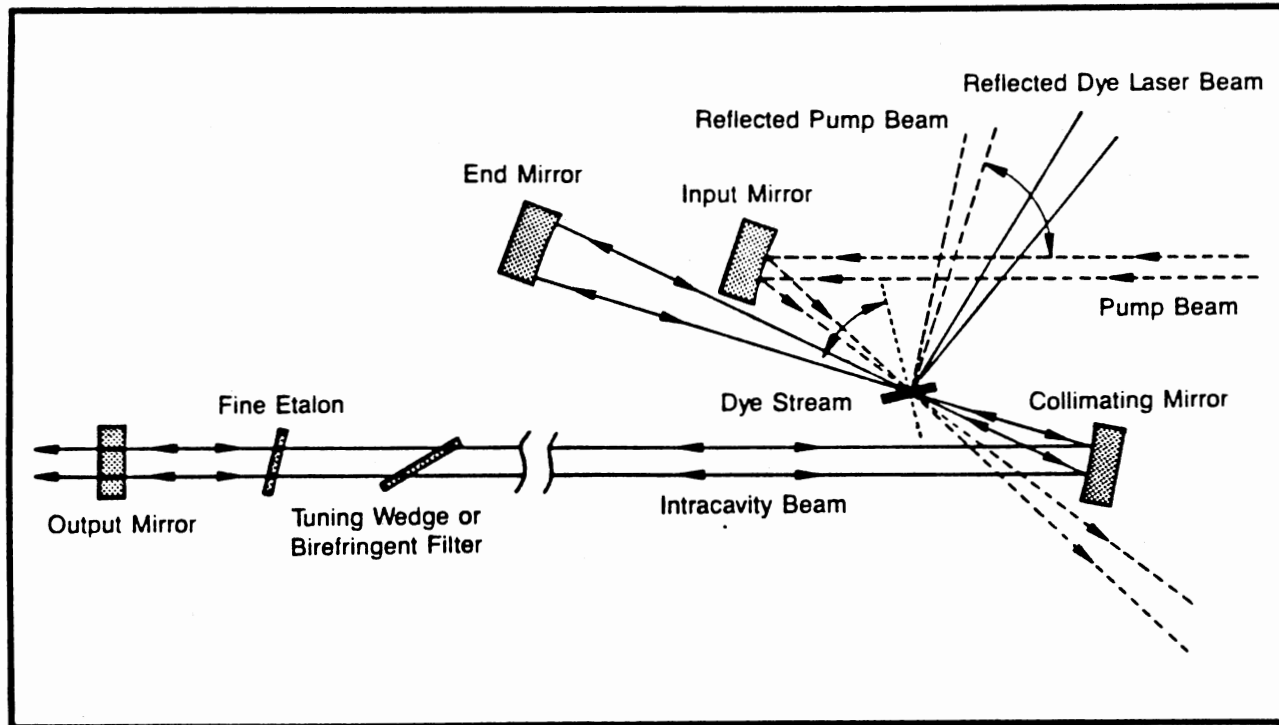


Figure 13. The dye laser beam path in the cavity.

set of hex-head screws inside. All the mounting for mirrors inside are by three adjustable screws. Thus, changing one of them will change distances as well as angles. The initial adjustment of the end mirror and the output mirror for the start of lasing is well documented in the manual. Simply stated, adjust the beam of one round trip to follow exactly the same path and one focal point. This is done more easily if we remove the tuning element which can be in or out without disturbing the alignment. If we put one edge of a thin piece of white paper in the cavity, we can verify if beams are on one path. Then we can usually see it lasing. If not, it is likely that the pump beam is not well focused on the dye jet although the beam seems passing the cavity focal point. Repeat the procedure with different pump beam positions. The focal point of the pump beam is independently adjusted by three screws, one top-outside, one side-wall-outside, and one inside as a pivot of the motion. The pivot screw inside should not be confused with end mirror screws. The only way to adjust the focal length of the pump beam is to turn the pivot screw in or out. One should try to align by a little turn of the pivot at one time and repeat it. Following those precautions has given us a good quality beam in nearly all the cases. In some cases, we could not get the best result after we exhausted the mechanical travel of some of adjustment screws. When this occurs, it is certain that the quality of the pump beam itself has deteriorated.

The pump laser has a few aspects of easy deterioration. The first possibility is at the beam steering mirror. When we put mirrors to steer the



pump beam to a convenient location for the dye laser, we have to use dielectric coated mirrors since an ordinary aluminum coated first-surface mirror significantly damages the pump beam spot quality. Make sure the coating is optimized to near  $45^\circ$  incident angle. After extended usage, the mirror showed a slight decoloring, which may indicate that it should be replaced. The second is deposits at Brewster window of the laser discharge tube. A continuous purging with a dry nitrogen flow can prevent the accumulation of deposits on the window of the tube. For cleaning brewster windows, we used  $\text{CaCO}_3$  wetted with acetone. Using self-holding tweezers with a piece of folded lens-cleaning paper, we scrub the window slightly. It seems better to leave laser on with low power since the observed increase of output power provides a good indicator to stop cleaning. The third and the most serious problem is the deterioration of the laser plasma tube. One symptom of the tube deterioration is difficulty in starting the discharge. The high voltage starting pulse shows bright flash at both the end of the tube in normal operation. We have observed a consistent low Ar-gas pressure in the tube. Then, the tube should be replaced. Finally, a few more minor failures are noticed. The normal water temperature is less than  $45^\circ\text{C}$ . If the water temperature goes up, a few of the passive-bank power transistors in the laser power supply have deteriorated, although they still look normal out of circuit. **One should turn off the power, before doing any check-up.** One way to locate bad transistors is checking the resistance between the chassis and collectors of transistors, with a digital multi-meter. Usually bad ones show

different readings from those of their neighbors. Replacing is the best solution.

In practice, the output power of Ar-ion laser is stabilized in about 30 min. Also, note that the alignments are dependent on the operating current. Thus, if the power level is changed, it is necessary to realign the laser after minimum ~10 min. Remember this adjustment also affects the dye laser since it changes the Ar-ion laser beam direction slightly. Some dyes showed higher output (by more than 50%) after pumping for about an hour. Therefore, when we preparing a long experiment, time should be allocated to ensure laser stabilization. The efficiency of the dye laser (peak beam power over total pump power we obtained in practice was usually between 5% to 15%, depending on the kind of dyes.

We have to know the accurate lasing wavelength with respect to the set position of the micrometer. The relation becomes considerably different after each cavity alignment. For the calibration of the wavelength, we measure them at five or more different micrometer positions accurately using the spectrometer, after each experiment. Then, by interpolation, the relation of the wavelength versus micrometer setting is obtained. The relation is generally quadratic in the micrometer scale. However, a ripple of changes of wavelengths within  $\pm 0.1 \text{ \AA}$  in a period of ~3 mils of the micrometer travel were noticed. It seems to originate from the small degree of interference between surfaces of optical elements consisting of the birefringent filter.

Before we carry out PLE, we should obtain PL spectra first. The spectrometer is then set to one position around the PL peak as desired. Following scanning of the dye laser, we obtain a PLE spectrum. Basic configurations and alignment procedures are the same for Raman scattering or resonant Raman scattering experiments. One more attention should be given in performing RS. The beam spot on the sample should be carefully selected to have the minimum amount of the scattered light directly from a rough sample surface. The direct scattered light from the surface becomes the background to Raman signals. Thus RS should be done after careful cleaning. Also, the many spurious direct reflections from the dewar window are carefully identified and blocked to prevent them from entering the collecting lens,  $L_1$ .

## Programs

The whole experiment controlled by software developed on the APL\*PC development system [57]. Specifically, particular structures and environment functions / variables were created for experiments completed in this thesis. For general information about APL-language, see Reference 58. The language is conceptually object-oriented. The advantage of APL is in its flexibility, which results from being an interactive interpreter. Variables and functions are stored as objects in local workspaces in memory, and, hence, they are available to an operator at any levels of executions. When the execution of a function is suspended, local variables and local workspaces are preserved,

until an instruction is given to nest to the next level. Therefore, various data-fetching routines and experimental parameters are easily accessed and modified. Programming using APL consists of generating a function which is simply a concatenated list of object operations. Each function can contain other functions. There is no fixed difference in the definition between the main routine and subroutines. Parameters can be passed as arguments of functions. The strength of APL language is in its matrix manipulations. Essentially, all the variables are matrices or vectors so that a scalar is equivalent to a zero-length vector, and a matrix of 2 or more dimensions is the concatenation of vectors. The arithmetic or logical functions, etc., are intrinsic and they can perform the operation with any dimensional matrices as long as it is logically valid. This offers a great advantage in processing experimental data which is usually a two dimensional array. Such data can be represented by a single-name variable and almost all intrinsic operations are possible since they are based on the parallel correspondence between indexed elements without explicit indices. The need for indexed-loops is thus greatly reduced compared with other languages such as, FORTRAN. One set of objects, such as, variables, environment parameters, and functions can be incorporated in a group, called *a workspace*. The APL workspace is in fact a disk copy of the whole system memory map (maximum limited by the system memory size; ~300 kbytes under IBM-PC disk operating system). Therefore, temporal running conditions as well as an environment developed for a specific purpose can be preserved so that it can recover and continue precisely

from the previous status. A specific workspace developed in this thesis was named as *DYESPEX*, for convenience. Program functions are listed in the Appendix.

In general, experiments proceed by choosing one of the paths shown in the flow chart in Figure 14. Tasks of *DYESPEX* workspace are:

- a. To control two different spectrometers - set at one frequency, or scan the frequency within a range of frequency by a given increment.
- b. To control of two dye lasers (pulsed Lambda-Physik dye laser, and CW dye laser) - set at one frequency, or scan the frequency within a range of frequency by a given increment.
- c. To accommodate the data-fetch from detectors - photon-counting or A/D conversion.
- d. To show the spectrum on the screen and save data in a file.
- e. To analyze data - regression, fitting, change of units, compression, interpolation, smoothing, etc.

Above tasks are performed approximately in the sequence as shown. The major functional block can be grouped by four subsystems for an easy description. In following subsections, CAPITAL words denote names of actual functions or variables.

### Interface subsystem

The interface subsystem is a menu-driven mediator system which transfers the program control to/from other subsystems. It is the first routine

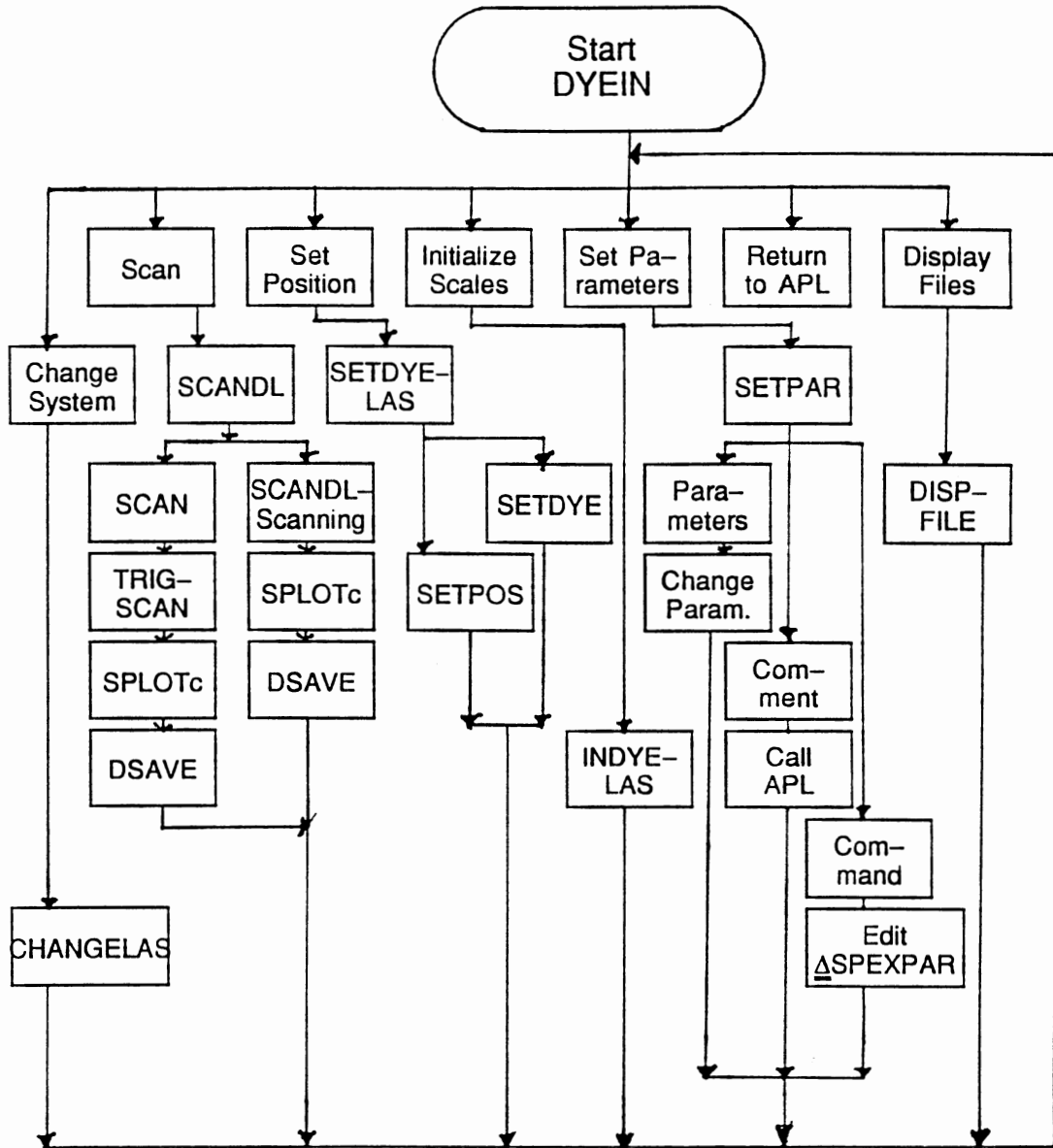


Figure 14. Basic block flow chart of software.

when the system is initialized. Function names are shown, such as DYEIN with capitals, in Figure 14. There are three modes of operations, which are also selected in this subsystem. The modes are:

- a. Spectrometer control. --named SPECTROMETER
- b. Continuous-wave (CW) dye laser control. -- named CW\_DYE
- c. Pulsed-dye laser control. --- named PULSED\_DYE

The pulsed laser system was not used in the experiment. The main roles of this interface subsystem are:

- a. Recover proper experiment description parameters from the disk.
- b. Choose a starting mode and set current parameters with parameters associated with the mode.
- c. Initialize the menu screen.
- d. Reset proper environment variables.

The choice of running other subsystem is given on the screen. When the user presses ENTER - key, the system immediately executes the function associated with the choice. Choices are:

- a. Change the modes -- execute CHANGELAS
- b. Initialize the scale -- execute INDYELAS only if the mode is not SPECTROMETER.
- c. Set position -- execute SETPOSITION.
- d. Scan -- execute SCANDYE.
- e. Set parameters -- execute SETPAR.
- f. Display files -- execute DISPFILE.

- g. Exit to APL --- exit to the original APL environment after saving the parameters of four sets, i.e., the current one, and those of three modes.

CHANGELAS swaps current parameters for a set of parameters of choice. INDYELAS updates current scales of dye lasers. Users are instructed to type in the current reading of the scale after the program moves the scale once-forward and once-backward in order to compensate for the mechanical backlash. This is ignored in SPECTROMETER mode because the spectrometer interface automatically does the work. (CD2A, Spex industry). SETPOSITION executes, in turn, either SETPOS if in SPECTROMETER mode, or SETDYE in CW\_DYE or PULSED\_DYE modes. The function is to move the micrometer scale to a value given by the user. The re-direction of the control pulses between the pulsed dye laser and the CW dye laser is completed manually by an external switch. The user is instructed on the screen as appropriate. SCANDYE chooses between functions SCAN or SCANDL. SCAN drives the spectrometer using TRIGSCAN which controls CD2A. SCANDL scans dye laser scales, by setting a new position repeatedly by a given increment. Parameters, such as, start-scan positions, end-positions, increments, etc., are entered interactively in functions TRIGSCAN, or SCANDL. SETPAR has two roles. One is to alter parameters manually, and the other is to execute various APL functions without leaving the environment. Inside the function, users are asked to choose one of three operations, Comment, Parameter, and Command. The comment parameter ΔSPEXPARG is an editable text describing conditions of



experiments. Three modes have different comment texts. When switched to another mode, the experimental description is the most recent one of the chosen mode. In this way, the user does not need to change the description each time when he switches modes. Parameters, here, refers to a few selected ones, such as calibration factors for dye-scales vs. the number of the control pulses, pulse duties for driving stepping motors, etc. DISPFIL allow the user to see previous data files in a graphic-form. APL component files are structured that many sets of data can be stored in a one APL-file (the extension is \*.ASF) as they are concatenated. Each set is called a component. Our structure is shown in Figure 15. Each samples is assigned to one file, the first component describe the general characteristic of data in the whole file. After that, a description of each experiment is followed by data. In DISPFIL the user can review data and description by choosing component numbers of a file. Each function referred to so far consists of various functions from following subsystems.

### Graphics Subsystem

This subsystem is designed to display data on the screen as a graph, and if the proper command is received, it dumps the screen to the printer. SPLOTc is the main function. It consists of 1) reforming input data, 2) initializing the graphic screen, 3) drawing the frame of a graph, 4) finding the scaling factor for the x and y axes of the graph automatically, 5) decoding line drawing types, 6) drawing graphs, and 7) dumping the graph screen to a printer for a hard copy interactively.

component number	description
#1	Overall description of file
#2	Description for data in #3
#3	The first data
#4	Description for data in #5
#5	The second data
#6	Description
#7	Data
.	.
.	.
.	.

Figure 15. The APL-component file structure for the experimental environment.

## Scanning Subsystem

The scanning subsystem consists of functions to control the spectrometer, the dye laser, and the pulsed dye laser. In general, it first asks the user for parameters and data-fetch functions, and then it starts scanning. When the scanning is completed, it calls SPLOTc to show data obtained, then prompts to the user, whether it will save the data in a component-file. In doing so, users are given a chance to modify the experimental description,  $\Delta$ SPEXP. On exit, it usually returns to the interface subsystem. In SETDYE, PULSE1 calls a machine language routine  $\Delta$ PULSE to generate a number of square pulses at a binary output port to be used for the dye-laser driver. SCAN, SCANDL, SETPOS, SETDYE and their subfunctions from function-tool subsystem belong to this.

## Data-fetch subsystem

For data acquisition, three functions are designed to obtain data by photon-counting, A/D-conversion, and Raman-scanning. For photon-counting, PCOUNT is designed. Inside of this function, an assembler language routine  $\Delta$ PCOUNT is called. It sets up two 16-bit counters, one for counting pulses from the photomultiplier tube (PMT), and one for the time-base. The exit condition can be two-fold, either the maximum-count determined, or the time-duration determined. The first has a higher priority. Results are given in the unit of count per second, by dividing two numbers properly. A to D conversion function, ADN, also calls a machine language routine  $\Delta$ ADN to

get an average of the data, for a given time-duration, from a proper A/D converter port. Non-averaging A/D conversion is done by VOLTIN. RAMANSCAN is for Raman scattering experiments exclusively. It is in fact a function for scanning the spectrometer. It is designed to scan the spectrometer around a current position, in a given range by a given increment. Results are given by detecting two (or any numbers of) peaks within a predetermined width-range from obtained data with PCOUNT. It uses TRIGSCAN and RAMANPEAK functions. RAMANPEAK is for reading two peak intensities of LO and LO<sub>1</sub> phonon-modes. It calls PEAK function in the function-tool subsystem.

### Function tool subsystem

There is a large number of functions (~60) to help manipulation of data efficiently. Each of them carries a very specific role of data or interface manipulation. There are so many that we describe only a few here:

AND: Concatenates two individual vectors of same length to be a x-y data array.

AUTOSC: Gives an automatic minimum and maximum of a 2-dimensional matrix both in x-scale, and in y-scale.

INIT, CLOSE: Initialize, de-initialize the graphic-screen and normal text-screen.

- DECBCD, BCDDEC:           Number conversion between decimal and binary-coded-decimal (BCD) numbers.
- DIM:           Gives lengths of partitioned strings delimited by a given delimiter from a larger string variable.
- PIC:           Picks a partition of a string delimited by its first character.
- PICARG:       Picks a partition like PIC does, and changes the results into a vector of numbers.
- PEAK:         Extracts peak values of the first, second, etc., with a given resolution, simply by rearranging or sorting elements of the input vector by their magnitudes.
- TCKL2:       Marks fine ticks in graphs, by given parameters.
- ΔFxxxxx:     For various I/O operations to a component file.
- ΔNxxxxx:     For various I/O operations to a natural file (IBM-PC DOS-ASCII format).

## CHAPTER IV

### SAMPLES FOR EXPERIMENTS

Samples used in this thesis were grown by molecular-beam-epitaxy (MBE) technique to ensure high quality. High quality of samples is prerequisite to observing detailed properties of excitons. In this Chapter, first, we explain MBE techniques briefly, and a few techniques for the characterization of sample parameters. Secondly we give descriptions of materials and dimensions of all the samples.

MBE has been very successful in growing III-V family of semiconductors, especially GaAs and AlAs or their alloy,  $\text{Al}_x\text{Ga}_{1-x}\text{As}$ . For a list of works about MBE for III-V semiconductors refer to Reference 59. The current status of technology is that we can control 1/2 monolayer (1 ML = 2.83 Å) in the thickness of layers. MBE technology utilizes migration of molecules in the ultra-high vacuum (UHV;  $10^{-10}$  torr or less). In the growth chamber (see Figure 16) [3], there are gallium, arsenic, aluminum molecular sources (effusion cells), or other sources, shrouded by liquid nitrogen, and equipped with individual shutters. Walls of effusion cells are cooled to improve isolation and to prevent outgasing into UHV. In direct paths from those sources lie highly-clean substrates, usually (001)-GaAs, on a temperature-controlled mount. Due to the ultra-high vacuum which requires time-

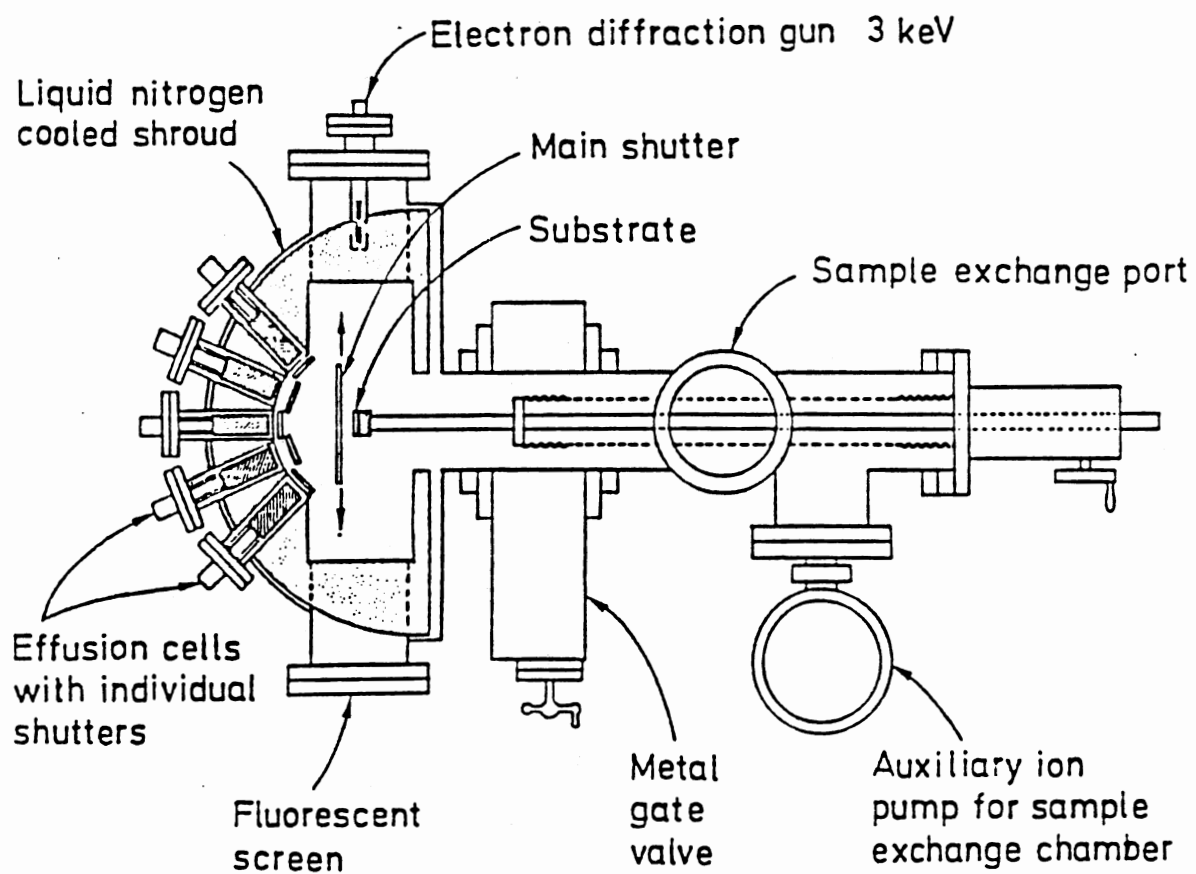


Figure 16. A simple Molecular-Beam-Epitaxy growth chamber. (After 3)

consuming procedures to reach, substrates pass through double (or more) successive vacuum chambers each of which has a different degree of vacuum so that we can change samples without breaking the vacuum of the main chamber. To monitor the thickness of layers deposited, *in situ* low-energy electron diffraction (LEED), or reflection high energy electron diffraction (RHEED) are used. Other characterization tools are usually incorporated. Sometimes, Raman scattering is used while growing samples to measure the concentration of excited carriers by the plasmon-frequency. The thickness is controlled by the length of time when the shutter is open.  $\text{Al}_x\text{Ga}_{1-x}\text{As}$  layers of various  $x$  values are grown by proportional fluxes Ga- and Al-sources. There was an important technological progress in the interface quality-control when a number of groups discovered, so called, the Interrupt Growth. Namely, the growth of layers is stopped for a few minutes before growing different kind of layers [60]. Nowadays, the interface can be made well-defined within  $1/2$  ML so that we can grow SLs with the period of only a few monolayers (less than 10 ML) precisely from a GaAs-AlAs system.

Substrates of all the GaAs- $\text{Al}_x\text{Ga}_{1-x}\text{As}$  superlattice (SL) samples investigated in this thesis are a semi-insulating (100) GaAs. SL samples consist of 20 to 50 periods of well- and barrier-layers; thus SL layers are about  $0.5 \sim 1.5 \mu$  thick. Sample parameters are chosen to be in a few different sets. In each set, their growth conditions are kept as uniform as possible by growing in the same vacuum chamber within a relatively short period of time. In one set, the well size and the aluminum concentration in



the barrier layer were fixed. Well widths are between 60 to 150 Å, barrier widths are 30 to 180 Å, and the aluminum concentration at the barrier is  $x$ , and it was 14%, 18%, 22%, and 21%. Sample parameters are determined initially by MBE growth conditions. Optical transitions are measured at 5 K or 15 K using PL and PLE techniques. Positions of transitions are compared with a theoretical calculation using parameters from growth conditions. Then, values are modified and the energy is recalculated. Values are finalized after a few of such iterations. For  $L_b$  and  $L_z$ , we compared values obtained by PLE to cross sectional transmission electron microscopy (TEM). The results were very consistent between both the methods. See Table VI for a comparison on a set of samples.

The aluminum concentration in the barrier,  $x$ , is determined by measuring the low energy side onset of PL signal, which is the bandedge of the material. Since the energy is given by for  $\text{Al}_x\text{Ga}_{1-x}\text{As}$  as Equation (2), we can obtain  $x$ . The value of  $x$  can be also measured from Raman scattering. The energy of phonon modes is unique so that the accurate measurement of Raman spectra can give  $x$ -values. We determine the  $x$ -value relatively as shown in Figure 17. Three curves corresponds to three different  $x$ -values. The absolute phonon energies measured with SL samples, however, are slightly different from bulk phonon energies given by widely-quoted values in Reference 9. Usually the discrepancy is too small compared to the experimental accuracy to claim the differences. In a bulk  $\text{Al}_x\text{Ga}_{1-x}\text{As}$ , the energy of the GaAs-like LO mode (denoted by  $\text{LO}_1$ ) has been known as [9]

TABLE VI  
THE COMPARISON OF SAMPLE PARAMETERS  
-AN EXAMPLE-

	PLE	TEM	Raman	X-ray
	$L_z[A]$	$164 \pm 3$	$163 \pm 2$	$169 \pm 5$
A	$L_b[A]$	$158 \pm 3$	$159 \pm 2$	$169 \pm 5$
	X[%]	$21 \pm 0.5$	$21 \pm 0.3$	$20 \pm 1$
	$L_z[A]$	$74 \pm 3$	$78 \pm 2$	$76 \pm 5$
B	$L_b[A]$	$74 \pm 3$	$74 \pm 2$	$76 \pm 5$
	X[%]	$21 \pm 1$	$21 \pm 0.3$	$20 \pm 1$
	$L_z[A]$	$79 \pm 3$	$78 \pm 2$	$80 \pm 5$
C	$L_b[A]$	$59 \pm 3$	$60 \pm 2$	$70 \pm 5$
	X[%]	$18 \pm 1$	$18 \pm 0.3$	$17.5 \pm 1$

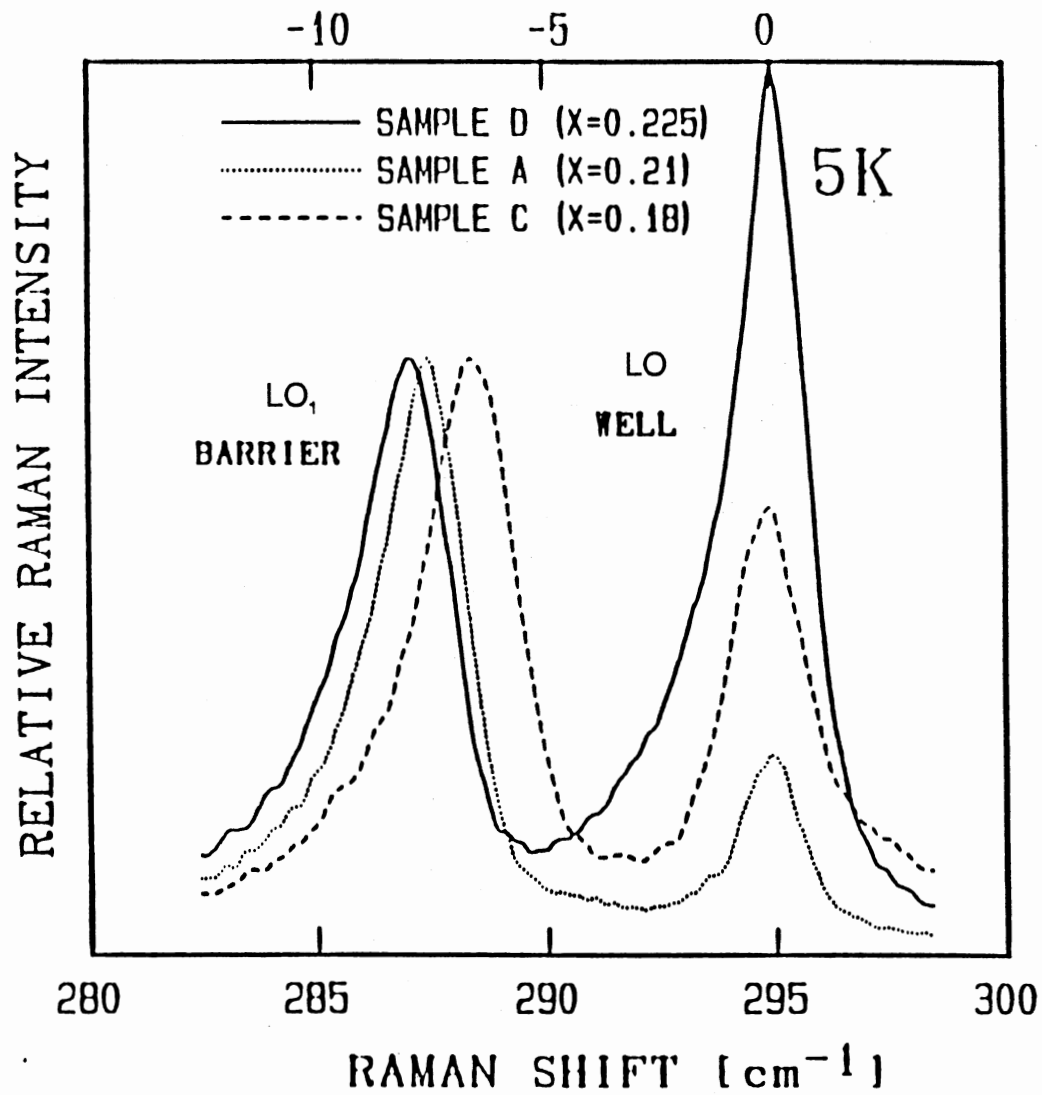


Figure 17. The relative determination of  $x$  from Raman spectra. The differences between LO and LO<sub>1</sub> depending on  $x$  values are illustrated. The aluminum concentration in the barrier,  $x$ , can be determined with high accuracy, better than any other characterization techniques.

$$E_{LO1} = 36.25 - 6.55x + 1.79x^2 \quad [\text{meV}]. \quad (32)$$

Our result shows only the first order coefficient,  $dE_{LO1}/dx = -4.34$  [meV/x], which is obtained by the least-squared-error estimation starting from roughly known values of  $x$  of three samples. Some of them were sent out to verify the values by X-ray diffractometry known as *X-ray rocking curve fit* where the difference between internal stresses in GaAs and  $\text{Al}_x\text{Ga}_{1-x}\text{As}$  layers are detected by the shape of a particular peak in X-ray scattering.

The summary of parameters of samples used in this work is listed in Table VII. In the first series, SL I.1-I.4 are designed to investigate the first unconfined states. Thus, widths of well and barrier are chosen to ensure that resonant conditions are met with those values. In the second series, SL II.1-II.5, we observed other kinds of resonances presented in this thesis. The third series, SL III.1-III.4, showed a little smaller dispersions than SL I-series, due to the higher  $x$  and had the same purpose as the second series. For each of the latter two series, a thin film sample of  $\text{Al}_x\text{Ga}_{1-x}\text{As}$  layers are grown with the same condition as corresponding SL samples to verify the value of  $x$  more precisely and independently.

TABLE VII  
THE LIST OF SAMPLES USED IN EXPERIMENTS

Sample name	$L_z(\text{Å})$	$L_b(\text{Å})$	$x$	$N^\dagger$	comment
SL I.1	150	180	0.22	20	
SL I.2	150	150	0.22	20	
SL I.3	150	120	0.22	20	
SL I.4	150	70	0.22	20	
SL II.1	82	150	0.18	25	
SL II.2	75	105	0.18	30	
SL II.3	75	60	0.18	40	
SL II.4	75	35	0.18	50	
BL II.5	-	-	0.18	-	Thin film
SL III.1	59	130	0.14	25	
SL III.2	59	99	0.14	30	
SL III.3	59	75	0.14	40	
SL III.4	59	51	0.14	40	
SL III.5	59	32	0.14	50	
BL III.6	-	-	0.14	-	Thin film
SL IV.1	70	70	0.21	20	

<sup>†</sup> Number of the periods.

# CHAPTER V

## EXCITONIC RESONANCE IN FIRST UNCONFINED STATES

### Doublet Above Potential Barrier

In quantum well structures, quantized electronic states confined in GaAs layers occur with energies below  $\text{Al}_x\text{Ga}_{1-x}\text{As}$  potential barriers. These states have been extensively studied [61,62]. In superlattices, quantized electronic states can also be formed above the periodic potential barrier. These are called unconfined states or extended states [65]. They have not received as much attention [63-66]. It has been reported experimental and theoretical results on the sensitivity of the strengths of optical transitions between unconfined valence and conduction states to the barrier layer thickness [66]. According to those results, excitonic wavefunctions can resonate to the width of the barrier in such unconfined states for a certain range of barrier widths.

As the first case of an excitonic resonance, in this section, we discuss the observation of energy splitting by means of photoluminescence excitation (PLE) spectroscopy, in optical transitions between unconfined electron and hole minibands in  $\text{GaAs-Al}_x\text{Ga}_{1-x}\text{As}$  superlattices. The energy splitting arises from different transition energies at the Brillouin zone (BZ) - center (ZC) and

the BZ - edge (ZB). We find that the energy separation between two optical transitions is very sensitive to the width of the GaAs-Al<sub>x</sub>Ga<sub>1-x</sub>As barrier. The observed splitting is in excellent agreement with theoretical calculations based on a two-band tight binding model (TBA) [14,66].

The energy level splittings discussed in this section are associated with the dispersion of energy states along  $k_z$ , the wave vector along the superlattice growth direction (z-axis). Figure 18 depicts a simplified picture of the energy dispersion of an electron and a hole state along  $k_z$ . As we discussed in Chapter I, this dispersion leads to the formation of a miniband in superlattices for each quantized state, as indicated by hatched lines in Figure 18. The width of the miniband is the energy difference between the quantized state at  $k_z = 0$  and  $k_z = \pi/d$ , where  $d$  is the sum of the well layer thickness,  $L_w$ , and the barrier layer thickness,  $L_b$ . Since optical transitions can take place between the valence and the conduction minibands at any point along  $k_z$ , the optical transition energies vary as a function of  $k_z$ . The strengths of transitions also vary along  $k_z$ .

Peaked structures in PLE spectra, which will be discussed below, imply that there is a certain kind of excitonic enhancement occurring for the transitions of concern here. The first unconfined conduction miniband decreases in energy away from the Brillouin zone center, while the heavy hole band increases in energy. Assuming that the energy dispersion is bulk-like in the direction parallel to the superlattice layers, the transition at the zone center is that of the  $M_1$  critical point, and that at the zone edge is more

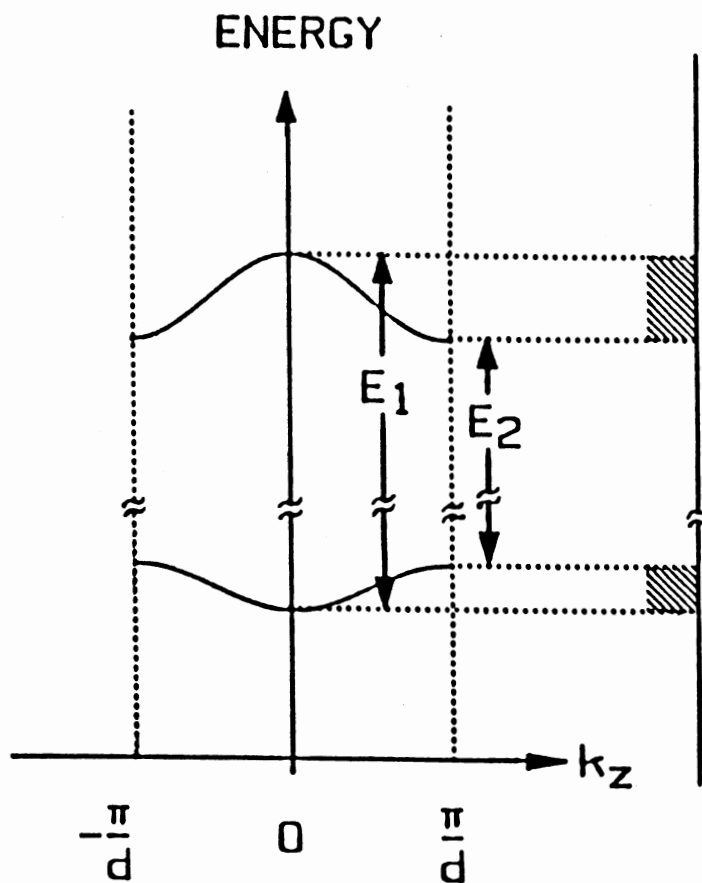


Figure 18. Simplified energy band diagram. One representative conduction and valence miniband are shown. The optical transition energies at the Brillouin zone (BZ) center and the BZ edge are denoted by  $E_1$  and  $E_2$ , respectively. The hatched areas show the widths of the minibands.



familiar  $M_0$  critical point. Since the  $M_1$  critical point represents a saddle point, the exciton is degenerate with the minibands and must therefore be a resonance.  $M_1$ , as well as the usual  $M_0$ , critical points have been shown theoretically to support enhanced and sharpened features in the absorption spectra [67]. Consequently, the transition between these valence and conduction minibands can indeed appear as doublets in the spectra. The separation between the two transitions,  $\Delta E$ , will be  $\Delta E = E_1 - E_2$ , where  $E_1$  and  $E_2$  denote the transition energies at  $k_z = 0$  and  $\pi/d$ , respectively. Here, we assume that the binding energies of the excitons are approximately the same at the two critical points. We will show experimentally that these splittings can be very sensitive to the barrier layer widths.

The GaAs- $\text{Al}_x\text{Ga}_{1-x}\text{As}$  superlattice (SL) samples investigated in this section were grown by molecular-beam-epitaxy (MBE) on (100) GaAs substrates. The well size and the aluminum concentration in the barrier layer were fixed. The barrier widths of the SLs were varied from 70 Å, to 180 Å. The sample parameters were determined by the MBE growth conditions and transmission electron microscopy measurements. The details are given in Chapter IV. The samples are SL I.1 to I.4 in Table VII. The optical transitions were measured from SLs at 5 K using photoluminescence (PL) excitation spectroscopy techniques [66].

Figure 19 shows PLE spectra taken from the four GaAs- $\text{Al}_{0.22}\text{Ga}_{0.78}\text{As}$  superlattices with  $L_z = 150$  Å in the vicinity of the barrier energy gap  $E_B \sim 1.793\text{eV}$ . The detector was set at the PL peak of each sample, which occurred

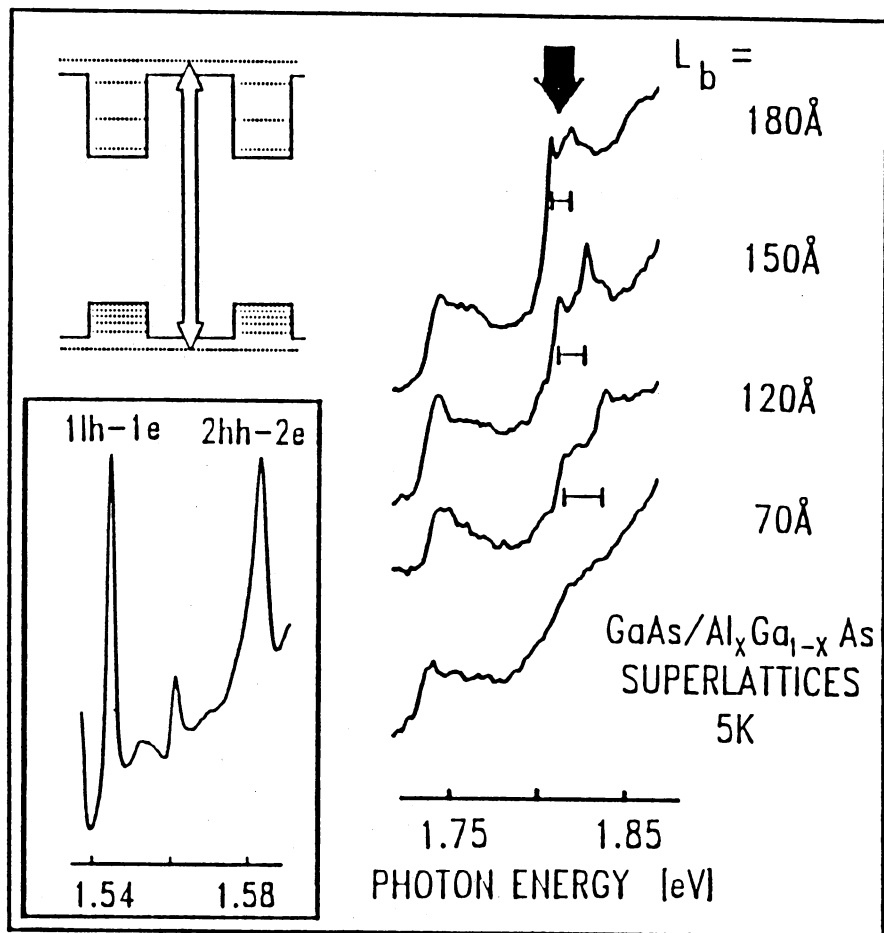


Figure 19. PLE spectra taken from GaAs/Al<sub>0.22</sub>Ga<sub>0.78</sub>As superlattices (SLs) with well widths  $L_z = 150 \text{ \AA}$ . The barrier widths  $L_b$  are  $180 \text{ \AA}$ ,  $150 \text{ \AA}$ ,  $120 \text{ \AA}$ , and  $70 \text{ \AA}$ . The PLE doublets are indicated by the thick arrow in the spectra and the corresponding transitions are depicted on the upper left corner. The separations of doublets are indicated by the horizontal bars. The inset shows the low energy side of the PLE spectrum taken from the SL sample with  $L_b = 150 \text{ \AA}$ . Similar spectra were obtained in this region from the other SLs shown here.

at  $\sim 1.529$  eV. The inset in Figure 19 shows an example of the low energy side of the PLE spectra. The excitonic transitions marked (1lh - 1e) and (2hh - 2e) represent optical transitions from  $n = 1$  light-hole to  $n = 1$  electronic states and  $n = 2$  heavy-hole to  $n = 2$  electronic states, respectively. Also, the peak at  $\sim 1.74$  eV in Figure 19 varies only slightly with the changes in the barrier width. Theoretical calculations indicate that this peak is probably a combination of several closely spaced transitions, including (4hh - 4e).

Strong variations in the spectra are noticed above  $E_B$  with the changes in the barrier widths. The large step indicated by the thick arrow is very significant for  $L_b = 180$  Å, whereas it is hardly distinguishable for  $L_b = 70$  Å.

A similar trend was also observed in a series of GaAs-Al<sub>0.2</sub>Ga<sub>0.8</sub>As superlattices with  $L_z = 150$  Å and  $L_b = 30$  Å, 70 Å, and 150 Å [66]. The step is due to the transition from the first unconfined valence state to the first unconfined conduction state. These are the sixth heavy-hole (6hh) and the fourth conduction (4e) states counting from the top of the valence band and the bottom of the conduction band of GaAs. We previously reported that the strengths of these transitions are barrier-width-dependent [66]. According to calculations carried out for the four superlattice barrier thicknesses, the transition matrix elements are insignificant for the  $L_b = 70$  Å sample, whereas they are very large for the others. This is consistent with experimental observations.

In Figure 20, we demonstrate the resonance behavior of those wavefunctions. A large overlap between the valence and conduction states

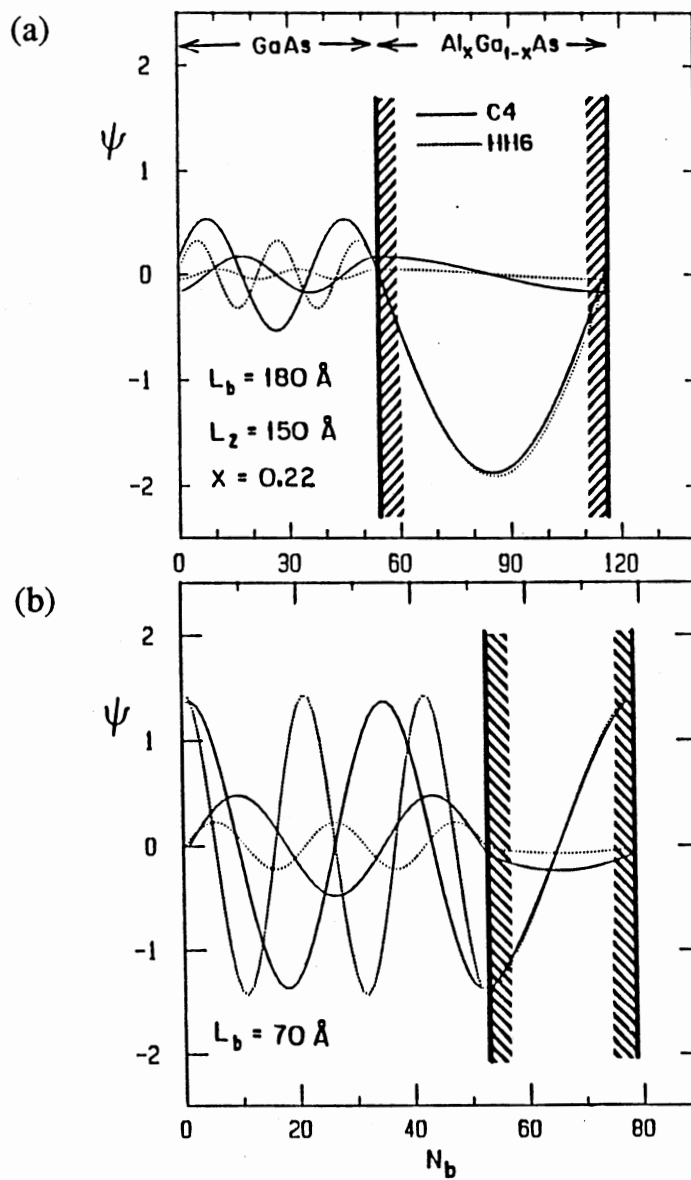


Figure 20. Comparison of wavefunctions of first unconfined states, between two samples; (a)  $L_b = 180 \text{ \AA}$ , and (b)  $L_b = 70 \text{ \AA}$ . The wave functions represent the first unconfined valence (HH6), dotted line, and conduction (C4), solid line, states at zone center of GaAs- $\text{Al}_x\text{Ga}_{1-x}\text{As}$  superlattices with  $L_z = 150 \text{ \AA}$  and  $x = 0.22$ .  $N_b$  is the number of GaAs and  $\text{Al}_x\text{Ga}_{1-x}\text{As}$  atomic layers.

leads to a large optical transition intensity. The  $L_b = 180 \text{ \AA}$  case (a) shows a larger portion of the wavefunction confined in the barrier region, in comparison to the  $L_b = 70 \text{ \AA}$  case(b). This resonant behavior at the barrier region can not appear either in confined states below barrier height or in single quantum well cases, because the wavefunctions are either damped rapidly into the barrier or are propagating in nature, giving a trivial overlap intensity. An exact picture of the excitonic behaviors, however, is more complicated than shown here since the calculation does not include the excitonic interactions which cause the sharp structures in Figure 19. The parameters used in the calculation are the same as given in the second section in Chapter I. And the valence band offset is 40% of the energy gap difference.

In Figure 19, two peaks are found for each spectrum between 1.8 and 1.85 eV, except for the one with  $L_b = 70 \text{ \AA}$ . Both of the doublet peaks are due to the first unconfined miniband transitions. The lower energy peak is attributed to the BZ-edge transition, whereas the higher one, to the BZ center transition. The energy separations between the two peaks, which are indicated by the horizontal bars, correspond to  $\Delta E = E(k_z = 0) - E(k_z = \pi/d)$  in Figure 18. In the spectra, these energy splittings are found to be dependent upon the barrier layer widths.  $\Delta E$  becomes smaller as  $L_b$  increases. The experimentally measured energy splittings are in very good agreement with calculated energy separations  $\Delta E$  as shown below. There may be other optical transitions in the vicinity of the doublets shown in Figure 19. In our

calculations, however, we could not identify any such transitions with energy separations matching the observed splittings.

In Figure 21, the calculated energy splittings of the unconfined transition,  $\Delta E$ , are plotted as a function of the barrier width. The squares represent experimental data points. The measured splittings are 11.5 meV, 15 meV and 22 meV for sample with  $L_b = 180 \text{ \AA}$ ,  $150 \text{ \AA}$ , and  $120 \text{ \AA}$ , respectively. These values are in very good agreement with calculated values [solid line, Figure 21(a)] of 9.6 meV, 15.0 meV, and 23.8 meV for the corresponding  $L_b$  values. For the SL with  $L_b = 70 \text{ \AA}$ ,  $\Delta E$  is calculated to be 40.1 meV. It is difficult to identify well defined peaks in the experimental data, but this is consistent with the theoretical calculation that the strength of the transition is very small for this case [66].

We also show, in Figure 21(b), the plot of  $\Delta E$  vs  $L_b$  for  $n = 3$ ,  $\Delta n = 0$ , confined heavy-hole optical transitions calculated for the same sample parameters. As can be seen, there is a marked difference between  $\Delta E$  vs  $L_b$  for the confined transitions and  $\Delta E$  vs  $L_b$  for the first unconfined transitions. In fact, for small  $\Delta E$ s such as those obtained for 3hh excitons, the splittings may be masked by exciton broadenings. For unconfined transitions, it is apparent that  $\Delta E$  is closely related to  $L_b$ . In particular, the dispersion of  $\Delta E$  with respect to  $L_b$  is quite significant for  $L_b < 250 \text{ \AA}$ . This implies that the  $L_b$  values can be deduced from the measurement of the energy splittings of the first unconfined states, once the other sample parameters are known.

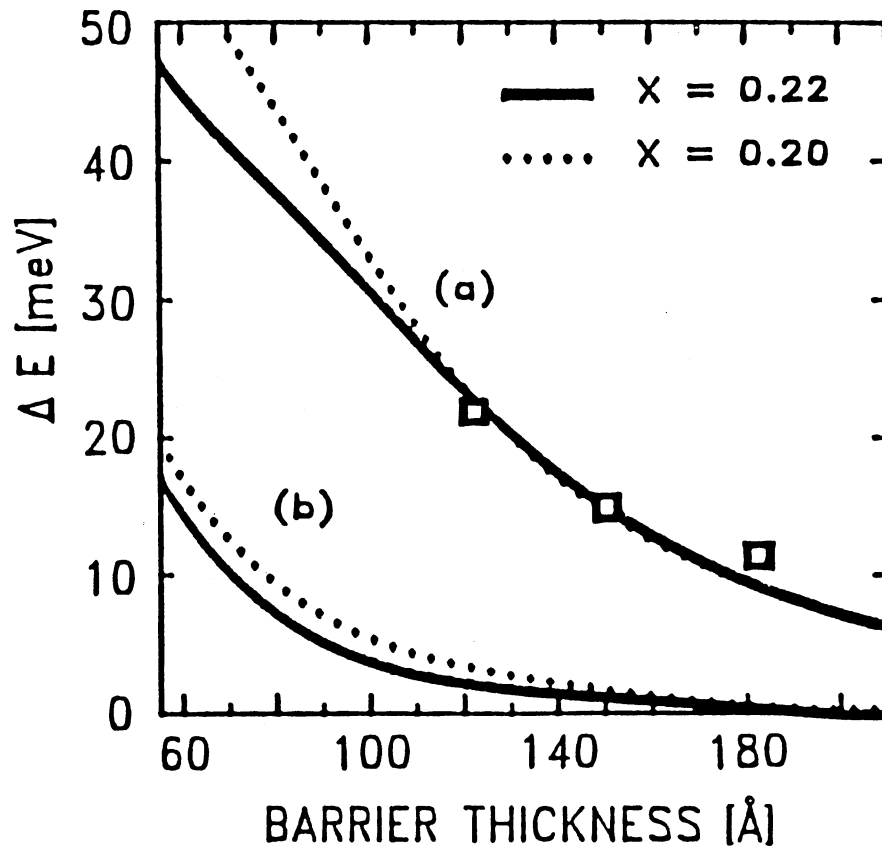


Figure 21. Energy splitting of doublets and dispersions. The energy splittings,  $\Delta E$ 's, of the first unconfined transitions (curve a) and of the (3hh-3e) transitions (curve b) of GaAs-Al<sub>x</sub>Ga<sub>1-x</sub>As superlattices are plotted against the barrier widths  $L_b$ . The solid and dotted curves are calculated values for  $x = 0.22$  and  $x = 0.20$ , respectively. The  $\Delta E$ 's are nearly the same for the two different  $x$ -values. The squares represent experimental data points taken from the four SL samples shown in Figure 19.

The splitting is not as sensitive to the aluminum concentration ( $x$ -values) as to the barrier width. In Figure 21, the calculated  $\Delta E$  vs  $L_b$  for  $x = 0.20$  is also plotted (dotted line). Although the barrier energy gap  $E_B$  changes by 24.9 meV, the  $\Delta E$  values can be seen to change by much less for  $x = 0.22$  and  $0.20$ . We also obtained very similar  $\Delta E$  values to those plotted in Figure 21, for  $x = 0.24$ . In this case, the first unconfined transition takes place between the 7hh and 4e states since one more hole state is confined due to the increased well depth. The small changes of  $\Delta E$  with changes in the  $x$ -value indicate that the measurement of  $\Delta E$  can be a very useful way of determining  $L_b$  independent of  $x$ .

We have shown that an excitonic resonance can be observed as the doublet peaks at ZC and ZB of minibands. One can expect that such a doublet can be resolved more clearly if the spacing is increased while preserving the strength. Indeed, we could observe clearly resolved peaks both at the ZC, and at the ZB of minibands for another set of samples. In this case, well widths are decreased to increase the miniband dispersion. Also a lower concentration of aluminum in the barrier is adopted to have larger coupling between wells while keeping the well width not too small. The larger well will allow us more tolerance over the monolayer fluctuations which occur in the fabrication process.

Figure 22 shows data. All the same as before,  $L_z$  and  $x$  are fixed at 59Å and 14%, respectively.  $L_b$  varies from 130, 99, and 71 Å. The behavior of the resonance is clearly reproduced. In comparison with Figure 19,



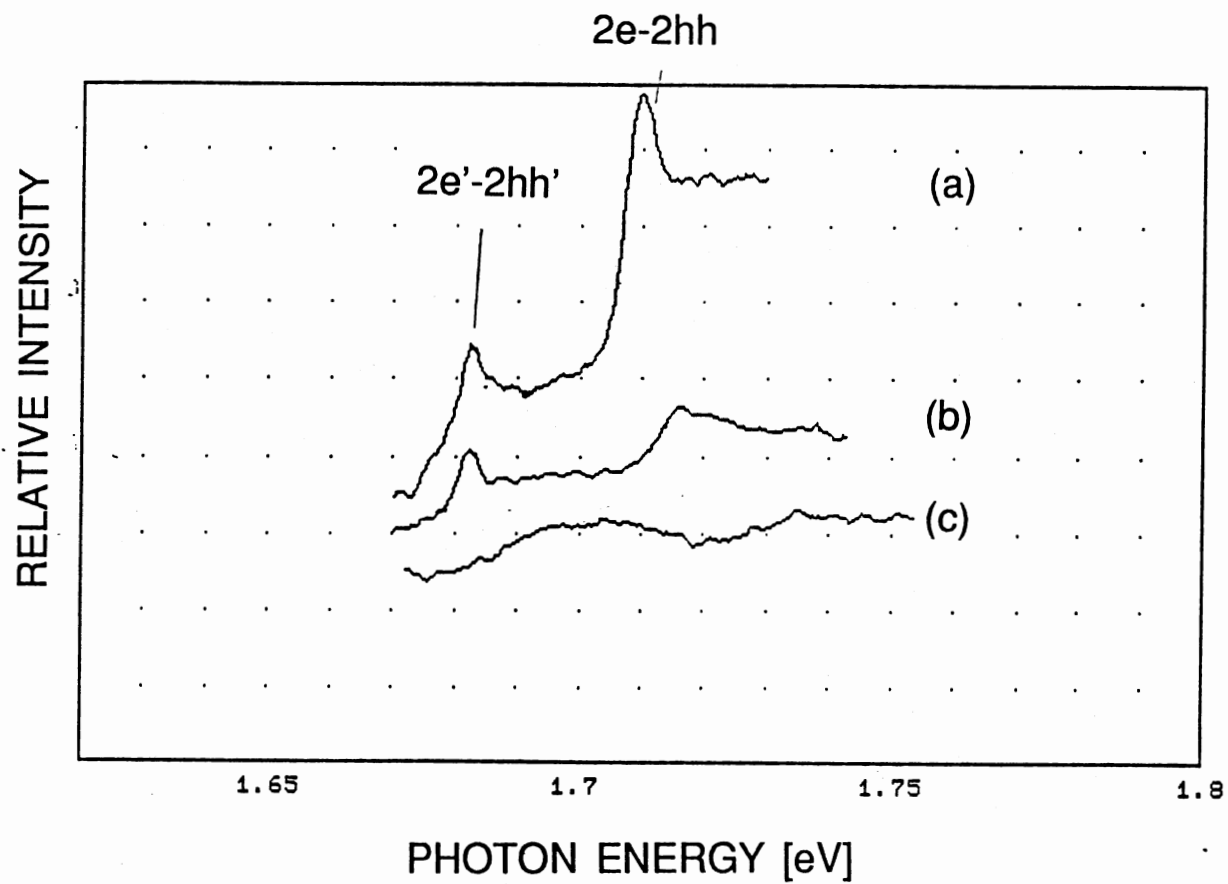


Figure 22. Unconfined transitions from another set of samples.  $L_z$ ,  $x$  are fixed at 59 Å and 14 %, respectively.  $L_b$  varies from 130 Å (a), 99 Å (b), and 71 Å (c).

doublets are now two separate peaks indicated by  $2e-2hh$  (ZC) and  $2e'-2hh'$ (ZB).  $2e-2hh$  is the transition between  $n=2$  heavy hole state ( $2hh$ ) and  $n=2$  conduction state ( $2e$ ) at ZC and primes indicate those at ZB.  $2e'$  and  $2e$  are the first unconfined states at the conduction band. The wavefunction (not shown) at the state  $2e'$  shows the resonance of wavefunctions at the barrier region as the previous case [Figure 20(a)]. Although  $2hh'$  is below the valence band barrier height, the calculated wavefunction shows the magnitude of  $2hh'$  at the barrier is still significant due to the large leak into the barrier without any nodes. Therefore, combined with the first unconfined  $2e'$  state, there can be a significant magnitude of optical transition matrix elements. At ZC, the situation seems more complicated. Note that the distinct jump in the spectrum in Figure 22(a). Lineshapes are more asymmetric at ZC than ZB. It is likely that there are contributions from other unconfined transitions such as  $2e-3hh$  and  $3e-2hh$  as well as the saddle-point excitons [29].

In this section, by PL excitation spectroscopy, we have found optical transitions between the first unconfined heavy-hole and conduction minibands in GaAs- $Al_xGa_{1-x}$ As superlattices. The peaks are found to be doublets. The separation of the doublet peaks depends on the barrier layer thicknesses. As  $L_b$  increases, the energy separation between the doublet peaks decreases. The origin of the doublet is attributed to excitonic resonances formed at two different points in the BZ, namely the center and the edge of the zone. In SLs with larger dispersions, those doublets clearly resolved into two separate peaks, thus verifying the existence of excitonic enhancements. This

attribution is supported by good agreement found between the calculated and the observed energy splittings.

In particular, in Figure 19,  $\Delta E$  changes from 15.0 meV to 23.8 meV as  $L_b$  changes from 150 Å to 120 Å. This corresponds to a  $\Delta E$  change of  $\sim 0.8$  meV for one atomic layer difference (2.83 Å) in  $L_b$ . In the second set, it is  $\sim 1.0$  meV. The difference is due to the difference in magnitudes of the dispersions mainly due to different well widths. These can be utilized in determining the barrier width. Optical methods for the determination of barrier widths are rarely found other than this method.

## Resonant Raman Scattering

Before we discuss results from resonant Raman Scattering (RRS) experiments, we will briefly introduce some of fundamental aspects about Raman scattering associated with resonance effects.

### Phonon Interactions in Resonance

In Chapter I., we have dealt with general characteristics of Raman scattering. If either the energy of incident photon ( $E_i$ ) or that of the scattered photon ( $E_s$ ) is as same as the optical transition energy between one of pairs of electron and hole states, an enormous enhancement of Raman efficiency is possible. This is called resonant Raman scattering (RRS). In RRS experiments, the intensity of one of Raman modes is measured with respect to the incident photon energy that is varied. Thus  $E_i - E_s = \pm \hbar \omega_{ph}$ , where  $\omega_{ph}$  is the

frequency of the phonon involved (+,Stoke's scattering; -,anti-Stoke's scattering). The resultant spectrum is often called a Raman profile. In such cases, the Raman tensor  $R$  can be given by the second order perturbation theory in  $H_{ep}$  by the sum of terms, such as, [69]

$$R_{uv} = \sum_{m,n} R_{mn} = \sum_{m,n} \frac{\langle s|p|m\rangle \langle m|H_{ep}|n\rangle \langle n|p|i\rangle}{(E_m - E_i)(E_n - E_s)}, \quad (33)$$

where  $\langle s|$ ,  $\langle i|$  are the scattered, and incident states for the photons in the quantized representation [68],  $m,n$  are intermediate states, and  $E$  with subscripts means the energy of the state. Usually it is enough to consider only resonant terms among many possible terms in the complete expression. The resonance occurs when energy  $E_i$ , or  $E_f$  is close to  $E_m$ ,  $E_n$ , or both, so that the efficiency can be divergent. In reality, the efficiency will have a finite magnitude due to the finite lifetime at the intermediate states [69]. RRS has been performed with many kinds of materials. The first RRS with semiconductor superlattices was reported by Manuel et al [70]. In RRS, phonons interact (Hamiltonian,  $H_{ep}$ ) with electrons, holes, and excitons at real states of semiconductor crystals such as GaAs and  $Al_xGa_{1-x}As$ . A few of important mechanisms are briefly discussed below [42].

### Deformation Potential (DP)

Phonons are vibrational modes of lattice displacements. Displacements can be regarded as if the crystal has temporally a slightly different lattice constant. The change results in a proportional shift of the bandgap of the

crystal. The coefficient is in the unit of a potential (energy/displacement). This is called the *differential potential (DP)*. In backscattering configuration at crystal (100) surface, DP are found to induce non-zero off-diagonal elements in Raman tensors. Since the pure longitudinal displacement of lattice points does not interact with the optical field which has a transverse electric fields ( $\mathbf{x} \cdot \mathbf{e} = 0$ ,  $\mathbf{x}$ :displacement,  $\mathbf{e}$ :polarization), only TO modes are usually considered to appear by DP. However, there are a few cases, where LO are involved due to DP. Near the resonance of forbidden (q-dependent) scattering, where Loudon's selection rule fails, DP enhances modestly both LO- and TO-mode scattering.

### Fröhlich Interactions (F)

The lattice displacement due to LO phonons also induces a temporal charge displacement of electrons or holes in the propagation direction. This produces electric fields, which, in turn, make electrons, holes, and excitons interact with phonons [71]. This kind of interaction is called *Fröhlich (F) interaction*, and the process is called F-process. This is effective only in a polar crystal such as GaAs, and it is zero for Si or Ge. The F-process generates a momentum (of phonon,  $\mathbf{q}$ ) dependence in Raman coefficients and it is mainly important in LO-phonon scattering. By the q-dependence, Loudon's selection rules are relaxed in this process. In particular for the interaction with excitons, the contributions from holes and electrons are opposite in sign and only the difference is effective. The F-process is

responsible for the observation of very strong resonance enhancements of LO modes in RRS with semiconductors in the forbidden back-scattering configuration. Experiments in this thesis belong to such cases.

### Interface Modes (IF)

The macroscopic dielectric constant can be different at the interface of two different materials, i.e., GaAs and  $\text{Al}_x\text{Ga}_{1-x}\text{As}$ . The discontinuity generates a phonon mode whose magnitude is mostly localized only around the interfaces. This interface mode (IF) can appear strongly resonant to excitonic states like other confined phonon modes, such as LO or TO. As results, the spectra appear rather broad and, in some cases, with non-Lorentzian shapes. It seems that the peak is assigned IF if it appears near the LO or TO frequency and yet can not be attributed to them.

### Impurity Assisted Processes

The Fröhlich interaction also combines excitons and impurity states. This is called an impurity-assisted Fröhlich interaction (FI). This process relaxes selection rules considerably. However, the strength is strictly a function of the concentration of the impurity.

### Incoming and Outgoing Resonances: Double Resonance

In RRS, the resonance can occur at the energy of incoming photons, or at that of scattered photons (outgoing). As a result, a double-peak<sup>§</sup> appears in the Raman profile. See Equation (33). When  $E_i$  is varied, the peak at  $E_f=E_m$ , or  $E_n$ , whichever is the energy of a real intermediate state, is called *outgoing resonance*. The peak at  $E_i=E_m$  is called *incoming resonance*. The outgoing one is at a higher energy level than the incoming one in Stoke's scattering. It is opposite in anti-Stoke's scattering. The difference between two peaks is close to the phonon energy of the crystal. Sometimes, it appears slightly deviated from the energy, if strengths of the resonances are too much different. The presence of the double-peak has been called as a double-resonance. Contrarily, note the case where both  $|m\rangle$  and  $|n\rangle$  become resonate to  $\langle i|$  and  $\langle f|$ , respectively. This has been said to be *doubly-resonant*. Those two cases are different since if a process is doubly-resonant, two real states are involved instead of one in a double-resonance.

### Resonant Raman Spectra

In Figure 23, a series of typical resonant Raman spectra is displayed. In the experiment, the detection spectrometer scans a region which is different by a given amount of energy ( $275\text{-}310\text{cm}^{-1}$ ) from the excitation energy. After

---

<sup>§</sup> To avoid the possible confusion between the doublet in PLE from two critical points of a miniband, we choose to use this term, although the term *doublet* has been used historically.

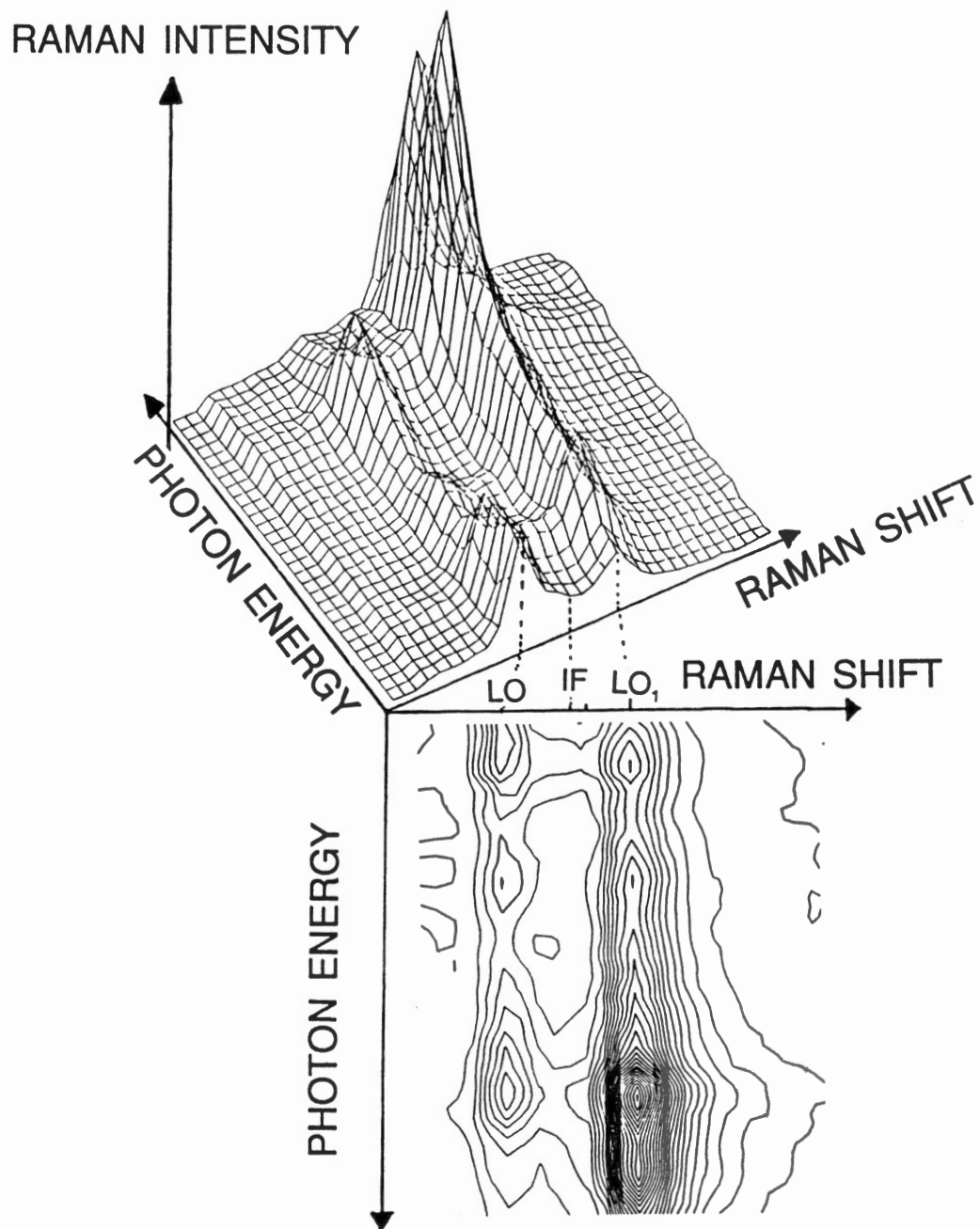


Figure 23. Resonant Raman spectra. RRS spectra are taken by measuring the spectra at the range apart from the excitation wavelength by a fixed value. The Raman shift denote the difference from the excitation wavelength.  $LO_1$  is for the GaAs-like phonon from  $Al_xGa_{1-x}As$ ,  $LO$  is for the GaAs phonon from the well.  $IF$  is a weak mode between them at  $290\text{cm}^{-1}$ .



each scan, the excitation wavelength is varied between 1.79-1.86 eV by a given increment following the next scan. Figure 23 shows a bird-eye view on the top where the vertical height is the Raman intensity. At the bottom, the relative intensity is shown on a contour map. On each contour, the intensity is constant. Unlike other Raman spectra shown in Chapter I, it is taken near the energy of the unconfined states of Sample A. A careful inspection reveals bumps between the dominant LO (from GaAs; wells) and  $LO_1$  (from  $Al_xGa_{1-x}As$ ; barriers; GaAs-like) peaks. A phonon mode relevant to this bump is the interface mode (IF) [52,72] which is, in these spectra, located near  $290cm^{-1}$ . In Figure 23, we can see that this structure exists only within a relatively small range of incident phonon energies. A detailed explanation of such an identification can be found in Reference 75.

### RRS in the First Unconfined State.

In this section, we discuss results of RRS performed with the same samples with which we discussed the first unconfined states (FUS), previously. We were able to resolve clearly a set of four peaks (both incoming, outgoing, and ZC, ZB) for most of the samples. The strength of the individual peak is found to vary consistently depending on their origins. Such a consistent observation of RRS spectra was never realized up to this date. This is, in part, due to high resolutions in measurements and a precisely controlled fabrication of high-quality superlattice (SL) samples. To analyze the behavior quantitatively, we adopt a fitting process using *lumped*

*parameters.* Parameters are *effective-lifetimes*, representing an overall temporal-damping of states. With the SL samples, we have found that strong resonances occur in SL both at  $M_0$ - and  $M_1$ -type critical points of FUS, where we observed an excitonic resonance by PLE. Consistent with the results of PLE, the strength at  $M_1$ -point is quite as strong as that at  $M_0$ , up to about 70%. In addition, we have found, the intensity of barrier phonons depends more strongly on  $L_b$  than that of well-phonons.

We have seen by PLE that the first-unconfined transitions show a doublet at the energies corresponding to the Brillouin ZC and the ZB. An absorption spectra, which PLE spectra approximately represent, in fact, measures the imaginary part of the absolute dielectric susceptibility of the material. On the other hand, RRS has shown to be equivalent to measuring the differentials of that absolute susceptibility, between the energies of incident and scattered photons [42]. Thus it can be easier by RRS than by PLE to resolve peaks from  $M_1$ -type critical points. There have been many reports of investigating  $M_1$  critical points by RRS in bulk semiconductors.  $M_1$ -type critical points of GaAs bulk are  $E_1$ , or  $E_1 + \Delta_1$  gaps. Raman resonances were observed at the  $E_1$  with GaAs [74], Ge [85] and InSb [73] as early as 1972 [82,83]. More recently, GaSb-AlSb SLs have been used to investigate the bulk  $E_1$ -gap resonances [86]. Still, in those bulk cases, observed resonance profiles have been quite broad so that incoming and outgoing resonances are not resolved. Sometimes, other kinds of the resonance, those from  $E_1 + \Delta_1$ , overlap and become one broad peak [73].

In superlattices (SLs), critical points can be formed at the ZC and the ZB, for optical transitions between any minibands. In 1976, P. Manuel et al. showed experimentally that a RRS spectra performed at ground states of a few superlattice samples. The authors showed that there is a resonance enhancement of Raman scattering efficiency at those SL energy bands and levels [70]. They suggested that the efficiency of RRS,  $\sigma(E)$ , can be represented by a typical second order resonance equation:

$$\sigma(E_i) \propto \int dE \quad D(E) \frac{1}{(E_i - E)(E_s - E)} \quad \text{and} \quad E_s = E_i - E_p, \quad (34)$$

where  $D(E)$  is the joint density of states,  $E_i$ ,  $E_s$  are incident and scattered photon energies respectively, and  $E_p$  is the scattering phonon energy. The expression (34) indicates to sum up all contributions from intermediate states (the energy of which is denoted by  $E$  in above equation) that are now real resonating states across minibands. In their data, however, the incoming and the outgoing resonances were not well resolved. Those peaks appeared merged as a flat-top structure, not to mention that two different critical points are not resolved. After this work, there were a large number of reported RRS experiments in quantum wells (QWs) and SLs [75]. A majority of the work on GaAs-AlAs SLs has concentrated on the vibrational modes in thin layers (of only a few monolayers) of SLs, i.e., *zone-folding effects* [84]. On the other hand, RRS experiments on discrete excitonic levels in QWs have demonstrated well-separated incoming and outgoing resonance peaks. Separations between them agreed with the energy of the phonon involved in

scattering [76-80]. A dramatic increase in the efficiency was also noticed for the forbidden LO-phonon scattering at quasi-localized states in GaAs-AlAs and GaAs-Al<sub>x</sub>Ga<sub>1-x</sub>As QWs. These spectra showed sharp double (incoming and outgoing) peaks well-separated [87].

The first unconfined states, or extended states, in QW samples were observed by Zucker et al. using RRS [76]. Since the incoming- and outgoing-resonances were clearly resolved, the intensity ratio between them could be measured accurately. Such new information made it possible to examine scattering channels of phonons. Excitons are scattered via coupling between different excitonic bands nearby [80] through Fröhlich interactions (F-processes), or they have intra-band scattering via impurities in the structure [88]. Alternatively, the process was considered to be an interband impurity-assisted F-processes [89]. Zucker et al. [80] used a fitting process on RRS profiles with a two-level resonance formula, and found that the stronger outgoing resonance is assisted by excitons scattered to the higher quantum levels, or, conversely, that stronger incoming resonance is to the lower ones. Also, they found that the RRS profiles of GaAs (well) phonons indicate coupling to the states in lower energy, and the Al<sub>x</sub>Ga<sub>1-x</sub>As profiles do coupling to higher ones. Yet, the effects of finite miniband widths, or dispersions, of excitonic states have not been addressed since they used QW samples with negligible miniband widths.

FUSs of SLs with a finite barrier width show significant dispersion compared to the confined levels as we have already shown. Particularly the

excitonic resonance makes PLE spectra to show distinct doublets. One should be reminded that critical points formed at ZB and ZC are of two different kinds.  $M_0$  is at ZB, and  $M_1$  is at ZC for 4e-6hh states. The  $M_1$  type critical point is called a saddle point. The larger dispersion would help to separate two different critical points. As mentioned above, by adopting RRS techniques, one can expect to resolve the peak from the saddle point more clearly than by PLE techniques.

The Raman experiments were carried out at 5 K with longitudinal optical (LO) phonons. A near-backscattering geometry was used with the incident light polarized normal to the SL growth direction (z-direction). The collected light was unpolarized. DCM dyes were used in a CW laser pumped by an Ar-ion laser operating at 5145 Å. A typical power level incident on the sample surface was in the order of 10W/cm<sup>2</sup>. Samples examined here are Samples A(SL I.1), B(SL I.2) ,C(SL I.3), and D(SL I.4). The parameters are given in Table VII.

The GaAs-like LO-phonon energy of  $Al_xGa_{1-x}As$  is smaller than that of GaAs, with the energy difference depending on x-values [9].  $Al_xGa_{1-x}As$ , which is an alloy of GaAs and AlAs, shows two-mode behavior of a LO-phonon. In samples reported here, GaAs-like phonons in the barrier, which will be called  $LO_1$ , appear at 286.7 cm<sup>-1</sup>, while LO-phonons of the well layer (GaAs) are at 294.6cm<sup>-1</sup>. The other mode, or AlAs-like LO-phonons in the barrier layer, is at ~ 380cm<sup>-1</sup> and it is not considered here.

Figure 24 shows an example of a resonant Raman profile taken from a SL with  $L_z = 150 \text{ \AA}$  and  $L_y = 180 \text{ \AA}$  (Sample A). Doublet peaks are clearly seen between 1.8 and 1.83 eV with their separation energy of  $\sim 11 \text{ meV}$ , which is in good agreement with what is observed in PLE experiment. The outgoing resonance peaks which lie on the high energy side of incoming resonance peaks are also noticed above 1.83 eV. The difference between the incoming and the outgoing resonance peaks is approximately equal to the  $LO_1$  energy. The Raman profile in Figure 24 shows the plot of  $LO_1$  intensity against the laser excitation energy. As seen in the inset, relative intensities of LO and  $LO_1$  vary with the excitation laser wavelength. The lower Raman spectrum in the inset was taken at an incident wavelength,  $\lambda_c$ , below the barrier gap  $E_B$ , and the upper one, above  $E_B$ . Changes are clear in the relative intensity of  $LO_1$  to LO phonon. Firstly, such a RRS profile may result from the difference in channels of phonon scattering at various incident photon energies. So, the existence and the energy position of nearby quantum bands should be influential. Secondly, it can be a result from the different strength of various optical transitions, confined or unconfined, since wavefunctions at unconfined states have larger extent at barrier regions ( $Al_xGa_{1-x}As$ ), while for confined states they have more in well regions (GaAs). However, the second can only vary the relative intensity of LO to that of  $LO_1$ , monotonously across  $E_B$ , with respect to the incident photon energy, as it is shown in the inset of Figure 24.

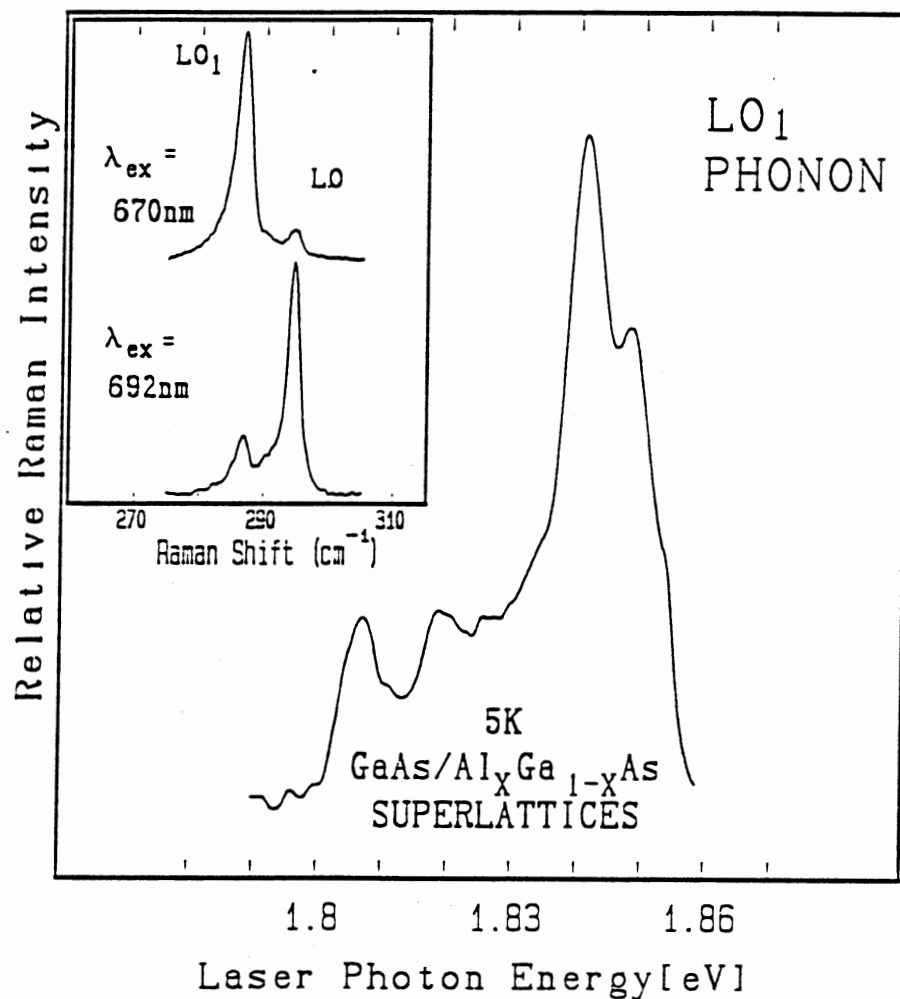


Figure 24. A typical RRS spectrum. The resonant profile of peak intensity of LO<sub>1</sub> with respect to the excitation energy. The inset illustrate the changes of Raman spectra by two different excitation wavelength.

To understand the profile by the first mechanism, we choose a lumped-parameter approach, where a limited number of parameters are used to fit the experimental observations and to describe general trends. This approach is more meaningful if we can associate parameters with physically measurable values. The parameter chosen here is an effective lifetime, denoted by  $\Gamma^{-1}$ , at states involved. In calculations,  $\Gamma$ 's are included as imaginary parts of energy  $E$  of states, such as  $E \leftarrow E + i\Gamma$ . In fact,  $\Gamma$ 's are lumping two effects, i.e., the relative change<sup>†</sup> of magnitudes of interactions (in numerators in Equation (36), below), and the true lifetime (damping) of the intermediate state. Note that peak magnitudes are given by  $1/\Gamma$  at the resonance for a normalized Lorentzian lineshape. Thus, this combination can be justified as long as the lineshape is Lorentzian and  $\Gamma$  is not much different from the accurate value. In a limiting sense, when the true lifetime is constant,  $\Gamma$  measured from experiments will be exactly the change in the product of matrix elements. On the other hand, the true lifetimes are, in principle, measurable. Then, we can deduce magnitudes of matrix-elements from the effective lifetime. An alternative to this may be choosing individual matrix elements as parameters, which requires more explicit knowledge of individual states to derive relations between them since not all the parameters are independent. Compared to this, the lumped-parameter approach is more general so that a similar method can be used in many different cases. We

---

<sup>†</sup> We only need to know the relative changes since the absolute intensity is not considered here.



can still theoretically derive proportions of the true lifetime using detail parameters of excitonic states involved, although the calculation would be very involved as we include the details, such as, an exact excitonic dispersion relation in each miniband. Therefore, effective lifetimes are suitable to the frame of our approach where we deduce simple and direct implications of experimental results by lumping overall effects into a minimum number of parameters.

If a Raman intensity  $I_R(E_i)$  is denoted by

$$I_R(E_i) = |\sigma(E_i)|^2, \quad (35)$$

then,

$$\begin{aligned} \sigma(E_i) = A [ & \sum_{m=c,b,a} \int_{E_{\min}}^{E_{\max}} dE D(E) \left\{ \frac{M_e M_{ep} M_m}{(E_i - E_m)(E_s - E)} \right. \\ & \left. + \frac{M_m M_{ep} M_e}{(E_i - E)(E_s - E_m)} \right\} \\ & + \sum_{n=c,b} \left\{ \frac{M_n M_{ep} M_a}{(E_i - E_a)(E_s - E_n)} \right. \\ & \left. + \frac{M_a M_{ep} M_n}{(E_i - E_n)(E_s - E_a)} \right\} ] \quad (36) \end{aligned}$$

where A is a constant. And the index m is for summation of  $E_c$ ,  $E_b$ ,  $E_a$ , and n for  $E_c$ ,  $E_b$  only.  $E_m$  and  $E_n$  are for resonating energy levels from critical points, such as,  $E_c$  is the energy level at ZC and  $E_b$  is one at ZB. E is for the intermediate exciton state and  $E_a$  is for an additional weak excitonic state observed close to spectral ranges concerned (used only for sample A, B).

Also,

$$M_m = \langle m|p|E \rangle = \langle E|p|m \rangle \text{ and} \quad (37)$$

$$M_n = \langle n|p|E_a\rangle = \langle E_a|p|n\rangle \quad (38)$$

are optical dipole transition matrix elements. The interaction associated with phonon and intermediate states (Hamiltonian,  $H_{ep}$ ) is represented by the matrix element:

$$M_{ep} = \langle E|H_{ep}|E_m\rangle. \quad (39)$$

Similarly,

$$M_{ep'} = \langle E_a|H_{ep}|E_n\rangle, \quad (40)$$

for the additional interaction with  $E_a$ .

Equation (36) contains a few selected resonant terms of similar orders from a more general expression of nondegenerate second-order perturbation theory [90]. The form is similar to expressions used by Zucker [76] and is only extended using notions in Equation (34) for SL cases. We include two resonating states, compared to one in Zucker's. First-two terms represent major contributions to RRS for most of our experiments. The exciton is excited by  $E_i$ , to a state  $\langle ml$ , then scattered by a phonon via  $M_{ep}$  to state  $E$  generating a phonon of energy  $\hbar\omega_{ph}$ , and then radiated in energy  $E_s$ .  $\hbar = h/2\pi$ , where  $h$  is Plank's constant. The last two terms in Equation (36) are included only in cases for SL samples showing a weak additional peak (Samples A and B). The intermediate state (energy  $E$ ) varies in energy between  $E_{min}$  and  $E_{max}$  which are determined as explained below. Because effective lifetimes are used, all matrix-elements are assumed to be an equal magnitude except those for interactions with  $E_a$ . For  $E_a$ , a scale factor  $\eta$  ( $0 \leq \eta < 1$ ) is multiplied to represent smaller magnitudes of  $(M_n M_{ep} M_n)$  since

peaks observed are small and within a narrow range.  $\eta$  can be independently determined by the relative peak height ( $I_p$ ) from the spectra, after normalization, such as,  $\eta = I_p \Gamma_a / \Gamma_R$ , where  $\Gamma_R$  is the width of one reference peak.

At the continuum state above or below a miniband, we consider that lifetimes are constant values of  $\hbar/\Gamma_0$ . However, within the miniband, they are assumed to vary in  $\mathbf{K}$ , the exciton wavevector. For simplicity, they are also assumed to be on the linear extension between two values, that is,  $\hbar/\Gamma_c$  (at ZC) and  $\hbar/\Gamma_b$  (at ZB) because we found that calculated profiles are not so much sensitive to different functional shapes as long as they are close to a linear function. A single value  $\Gamma_a$  is assumed at  $E_a$ . Under a similar basis,  $E_{\max}$ , or  $E_{\min}$  is chosen as follows. The true magnitude of  $M_{ep}$  will decrease if the intermediate energy is very far from the range of resonances. Therefore, it is reasonable to assume a finite  $E_{\max}$  and a constant  $\Gamma_0$ . Values are finally decided in order to produce a minimal change in overall results.

Summarizing the results,  $\Gamma(E)$  is given by,

$$\Gamma(E) = \begin{cases} \Gamma_0 & \text{if } E < E_b, \\ \Gamma_b + \varepsilon(\Gamma_c - \Gamma_b) & \text{if } E_b \leq E \leq E_c, \\ \Gamma_0 & \text{if } E \geq E_c. \end{cases} \quad (41)$$

where  $\varepsilon = (E - E_b)/\Delta E$ , and  $\Delta E = (E_c - E_b)$ .

Also, a quasi 2-D DOS,  $D(E)$ , is given by

$$D(E) = \begin{cases} D(E_b) & \text{if } E < E_b, \\ D(E_b) + \{D(E_c) - D(E_b)\} / \pi \arccos(1 - 2\varepsilon) & \text{if } E_b \leq E \leq E_c, \\ D(E_c) & \text{if } E \geq E_c. \end{cases} \quad (42)$$

Figure 25 shows results of fittings. Solid curves are the calculation by Equation (36) and the assumed baseline, and fine-dotted curves represent the experimental RRS data. The baseline is determined by the best-fit. They may have resulted from tails from RRS peaks of confined states not included in this model. In Figure 25(a), RRS spectra from LO<sub>1</sub>-phonon (at barriers) are shown for all four samples. In Figure 25(b), those from LO-phonons (at wells) are shown. The relative intensity between LO- and LO<sub>1</sub>-phonons in each sample is preserved in these particular data, although it is noticed that the ratio varies slightly by the incident intensity. Between different samples, those intensities are normalized to the maximum. In general, the agreements between Equation (36) and the experiments are excellent, which is surprising considering the simplicity of the model. We consider this as one evidence that the lumped-parameter approach may be justified.

For comparison, a dash-dotted curve is included for Sample A, in the top of Figure 25(a), calculated by a QW-model, where there are only three discrete levels  $E_b$ ,  $E_c$ , and  $E'$ , excluding the continuum contributions.  $E'$  denote a discrete level higher or lower than both  $E_b$  and  $E_c$ , similar to Zucker et. al's [80]. Let's first consider the case without the interaction of  $E'$  level. Then, only two terms are left involving only  $E_c$  and  $E_b$ , each subtracted by  $E_i$  or  $E_s$ , in denominators. If we calculate the intensity at resonances assuming four peaks are well-separated with finite widths of  $\Gamma_b'$  and  $\Gamma_c'$ , we find intensities of two out of four peaks are same, such as,

$$I(E_i=E_b') \approx I(E_i=E_c' + \hbar\omega_{LO}) \text{ and } I(E_i=E_c') \approx I(E_i=E_b' + \hbar\omega_{LO}), \quad (43)$$

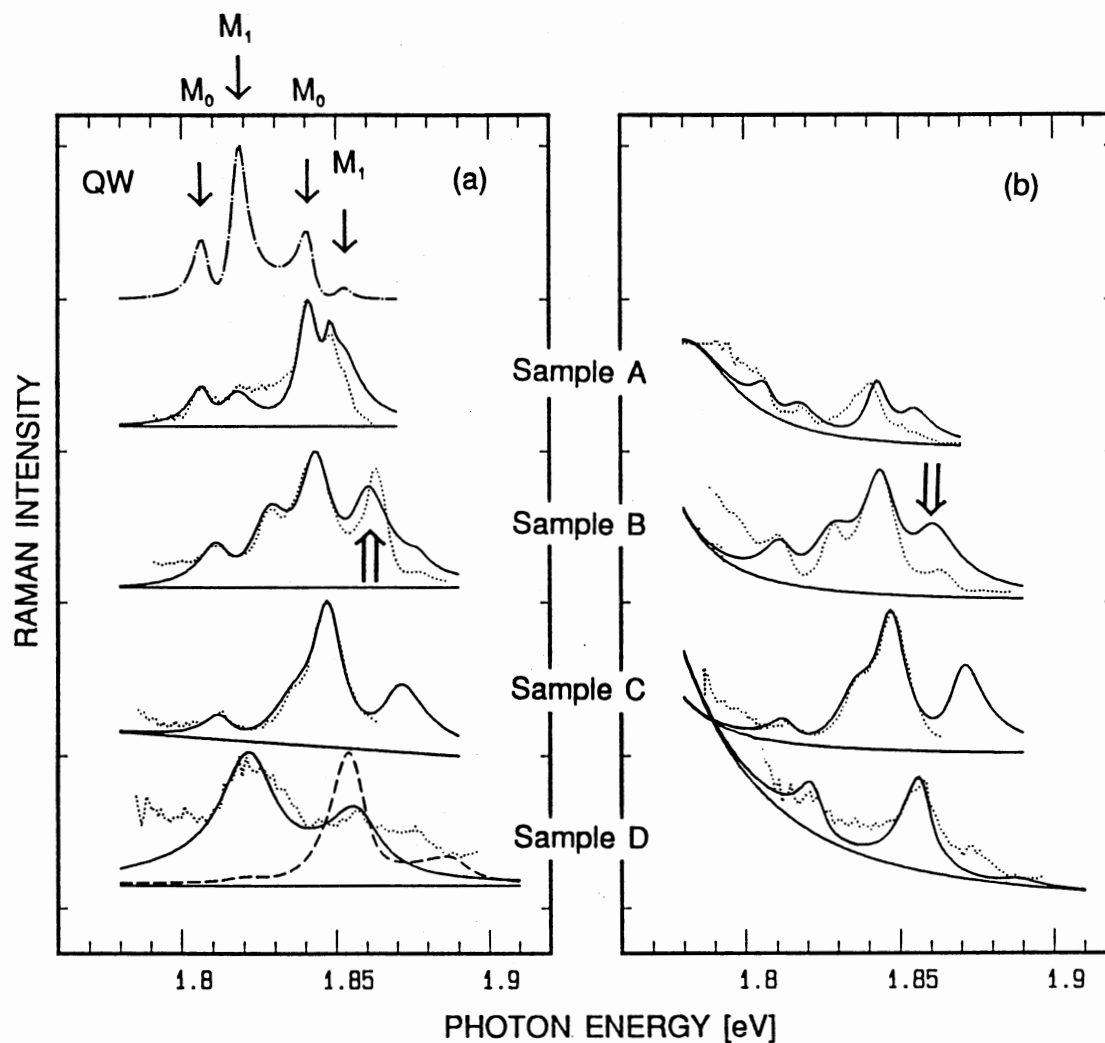


Figure 25. RRS spectra from Sample A to D. (a) Resonant profiles from  $LO_1$  phonons, and (b) those from LO phonons: The assumed baseline is given at each spectrum. QW case is obtained by assuming three discrete quantum levels. In Sample D, an additional graph is overlaid to show the upper continuum coupling (See text.).

where  $I$ 's stand for intensities and the arguments are energy positions. Even when  $E'$  is included, it turns out to be impossible to fit satisfactorily to the experimental data as shown by the dash-dotted curve. In particular, outgoing intensities are reduced as we increase the interaction with  $E'$  at higher energy positions, which is opposite to results from Zucker's case, where there are **only two levels**. We indeed obtain the same results, when we set  $E_b = E_c$  into our model to simulate the two level case. Therefore, a net improvement in our model results from including the above- or below-miniband continuum as DOS function prescribes, which is believed to be one of differences between a 2D quantum-well case and a quasi-2D SL case, where excitons are more delocalized. Parameters used to fit are listed in Table VIII. Listed are  $\Gamma$  values used in fitting of Equation (36). In Figure 26, they are drawn in scales of psec, using  $\tau = \hbar/\Gamma$ . Curves are drawn to guide eyes in considering the tolerances ( $\sim 1$  meV). Included for comparison, are values from a bulk GaAs at  $E_0 + \Delta_0$  ( $M_0$ -type) and  $E_1$  (a saddle point) [74] as well as one from a thin-period SL [91] and one from a QW ( $L_z=103\text{\AA}$ ,  $L_b=209\text{\AA}$ ,  $x=0.16$ ) [76]. Those values are read from an appropriate figure in each reference by the width of each peak. Those values are well within the extension of our results and it is approximately so in the QW case. Also, the values used for energies of LO and  $LO_1$  phonons ( $\hbar\omega_{LO}$ ,  $\hbar\omega_{LO1}$ ) are displayed in the table. They are smaller than separately measured values (36.5 meV for LO and 35.6 meV for  $LO_1$ ) and are believed to be within the resolution of the RRS experiment ( $\sim 2$ meV).

TABLE VIII  
THE PARAMETERS USED IN CALCULATIONS OF  
RESONANT RAMAN SCATTERING.

	$L_z$ (Å)	$L_b$ (Å)	$\Gamma_b$ (meV)	$\Gamma_c$ (meV)	$\Gamma_0$ (meV)	$\Delta E$ (meV)	$hw_{LO,LO1}$ (meV)
<b>For Al<sub>x</sub>Ga<sub>1-x</sub>As LO<sub>1</sub> phonons:</b>							
Sample A150	180		4	6	20	11	34
Sample B150	150		6	7.2	30	16	31.5
Sample C150	120		5.5	8.25	15.4	22.5	34.5
Sample D150	70		10	50	15	30.5	35
SL <sup>1</sup>				40			
<b>For GaAs LO phonons:</b>							
QW <sup>2</sup>	103	209	10			-	35.6
Sample A150	180		4	6	48	11	34
Sample B150	150		6	8.4	30	16	31.5
Sample C150	120		5.5	6.6	15.4	22.5	34.5
Sample D150	70		5	7	7.5	30.5	35
GaAs bulk <sup>3</sup>				50	70		35.6

<sup>1</sup> T. A. Grant, M. Delaney, M. V. Klein, R. Houdre, and H. Morkoc, Phys. Rev. B **39** (3) 1696 (1989-II).

<sup>2</sup> J. E. Zucker, A. Pinczuk, D. S. Chemla, A. C. Gossard, and W. Wiegmann, Phys. Rev. Lett. **51** (14) 1293 (1983).

<sup>3</sup> R. Trommer and M. Cardona, Phys. Rev. B **17** (4) 1865 (1978).

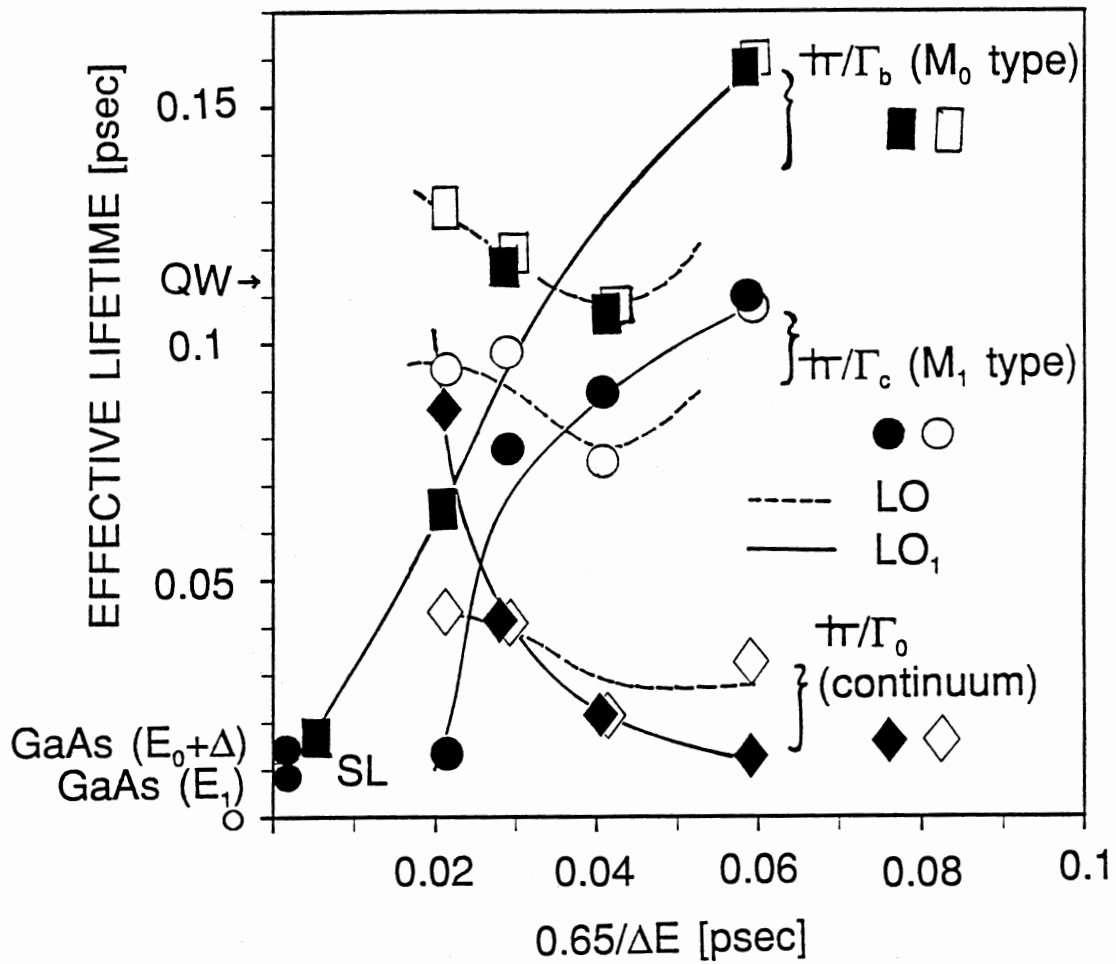


Figure 26. Effective lifetimes obtained from fitting process. The lines are to guide eyes. Solid lines are for LO<sub>1</sub> phonons, broken lines are for LO-phonons. The symbols are data points from Table VIII. Closed squares: M<sub>0</sub>-type LO<sub>1</sub>. Open squares: M<sub>0</sub>-type LO. Closed circle: M<sub>1</sub>-type LO<sub>1</sub>. Open circles: M<sub>1</sub>-type LO. Closed diamonds: continuum state LO<sub>1</sub>. Open diamonds: continuum state LO.



As we can find in the Figure 26, the lifetime at a saddle point is shorter than that of the  $M_0$  -type, indicating that the strength of the resonance is weaker. Nevertheless, they are still within the similar ranges. Thus, the existence of excitons at the saddle point on FUS is more likely. Accordingly, by comparing energy positions, we can see that those doublets in PLE may be truly coming from miniband critical points.

One aspect to notice is that curves of continuum lifetimes,  $\Gamma_0$ 's, are interpreted different in origin from  $M_0$  and  $M_1$  type curves. These continuum states are from exciton wavevectors in the parallel direction to SL layers. The lifetimes at those would be very short and have no apparent reason to vary depending on the miniband dispersions. Thus the variation shown here are considered mainly from the change in the strength of interaction. In the figure, one can realize that the continuum contributions become stronger at almost the same phase as the rapid decay of lifetimes on saddle-point states. As  $L_b$  is smaller, the dispersion is larger. We find thus that in a state where there is large coupling between excitons in the neighboring wells, it seems the continuum above (or underneath - this will be explained later) the miniband plays a significant role in the annihilation of saddle point excitons. The general trends of decaying lifetimes at  $M_0$ , and  $M_1$  type points can be understood as the delocalization of electrons and holes so that the exciton may become weaker. The behavior of GaAs LO-phonons is, however, relatively constant with respect to such delocalization. It only depends on types of states. It is not fully explainable but it may be an indication that

those phonons interact less with continuum. It can be noted, though, that structures in GaAs LO profiles have more background which may have reduced the accuracy of the fitting process.

In Figure 25, calculated curves show more deviations on the higher energy sides. For example, look at the  $LO_1$ -profile of sample A. The experimental curve between 1.825 and 1.86eV is following under a decaying slope of the calculation. Also the same trend can be found in  $LO_1$  of Sample B, as well as both LOs in Samples A and B. This can be attributed to a significant variation in the absorption in those energy ranges due to the shorter wavelength. Both the incident and scattered lights are likely to suffer absorption. A slight exception is near the outgoing ZC-peak ( $LO_1$ ) of Sample B. Compare  $LO_1$  and LO profiles in Sample B near vertical arrows. This sample has shown a strong enhancement at the ZC transitions in its PLE spectra (See the first Section) due to the wavefunction resonant at barrier regions. It is dramatic that experimental points at 1.86eV of  $LO_1$  overshoot the calculation, while other corresponding peaks in Samples A and B are lower than calculations. Remembering that the calculation assumes constant matrix elements, we can say specifically they are larger at the ZC transition than ZB, which is an additional experimental sign that was not given so clearly by PLE technique.

Another evidence of larger matrix elements is from the identification of additional levels of  $E_a$ . It is most likely to be the transition of  $5e-7hh$  which has relatively larger optical matrix elements according to a TBA calculation.

Other possibilities such as barrier impurities are excluded by its sharpness and its energy position. Therefore, we can label it as the second unconfined state (SUS). For  $L_b=180\text{\AA}$  (Sample A), the peak at  $E_a=1.848\text{ eV}$  appears most strongly, while the relative strength is still small ( $\eta = 0.02$ ). This state moves to  $1.878\text{eV}$  (Sample B) with  $\Gamma_a = 40\text{ meV}$  which corresponds to a decrease in peak intensity by 1/20 times from Sample A ( $\Gamma_a = 2\text{meV}$ ). The resonance of wavefunctions in the barrier region occurs in this SUS when that of  $5e$  and that of  $7hh$  have a same form at the barrier with one node at the middle, only when  $L_b$  is  $180\text{\AA}$  [similar to those in Figure 20(b)]. Otherwise the overlap becomes smaller. On the contrary, in FUS, there is no node with this  $L_b=180\text{\AA}$  as in Figure 20(a) when the overlap is the largest. Thus the SUS gives a smaller strength than the FUS. The wavefunctions in resonance are different in different minibands, which has been addressed in Reference 66. It is interesting that by RRS technique, such a transition not shown-up in PLE is clearly resolved, adding more information about the details of energy structures of SLs.

We find in Figures 25, 26 that as barrier widths decrease the strength of the saddle point peak is reduced. For sample C ( $L_b = 120\text{\AA}$ ), incoming and outgoing peaks of ZB and a weaker incoming resonance at ZC (a saddle point) are shown. A profound decaying of the strength of saddle point excitons is noticeable compared with the strength of those at  $M_0$  critical point as seen in curves of Figure 26. Finally, in Sample D ( $L_b = 70\text{\AA}$ ), saddle point peaks become undetectable in both experiments and calculations.

Outgoing peaks that are predicted to be strong by the calculation in LO and LO<sub>1</sub> profiles of Sample C are not likely to appear so strong in experiments, because outgoing peaks turn out to be reduced significantly by coupling to lower quasi-confined energy bands if L<sub>b</sub> becomes small. This is explained below for Sample D case. In Figure 25(b), the effects of different physical volumes of the well and the barrier has been included by multiplying the ratio of (L<sub>b</sub>/L<sub>w</sub>) to LO phonon profiles. The heights of LO-profiles (from GaAs in wells), compared with the LO<sub>1</sub> counterparts, increases slightly as the barrier width becomes thinner. This may indicate that coupling into lower states progresses steadily.

For samples A,B, and C, we used coupling only to higher continuum states, by having  $D(E_b) = 0$ , and  $E_{\min} = E_b$ . However, in Figure 25(a), at the bottom curves, the dashed curve shows a drastic deviation from the data. This curve is the best-fit with the same condition as previous samples - higher continuum coupling. For this sample, FUS seems to couple dominantly with lower states. The outgoing peaks become smaller in comparison to the incoming ones. The closeness of the fit is surprising when we use

$$D(E_c) = 2 D(E_v), D(E_v) \neq 0, \text{ and } E_{\max} = E_c. \quad (44)$$

As the SL become closer to a bulk, excitons in FUS are more coupled to confined states below the barrier by GaAs phonons via the continuum underneath. It may be also helped by larger proportions of matrix-elements from well regions. Therefore, we can conclude according to these results that

including the coupling with the continuum is essential in order to fully describe the exact mechanism of weakening of saddle-point excitons.

In summary, we have shown that RRS can measure effectively and sensitively many details of band structures of SLs and QWs. Also, RRS profiles in FUS energy regions can be represented by a simple perturbation theory expression with inclusion of the interaction from the above or underneath continuum states. We have shown that the different strength of coupling to other states can be modeled by a few lumped parameters, i.e. effective lifetimes at those resonating excitonic states. In particular, we found consistent behaviors in the strength of the excitonic resonance both at the ZC and at the ZB. Also we have verified the enhancement due to the resonance of wavefunctions at the barrier width both in FUS and in a second unconfined state. Saddle point excitons are demonstrated to exist with a significant strength in FUS, if the barrier is thick enough. For cases of thin barriers, the strength of saddle-point excitons is found to decrease due to the larger interaction with the continuum underneath of the miniband. Those results also suggest that RRS techniques have a good analytic capability for investigation of unconfined states.

## CHAPTER VI

### EXCITONIC RESONANCE AT THE GROUND STATES

At the ground state of a superlattice, it has been known that more pronounced excitonic effects exist. However, such effects associated with the significant dispersion of the state have not been so much discussed. The energy of the Brillouin zone center and the boundary is brought apart significantly as the dispersion becomes larger. We have observed new kinds of structures of excitonic peaks in PLE spectra. Those large dispersions also are found to make optical phonons resonate to states in minibands. Raman spectra show strong resonances which indicates that excitons follow down a resonant path scattered by phonons via a ladder of states from broadened minibands of different quantum numbers. These effects appear as multiple-phonon multiple-resonance scattering in Raman spectra.

#### Dispersion Associated Resonance in Superlattices

Excitons in quantum well structures have been investigated extensively both experimentally and theoretically [118,119]. However, excitons in

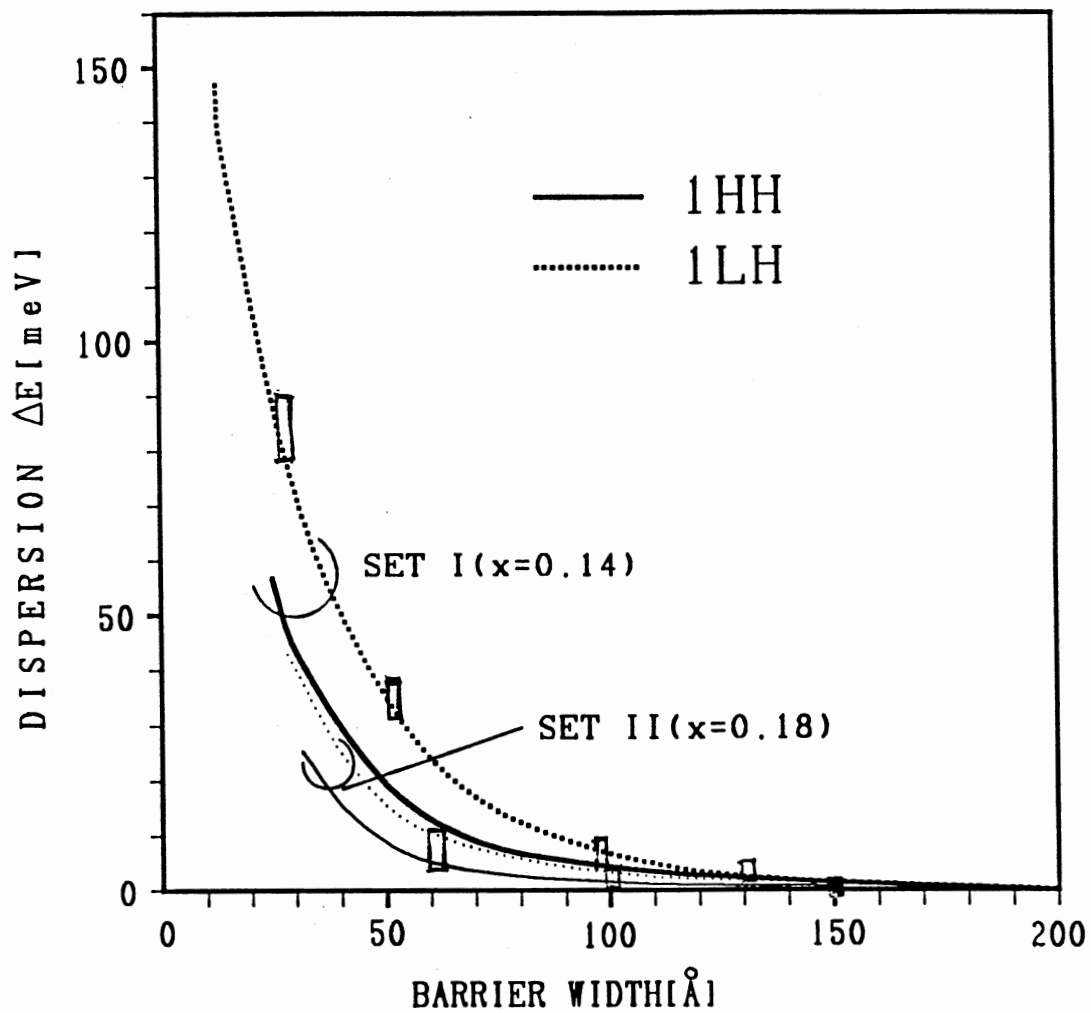


Figure 27. The range of the dispersion designed for samples. The sets of the sample parameters are specifically designed to cover the wide range of the dispersions in the SLs. The small rectangles indicate the dispersions of samples we examined.

superlattices where the well-to-well coupling is significant, have not received as much attention so far. In this section, we discuss the excitonic resonance associated with the saddle points ( $M_1$ -type critical points) and miniband dispersions at the ground states of superlattices. We show that observed spectra can be interpreted by a theory which incorporates Coulomb interactions and the valence band mixing. By using PLE, we have observed drastic changes in the spectra with variations in the barrier width  $L_b$  of the superlattice samples. The sets of the sample parameters are specifically designed to cover a wide range of dispersions. The magnitudes of dispersions are shown in Figure 27.

In thin-barrier SLs, pronounced peaks and bumps appeared in addition to major heavy-hole (HH) and light-hole (LH) exciton peaks. These additional structures arise from Coulomb interaction between electrons and holes associated with saddle points of the superlattice band structure. In a bulk crystal,  $M_0$  critical points are formed at the center of the Brillouin zone (BZ). In superlattices, critical points can be formed at two points of the BZ. For the  $n=1$  miniband,  $M_0$  is at the mini-zone center (ZC) and  $M_1$  (the saddle point) at the zone boundary (ZB). For  $n=2$  miniband, due to the different quantum number, the  $M_1$  point is at the ZC and  $M_0$  is at the ZB.

Recently, Chu and Chang theoretically investigated Coulomb interactions of electrons and holes associated with saddle-point states in super-lattices [120]. They calculated photoabsorption line-shape changes of 1HH excitons in GaAs-Al<sub>0.25</sub>Ga<sub>0.75</sub>As superlattices with  $L_z = 80\text{\AA}$  as functions of  $L_b$  ranging



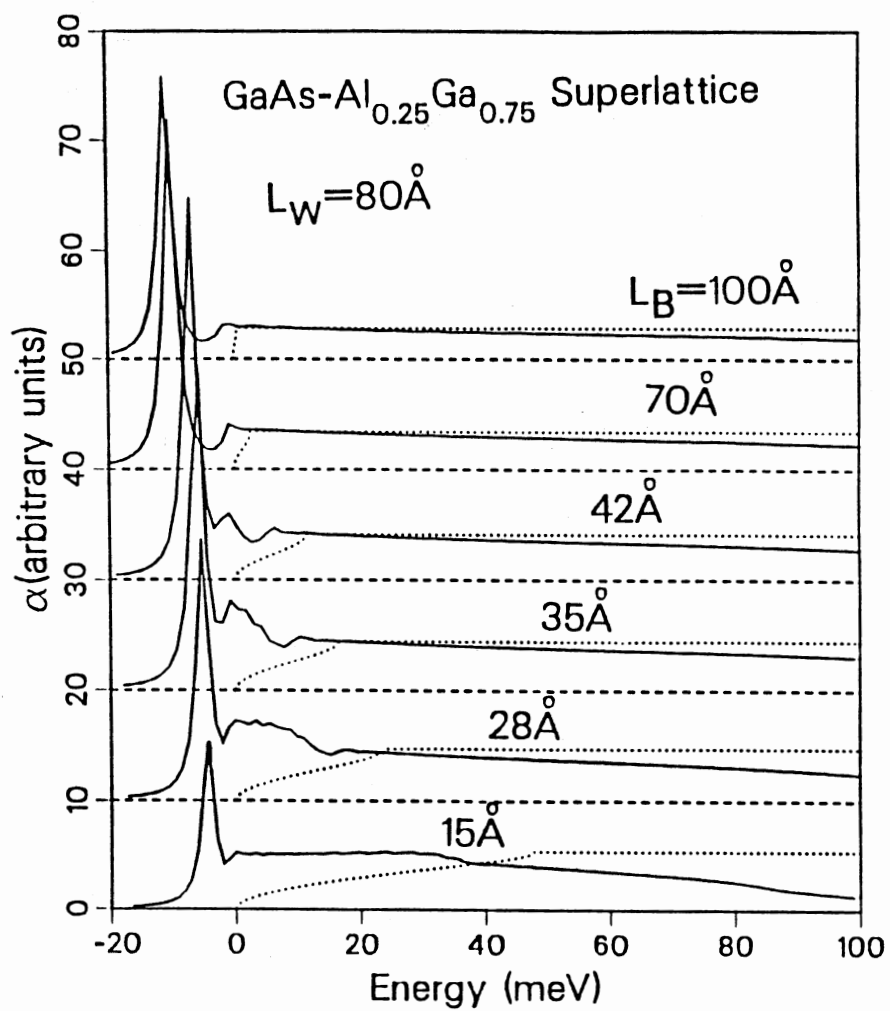


Figure 28. Calculated photoabsorption lineshapes of 1HH. Sample are GaAs-Al<sub>0.25</sub>Ga<sub>0.75</sub>As superlattices with  $L_z = 80 \text{ \AA}$  and  $L_b$  ranging from 100 to 15  $\text{\AA}$

to  $15\text{\AA}$ , as shown in Figure 28. For a thick barrier case ( $L_b = 100\text{\AA}$ ), the band structure is dispersionless in the growth direction and the calculated absorption spectrum is similar to that of a quantum well. For the thin-barrier case, the miniband dispersion in the growth direction is large and resulting absorption spectrum below the saddle point is similar to that of the bulk GaAs. For energies near the saddle point, the absorption dips down and smoothly joins a curve appropriate for a two-dimensional system. Only in the intermediate regime ( $L_b = 28\text{-}70\text{\AA}$ ) were prominent structures found between the main exciton peak and the saddle point indicating a redistribution of oscillator strengths by Coulomb interaction.

Figure 29 shows PLE spectra taken from a series of GaAs- $\text{Al}_{0.18}\text{Ga}_{0.82}\text{As}$  SL samples with  $L_z = 75\text{\AA}$  in the vicinity of  $n=1$  LH excitonic peaks.

Figure 29(a), 29(b), and 29(c) correspond to the SL's with  $L_b = 105, 60,$  and  $35\text{\AA}$ , respectively. A small aluminum concentration is chosen here, so that the miniband has a substantial dispersion even with a large barrier width. The detector was set at the peak of  $n=1$  HH exciton of each sample. The spectrum in Figure 29(a) is similar to one that has been observed in isolated wells [27] whereas spectra in Figures 29(b) and 29(c) are significantly different. For  $L_b = 105\text{\AA}$ , a bump appears on the high energy side of 1LH separated by  $\approx 10$  meV. No additional structures were noticed near this bump, which indicated by L in Figure 29(b). The corresponding bump for 1HH is indicated by H. These structures, H and L, develop into clear peaks for  $L_b=60$  and  $35\text{\AA}$ .

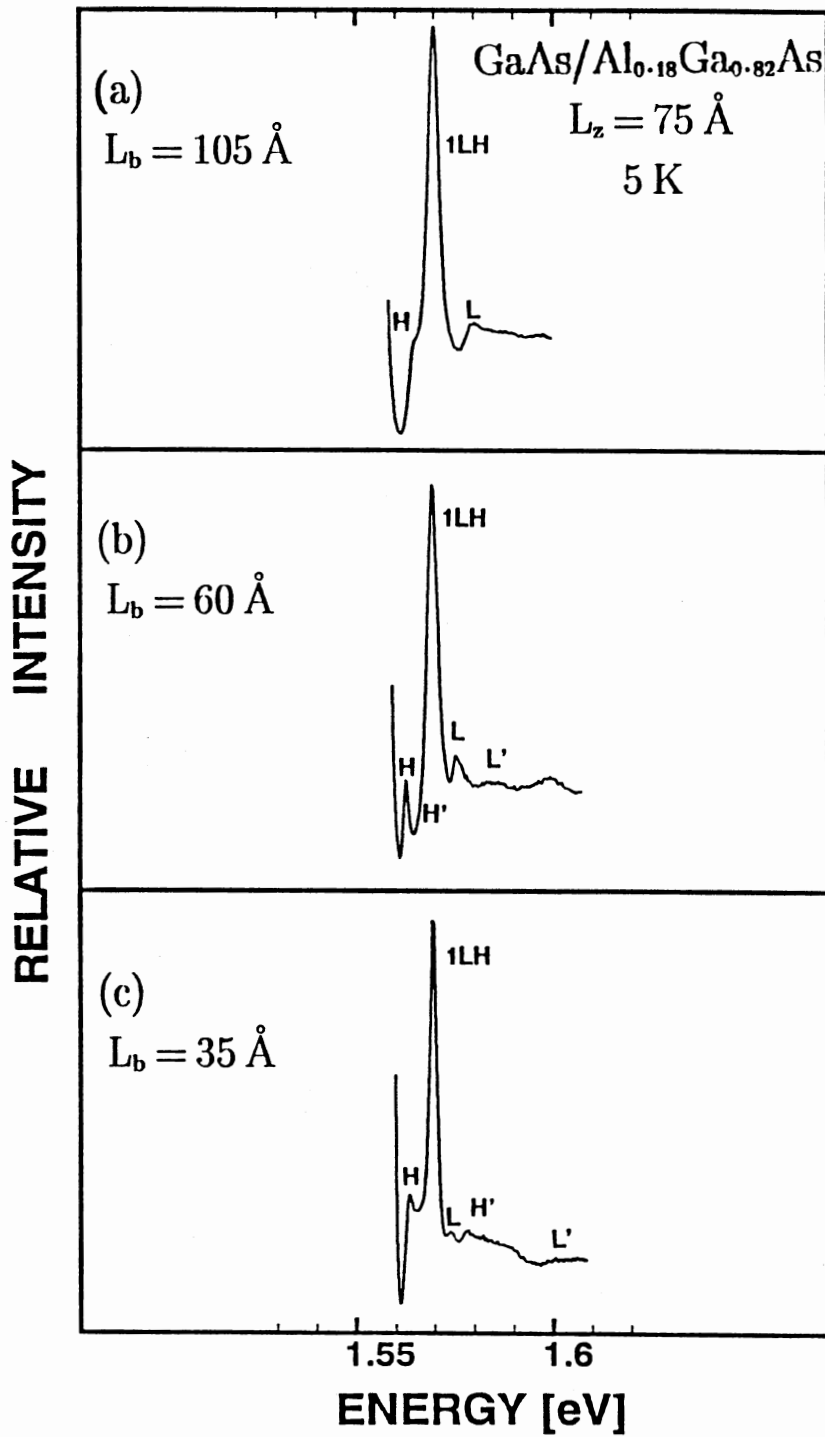


Figure 29. PLE spectra taken from a series of GaAs-Al<sub>0.18</sub>Ga<sub>0.82</sub>As SL. The samples are of  $L_z = 75 \text{ \AA}$ . Spectra (a), (b), and (c) correspond to the SL's with  $L_b = 105$ ,  $60$ , and  $35 \text{ \AA}$ , respectively.

Those trends are clearly visualized in PLE spectra from another series of GaAs-Al<sub>x</sub>Ga<sub>1-x</sub>As SL samples. In Figure 30, those spectra are shown. In these cases, the detector position was set at ~1meV below the HH PL peaks, so that we can detect both 1HH and 1LH peaks.  $L_z$  and  $x$  values were fixed at 59 Å and 0.14, respectively, whereas  $L_b$ 's were 130, 99, 72, 51, and 31Å. Peaks H and L are clearly seen in samples in intermediate range of  $L_b$ . The line shape of the spectrum for  $L_b = 130$  Å is essentially as same as that in Figure 29(a).

We attribute peaks H and L to a mixture of 2s exciton states and band-edge resonance arising from a redistribution of oscillator strengths caused by Coulomb interaction. In a quantum well with no miniband dispersion such as sample in Figure 29(a), H and L are most likely 2s states merged to a steplike band continuum. In superlattice with large miniband dispersion, a significant portion of H and L strength can come from the lower band-edge resonance, as we have mentioned above. The relative intensity contributions are difficult to determine because the line shape changes with sample parameters, such as  $L_b$ . The portion of spectra are redrawn in Figure 31 from samples with  $L_z = 75$  Å,  $L_b = 60$  Å,  $x=0.18$  and  $L_z = 59$  Å,  $L_b = 99$ Å,  $x=0.14$ . In contrast to the nearly symmetric line shape of the fundamental excitonic peaks, H and L exhibit asymmetric line shapes. The degree of asymmetry increases with an increase in the miniband dispersion. It is mostly evidenced in the inset of Figure 31, where peak L has a longer tail toward the high-energy side than peak H. It appears that the sharp rise of these

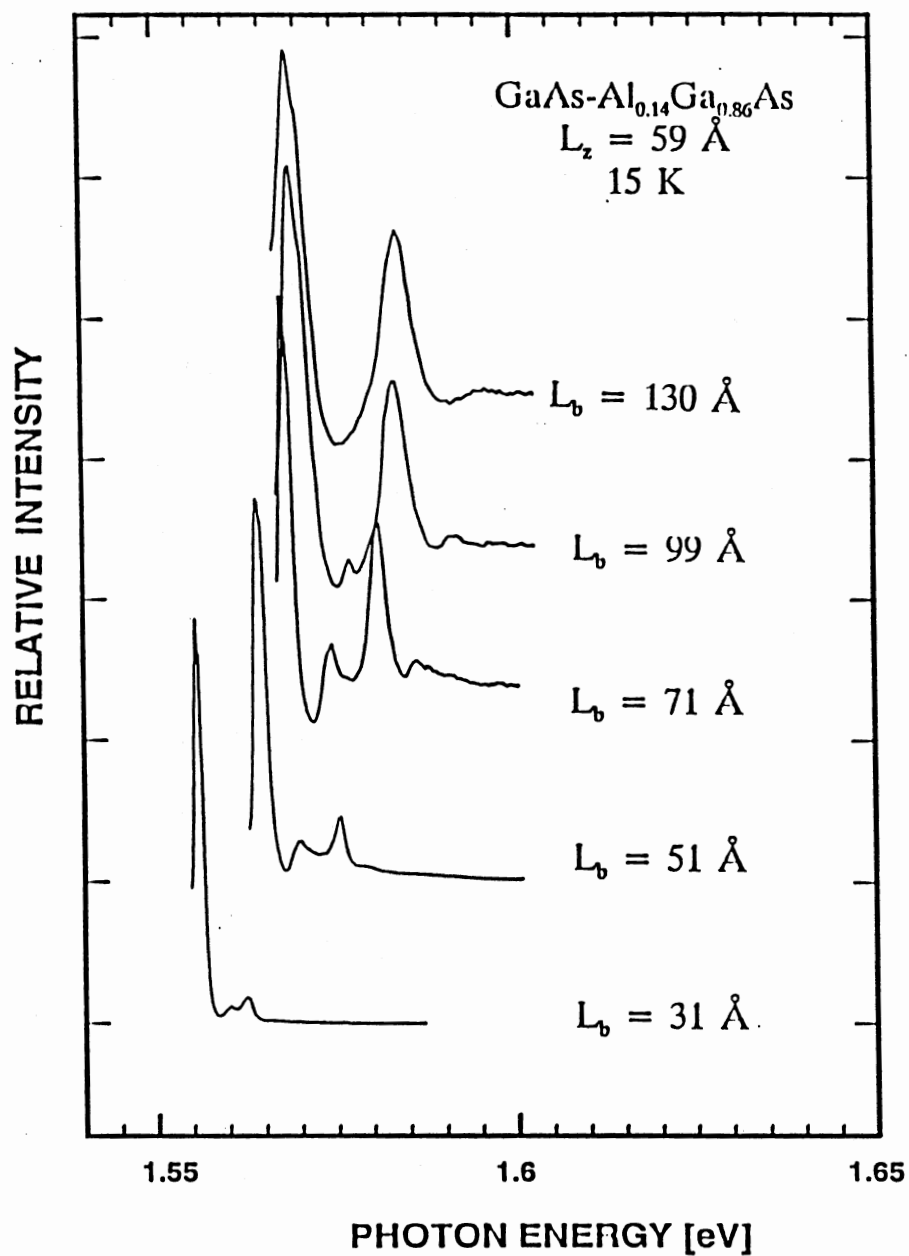


Figure 30. PLE spectra from a series of GaAs-Al<sub>x</sub>Ga<sub>1-x</sub>As SL samples. The detector position was set at ~1meV below the HH PL peaks, so that we can detect both the 1HH and 1LH.  $L_z$  and  $x$  values were fixed at 59 Å and 0.14, respectively, whereas the  $L_b$ 's were 130, 99, 71, 51, and 31 Å.

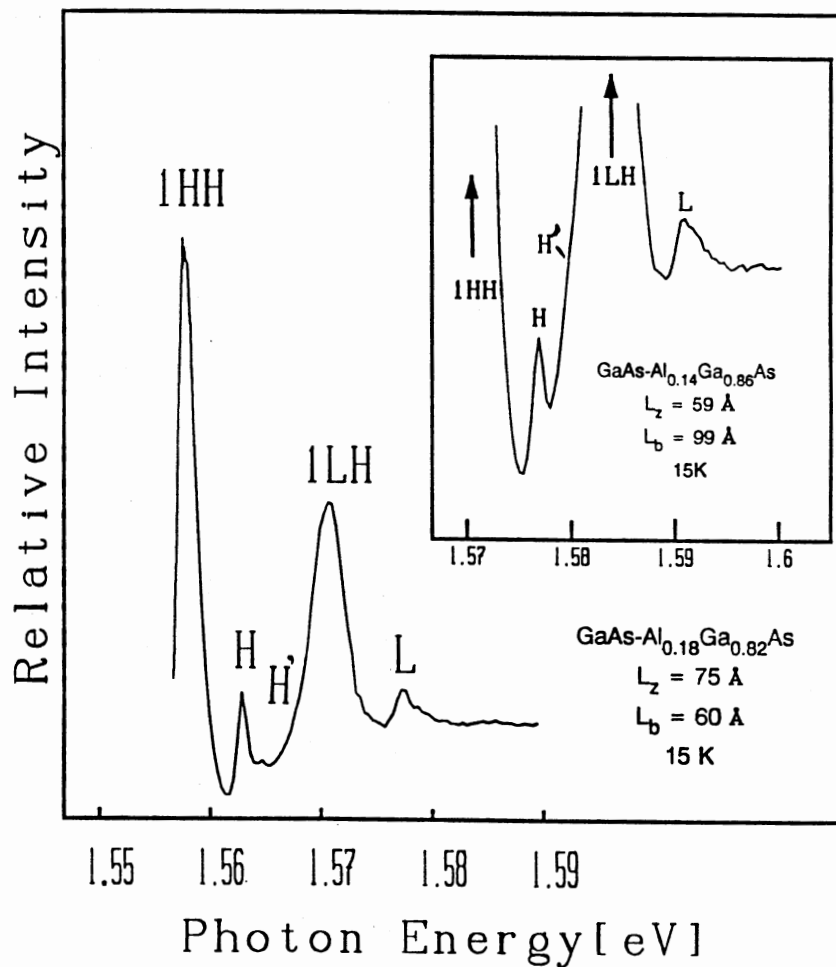


Figure 31. The portion of the spectra for H and L. The spectra are from samples with  $L_z = 75 \text{ \AA}$ ,  $L_b = 105 \text{ \AA}$ ,  $x=0.18$  and  $L_z = 59 \text{ \AA}$ ,  $L_b=99 \text{ \AA}$ ,  $x=0.14$ . H and L exhibit asymmetric line shapes. The degree of asymmetry increase with an increase in the miniband dispersion. In the inset, L has longer tail toward the high-energy side than peak H.

asymmetric peaks originates from 2s states, and the slowly decreasing tail from the band-edge resonance. Such asymmetric line shapes can be generated theoretically as we describe later.

In addition to the forementioned peaks H and L, we detect other peaks and structures in the spectra, which can not be assigned to any optical transitions between the states with  $n \neq 1$  such as the forbidden transition between  $n=2$  heavy-hole and  $n=1$  conduction states. According to theoretical calculations, exciton resonance can also occur near saddle points of  $n=1$  minibands [120,121]. The degree of the resonance enhancement depends on  $L_b$ . These resonance peaks are less pronounced than those secondary peaks near  $M_0$  points. Therefore, they should be harder to detect than H and L. In the spectra, we observed, peaks marked as H' and L' in Figure 29(b),(c) are attributed to the saddle-point resonance enhancement. Our attribution is based on the consideration of transition energies and systematic experiments varying only one parameter.

The theoretical calculations for such line shapes are based on the method described in Reference 120. To get realistic absorption spectra, we have included the effect of valence-band mixing. To make the computation feasible, the axial approximation introduced by Altarelli [122] was used. This allows us to reduce the number of valence minibands by a factor of 2 (each valence miniband becomes doubly degenerate.) Furthermore, the valence-miniband structure becomes spherical in the x-y plane. A specific angular-dependent phase factor was introduced in the exciton envelope

function in the same way as described in Reference 123. Since the number of states is substantially larger in this situation, a brute matrix diagonalization is impractical. Thus we adopted the recursion method [124] to calculate the density of states for each heavy- or light-hole component (labeled with  $\nu=3/2$  or  $1/2$ ), which in turn gives rise to the absorption spectrum when multiplied by the proper optical matrix element squared. The problem is therefore substantially simplified. We shall consider excitonic states with orbital angular momenta  $l = 0$  and  $1$  (i.e. s-like and p-like) only. The higher angular momentum states are much less important in the calculation of the absorption coefficient. Due to the symmetry, the two sets of excitonic states described by [(s-like, $\nu=3/2$ ),(p-like, $\nu=1/2$ )] and [(p-like, $\nu=3/2$ ),(s-like, $\nu=1/2$ )] are decoupled. To obtain accurate results, many miniband states of different quantum numbers are needed in the expansion of excitonic states. In the present calculation, we included both s-like and p-like excitonic states associated with 1HH, 2HH, and 1LH valence minibands only. We refer to this as a three-band model. The adequacy of this model was tested by including more miniband states but with smaller number of mesh points in K space and we found qualitatively same results.

Figure 32 shows the calculated absorption coefficient for excitonic states associated with the first conduction miniband of a GaAs-Al<sub>0.18</sub>Ga<sub>0.82</sub>As superlattice ( $L_z=75\text{\AA}$ ,  $L_b=100\text{\AA}$ ) and a SL ( $L_z=75\text{\AA}$ ,  $L_b=60\text{\AA}$ ) obtained in the three-band model (dashed curves). The experimental data (solid curves) are superposed for comparison. The agreements are remarkable. The presence



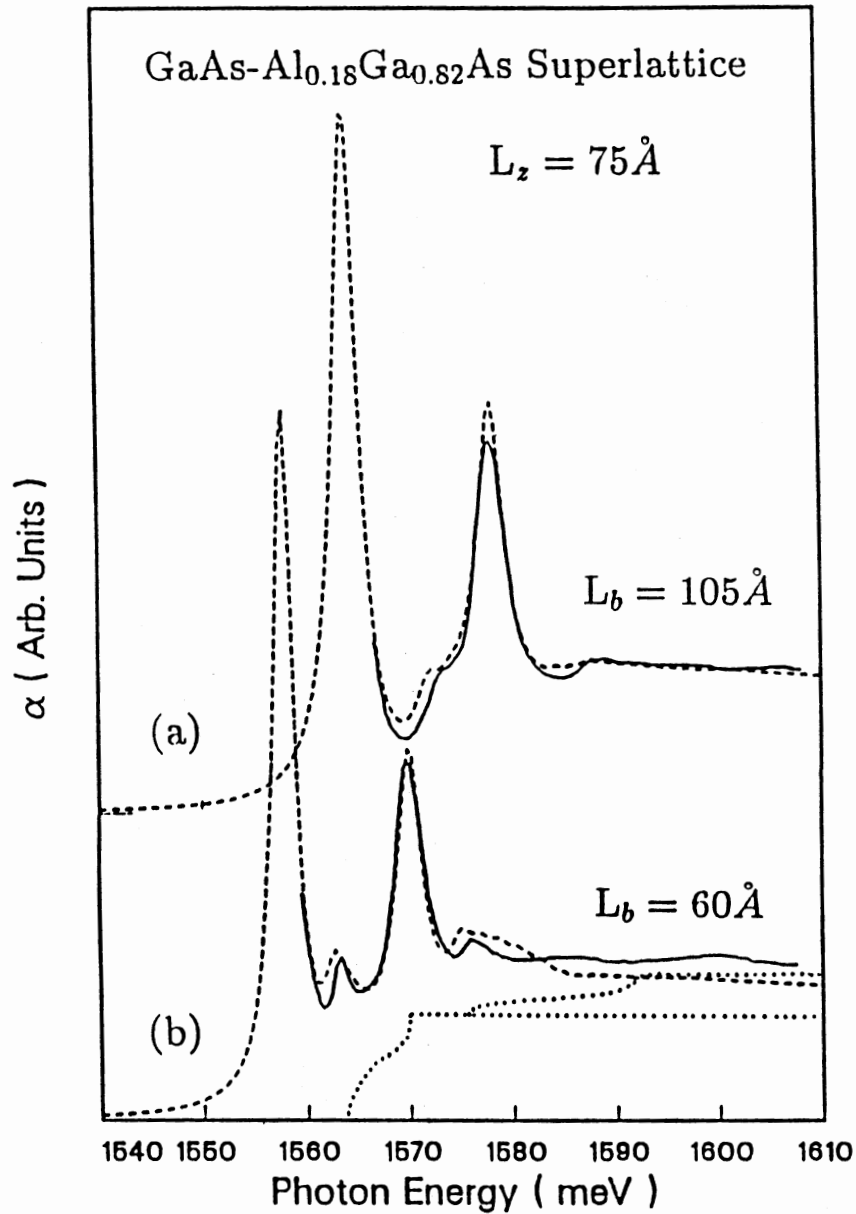


Figure 32. Calculated absorption coefficient for excitonic states. It is associated with the first conduction miniband of a GaAs-Al<sub>0.18</sub>Ga<sub>0.82</sub>As superlattice ( $L_z=75 \text{ \AA}$ ,  $L_b=100 \text{ \AA}$ ) and a SL ( $L_z=75 \text{ \AA}$ ,  $L_b=60 \text{ \AA}$ ) obtained in the three-band model (dashed curves). The experimental data (solid curves) are superposed for comparison.

of discrete peaks, positions and asymmetric lineshapes are produced well by the theory without adjusting parameters.

What we have discussed so far for  $n=1$  states can be extended to the  $n=2$  case. The same kind of H peak appears as an indication of miniband dispersion in superlattices but they are absent in quantum wells. In Figure 33, shown is the excitonic peak from the transition between the  $n=2$  heavy-hole band to the  $n=2$  conduction band of a SL ( $L_z = 75 \text{ \AA}$ ,  $L_b = 75 \text{ \AA}$ ,  $x=0.21$ ). Those bumps marked as H are interpreted of the same origin as peak H in Figure 31. The dotted line is from the theoretical calculation using the same model as above. The main excitonic peak is indicated as 2HH. The 1lh-2e forbidden peak shows up as a small structure here due to the valence-band mixing. Therefore, the redistribution of oscillator strengths across the miniband dispersion can be observed either in ground states, or excited states. Obviously, in thick barrier samples, as QWs, the peak H is not observable as shown in the inset, ( $L_z = 75 \text{ \AA}$ ,  $L_b = 150 \text{ \AA}$ ,  $x=0.18$ ) The identification of the H and L peaks can be utilized to determine the excitonic binding energies as we will discuss in Chapter VII.

In summary, we have observed a detailed energy structures of the superlattices with significant dispersions, in a systematic experiment. A new kinds of peaks are clearly observed as a consequence of Coulomb interaction associated with the dispersion at the ground state as well as in the second miniband. In the lower energy side, peaks H and L contained 2s-exciton contributions and the lower bandedge excitonic resonances showing a

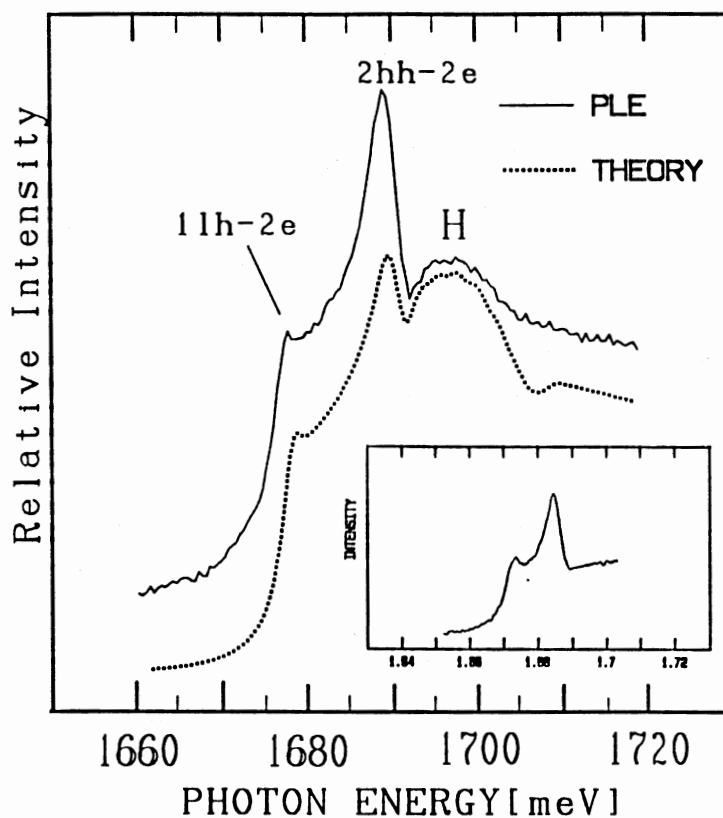


Figure 33. The  $n = 2$  heavy hole miniband excitonic effects. Shown is the excitonic peak from the transition between  $n=2$  heavy hole band to the  $n=2$  conduction band of a SL ( $L_z = 75 \text{ \AA}$ ,  $L_b = 75 \text{ \AA}$ ,  $x=0.21$ ). Those bumps marked as H are interpreted of the same origin as peak H in Figure 31. The dotted curve is from the theoretical calculation using the same model as the  $n=1$  case. The main excitonic peak is indicated as  $2hh-2e$ . The  $1lh-2e$  forbidden transition structure shows up here due to the valence-band mixing.

characteristic asymmetric line shape, whereas at the higher side H' and L' are excitonic resonances near the saddle points for the ground states. For  $n=2$  miniband, it is clear that a similar kind of H peak is observed while it is absent in a quantum-well sample. The agreement between experiments and the theory is remarkable. The theory incorporates a three-band model with Coulomb interaction of the saddle point exciton effects as well as valence band mixing. Those resonances can be used for a direct observation of the excitonic binding energies.

### Multiple Resonance and Phonon Scattering

We have discussed, in sections in Chapters II and V, several aspects of Raman processes involving only one phonon. As many of the other particle-scattering processes, more than one phonon can be involved in scattering. Two-phonon Raman scattering has been observed in many kinds of crystals [42,69]. In higher order processes, the efficiency is much lower [39]. Thus multi-phonon scattering phenomena were observed in limited kinds of semiconductor crystals, for example, GaP [125], CdS, CdSe, ZnSe, ZnTe, ZnO [42]. In many of those, resonances to electronic or excitonic states has been observed to enhance the efficiency dramatically. In CdS, multiple phonon effects up to  $m=10$  are clearly observed when scattered light is resonant to excitonic states below the bandedge [126]. For CdTe [127], the resonance also is clearly demonstrated by groups of distinct sharp lines. Here, excited excitonic states (up to quantum number 3) of bulk excitons

showed up both at the incoming and outgoing resonances. Separations between them are close to one LO-phonon energy. However, it is rare when multiple ( $m > 2$ ) phonon effects are reported in bulk GaAs [128] or  $\text{Al}_x\text{Ga}_{1-x}\text{As}$ . It may indicate the weakness of the strength in resonance at those critical points of bulk semiconductors, such as the fundamental bandedge ( $E_0$ ), so called  $E_0 + \Delta_0$ , and  $E_1$  [42,128,129]. Nowadays, with quantum-wells (QWs) and superlattice (SL) structures, additional critical points in band structures can be realized (See Chapter I). Among others, with GaAs and  $\text{Al}_x\text{Ga}_{1-x}\text{As}$ , high quality samples of SLs or QWs are fabricated with well-defined interfaces down to less-than-monolayer precision. QWs have discrete energy levels. Compared to a bulk GaAs, the valence band degeneracy is removed into two discrete bands, the heavy hole and light hole bands, as explained in Chapter I. Such changes in the band structure bring us enhanced resonances for phonon interactions that have been cancelled or reduced in bulk crystals [42].

Quantized states with a proper energy spacing make appear the multiple phonon scattering resonant between  $n=1$  and  $n=2$  electron states [130,131,89], or  $n=1$  heavy hole and light hole states [132]. In this section, we show that large excitonic dispersions in superlattice minibands results in higher-order phonon combinations and overtones in spectra via multiple-resonant Raman scattering. Furthermore, by utilizing the phenomena, we can suggest to construct a detailed path of the scattering process, which might allow us to verify experimentally the dispersion relation of SL band structure or some dynamic properties such as excitonic lifetimes. The combination refers to a

scattering process by two or more phonons from different branches, while the overtone is by phonons from the same branch.

The multiple-resonant Raman peaks are observed in two of superlattice samples with relatively thin barrier widths. One of them has particularly lower luminescence than other samples. The low luminescence effectively separates peaks from the background, which has also been noted in Reference 89. We have found they are resonant to  $1e-1hh$ ,  $1e-2hh$ , and  $1e-3hh$  SL exciton states, using the conventional notation as before. The observation of various combinations and overtones of phonons (LO and TO) is unique. In a recent similar work [131], only overtones were observed up to the 3rd order which was very weak. On the contrary, we observed clearly peaks of one LO, LO+TO, 2LO, TO+2LO, 3LO, TO+3LO, and 4LO. Therefore, it became possible to analyze relative intensities and line-widths among those modes. These improvements result from using SLs with large dispersions. The positions, separations, relative intensities, and the full-width-half-maximum (FWHM) are summarized in Table IX.

Experiments are performed at a LHe temperature of 15K, using a near backscattering scheme ( $\theta \leq 8^\circ$  inside of crystal) with  $\theta = 0^\circ$  along the z-axis which is the sample growth direction. The light from the dye laser is linearly polarized, and so is the detection (extinction ratio better than 10 at 800nm). The detector, Hamamatsu GaAs PMT, cooled down to  $-40^\circ\text{C}$ , is set at the 1HH energies or close to it. Light gathering optics are as described in Chapter III, with one lens ( $L_1$ ,  $f=15\text{cm}$ ,  $F=1$ ) closer to the samples and the

TABLE IX

INTENSITIES, FULL-WIDTH-HALF-MAXIMUM, POSITIONS, AND  
POLARIZATIONS OF VARIOUS RAMAN MODES.

modes	Position	separation	Intensity	$I_{\perp} / I_{\parallel}$	FWHM
	A (B)	A (B)	A (B)		$\pm 0.1\text{cm}^{-1}$
	( $\text{cm}^{-1}$ )	( $\text{cm}^{-1}$ )	(a.u.)		( $\text{cm}^{-1}$ )
1LO	295.2	-	76.2	0.18	3.5
TO+LO	563.5(563)	268.4	18.7(1.7)	0.87	4.7
2LO	586.2(583)	291.1	48.2(15)	0.25	6.7
TO+2LO	858.0(856)	271.8	19.6(2.0)	0.93	8.4
3LO	878.2(878)	292.0	4.0(10.4)	0.67	6.9
TO+3LO	(1150 $\pm$ 1)	272	(2.2)	-	(15 $\pm$ 3)
4LO	(1170 $\pm$ 1)	292	(11.4)	-	(9 $\pm$ 1)

other ( $L_2$ ,  $f=30\text{cm}$ ,  $F=2.5$ ) after that. The resolution of the spectrometer was better than  $1.5 \text{ \AA}$  (FWHM). Spectra are obtained by scanning the dye laser (FWHM  $\sim 0.1\text{meV}$ ) at a few fixed detector positions.

The spectra are shown in Figure 34. Extremely sharp structures appear in both the polarization configurations, i.e.,  $z(x',x')\bar{z}$ , and  $z(x',y')\bar{z}$ .  $x'$  and  $y'$  indicate  $[110]$  or  $[\bar{1}\bar{1}0]$ . The spectrum A and B are obtained separately with two different kinds of dyes due to the wide range. Sharp peaks marked as  $m\text{LO}$ , or  $\text{TO}+m\text{LO}$ , ( $m = 1,2,3,4$ ) are resonant Raman peaks. The ordinary PLE structures are indicated by  $1e-2hh$ , etc. These assignments are based on results by the two-band TBA calculation [14]. Those pedestal structures under the sharp ones are verified stationary in experiments for different detector positions, while sharp ones move in parallel with separations which agree with energies of phonon modes. This proves that the peaks are indeed from Raman scattering. In Figure 35,  $1\text{LO}$  Raman spectra around  $1e-1hh$  PL position are shown when the excitation wavelength is varied within  $\pm 0.7\text{nm}$ . We can notice the strong resonance when  $\text{LO}$  peak is coincident to  $1e-1hh$  PL peak. The shifted frequency was almost constant  $36.38 \pm 0.08 \text{ meV}$  ( $293.5 \pm 0.6 \text{ cm}^{-1}$ ). Particularly, in Figure 34, the first order Raman spectra at any of those peak positions of  $m \geq 2$  are not detectable. We understand this as the contributions from other non-resonant processes are negligibly small. In the other sample, only  $2\text{LO}$  are observed unambiguously, but it was merged above a larger PL background than the previous sample.



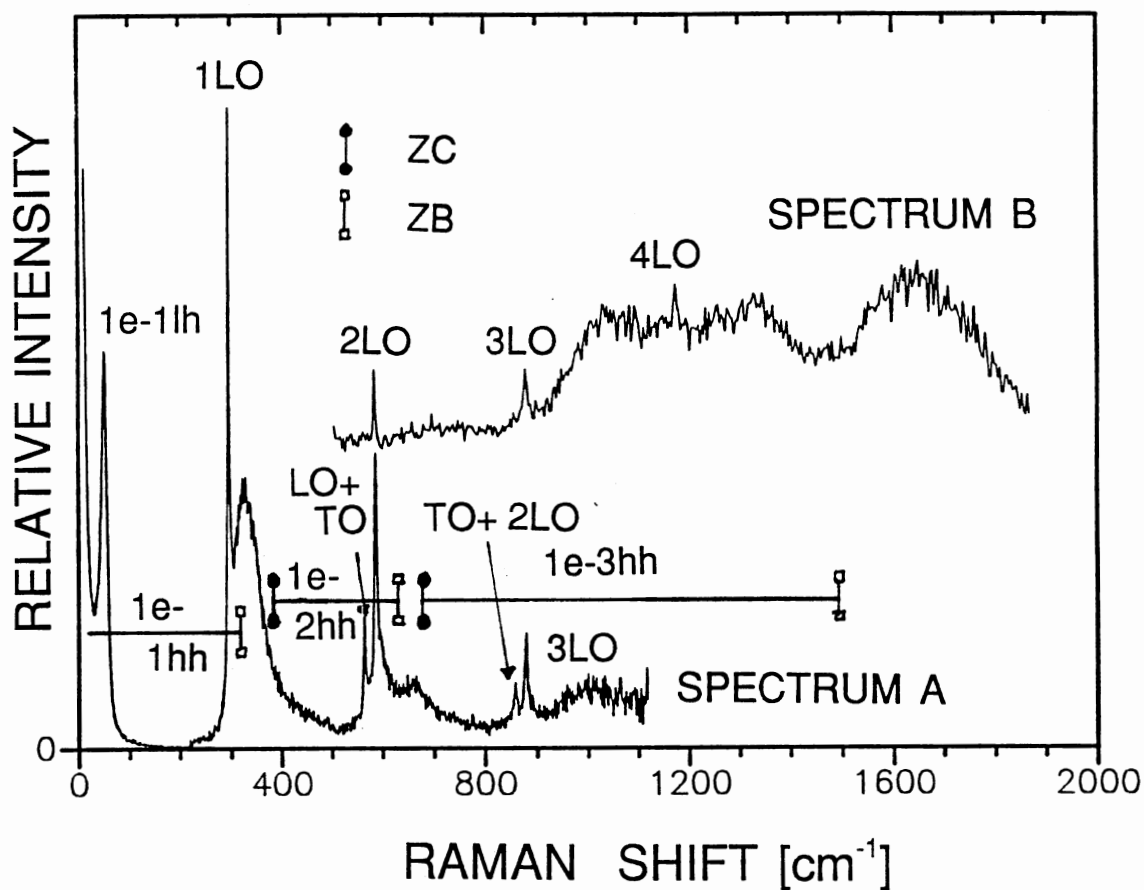


Figure 34. Multi-phonon Raman spectra. The spectra were obtained with two different dyes (Spectrum A and Spectrum B). The detector was fixed at one position, and the dye laser was scanned. Sharp peaks are Raman peaks ( $mLO$ ,  $TO+mLO$ ), and the broad spectra ( $1e-2hh$ ,  $1e-3hh$ ) underneath are photoluminescence.

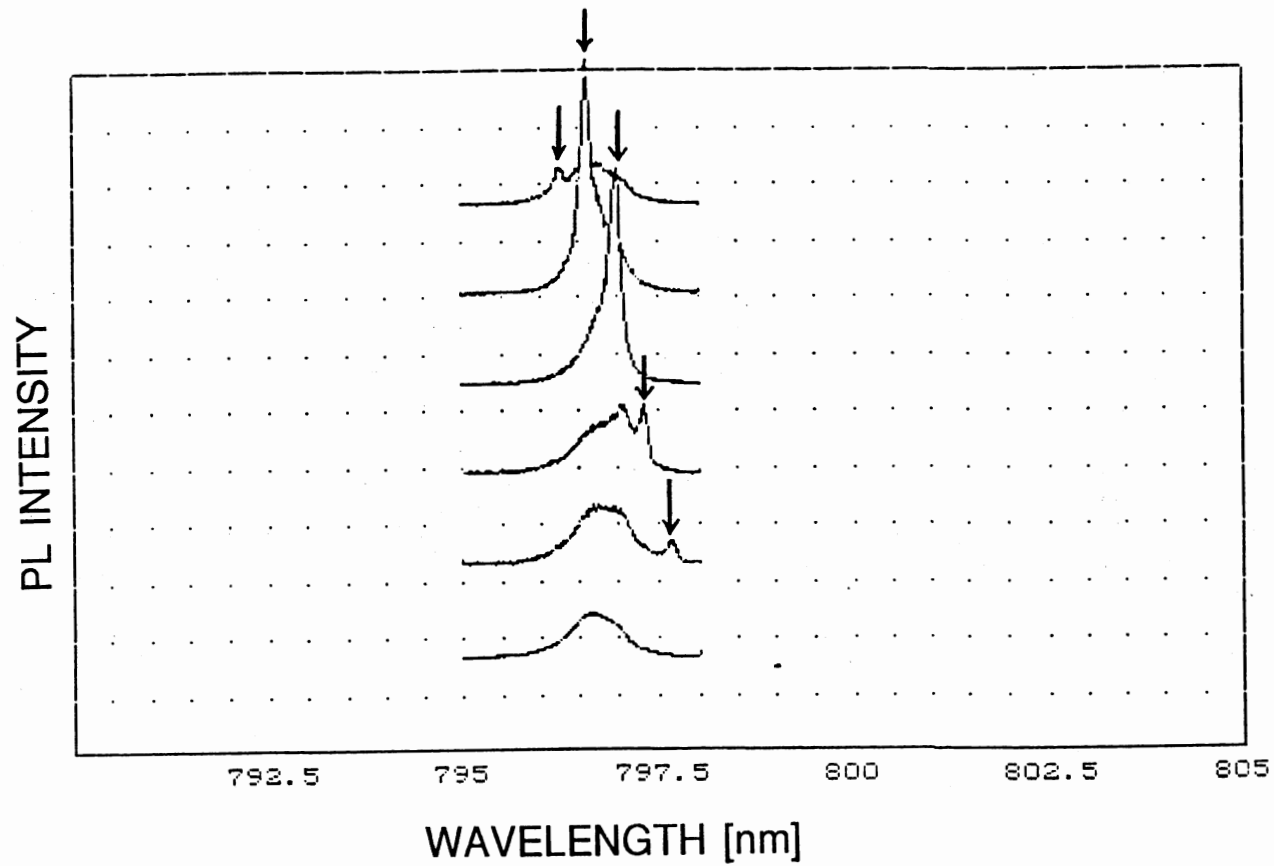


Figure 35. Photoluminescence and a resonant Raman peak. While the dye laser is scanning, Raman shifted 1LO peak (indicated by small arrows) is crossing the broad PL structures. The bottom one is when there is no Raman peak in the range.

In Table IX, also included are the measured polarization dependence in ratios of two intensities of orthogonal polarizations. LO's are stronger in  $z(x',x')\bar{z}$  configuration. Peaks with TO phonons are not so much affected as mLO peaks are. In other words, they are more depolarized. It has been pointed out that TO phonons are scattered via mainly by deformation potential and are unpolarized compared to the LO counterpart near the resonance [42].

The separations of peaks agree well with the energies of bulk phonons, but there are some variations as manifest in Table IX. They decrease slightly and uniformly. This may indicate that the higher orders ( $m \geq 2$ ) are scattered with larger momenta ( $q \neq 0$ ) which result in smaller phonon energies. The difference between 2LO and 1LO is smaller than others and the detected 1LO position corresponds to a slightly higher energy. It may be due to a larger tolerance in the calibration of the dye laser wavelength. Except for 1LO, differences are accurate within  $\pm 0.5 \text{ cm}^{-1}$ .

Those combinations and overtones can be qualitatively analyzed. Generally, they are results of resonant-cascade-multi-phonon scattering. The peaks appear when photo-excited excitons relax down a ladder of states one step after another. The condition of one or more resonant transitions (double, or triple resonance Raman scattering) is required to explain why such sharp, relatively strong peaks appear even at high orders, while the first order scattering is very small at the same positions. In other words, one, two, or more intermediate states must be real. Therefore, we can explain those observed peak positions and intensities, by finding appropriate scattering paths

on an excitonic dispersion diagram, using those conservation rules and phonon dispersion relations. Instead of the excitonic diagram, one could imagine different scattering schemes by using hole-only or electron-only dispersion diagrams. We found after a few trials, however, that within the tolerance of sample parameters, it is very difficult, if not impossible, to satisfy the multiple-resonance as prescribed by experimental data except for the excitonic diagram.

Phonons in SLs have been shown to appear at energy values corresponding to the bulk dispersion sampled at  $q_z = n\pi/d$  ( $n=1,2,\dots$ ) because phonon branches are folded to  $q=0$  point by the period  $d$  of a superlattice. See LO-phonons in GaAs in References 51,53,72,133-137. TO-phonons in Reference 48. In our case, the period ( $d$ ) is more than  $32a$ , where  $a$  is the lattice constant of GaAs, and then the energy value corresponding to  $\pi/d$  is too small to be resolved ( $\sim 1 \text{ cm}^{-1}$ ). Thus the discrete nature will not be observable. However, it can be certain that phonons (LO and TO) have almost same dispersion relations as a bulk in our SLs.

LO phonons are forbidden in backscattering schemes by Loudon's selection rules [138]. They are, though, observed via the interband Fröhlich process [71] (See the second section in Chapter V) and they are strongly polarized [42]. In particular, near resonances, the enhancement can be so dramatic that high order Raman scattering up to the 10th were observed in CdS [126]. The other possible strong enhancement is via impurity assisted processes [139], which can make the outgoing resonance stronger than the

incoming one when the impurity concentration is rather high. According to Zucker's recent results [80], the interband F-process also can enhance the outgoing strength strongly due to coupling to an different exciton quantum state. In our data, the peak we observed near  $1e-1hh$  position corresponds to the outgoing resonance by one LO, while incoming resonance could not be resolved due to the PL background. The concentration of the impurity of samples examined here are less than those for the impurity processes. The polarization of LO's are rather distinct in this work. Therefore, we can conclude that component of impurity scattering are negligible here and the scattering is through F-processes.

On the other hand, TO are forbidden in our orientation of samples. Consequently, we could not have the first order TO peak. The combination of TO's however can be resonant via the deformation potential while overtones can not be, which is shown with two-phonon process case in Reference 42. Experimentally, TO+LO were detectable in CdS [126 and Ref. 3.42 in 39] and TO, LO+TO were observed to resonate strongly at  $E_0$  of GaP [125]. Those facts explain well the lack of TO-overtones in our data and that there are only combinations with one TO. Thus, we find that final two steps of the TO combinations are by either a TO after a LO mode, or vice versa, resonant to states in minibands.

The intermediate states in a multiple Raman process can be either real or virtual. It is necessary to explain differences between two cases in relation to the ratios between intensities of successive orders. Although there have

been a few theoretical, or experimental approaches to this problem [42,69,140], a satisfactory theoretical model of scattering processes with a specific SL band structure is not readily available for those high order resonant scattering. Thus we derive a simple relation utilizing concepts from the method by Cardona [42] which is originally from Martin and Varma [141]. Here, we need a modification from the model when all the intermediate states are real. In their original configuration, the emission from each state is detected, while in ours only those that reach final ground states are detected. In addition, we will consider a specific case of double resonance where final two intermediate states are real in all the cases we consider here.

Suppose  $m$  number of scattering has occurred in a cascade manner before arriving at the ground state. First, let us consider the case when the intermediate states are all real. The intensity would be proportional to a *retaining ratio*,  $\rho$  at each state. Assuming  $\rho$  is same in every state, the final intensity  $I_m$  will be

$$I_m = I_1 \rho^m. \quad (45)$$

$\rho$  is related by

$$\rho = (1-S). \quad (46)$$

The branching ratio  $S$  is given by the ratio of lifetimes as same as that originally defined [141], that is,

$$S = t_{LO} / t_R, \quad (47)$$

where  $t_{LO}$ ,  $t_R$  are lifetimes of phonons and the state respectively.

Secondly, suppose that all the intermediate states except the final two are virtual. Then, considering the number of possible scattering paths in  $(m-2)$  cascade scattering and two real transitions at the end, the intensity will be

$$I_m = \rho\rho'/(m-2)! \quad (m \geq 2), \quad (48)$$

where  $m$  is the sum of numbers of LO and TO.  $\rho'$  indicates a separate retaining ratio for TO. In Figure 36, relative intensities are plotted in a semi-logarithm scale after correction by approximate absorption coefficients such as

$$\alpha(m) = \alpha_0 m^{1/2}, \quad (m=1,2,3,\dots) \quad (49)$$

where  $\alpha_0$  is a constant and a 3D-type absorption coefficient is used. Trends of LO-overtones and TO-combinations clearly depart from each other. Equation (45) is plotted as the solid line, and the dashed line represents Equation (47). The intensity of mLO peaks (circles-Spectrum A, triangles -Spectrum B) corresponds to a real-state case except for  $m \geq 3$ , while all the TO-combinations (squares) are close to a virtual-state case. The agreement in trend in both cases is good. Therefore, we find that scattering processes in the TO-combination is via virtual states following 1TO and 1LO resonant scattering at the final stages (their ordering will be discussed later). LO overtones up to  $m=3$  seem scattered via various real minibands. For 4LO, it is obvious the intermediate state is virtual, as it flattens out after 3LO. It would be worth mentioning that the energy is high enough to have some contributions from the near-continuum states above the potential barrier.

From the slope we can deduce  $\rho=0.52$  using Equation (45). The relatively small value is likely due to the small matrix element for such

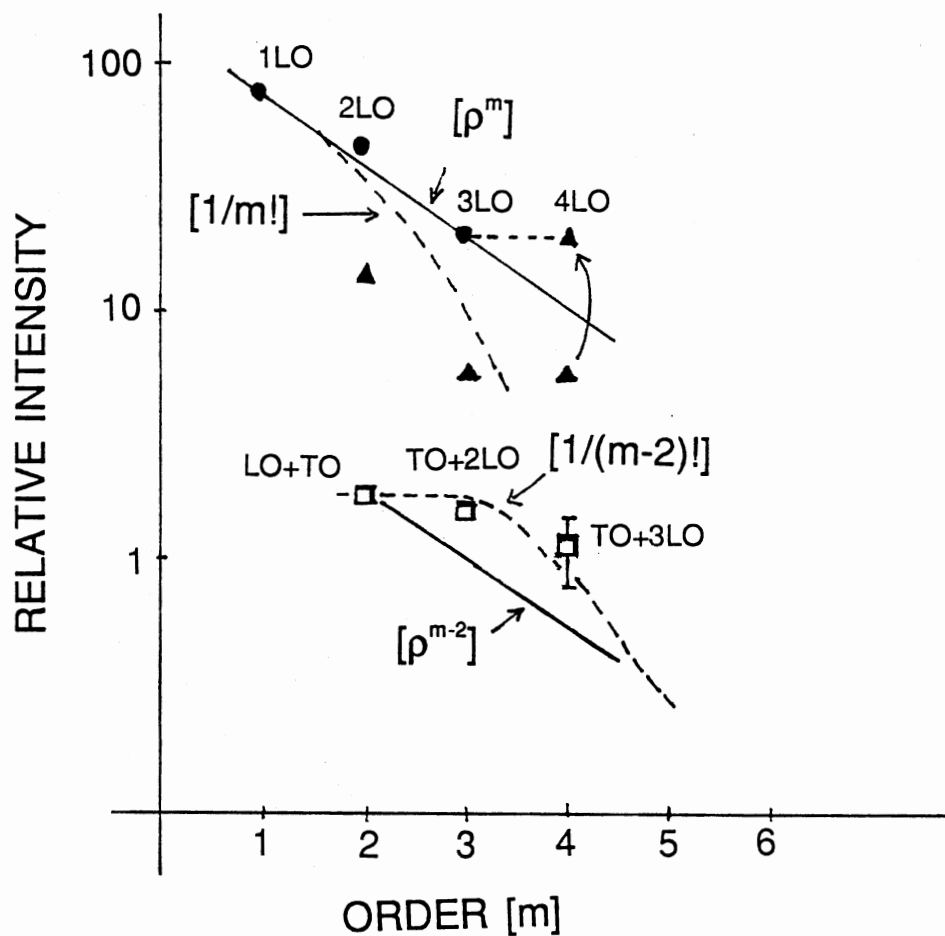


Figure 36. The relative intensity of the overtones and the combinations. The order of a combination are given by the sum of orders in TO's and LO's. Dotted lines are for virtual intermediate states, and solid lines are for real intermediate states cases. The intensities from Spectrum B are shifted to fit to those of Spectrum A to determine the relative 4LO intensity. The vertical scale is in logarithm.



coupling. The rest may go either to PL or non-radiative relaxation via interfaces mainly with the help of the acoustic phonons, which are non-resonant. We can approximately derive  $\rho'$  for TO by comparing 1LO (the average of the both polarizations) and LO+TO intensities, which results in  $\rho'=0.064$  and it is much smaller. Thus, it is consistent with the fact that none of TO-overtone are observed.

Based only on those findings, we can construct a *path-map* of scattering processes for LO overtones as well as for TO combinations as shown in Figure 37. The thick solid curves represent dispersion relations of 1e-1hh, 1e-2hh, and 1e-3hh miniband transitions (from the bottom) based on a two-level TBA calculations ( $L_z = 59 \text{ \AA}$ ,  $x = 0.14$ ). Other energy states not shown are those of light holes and they are not involved in this analysis. Thick lines are heavy-hole exciton dispersion curves. Straight lines are the paths for LO-overtone and TO-combinations. Markings in rhs and lhs of vertical axes indicate positions of the modes. Note that initial states with  $|\mathbf{K}_i| (\neq 0)$  indicate the process has non-zero momentum of  $q_z$ . For phonon modes in SL, the original inversion symmetry is broken by the SL potentials in the z-direction. Thus such an exciton-phonon interaction of with non-zero  $q_z$  becomes possible in the F-process [89]. However, in the parallel direction, the total momentum should be conserved, which is true in our case.

For the cascade model, intermediate excitonic states are real. In such case, there have been controversies about whether they are Raman processes or hot luminescence [142,145,146]. It is enough to mention here that in our

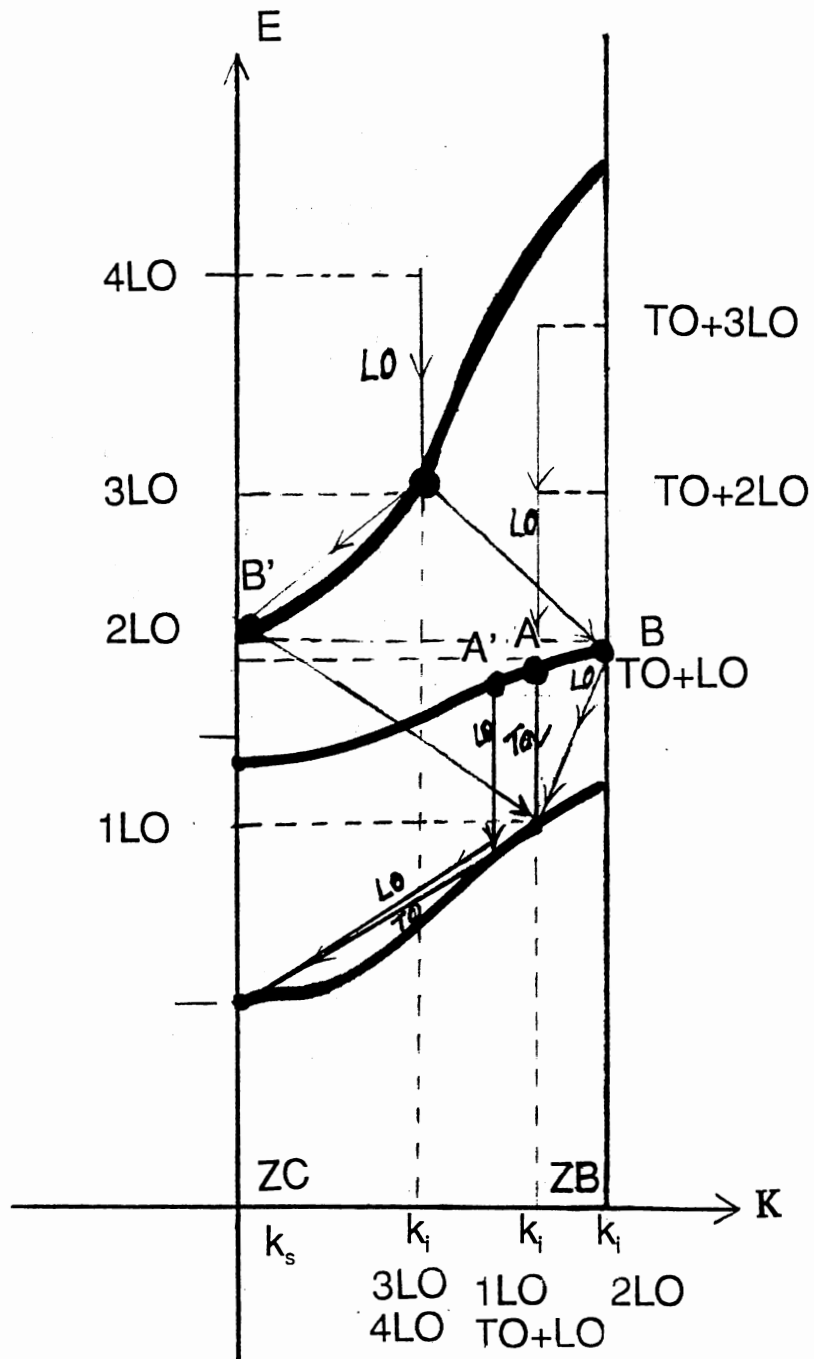


Figure 37. Energy dispersion diagram SL sample. In the vertical axis, the energy positions of the overtones (lhs) and the combinations (rhs) are indicated. A and B refer to intermediate excitonic states for (TO+LO) and 2LO, respectively. A' is on the alternative path where LO is emitted first in (TO+LO) case. B' is on the alternative for 2LO.

cases, the frequency differences are strictly conserved (coherent) and they are strongly resonant to excitation frequencies. According to Yu [142], resonant Raman scattering is possible in this case when

$$\hbar\omega_i = \hbar\omega_0 + E(\mathbf{K}) + \hbar\omega_p(\mathbf{q}) \quad (50)$$

where  $\omega_i$ ,  $\omega_0$  are incident and scattered frequencies and  $E(\mathbf{K})$ ,  $\omega_p(\mathbf{q})$  are dispersion relations of excitons and phonons respectively.

The path map is constructed with Equation (50) and using following rules:

- (i) mLO are via real excitonic states if  $m \leq 3$  and TO+mLO are virtual except  $m=1$ .
- (ii) The exciton dispersion curve can be slightly different due to  $\pm$ one monolayer fluctuation.
- (iii) The phonons involved have momentum  $q \approx 0$ .

It is quite surprising that under these simple rules paths are uniquely determined according to Equation (50). Rule (iii) is from the fact that  $|q| \ll |k|$ , where  $k$  is the photon momentum. One can consider possible alternative path other than indicated in the diagram, for cases of 2LO and TO+LO. Point A can have A' as the alternative if the scattering occurs by a LO followed by a TO, vice versa. However, the alternative is not likely valid here because the observed energy of LO+TO is much higher than what is predicted by point A'. Also, as we mentioned, we could not observe the first order TO-mode RRS. A similar comparison applied to B and B' for 2LO. Note that the separation between 2LO and LO is obviously smaller than other mode's separations and that B' is higher energy than B even we take into account the uncertainty in sample parameters.

Above all, those paths can be realized only because the SL has significant dispersions. Otherwise, those resonances are possible in QWs with very narrow range of sample parameters, which does not seem practical. Even so, it is not likely to satisfy simultaneously for modes higher than second order in square-shape QWs.

Finally, line-width measurements shown in Figure 38 support those interpretations by being grouped as Lines 1,2 and 3. Generally higher order ones are broader than lower orders [146] since the momentum conservation rule is more relaxed. Due to strong resonances at individual stages as here, the situation is somewhat different because the momentum is decided by Equation (50), which means that only limited range of  $q$  is participating at each scattering regardless of the orders. Remarkably, line widths increase very much linearly. Thus lines are broadened only by the addition of same magnitudes of broadening at each scattering. Also, they show a stronger dependence on the kind of minibands than whether they are virtual or real. For example, note from Figure 38 that Lines 1 and 2 are for transitions involving the 1e-2hh states and Line 3 is from the 1e-3hh miniband. For real transitions of LOs, Line 1 approaches  $\approx 1 \text{ cm}^{-1}$ , which is the resolution ( $\delta$ ) of the measurements. Similarly, TO-combinations (Line 2) approach  $\delta$  at the  $m=1$  point, although they are virtual transitions. On the other hand, In line 3, the 3LO and 4LO are nicely on an extension from  $\delta$  and  $m=0$ , although 4LO is via virtual states. These dictate that broadening per one order ( $\delta v$ ) is not different between real and virtual states. In addition, consider that the

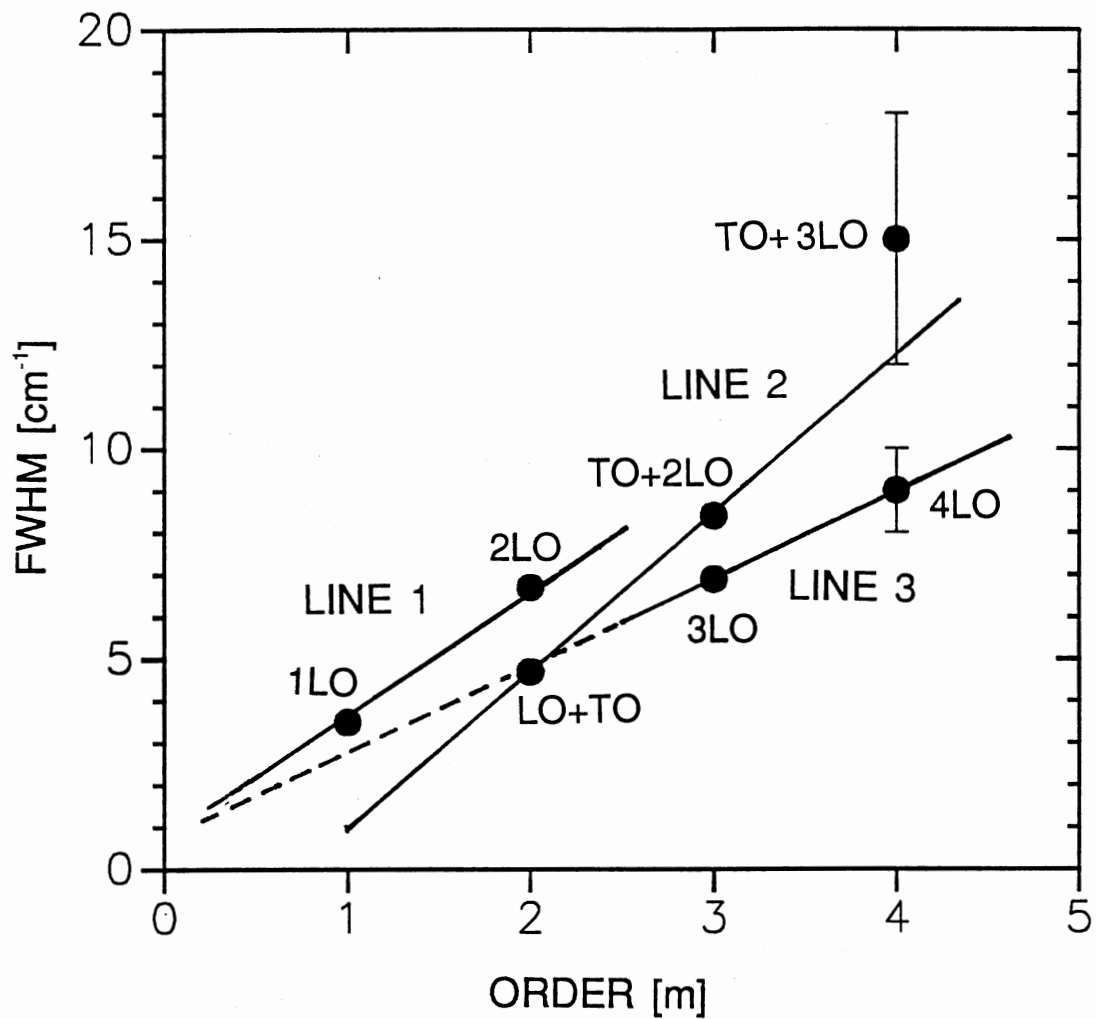


Figure 38. Change of FWHM of phonon modes. Lines 1, 2, and 3 are drawn to show the slopes of the various kinds of the phonon scattering. Line 1: real intermediate states for  $1e-2hh$ , Line 2: virtual intermediate state. Line 3 is for only 3LO and 4LO.

difference in slopes in lines 1 and 2 ( $\delta v = 2.9$  vs.  $3.8 \text{cm}^{-1}$ ) is small and that the slope ( $\delta v = 2.0 \text{cm}^{-1}$ ) in line 3 is much smaller than the formers. Then, we conclude that lifetimes of excitonic states are mainly decided by the kind of minibands. We can calculate the lifetimes of the excitonic states according to Equations (46) and (47). By using the uncertainty relation,

$$t_{LO} = \hbar/\delta v = (1-\rho) t_R \quad (51)$$

The results are shown in Table X for LOs. We use the average slope from Lines 1 and 2 for the  $1e-2hh$  state. The value of  $t_{LO}$  was measured in a bulk GaAs by a fsec laser as  $\sim 4$  psec [147]. This is a good agreement considering the non-rigorousness of the model. Although analytical calculations are needed to be numerically accurate, we can suggest this is one method to measure the lifetimes on such dipole-forbidden optical transitions. The measurement of lifetimes (or the intrinsic broadenings) of such transitions can be very difficult or ambiguous with PL or PLE, not only because signals usually are weak, but also because parameter variations often cause spurious broadenings as we will discuss in Chapter VII.

Another application may exist if we can utilize Equation (50). That is the possibility of verifying  $E(\mathbf{k})$  experimentally. Also, those additional branches of the phonons like TO+LO combinations may be utilized for more information about SLs compared to the QW cases [131]. All of these possibilities are made possible by the significant dispersions in SLs.

In summary we have shown that the significant dispersion in thin barrier superlattices also gives rise to a multiple-resonant Raman scattering. Energy

TABLE X  
EXAMPLES OF CALCULATION OF EXCITONIC LIFE TIMES OF  
SUPERLATTICE MINIBANDS.

	1e-2hh	1e-3hh
LO-Phonon lifetimes ( $t_{LO}$ )	1.6 psec	2.6 psec
Exciton lifetimes ( $t_R$ )	3.3 psec	5.5 psec

positions, separations, strengths, and the width of Raman lines shows that they result from significant dispersions in SL minibands. We have observed combinations of LO-modes up to the 4th order, overtones of TO+mLO up to  $m=3$ . Based on a cascade-resonant scattering model, we found that overtones of LO modes are from the resonance to several real exciton states of minibands, and that LO-TO combinations are via virtual states. Line width changes are sensitive to the kinds of minibands involved.

In this Chapter, we have discussed resonant behaviors of excitons in the ground states of SLs when dispersions are significant. We find that there exist varieties of resonance effects in SLs so that understanding of those properties could result in more precise control of SL-structure designs and also it may lead to many practical applications.



# CHAPTER VII

## EXCITONS IN THIN BARRIER SUPERLATTICES

In this Chapter, we discuss how excitonic spectra change as barrier widths get thinner. The behavior concerned in this Chapter is in the limit that the SL structure approaches a bulk state, since the quantization in the  $z$  direction becomes weak. Coupling between neighboring wells gets more significant. We will show drastic changes in 1HH and 1LH excitonic spectra as barrier widths ( $L_b$ s) decrease in two series of superlattices. Significant dispersions are achieved by adopting a low aluminum concentration in the barrier, and relatively large well widths. The changes of excitonic transitions are drastic in the full-width-half-maximum (FWHM) and intensities, as well as in their energy positions and binding energies. It is found those changes are closely correlated to the magnitude of miniband dispersions.

Experiments are carried out at 15K using CW dye lasers. The dyes used are Styryl 8. PLE techniques are used. The detector is set both at the peak of PL and  $\sim 1.0$  meV ( $\sim 0.5$ nm) below the peak in order to allow both 1HH and 1LH peaks to be detected. Changes in the shape of PLE spectra

with respect to the detector position are tested and found small for this set of samples, which is an indication of their high quality. PMT and a photon counting system are used as well as SPEX triplemate spectrometer. The dye laser scanning is completed as previously addressed. A typical resolution is 0.1meV.

GaAs-Al<sub>x</sub>Ga<sub>1-x</sub>As superlattice samples exhibit a wide range of subband dispersion, which is changed by varying barrier widths. The samples examined are called set I. It has  $L_z = 60 \text{ \AA}$ ,  $x = 0.14$ , and  $L_b = 130, 100, 71, 51, \text{ and } 31 \text{ \AA}$ , and  $x=0.14$ . (Sample SL I.1-I.5, Table VII) 5K PL spectra from thin-film samples showed a narrow width of  $\sim 1 \text{ meV}$ .

Dispersions are calculated by a two-level tight-binding-approximation [14]. The dispersion ranges ( $x=0.14$ ) from 1.1 to 42.5 meV for 1HH and 2.3 to 69.5 meV for 1LH. The magnitude of dispersions is shown in Figure 27. Note that for the sample with  $L_b = 130 \text{ \AA}$ , the width is not thick enough to suppress well-to-well coupling, hence, there is a non-negligible miniband dispersion.

## Excitonic Line Width

There has been many discussions about effects of well-width ( $L_z$ ) fluctuations upon the line width of luminescent spectra of quantum-well (QW) structures [92-102]. We found that there are additional mechanisms which makes the PLE line-width narrow in thin-barrier SLs. These includes coupling

between excitonic states and a random fluctuation in SL potentials effective to the ground states.

The energy of ground states depends on sample parameters. If a SL is composed of wells with slightly different widths (e.g.  $\pm$ one monolayer of Ga or As) along the z-direction, the total PL signal will be the sum of the spectra from individual wells each of which has a different peak position, and multiple peaks can be observed, in a specific case. If the separation is small enough, the resultant excitonic peak will look like a broad peak. This kind of variation in width is called interlayer fluctuations (INTER-F). Each well also can be different in the plane parallel to layers (the x,y direction). A region of a same well size in this plane is called an island. These variations are called intralayer fluctuations (INTRA-F) which cause individual peaks to broaden [99]. Also INTRA-F can result in a smaller broadening due to *averaging effects* [100], if the radii of excitons in the x-y plane are larger than island sizes [102]. See Figure 39 for a schematic description. In superlattices, both well widths and barrier widths can have interlayer fluctuations as well as intralayer ones. Particularly in superlattices, excitons in neighboring wells are coupled through narrow barriers. Thus effects of barrier width ( $L_b$ ) fluctuations become more important than in QWs. However, combined effects of fluctuations in both  $L_b$  and  $L_z$  have been rarely mentioned in a SL with considerable well-to-well coupling [93]. Moreover, in QWs, those mentioned fluctuations result in broadening of excitonic peaks. As barrier widths get thinner, we observed excitonic line-widths in SLs

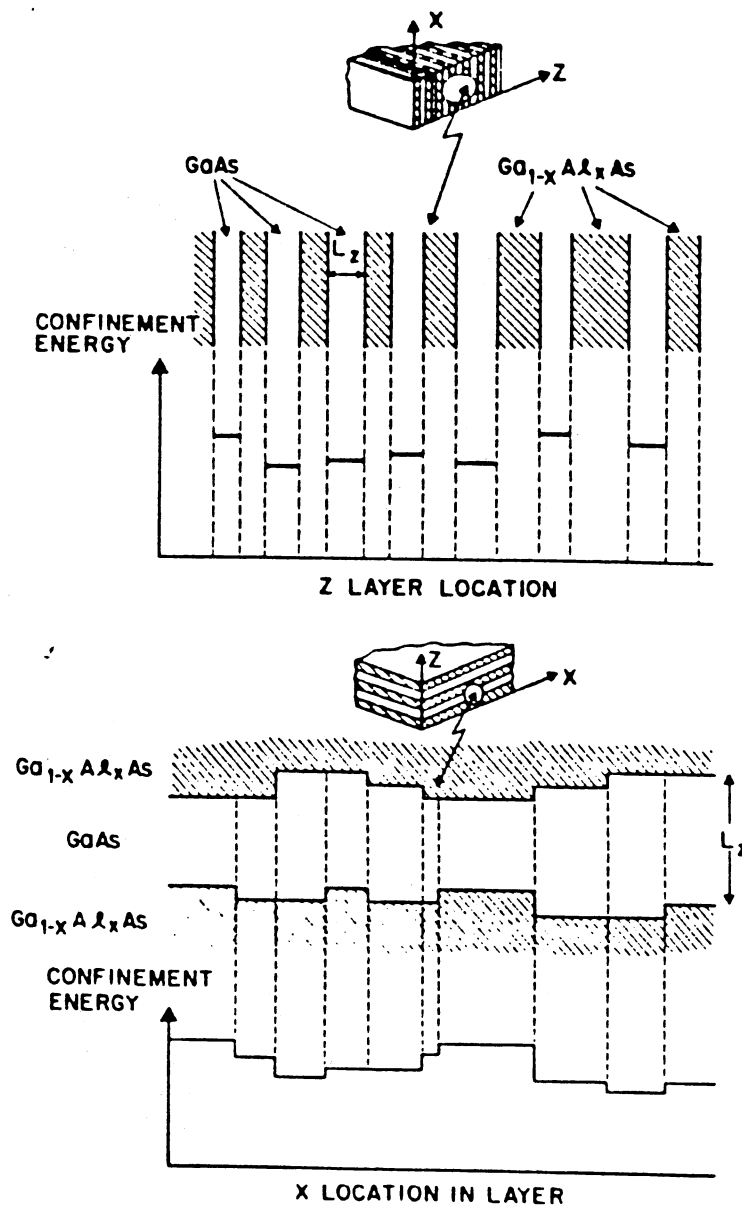


Figure 39. Two types of width fluctuations and resulting energy levels in QWs. Top: Interlayer fluctuations. Well-widths vary layer to layer along the z direction. (INTER-F). Bottom: In one layer, well-widths can vary in plane parallel to the layers (x,y-direction) (INTRA-F).

become narrow. These phenomena of narrow line-widths in short period superlattices seemed observed in Reference 99, but they are not explained. Here, we investigate the line width of excitons in thin-barrier SLs in relation to the miniband dispersion.

Figure 40 shows changes in the line width in PLE spectra. Each experiment is performed under a similar condition. Narrowing of line-widths is quite obvious both in HH and LH excitation spectra. For those samples with thick barriers, line widths are consistent with previously reported results in QWs [92,99,102] as shown in spectra (a). While PL spectra of those samples do not reveal any structures, 1HHs have slightly asymmetric lineshape which is not fully accounted for here. This may be an indication of intralayer fluctuations(FL), giving less-than-one monolayer-fluctuations. Data have been reported with such a slight asymmetric line-shapes [Figure 1, Ref. 102]. In our data, that asymmetry is maintained along with line-width narrowing as  $L_b$  gets thinner. It is not certain whether it is related to a localized state due to disorder [17]. Other than the asymmetry, we do not find any structures corresponding to interlayer fluctuations. Similar results of fewer or lacking peaks in a small-period superlattices PLE are also mentioned in Reference 98.

Measurements of line-widths can be ambiguous when peaks are superimposed on the continuum. For light holes, this is the case. Here, base-lines are drawn assuming there is no interference between peaks and the background continuum. In most cases, it is not so difficult, except for the

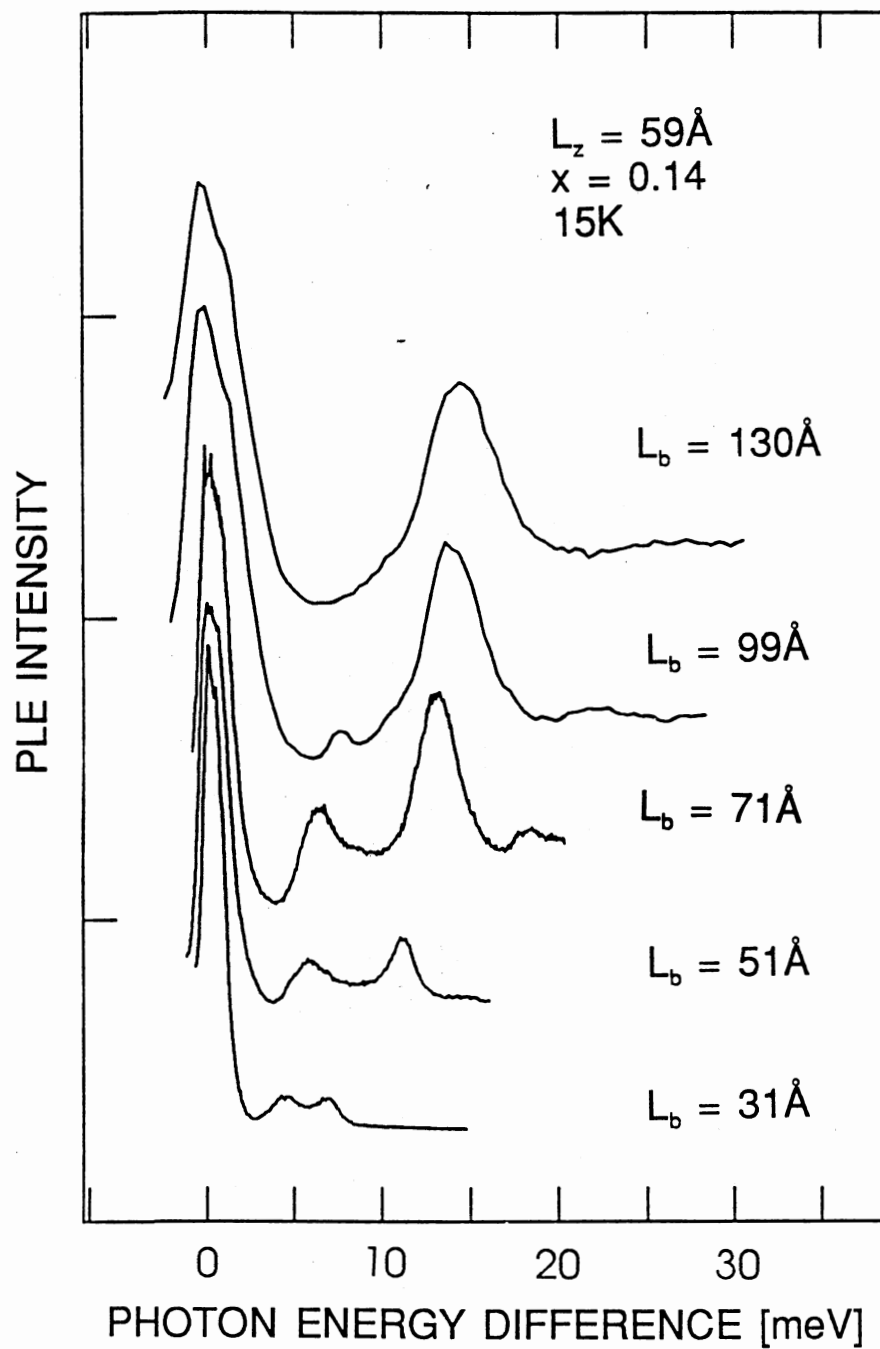


Figure 40. PLE data SET I showing narrowing in the line-width. Dispersions are varied by different  $L_b$  in each sample.

thinnest barrier sample which has the smallest peak. There are more uncertainties in LH peaks than in HH, as a result. Measured FWHMs are as following. For Set I, they decrease from 4.14 meV to 1.28 meV for LH1 and 4.3 meV to 1.28 meV for HH1, as  $L_b$  decreases from 130 to 31 Å.

What has often been considered to be the line-broadening mechanism is the layer fluctuations, as mentioned, in quantum wells and superlattices [102]. For well-width fluctuations in QWs with a certain set of parameters, line widths get narrower as  $L_z$  gets smaller because energy levels are saturated to a bulk value [92]. In our cases of SLs, however, such saturation effects are found to be less effective in narrowing line widths. On the contrary, INTER-F of  $L_b$  should widen peaks as  $L_b$  gets smaller when  $L_b$  is as small as two or three monolayers, although energy levels approach the bulk value. This is because the energy fluctuation due to the monolayer difference (EFMD) of  $L_b$  is increasing as  $L_b$  decreases since obviously the fractional change of a monolayer in  $L_b$  is larger. For  $L_z$ , it is found that EFMD is decreasing as  $L_b$  decreases. But, combined effects of  $L_z$  and  $L_b$  show that the overall EFMD should increase as  $L_b$  decreases. Suppose EFMDs of  $L_b$  and  $L_z$  are independent of each other. The total EFMD,  $\Gamma_f$  by both  $L_b$  and  $L_z$  can be estimated as;

$$\Gamma_f = \sqrt{\gamma_z + \gamma_b}, \quad (52)$$

where EFMD in  $L_z$  is  $\gamma_z$  and that of  $L_b$  is  $\gamma_b$ . In the above expression, we concern only INTER-F effects. The other one, i.e., INTRA-F, will be later briefly discussed.

When the barrier width becomes smaller, another mechanism can be effective. As the dispersion gets larger, Bohr radius of an exciton can be larger than one  $L_b$ . It can not only penetrate barriers, but also it can extend over neighboring wells. Fluctuations in well and barrier widths affect the exciton energy in an average sense rather than a local sense. Then, excitonic line widths can be calculated in much the same way as for excitons in the random potential in an alloy material. The self energy  $\Sigma(E)$  of an exciton (with energy  $E$ ) in a perfectly random potential can be obtained numerically under the assumption of *Coherent Potential Approximation* (CPA) [107] as

$$\Sigma(E) = \underline{\Sigma} + \langle T \rangle (1 + G \langle T \rangle)^{-1} \quad (53)$$

where

$$T = (U - \underline{\Sigma}) [1 - G (U - \underline{\Sigma})]^{-1}, \quad (54)$$

$G$  is the excitonic Green's function of the perturbed system,  $U$  is the random potential representing well- and barrier-width variations, and  $\underline{\Sigma}$  is a complex reference potential which is adjusted by iteration until the configuration average of the **T-matrix** [105], i.e.  $\langle T \rangle$ , vanishes. This method is called an *iteration-average-t-matrix-approximation* (IATA) [106]. Here, IATA is used under CPA. The random potential is assumed to be either a Gaussian or a Lorentzian distribution around a value of zero, with a width of  $U_0$ . Then,

$$U_0 = \Gamma_r, \quad (55)$$

under the assumption that the fluctuation is a monolayer on the average. In each stage of iterations,  $G(\mathbf{K})$  is calculated by assuming the excitonic dispersion relation for heavy hole  $n=1$ , as



$$E_x(K_{\parallel} = 0, K_z) = E_0 + \Delta E [1 - \cos(K_z d)]/2 \quad (56)$$

where  $K_{\parallel}$ ,  $K_z$  are the momentum of the exciton,  $E_0$ ,  $\Delta E$  are the minimum energy and the width of the miniband, respectively,  $d$  is the period of the SL, and  $\hbar$  is Plank's constant. (See Reference 111.) In the x-y directions,  $E(K_{\parallel})$  is a parabolic function as usual. The resultant excitonic width  $\Gamma_1$  is the imaginary part of the  $\Sigma(E_0)$ , viz,

$$\Gamma_1 = \text{Im}\{ \Sigma(E_0) \}, \quad (57)$$

which is similar to the frequency-width of a damped oscillation. At the same time, under CPA, the density of state function (DOS) of this system,  $D(E)$ , is approximately proportional to  $\Gamma_1^{\S}$ . Since in a one-band model DOS is inversely proportional to the width of the miniband,  $\Gamma_1$  will be approximately proportional to  $(\Delta E)^{-1}$ . Thus it will be convenient to compare

---

<sup>\S</sup> According to the Reference 108, the density of states function (DOS)  $D(E)$  of multiple scattering model is given as

$$D(E) = - (1/\pi V_K) \int d^3K \left[ \frac{\Gamma_1}{\{E - E(K) - \text{Re}(\Sigma)\}^2 + \Gamma_1^2} \right]$$

where  $\text{Re}(\Sigma)$  is the real part of  $\Sigma$ ,  $E(K)$  is the exciton dispersion relation given in the text, and the summation is substituted by an integral.  $V_K$  is a normalization volume in  $\mathbf{K}$ -space. The relation between  $\Gamma_1$ , and the magnitude of the dispersion  $\Delta E$ , is not obvious due to the complex expression in the denominator of the integrand. In 1D case where  $E_{1D}(K) = \delta(K)$ , DOS is inversely proportional to  $\Gamma_1$ , since it is a Lorentzian function. In general, precise calculation is required. In our case, we can check the validity using the experimental values.  $D(E)$  is evaluated numerically, with given various  $\Delta E$ , and  $\Gamma_1$ , then we truly find approximate proportionality between  $\Gamma_1$  and  $1/\Delta E$ , which is similar to Equation (59). The meaning is that at the lower edge of the miniband, DOS is given by summation of all BZ contributions, each of which has broadening of  $\Gamma_1$ . Therefore, the total contributions can be proportional to the width, depending on the specific dispersion relation. This is an indirect proof of the model we are examining.

results in  $(\Delta E)^{-1}$ . In above equations, an exciton is treated as one particle with a reduced mass and its combined wavefunction is taken as a multiplication of electron and hole wavefunctions. According to Chang [109, 110], results of the calculation are represented as

$$\Gamma_1 = U_0 g(\Delta E/U_0), \quad (58)$$

with

$$g(x) = (1 + x/0.7)^{-0.4}. \quad (59)$$

Other possible mechanism is from the random fluctuation in well-, and barrier-widths in x,y directions (INTRA-F) which is denoted by  $\Gamma_r$ . However, those effects will be less sensitive to barrier widths [109]. Note in above CPA calculations, only the z-directions is considered. Most of experimentally observed peaks showed narrower than EFMD in the range of our sample parameters. Therefore, INTRA-F is neglected in this analysis since it is considered constant and small.

The condition of the random potential becomes unsatisfactory when excitons are sufficiently localized in the well due to thick barriers, in QW cases. Figure 41 shows the comparison of the first two mechanisms, with experimental data in x-scale of  $1/\Delta E$ . As we notice, experimental data are in clear agreement with CPA model ( $\Gamma_1$ ) for the thinner barrier case (SL-case), while they approach values predicted by EFMD ( $\Gamma_r$ ) for the thicker barrier case (QW-case). Conversely, they deviate significantly from curves for  $\Gamma_r + \Gamma_0$  in SL cases and they depart from  $\Gamma_1$  in QW cases. Note in the figure,  $\Gamma_r + \Gamma_0$ , or  $\Gamma_1 + \Gamma_0$  are used taking  $\Gamma_0$  as 0.7 meV for the best fit.  $\Gamma_1$  is calculated

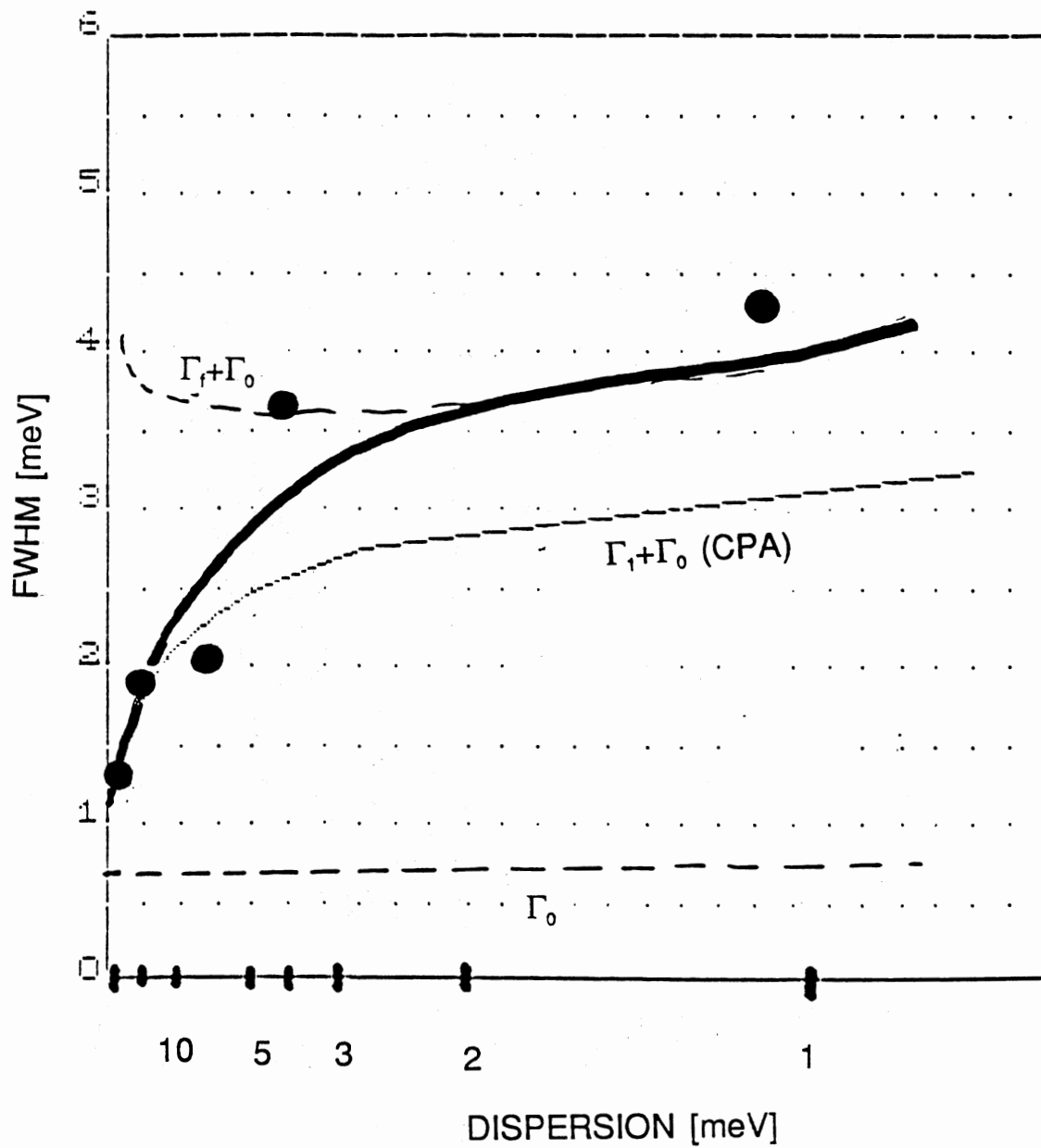


Figure 41. Two mechanisms of line-width narrowing. ( $\Gamma_1 + \Gamma_0$ ) indicates the trend of the line width according to the CPA model; ( $\Gamma_t + \Gamma_0$ ) is from INTER-F. Each mechanism dominates at the different range of the dispersions. Black circles represent experimental data.

without adjustment from Equations (59) and (57), yielding  $\Gamma_0$ . In doing so,  $\Gamma_f$  is fixed as 2.9meV, since it is approximately constant as we see in Figure 41. A small inconsistency at quantum well cases can be attributed to INTRA-F, which is ignored here.

Therefore, the overall width  $\Gamma$  can be represented as

$$\Gamma = \begin{cases} \Gamma_0 + \Gamma_1 & \text{for SLs,} \\ \Gamma_0 + \Gamma_f & \text{for QWs,} \end{cases} \quad (60)$$

where the intrinsic width of excitons is included in  $\Gamma_0$ , in order to cover other broadening mechanisms that are more or less insignificant. For example, alloy scattering [96,97] has been estimated in  $\text{Al}_x\text{Ga}_{1-x}\text{As}$  bulk cases using the slope of the bandgap of the material, to be  $\sim 2\text{meV}$  if  $x$  is 0.14. The corresponding value for thin barrier superlattices is much reduced due to the smaller ratio of the excitonic volume over the  $\text{Al}_x\text{Ga}_{1-x}\text{As}$  barrier. Here, the estimation should use the slope of the energy position of 1HH with respect to the changes in  $x$ . For example, we estimated by using TBA and found that the slope is  $\sim 0.1$  times that of the potential barrier, slightly depending on  $L_b$ . This will give us  $\sim 0.2\text{meV}$ . Thus we believe about one third of  $\Gamma_0$  is from the alloy scattering in the barrier.

Therefore, we found that in SLs, the line width narrows as the dispersion of the miniband widens because excitons see fluctuations in the widths in an average manner. In another way, we can understand that excitons resonate only in a narrow range of energy states coming from layers with a specific set of  $L_b$  and  $L_z$  among all the SL layers. A large EFMD in

thin-barrier SLs also will hamper simultaneous excitation to excitons by different sets of parameters. A strong coupling between neighboring wells contributes to this effect.

In fact, due to this self-narrowing mechanism, we do not observe clear structures of monolayer fluctuations in spectra of samples. Particularly, in  $L_b = 30 \text{ \AA}$ , monolayer fluctuations are not resolved, although individual lines are the sharpest. This is in very strong contrast to QW cases, where individual PL peaks from wells with even effective-1/2-monolayer differences are resolved rather clearly [101]. Line-width narrowing in SLs is believed, in part, to have contributed in the observation of 2s-combination peaks which appear only within a certain range of dispersions of superlattices as we discussed in the previous chapter.

## Intensities and Energies

The peak intensity of excitonic transitions can be important parameters to the sensitivity of a device utilizing excitonic phenomena. However, experimental work has been rarely reported despite of its importance. This may be due to the fact that high quality superlattice samples have not been available until recently. We have observed a systematic variation of excitonic intensities, excitonic binding energy, and energy positions in PLE spectra. Particularly, the variation of the intensity is found in agreement with a similar model to the line-width case which was discussed in the previous section. Also, the experimental measurement of exciton binding energy as a function

of  $L_b$  has never been reported previous to this work. First, the excitonic binding energy is obtained by measuring energy positions of 2s-combination peaks (See Chapter VI, the first section). We have found that the excitonic binding energy decreases systematically as we decrease the barrier width ( $L_b$ ).

In fact, as  $L_b$  decreases, the structure approaches a 3D bulk. The trend can be understood by considering two extreme cases. In ideal 2D quantum wells, excitons are totally confined in wells. Electrons and holes have a greater chances of staying together since they are spatially localized in wells. It is more difficult to separate them (to annihilate excitons) due to Coulomb force between electrons and holes. In another words, they have larger binding energies. On the other hand, in 3D bulk crystals, they are relatively free within a Brillouin zone, thus the binding energy is consequently smaller. Excitons in bulk materials have been observed only at low temperatures [26,112]. Thus the binding energy of SLs will vary between those two extremes depending on parameters,  $L_b$ ,  $L_z$ , and  $x$ . In cases of isolated wells with thick barriers, the binding energy  $E_{xb}$  is reported to be 8 ~ 12meV for heavy hole excitons, and 10 ~ 15 meV for light hole ones [See Table XI]. As  $L_b$  gets smaller, SL samples become closer to bulk GaAs.  $E_{xb}$  should approach that of GaAs, i.e., 4.2meV [10].

It has been known that binding energies of excitons vary as parameters in SLs and MQWs [115,116]. Previous experimental data so far reported showed large variations, largely due to the ambiguity in the position of the exciton continuum. To obtain the energy position, one can use a varying

TABLE XI  
EXCITON BINDING ENERGY

$L_z$ (Å)	$L_b$ (Å)	x	Heavy Holes		Light Holes	
			$ E_{1s}-E_{2s} $ (meV)	$E_{xb}$ (meV)	$ E_{1s}-E_{2s} $ (meV)	$E_{xb}$ (meV)
This work:						
59	130	0.14	11.1	14	12.7	16
59	99	0.14	8.0	10	8.5	11
59	71	0.14	6.4	8	5.3	7
59	51	0.14	5.9	7	4.3	5
59	32	0.14	4.2	5	3.4	4
Chomette et al. (1987) [113]:						
106	98	0.3	-	8.1	-	-
64	63	0.3	-	9	-	-
53.7	56.5	0.3	-	8	-	-
30	30	0.3	-	4.3	-	-
Miller et al. (1981) [27]:						
75	-	0.37	~8.2(~8.2)	(~13)	~8.5(~8.5)	(~14.5)
Moore et al. (1986) [114]:						
55	-	0.35	~12.0	-	-	-
75	-	0.35	~10.0	-	-	-
Dawson et al. (1986) [115]:						
75	-	0.4	9.5(9.5)	(11.2)	10.3	-
Andreani et al. (1988) [116]:						
75	-	0.4	9.5(8.5)	(10.18)	10.3(10.6)	(13.25)
92	-	0.35	8.5(7.9)	(9.44)	10.2(9.4)	(11.96)
112	-	0.35	-	-	9.1(8.6)	(11.03)
Molenkamp et al. (1988) [117]:						
76	-	0.33	8.9±0.5	-	-	-

NOTE: Shown are the exciton binding energies obtained from experiments in this thesis and those previously reported.

- indicates being unavailable.

~ means that data are read from graphs.

( ) are values obtained by theoretical calculations.

magnetic field [99], or vary the temperature [113], and then extrapolate results. On the other hand, the most direct unperturbed estimation of  $E_{xb}$  is possible with PLE, by 2s peak positions [27,114,115]. In our case, they are located near H, L peaks. Peaks H and L have asymmetric line shapes with 2s states located on their rising edge. The separation between the primary exciton peaks and onset of the 2s-combination peak can be used in estimating the binding energy from 1s-2s energy separations, either by variational calculations [27], or other methods [27,114,115]. Calculations for SLs with finite  $L_b$  are not readily available and a detailed theoretical calculation for this case has yet to be done. Therefore, for a first order approximation that the excitons are more-or-less bulk-like, we use Equation (9). Then,  $E_{xb} = 1.25 |E_{1s} - E_{2s}|$ . Results including  $|E_{1s} - E_{2s}|$  are listed in Table XI. Obtained values are within a reasonable range. For comparison purposes, some of values reported are listed. However, we have to note that the uncertainty is larger if  $L_b$  is too small since 2s-combination peaks become weaker. As we see,  $|E_{1s} - E_{2s}|$  data for 1LH of the  $L_b = 32 \text{ \AA}$  case reflects this uncertainty.

We found energy positions of H and L peaks approach the GaAs bandgap slowly as  $L_b$  decreases, and then rapidly at a few monolayers of barrier. They shift to lower in energy. Positions of H,L peaks also more directly indicates the location of the start of non-excitonic bandedges. Thus we can compare those positions with values from a non-excitonic calculation more precisely. Figure 42 shows a comparison with calculations based on TBA [14]. The good agreement between the experiment and the theory is an



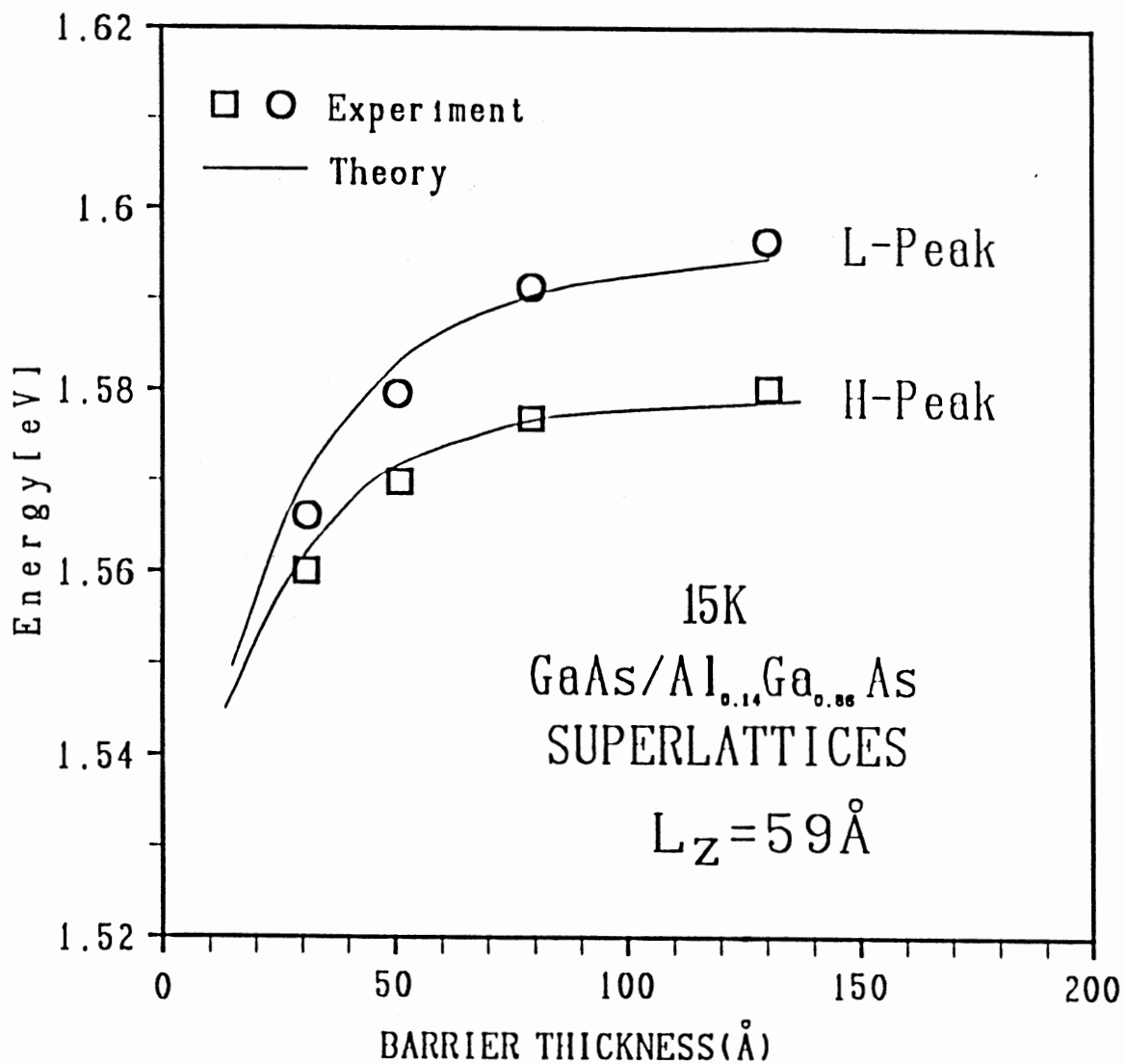


Figure 42. Comparison between positions of L and H peaks with calculated ones from TBA. The calculation and the experiment agree well while they are approaching to the GaAs bandgap rapidly at small barrier widths. Open squares and circles represent measured data.

indication of the accuracy of our sample parameters. What is most surprising to us is that the rate it approaches the bulk bandgap (1.519eV for GaAs) as  $L_b$  goes to zero. The asymptotic approach has not obvious until down to 11 monolayers of barriers, which would have been considered close enough to a bulk.

The absolute 1LH, 1HH excitonic PLE intensities are also decreasing as  $L_b$  decreases. The intensity, however, is more complex and difficult to understand than the binding energy. It is a combination of the absorption coefficient and the relaxation mechanism (collection efficiency of electron and hole pairs). If we assume those changes caused by relaxation mechanisms are constant, the situation can be very much simplified. As an approximation, we can consider it is constant, partly because parameters,  $L_z$  and  $x$ , are fixed. Then, the absorption coefficient at the peak of 1HH exciton can be compared to the density of states (DOS) function at the energy.

In the previous section, by measuring FWHMs, we have found that excitons in thin barrier SLs shows *an average effect* with respect to fluctuations of SL parameters. From this, we can expect a similar behavior in the PLE intensity, as well. DOS is calculated at the minimum energy point of a miniband, for each different  $L_b$  by using the relation given in the footnote of the previous section. Indeed, we find an overall agreement as shown in Figure 43. The solid line is for 1HH, and the dotted line is for 1LH. The calculation uses Equation (58) for  $\Gamma_s$ , and the calculated dispersion  $\Delta E$  shown in Figure 27. The  $Re(\Sigma)$  is assumed to be zero. The vertical scale

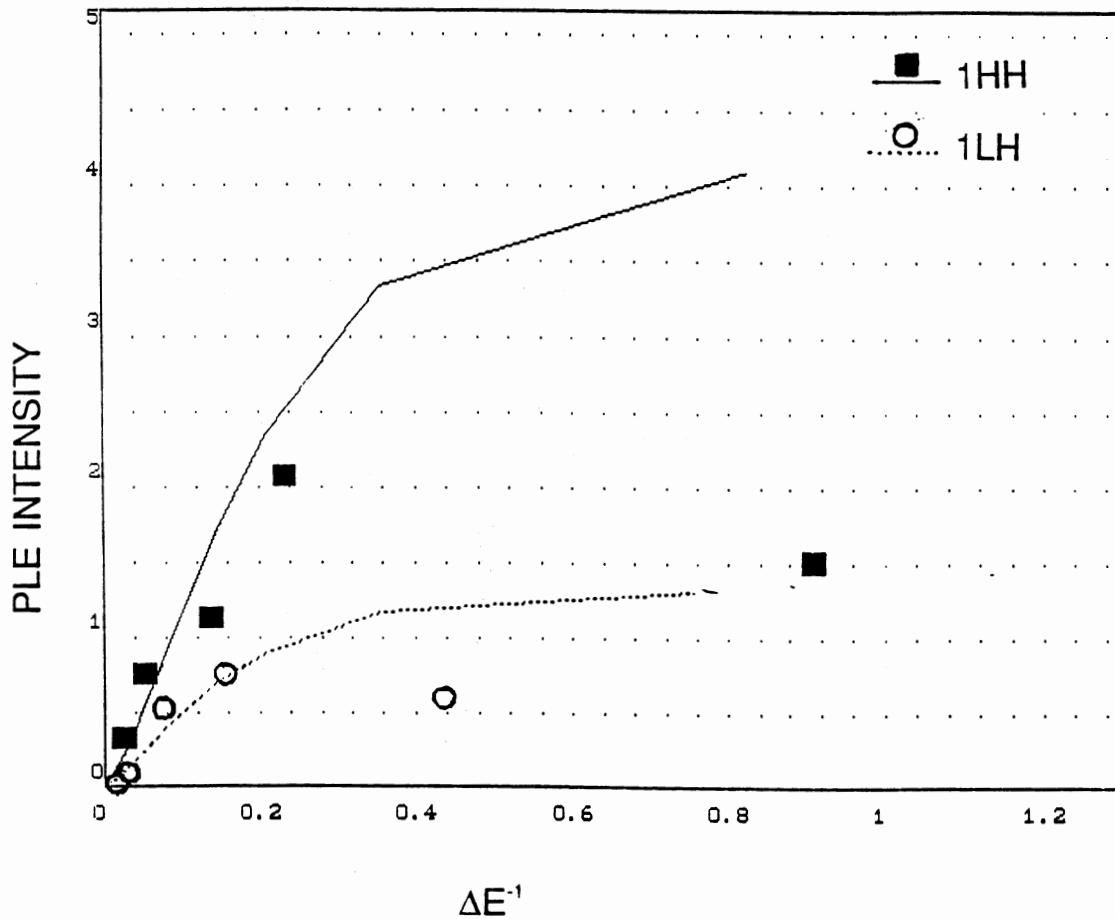


Figure 43. Comparison of PLE intensities and CPA calculations. The dotted curve is for 1LH, and the solid curve is for 1HH. Larger discrepancies in data at small dispersions (QW-cases) may be caused by mechanisms other than the CPA model.

of the curve is adjusted arbitrarily for an easy comparison but the relative ratios between those of 1HH and 1LH are not adjusted. Particularly the 1LH intensity is multiplied by 1/3 because of the different transition path. Data points are obtained by integrating the area below peaks after a normalization by different incident intensities. The horizontal scale is as same as before,  $\Delta E^{-1}$ . We estimate the error of the measurement to be about 30% of each intensity except for the data of the largest  $\Delta E^{-1}$ . Nonetheless, trends are unambiguously displayed. A larger discrepancy for data at small dispersions (QW-cases) indicates that the exact mechanism may be different, as we noticed previously. By those results, we verify the averaging effect again.

Finally, one of the important implications of this chapter is motivating future researches, namely, more detailed investigations of a SL structure at this regime. We have observed a few characteristics absent in 3D-bulk cases, or in QW cases. Those includes line-width narrowing, rapid variations of energy positions, and variations of the exciton binding energy with  $L_b$ , as well as excitonic intensities.

## CHAPTER VIII

### SUMMARY AND CONCLUSION

The excitonic enhancement at Brillouin zone center (ZC) and the zone boundary (ZB) of minibands of GaAs-Al<sub>x</sub>Ga<sub>1-x</sub>As superlattices (SLs) are studied by PLE and resonant Raman scattering techniques. In general, enhancements are found to be a function of the barrier width ( $L_b$ ).

First, with PLE on one series of samples ( $L_z=150\text{\AA}$ ,  $x=0.22$ ), clear doublets are observed. Each peak of the doublet is attributed to ZC and the ZB optical transitions of the first unconfined states. In resonant Raman spectra obtained at the same transition energy range, those enhancements more clearly appear as four distinct peaks, i.e., incoming-, outgoing- resonances at both the  $M_0$ -type (at ZB) and  $M_1$ - type (at ZC) critical points. The strength of those peaks are represented by an effective lifetime of each state. As results, it is found that coupling from continuum states above or below minibands plays a role in varying the strength. In most of samples, barrier phonons are more involved than well phonons except for the sample with the thinnest barrier. For thin barrier SLs, coupling to lower continuum becomes dominant via GaAs phonons due to the larger relative volume of well regions.

Using another series of SL samples with well width ( $L_z$ ) of  $59\text{\AA}$  and  $x=0.14$ , ground states are investigated. The excitonic resonance produces

extra peaks which are attributed to the combination of the 2s-excited state of excitons and the enhancement at the bandedge via Coulomb interaction (excitonic). The strength of those structures are dependent on the magnitude of the dispersion of the ground state, which is a function of the barrier width. Similar structures are also verified in the second miniband ( $n=2$ ) of a SL sample.

For particular SLs with thinner barriers among the samples, resonant multi-phonon Raman spectra (MRS) are observed. Those resonances are made possible by the significant dispersion of minibands due to the thin barrier. MRSs show, for the first time in GaAs-Al<sub>x</sub>Ga<sub>1-x</sub>As SLs, distinct peaks of phonon combinations up to TO+3LO, and overtones up to 4LO. By applying a cascade resonant scattering model where a few or all of the steps in MRS are resonant to real states of SL minibands, we found strengths, as well as Raman line widths, are consistent with a schematic scattering path map in a band dispersion diagram of excitons.

Finally, ground state excitonic peaks in SLs show a few characteristic behaviors in PLE spectra when the barrier width becomes smaller, thus the SL is becoming bulk-like. In this regime, line widths are found to become narrow. Experimental data are compared to a theoretical model based on Coherent-Potential Approximation. Narrowing results because excitons are influenced only in an averaged manner by effects of spatial variations in parameter values, specifically,  $L_z$  and  $L_b$ . Still, at thick barrier cases (MQW), we can verify direct broadening mechanism due to parameter fluctuations.

The absolute intensity of ground states of heavy holes and light holes is also shown to follow a similar trend of line widths within a reasonable experimental tolerance. Utilizing 2s-combination peak positions we estimated changes in the exciton binding energy as a function of the barrier width. They decrease monotonously from values of QW cases towards to those of a GaAs bulk crystal. In addition, from experimental data, it is pointed out that absolute energy positions approach to the bulk bandgap rather slowly, then rapidly after the barrier width is extremely small down to a few monolayers of  $\text{Al}_x\text{Ga}_{1-x}\text{As}$ .

In conclusion, we have systematically studied excitonic resonances and their behaviors in the transition from quasi-2D quantum well cases to a bulk-like SL structure by varying the width of barriers. Those findings in this thesis suggest that the excitonic resonance can appear in both critical points of a miniband. A new kind of resonances can also appear. The strength varies depending the magnitude of dispersions which result from coupling between potential wells in SLs. These effects on behaviors of excitons in superlattices in the transition from quantum wells to a bulk structure can be a strong basis for a future research of new optical properties.

## REFERENCES

1. F. Capasso, *J. Vac. Sci. Technol. B* **1** (2), 457; *Surf. Sci.*, **132**, 527 (1983).
2. B. A. Tavger and V. Ya. Demikhovskii, *Usp. Fiz. Nauk* **96**, 61-86 (Sept., 1968) [*Sov. Phys.-USP.*, **11** (5) 644 (1969)].
3. K. Ploog in *Crystals / Growth, Properties, and Applications* edited by L. F. Boschke (Springer, Heidelberg, 1979).
4. W. Richter, *Physics of Metal Organic Chemical Vapor Deposition*, in *Festkörperprobleme*, Vol. 26, p335, (Friedr. Vieweg, Brunschweig, 1986)
5. P. M. Frijlink, *An Introduction to OMVPE of III-V Compounds*, in *Heterojunctions and Semiconductor Superlattices*, edited by G. Allan, G. Bastard, N. Boccarda, M. Lannoo, and M. Voos, p226, (Springer, Berlin, 1986).
6. C. Kittel, *Introduction to Solid State Physics*, Sixth Edition, Chapter 1 (Wiley, New York, 1986).
7. J. S. Blakemore, *J. of Appl. Phys.* **53**, R123-R181 (1982).
8. E. O. Kane, in *Semiconductors and Semimetals*, vol. 1, edited by R. K. Willardson and A. C. Beer, Chapter 3, (Academic Press, New York, 1966).
9. S. Adachi, *GaAs, AlAs, and Al<sub>x</sub>Ga<sub>1-x</sub>As: Material parameters for use in research and device applications*, *J. of Appl. Phys.* **58** R1-R29 (1985).
10. D. S. Chemla, *Helv. Phys. Acta* **56**, 607-637 (1983).
11. L. Esaki, *A Bird's-Eye View on the Evolution of Semiconductor Superlattices and Quantum Wells*, *IEEE J. Quantum Electron.* **QE-22** (9) 1611 (1986).
12. H. C. Casey, Jr. and M. B. Panish, *Heterostructure lasers*, Part A. (Academic Press, New York, 1978)
13. C. Weisbuch, in *Semiconductors and Semimetals*, vol. 24, edited by R. Dingle, p. 1. (Academic Press, San Diego, 1987).
14. J. N. Schulman, in *Proceedings of the Symposium on Layered Structures and Epitaxy, Materials Research Society Symposia Proceedings*, Vol. 56 (1986), p 279.
15. U. Merkt, in *Festkörperprobleme*, Vol. 27, p109, (Friedr. Vieweg, Brunschweig, 1987)
16. H. Heinrich and J. M. Langer, *Bandoffsets in Heterostructures*, in *Festkörperprobleme*, Vol. 26, p251, (Friedr. Vieweg, Brunschweig, 1986)



17. L. Pavesi, E. Tuncel, B. Zimmermann, and F. K. Reinhart, *Phys. Rev. B* **39** (11) 7788 (1989-I).
18. M. W. Peterson, J. A. Turner, C. A. Parson, A. J. Nozik, D. J. Arent, C. Van Hoof, G. Borghs, R. Houdré, and H. Morkoç, *Appl. Phys. Lett.* **53** (26) 2666 (1988).
19. J. M. Luttinger, *Phys. Rev.* **102** (4) 1030 (1956).
20. R. Dingle, in *Festkörperprobleme*, Vol. 15, p21, (Friedr. Vieweg, Brunschweig, 1975).
21. J. O. Dimmock, in *Semiconductors and Semimetals*, vol. 3, edited by R. K. Willardson and A. C. Beer, Chapter 5, (Academic Press, New York, 1967).
22. R. J. Elliot, *Phys. Rev.* **108** (6), 1384 (1957).
23. *Electronic States and Optical Transitions in Solids*, by F. Bassani, and G. Pastori Parravicini, Chapter 5, (Pergamon Press, New York, 1975).
24. R. Dingle, W. Wiegmann, and C. H. Henry, *Phys. Rev. Lett.* **33**, 827 (1974).
25. F. L. Lederman and J. D. Dow, *Phys. Rev. B* **13**, 1633 (1976).
26. M. D. Sturge, *Phys. Rev.* **127**, 768-773 (1962).
27. R. C. Miller, D. A. Kleinman, W. T. Tsang, and A. C. Gossard, *Phys. Rev. B* **24** (3), 1134 (1981).
28. C. Weisbuch, R. C. Miller, R. Dingle, A. C. Gossard, and W. Wiegmann, *Solid State Commun.* **37** pp. 219-222, (1981).
29. J. C. Phillips, in *Solid State Physics*, edited by F. Seitz and D. Turnbull, vol. 18 (Academic Press, New York, 1966) and references therein.
30. M. Cardona, *Modulation Spectroscopy, Solid State Physics* supplement 11 (Academic Press, New York, 1969)
31. M. Cardona, *ibid*, Chapter II.
32. F. H. Pollak and O. J. Glemboki, *Proc. Soc. Photo-Opt. Instrum. Eng.*, **946**, 2 (1988).
33. H. Jung, A. Fischer, and K. Ploog, *Appl. Phys. A* **33**, 9-17 (1984).
34. H. Jung, A. Fischer, and K. Ploog, *Appl. Phys. A* **33**, 97-105 (1984).
35. M. Naganuma, J. J. Song, Y. B. Kim, W. T. Masselink, H. Morkoc, and T. Vreeland, Jr., *J. Appl. Phys.* **60** (5) 1740 (1986).
36. G. Bastard, C. Delalande, M. H. Meynadier, P. M. Frijlink, and M. Voos, *Phys. Rev. B* **29** (12) 7042 (1984).
37. J.-K. Maan, *Magnetic Quantization in Superlattices*, in *Festkörperprobleme*, Vol. 27, p137, (Friedr. Vieweg, Brunschweig, 1987)

38. T. Vreeland, Jr. and M. Paine, *J. Vac. Sci. Technol. A* **4** (6), 3153 (1986).
39. M. Cardona ed., *Light Scattering in Solids I*, 2nd edition, Chapters 1 and 2 (Springer, Berlin, 1983)
40. A. Pinczuk and E. Burstein, in *Light Scattering in Solids I*, edited by M. Cardona ed. (Springer, Berlin, 1983)
41. R. Loudon, *Proc. R. Soc. A* **275**, 218 (1963).
42. M. Cardona, *Resonance Phenomena in Light Scattering in Solids II*, edited by M. Cardona and G. Güntherodt, (Springer, Berlin, 1982)
43. H. Iwamura, T. Saku, H. Kobayashi, and Y. Horikoshi, *J. Appl. Phys.* **54**, (5), 1983.
44. J. E. Zucker, Ph. D. Thesis, Columbia University, 1985.
45. H. Bilz and W. Kress, *Phonon Dispersion Relations in Insulators*, (Springer, Heidelberg, 1979), p. 105. Phonon dispersion of GaAs.
46. J. Menendez and M. Cardona, *Phys. Rev. B* **31**(6), 3696 (1985).
47. C. Hilsum and A. C. Rose-Innes, *Semiconducting III-V Compounds*, Vol. 1, in *International Series of Monographs on Semiconductors*, edited by H. K. Henisch (Pergamon Press, New York, 1961).
48. Z. P. Wang, H. X. Han, G. H. Li, and D. S. Jiang, *Phys. Rev. B* **38** (12) 8483 (1988-II).
49. G. Abstreiter, E. Bauser, A. Fisher, and K. Ploog, *Appl. Phys.* **16**, 345-352 (1978)
50. V. Swaminathan, A. Jayaraman, J. L. Zilko, and R. A. Stall, *Material Letters* **3**, 325-330 (1985).
51. Z. V. Popovic, M. Cardona, L. Tapfer, and K. Ploog, *Appl. Phys. Lett.* **54** (9) 846 (1989).
52. R. Merlin, C. Colvard, M. V. Klein, H. Morkoc, A. Y. Cho, and A. C. Gossard, *Appl. Phys. Lett.* **39** (1) 43 (1980).
53. E. Richter and D. Strauch, *Solid State Commun.* **64** (6) pp. 867-870 (1987).
54. F. A. Jenkins and H. E. White, *Fundamentals of Optics*, Fourth Edition, Chapter 4. (McGraw-Hill, New York, 1976)
55. J. C. Tsang, in *Light Scattering in Solids V*, edited by M. Cardona and G. Güntherodt, Chapter 6. (Springer, Berlin, 1989)
56. Spectra-Physics, *Continuous-wave dye lasers properties and performance reports*, Laser Product Division, 1250 W. Middlefield Road, Mountain View, Ca 94039-7013 (1985).

57. APL\*PLUS Reference Manual, STSC, Inc. Technical Documentation, 2115 E. Jefferson Street, Rockville, Maryland, U. S. A. (1987).
58. L. Gilman, A. J. Rose, *APL: An interactive approach*, Second edition, (Wiley, New York, 1976).
59. K. Ploog and K. Graf, *Molecular Beam Epitaxy of III-V semiconductors*, A comprehensive Bibliography 1958-1983 (Springer, New York, 1984).
60. For example, see D. Bimberg, D. Mars, J. N. Miller, R. Bauer, and D. Oertel, *J. Vac. Soc. Technol. B* **4**, 1014 (1986); F.-Y. Juang, et al., *Appl. Phys. Lett.* **48**, 290 (1986); H. Sakaki, et al., *J. Appl. Phys.* **24**, L417 (1985); F. Voillet, et al., *Appl. Phys. Lett.* **48**, 1009 (1986); C. W. Tu, R. C. Miller, B. A. Wilson, P. M. Petroff, T. D. Harris, R. F. Kopf, S. K. Sputz, and M. G. Lamont, *J. of Crystal Growth* **81**, 159-163 (1987).
61. See for example, *Synthetic Modulated Structures*, edited by L. L. Chang and B. C. Giessen (Academic Press, Orlando, 1985).
62. A. C. Gossard, in *Thin Films : Preparation and Properties*, edited by K. N. Tu and R. Rosenberg (Academic Press, New York, 1983) p 13 and references therein.
63. J. N. Schulman and Y. C. Chang, *Phys. Rev. B* **31**, 2056 (1985).
64. K. B. Wong, M. Jaros, M. A. Gell, and D. Ninno, *J. Phys. C* **19**, 53 (1986).
65. J. E. Zucker, A. Pinczuk, D. S. Chemla, A. C. Gossard, and W. Wiegmann, *Phys. Rev. B* **29** (12) 7065 (1984).
66. J. J. Song, Y. S. Yoon, A. Fedotowsky, Y. B. Kim, J. N. Schulman, C. W. Tu, D. Huang, and H. Morkoc, *Phys. Rev. B* **34** (12) 8958 (1986).
67. *Electronic States and Optical Transitions in Solids*, by F. Bassani, and G. Pastori Parravicini (Pergamon Press, New York, 1975), pp 195-196.
68. R. Loudon, *Quantum Theory of Light*, Chapter 6, (Clarendon Press, Oxford, 1973).
69. R. M. Martin and L. M. Falicov, *Resonance Raman Scattering in Light Scattering in Solids I*, M. Cardona ed. (Springer, Berlin, 1983)
70. P. Manuel, G. A. Sai-Halasz, L. L. Chang, C.-A. Chang, and L. Esaki, *Phys. Rev. Lett.* **37**, 1701 (1976).
71. H. Fröhlich, *Adv. Phys.* **3** 325 (1954).
72. A. K. Sood, J. Menendez, M. Cardona, and K. Ploog, *Phys. Rev. Lett.* **54** (19) 2111 (1985).
73. W. Richter, R. Zeyher, and M. Cardona, *Phys. Rev. B* **18** (8) 4312 (1978).
74. R. Trommer and M. Cardona, *Phys. Rev. B* **17** (4) 1865 (1978).

75. B. Jusserand and M. Cardona, in *Light Scattering in Solids V*, M. Cardona and G. Güntherodt ed., Chapter 3. (Springer, Berlin, 1989)
76. J. E. Zucker, A. Pinczuk, D. S. Chemla, A. C. Gossard, and W. Wiegmann, *Phys. Rev. Lett.* **51** (14) 1293 (1983).
77. J. E. Zucker, A. Pinczuk, D. S. Chemla, A. C. Gossard, and W. Wiegmann, *Phys. Rev. Lett.* **53** (13) 1280 (1984).
78. J. E. Zucker, A. Pinczuk, D. S. Chemla, A. C. Gossard, and W. Wiegmann, *Phys. Rev. B* **29** (12) 7065 (1984).
79. J. E. Zucker, *J. of Luminescence* **31 & 32** 375-380 (1984).
80. J. E. Zucker, A. Pinczuk, and D. S. Chemla, *Phys. Rev. B* **38** (6) 4287 (1988-II).
81. J. E. Zucker, A. Pinczuk, D. S. Chemla, and A. C. Gossard, *Phys. Rev. B* **35** (6) 2892 (1987-II).
82. P. Y. Yu and Y. R. Shen, *Phys. Rev. Lett.* **29** (8) 468 (1972).
83. W. Dreybrodt, W. Richter, and M. Cardona, *Solid State Commun.* **11**, pp 1127-1130 (1972).
84. M. V. Klein, *IEEE J. of Quantum Electron.*, vol. **QE-22** (9) 1760 (1986).
85. M. I. Alonso and M. Cardona, *Phys. Rev. B* **37** (17) 10107 (1988-I).
86. C. Tejedor, J. M. Calleja, F. Meseguer, E. E. Mendez, C.-A. Chang, and L. Esaki, *Phys. Rev. B* **32** (8) 5303 (1985).
87. V. V. Gridin, R. Beserman, K. P. Jain, M. V. Klein, and H. Morkoc, *Superlattices and Microstructures*, vol. **3**, No.2, 1987.
88. W. Kausche, A. K. Sood, M. Cardona, and K. Ploog, *Phys. Rev. B* **36** (3) 1612 (1987-II).
89. D. A. Kleinman, R. C. Miller, and A. C. Gossard, *Doubly resonant LO-phonon Raman scattering observed with GaAs-Al<sub>x</sub>Ga<sub>1-x</sub>As quantum wells*, *Phys. Rev. B* **35** (2) 664 (1987).
90. See, for example, L. I. Schiff, *Quantum Mechanics*, 3rd Ed. Chapter 8., (McGraw-Hill, 1968, New York)
91. T. A. Grant, M. Delaney, M. V. Klein, R. Houdre, and H. Morkoc, *Phys. Rev. B* **39** (3) 1696 (1989-II).
92. E. S. Koteles, D. A. Owens, D. C. Bertolet, and K. M. Lau, *Phys. Rev. B* **38**(14), 10139 (1988-I).
93. E. Tuncel, L. Pavesi, D. Martin, and F. K. Reinhart, *Phys. Rev. B* **38**, 1597 (1988-I).
94. D. C. Bertolet, J. K. Hsu, and K. M. Lau, *J. Appl. Phys.* **62** (1), 120 (1987).

95. K. M. Lau, S. H. Jones, J.-K. Hsu, and D. C. Bertolet, *J. Appl. Phys.* **62** (6), 2466 (1987).
96. E. F. Schubert, E. O. Göbel, Y. Horikoshi, K. Ploog, and H. J. Queisser, *Phys. Rev. B* **30** (2), 813 (1985).
97. S. Hong and J. Singh, *J. Appl. Phys.* **62** (5), 1994 (1987).
98. J. Singh and K. K. Bajaj, *Appl. Phys. Lett.* **48** (16) 1077 (1986).
99. B. Deveaud, J. Y. Emery, A. Chomette, B. Lambert, M. Baudet, *Superlattices and Microstructures*, **1** (3) 205, 1985.
100. D. C. Reynolds, K. K. Bajaj, C. W. Litton, W. P. Yu, S. Singh, W. T. Masselink, R. Fisher, and H. Morkoc, *Appl. Phys. Lett.* **46** (1), 51 (1985); D. C. Reynolds, K. K. Bajaj, G. Peters, C. Leak, W. M. Thesis, W. P. Yu, and H. Morkoc, *Phys. Rev. B* **37**, 7133 (1988-II).
101. L. Goldstein, Y. Horikoshi, S. Tarucha, and H. Okamoto, *Jpn. J. Appl. Phys.* **22** (10), 1489-1492 (1983).
102. C. Weisbuch, R. Dingle, A. C. Gossard, and W. Wiegmann, *Solid State Commun.* **38** pp. 709-712, (1981).
103. J. J. Song, Y. S. Yoon, P. S. Jung, A. Fedotowsky, C. W. Nieh, and T. Vreeland, *J. Opt. Soc. Am. A* **4**(13), P116 (1987).
104. J. J. Song, P. S. Jung, Y. S. Yoon, H. Chu, Y. C. Chang, and C. W. Tu, *Phys. Rev. B* **39** (8), 15 March (1989).
105. J. L. Beeby and S. F. Edwards, *Proc. Roy. Soc. A. (London)* **274**, 395 (1963).
106. A. B. Chen, *Phys. Rev. B* **7**, 2230 (1973).
107. R. J. Elliot, J. A. Krummhanl, and P. L. Leath, *Rev. Mod. Phys.* **46**, 465 (1974), and references therein.
108. P. L. Taylor, *A quantum approach to the solid state*, p290 (Prentice-Hall, Englewood Cliffs 1970)
109. Y. C. Chang, Private communication, 1989.
110. Approximately, the reduced mass of the excitons is determined by the mass of electrons. We treat the exciton as a single particle. See 111.
111. The excitons are considered as a particle with a reduced mass, and dispersion of the sum of the dispersions of a heavy- or light- hole band and an electron band.
112. D. D. Sell, *Phys. Rev. B* **6**, 3750-3753 (1972).
113. A. Chomette, B. Lambert, B. Deveaud, F. Clerot, A. Regreny, and G. Bastard, *Europhys. Lett.* **4** (4), pp. 461-466 (1987).

114. K. J. Moore, P. Dawson, and C. T. Foxon, *Phys. Rev. B* **34** (8) 6022 (1986).
115. P. Dawson, K. J. Moore, G. Duggan, H. I. Ralph, and C. T. B. Foxon, *Phys. Rev. B* **34** (8) 6007 (1986).
116. L. C. Andreani and A. Pasquarello, *Europhys. Lett.* **6** (3), pp. 259-264 (1988).
117. L. W. Molenkamp, G. E. W. Bauer, and R. Eppenga, and C. T. Foxon, *Phys. Rev. B* **38** (9) 6147 (1988-II).
118. See, for example, *Excitons in Confined Systems*, edited by R. Del Sole, A. D'Andrea, and A. Lapicciarella (Springer, New York, 1987)
119. *Heterojunctions and Semiconductor Superlattices*, edited by G. Allan, G. Bastard, N. Boccara, M. Lannoo, M. Voos (Springer, New York, 1987)
120. H. Chu and Y. C. Chang, *Phys. Rev. B* **36**, 2946 (1987).
121. H. Y. Chu and Y. C. Chang, *Phys. Rev. B* **38**, 1246 (1989-II).
122. M. Altarelli, *Phys. Rev. B* **34**, 3917 (1986); A. Fasolino and M. Altarelli, in *Two-dimensional Systems, Heterostructures, and Superlattices*, edited by G. Bauer, F. Kuchar, and H. Heinrich (Springer, New York, 1984).
123. B. Zhu, *Phys. Rev. B* **37**, 4689 (1989); B. Zhu, and K. Huang, *ibid.* **36**, 8102 (1987).
124. D. M. Woodruff, S. M. Anlage, and D. L. Smith, *Phys. Rev. B* **36**, 1725 (1987).
125. B. A. Weinstein and M. Cardona, *Phys. Rev. B* **8** (6) 2795 (1973).
126. R. C. C. Leite, J. F. Scott, T. C. Damen, *Phys. Rev. Lett.* **22**, 780 (1969).
127. A. Nakamura and C. Weisbuch, *Resonant Raman Scattering by Excitonic Polaritons in Semiconductors*, *Solid State Commun.* **32**, pp301-304, 1979.
128. R. Trommer and M. Cardona, *Solid State Commun.* **27**, 153 (1977).
129. M. Cardona, in *Semiconductors and Semimetals*, Vol. 3, R. K. Willardson and A. C. Beer ed., Chapter 5 (Academic Press, New York, 1967).
130. R. C. Miller, D. A. Kleinman, C. W. Tu, and S. K. Sputz, *Doubly resonant LO-phonon Raman scattering via the deformation potential with a single quantum well*, *Phys. Rev. B* **34** (10) 7444 (1986).
131. R. C. Miller, D. A. Kleinman, and A. C. Gossard, *Solid State Commun.* **60** (3) pp213-216 (1986).
132. A. Alexandrou, M. Cardona, and K. Ploog, *Doubly and triply resonant Raman scattering by LO phonons in GaAs-AlAs superlattices*, *Phys. Rev B* **38** (3) 2196 (1988-II).

133. B. Jusserand, D. Paquet, J. Kervarec, and A. Regreny, *J. de Physique Colloq.* C5, no 4, Tome 45, p. C5-145, 1984.
134. B. Jusserand and D. Paquet, *Phys. Rev. B* **30** (10) 6245 (1984).
135. C. Colvard, T. A. Gant, M. V. Klein, R. Merlin, R. Fisher, H. Morkoc, and A. C. Gossard, *Phys. Rev. B* **31** (4) 2080 (1985).
136. S.-L. Zhang, M. V. Klein, J. Klem, and H. Morkoc, *Phys. Lett. A* **131** (1) 69 (1988).
137. T. Tsuchiya, H. Akera, and T. Ando, *Phys. Rev. B* **39** (9) 6025 (1989-II).
138. R. Loudon, *Advan. Phys.* **13**, 423 (1964).
139. A. A. Gogolin and E. I. Rashba, in *Proceedings of the Thirteenth International Conference on the Physics of Semiconductors*, edited by F. G. Fermi (Tipografia Marves, Rome, 1976), p. 284; *Solid State Commun.* **19**, 1177 (1976).
140. R. Zeyher, *Solid State Commun.* **16**, 49 (1975).
141. R. M. Martin and C. M. Varma, *Phys. Rev. Lett.* **26** (20) 1241 (1971)
142. P. Y. Yu, *Study of excitons and exciton-phonon interactions by resonant raman and brillouin spectroscopies*, in *Excitons*, K. Cho ed. (Springer, New York, 1979).
143. P. Y. Yu, Y. R. Shen, Y. Petroff, and L. M. Falicov, *Phys. Rev. Lett.* **30**, 283 (1973)
144. P. Y. Yu and Y. R. Shen, *Phys. Rev. B* **12**, 1377 (1975)
145. M. V. Klein, *Phys. Rev. B* **8** 919 (1973).
146. T. P. Martin, *Phys. Rev. B* **13** (8), 3617 (1976).
147. J. A. Kash, J. C. Tsang, and J. M. Hvam, *Phys. Rev. Lett.* **54**, 2151 (1985)

## APPENDIX

### Summary of Symbols

*These are only to help to notice the special symbols in the list of programs. For detailed information, see Reference 57.*

#### APL SYMBOLS:

^	and	⊞	matrix divide	!	factorial	f/	reduction last
←	assignment	⊞	matrix inverse	⊆	find	ρ	reshape
!	binomial	⌈	maximum	⌊	floor	⌊	residue
→	branch	∈	member of	∇	fn definition	⊖	reverse 1st
⌈	catenate 1st	⌊	minimum	≥	greater/equal	⊘	reverse last
.	catenate last	-	minus	>	greater than	?	roll
⌈	ceiling	∗	nand	[ ]←	index assign	⊖	rotate 1st
'	char identifier	⊖	natural log	⌊	index generate	⊘	rotate last
A	comment	-	negate	[ ]	index into	f⌈	scan 1st
f	compress 1st	∗	nor	⌊	index of	f\	scan last
/	compress last	~	not	f.g	inner product	ρ	shape
+	conjugate	≠	not equal	:	label	x	signum
?	deal	∨	or	<	less/equal	⊘	statement sep.
⌊	decode	∘.f	outer product	<	less than	OUT	susp. at input
÷	divide	⌊	output	∗	lock function	↑	take
∇	downgrade ch	( )	parentheses	⊙	logarithm	⌊	text input
∇	downgrade nm	⌈	pattern format	⌊	magnitude	∇	thorn format
↓	drop	∘	pi times	≡	match	x	times
⊖	dya. transpose	+	plus	⊖	transpose	▲	upgrade nums
T	encode	*	power	∘	trigonometric	~	without
=	equal	⌊	prompt	▲	upgrade chars	⊘	zilde
⌊	eval. input	A∇	pub. comment				
⊖	execute	.	ravel				
⌈	expand 1st	)	recall stmt				
\	expand last	+	reciprocal				
*	exponential	f/	reduction 1st				

### System Functions, Variables

Those start with  $\square$  are system functions and variables, such as;

$\square$ DR	Data representation
$\square$ ARBIN	Arbitrary Input/Output
$\square$ AV	Atomic Vector; ASCII table.
etc.	

For details, please refer to Reference 57.



## LIST of APL programs:

Interface Subsystem

```

      DVR 'DYEIN'
    ▽ DYEIN;FID;X
[1]  DELX←'ODM'
[2]  DWINDOW← 0 0 25 80
[3]  0ρ1 DPOKE 254 0 0ρ0 DPOKE 255 0 a DINKEY WAIT/CHR. CONTROL
[4]  0ρ7 DPOKE 164 0 a strong break-same as default.
[5]
[6]  WASCALDATA←'0 WASCAL' ΔFREAD 3
[7]  WASCALDATA←WASCALDATA[ΔWASCALDATA[;1];]
[8]  WASCALDATA[;2]+10000000←WASCALDATA[;2]
[9]  ΔSPEXPAR←'0 SPDYESCR' ΔFREAD 12+(ΔWHICHLASER='CPS')/13
[10] CHANGELAS
[11] DTCTFF 0 NORMSCR 0 FID←'0 SPDYESCR'
[12] ΔSPEXPARSP←FID ΔFREAD 15
[13] ΔSPEXPARPUL←FID ΔFREAD 14
[14] ΔSPEXPARCW←FID ΔFREAD 13
[15] ΔSPEXPAR←FID ΔFREAD 16
[16] a FID ΔFREAD 3
[17] a24 0 1 80 DWPOT 112
[18] a24 0 1 27 DWPOT 'Press space bar to continue'
[19] a0 0 ρDINKEY
[20] DTCTFF
[21] +(ΔWHICHLASER='S')/DLC+1 0 '...DON'T FORGET THE INITIALIZATION OF THE SCAL
    LE....' 0 0 ρDINKEY
[22] DTCTFF
[23] (FID ΔFREAD 12)SCRDYEFLLS FID ΔFREAD 7
    ▽
      DVR 'SCRDYEFLLS'
    ▽ R←SCR SCRDYEFLLS F;P;L;I;J;C;N;W;CMDS;O;CLOR;SCR;XXX;SCRO
[1]  a*** Full screen entry processor
[2]  aW=4↑F is the screen window
[3]  a4↑F are triplets describing the position and
[4]  a length of each field window
[5]  W←4↑F 0 F←4↑F 0 N←(ρF)÷3 0 F←(N,3)ρF 0 I←J←1
[6]  aCMDS is a list of executable commands
[7]  a corresponding to each field
[8]  CMDS←';CHANGELAS;INDYELAS;SETDYELAS;SCANDL;SETPAR;DISPFILE;DESCRF;DALLF;→E
    ND'
[9]  R←((1↑ρF),[ρF;3])ρ' '
[10] a P←0 DPOKE 149 a Auto insert off
[11] L←256ρERR a Create branch table
[12] L[33 31 42 ,(44+14),65+158]←OK
[13] L[33 31 42 ,(44+14),65+158]←OK
[14] L[134 136]←CR,CL a Special keys
[15] L[183 182]←ESC,BS
[16] L[133 139 14]←PEND,HOME,EXE
[17] L[137 138 165]←PGUP,UP,DOWN

```

*continued - SCRDYEFLLS*

```

[18] TOP1: 0 0 25 80 DWPUR △ATTR1] ◇ DCURSOR+2↑W ◇ SCR
[19] LO: a Display fields in rev. video
[20] (FCJ; 1 2],1,FLJ;3])DWPUR △ATTR2]
[21] +(1↑ρF)2J+J+1)ρLO
[22] TOP:
[23] DISLASSYSTEM
[24] J+1 ◇ DCURSOR+,FCI; 1 2]
[25] LP:C+BINKEY ◇ +LIDAV\C]
[26] OK:⊞+DTCBEL ◇ RCI;J]←,C
[27] →TOP
[28] BS:
[29] +(J=1)ρLP ◇ ⊞+DTCBS, ' ',DTCBS
[30] J+J-1 ◇ RCI;J]←' ' ◇ +LP
[31] CR:+(J=FCI;3])ρDOWN a Cursor right
[32] J+J+1 ◇ DCURSOR+DCURSOR+ 0 1 ◇ +LP
[33] CL:+(J=1)ρLP ◇ a Cursor left (←)
[34] J+J-1 ◇ DCURSOR+DCURSOR- 0 1 ◇ +LP
[35] ERR:⊞+DTCBEL ◇ +LP
[36] DOWN:I+1+(1↑ρF)I] ◇ +TOP
[37] UP:I+1[I+I-1 ◇ +TOP
[38] EXE:0← 0 0 25 80 DWGET 3 ◇ DTCTFF ◇ ±I PIC CMDS ◇ 0 0 25 80 DWPUR 0 ◇ +TOP
[39] ESC:R←0 ◇ +END
[40] FEND:I+1↑ρF ◇ +TOP
[41] HOME:I+1 ◇ +TOP
[42] PGUP:DTCTFF ◇ +TOP1
[43]
[44] END:DTCTFF ◇ '***You are now in APL execution mode.'
[45] '0 SPDYESCR;15' △FREPLACE △SPEXPASP
[46] '0 SPDYESCR;14' △FREPLACE △SPEXPAPUL
[47] '0 SPDYESCR;13' △FREPLACE △SPEXPAPCW
[48] '0 SPDYESCR;16' △FREPLACE △SPEXPAP
[49]

```

```

▽
DVR 'PLOTSIZE'
▽ PLOTSIZE;X;VTHZ
[1] X←INPUTS ' Vertical or Horizontal(normal) plotting? V/H'
[2] +(0=ρX)/OUT
[3] X+1↑X ◇ VTHZ← 2 1] ρ'HORIZONTAL.VERTICAL.
[4] +(X≠'V')/NEXT ◇ △GPC[3 4]← 1 1
[5] '...was ',VTHZ[DIO+1 DPOKE 234;]
[6] NEXT:
[7] +(X≠'H')/OUT ◇ △GPC[3 4]← 4 1
[8] '...was ',VTHZ[DIO+0 DPOKE 234;]
[9] OUT:

```

```

▽
DVR 'INDYELAS'
▽ INDYELAS
[1] +(△WHICHLASER='S')/0
[2] BAKLASH ◇ DISLASSYSTEM
[3] 'Grating position -----now--',(≠△DLPOS)
[4] △DLPOS←]

```

```

      OUR 'CHANGELAS'
    ▽ CHANGELAS
[11] X+INPUTS ')>>What do you want to SCAN--[C]w-dye, [P]ulse-dye or [S]pex---no
      w+>>',△WHICHLASER,'---'
[12] →(0≠pX)/DLC+1 ◇ →0
[13] →('PCS'=1↑△WHICHLASER)/P,C,S ◇ 'error in △WHICHLASER+>>',△WHICHLASER
[14]
[15] P:
[16] △DLPOSPUL+△DLPOS ◇ △ABPUL+△AB ◇ △AADNPUL+△AADN ◇ △AAUPPUL+△AAUP
[17] △LMTMAXPUL+△LMTMAX ◇ △LMTMINPUL+△LMTMIN
[18] △DUTYPUL+T12
[19] △BACKLASHPUL+△BACKLASH ◇ △COMMDPUL+△COMMD
[10] △CALPUL+△CAL ◇ datainPUL+datain
[11] △SPEXPARPUL+△SPEXPAP
[12] →NEXT
[13] C:
[14] △DLPOSCW+△DLPOS ◇ △ABCW+△AB
[15] △AADNCW+△AADN ◇ △AAUPCW+△AAUP
[16] △LMTMAXCW+△LMTMAX ◇ △LMTMINCW+△LMTMIN
[17] △DUTYCW+T12
[18] △BACKLASHCW+△BACKLASH ◇ △COMMDCW+△COMMD
[19] △CALCW+△CAL ◇ datainCW+datain
[20] △SPEXPARCW+△SPEXPAP
[21] →NEXT
[22]
[23] S:
[24] △COMMDSP+△COMMD
[25] datainSP+datain
[26] △SPEXPARSF+△SPEXPAP
[27] →NEXT
[28] NEXT:
[29] →((1↑X)='P')/PULSE
[30] →((1↑X)='C')/CW
[31] →((1↑X)='S')/SPEX
[32] '***** UNKNOWN SYSTEM *****' ◇ →1
[33]
[34] CW:
[35] △WHICHLASER+'C'
[36] DTCBEL ◇ 'CHANGE THE controller SW. TO <C.W> & <X drive>.' ◇ DINKEY ◇ →OUT
[37]
[38] PULSE:
[39] △WHICHLASER+'P'
[40] DTCBEL ◇ 'CHANGE THE controller SW. TO <PULSE>.' ◇ DINKEY ◇ →OUT
[41]
[42]
[43] SPEX:
[44] △WHICHLASER+'S'
[45]
[46]
[47] OUT:SCANPARA
[48] DISLASSYSTEM
[49]
    ▽

```

```

QVR 'SETPAR'
▽ SETPAR;S1;F1;ERRMSG
[11] ERRMSG←DTCBEL,'***Error, Unexecutable.'
[12] SINIT:DELX←'DDM'
[13] X←INPUTS ' Command to execute or Parameter values to change,or Quit? C/P/Q
---C→→→'
[14] +(O=ρX)/cmd
[15] +('Q'≠1↑X)/DLC+1 ◇ →0
[16] +('P'≠1↑X)/DLC+1 ◇ →PARAM
[17] +('C'≠1↑X)/DLC+1 ◇ →cmd
[18] →SINIT
[19] cmd:DELX←'ERRMSG◇DDMO→SINIT'
[10] X←INPUTS ''
[11] +(O=ρX)/DLC+1 ◇ →ΔCOMMD←X ◇ →DLC-1
[12] →SINIT
[13]
[14] PARAM:X←INPUTS ' >>>>>>ΔCALIB. FACTOR -----',(≠ΔCAL),'→→→'
[15] +(O=ρX)/DLC+1 ◇ ΔCAL←±X
[16] X←INPUTS ' >>>>>>ΔBACKLASH-----',(≠ΔBACKLASH),'→→→'
[17] +(O=ρX)/DLC+1 ◇ ΔBACKLASH←±X
[18] X←INPUTS ' >>>>>>PULSE DUTY-----',(≠T12),'→→→'
[19] +(O=ρX)/DLC+1 ◇ T12←±X
[20] PLOTSIZE
[21] A 0ρDINKEY
[22] A S1←'O SPDYESC' ΔFREAD 9
[23] A F1←'O SPDYESC' ΔFREAD 11
[24] F1←12+('CPS'=1↑ΔWHICHLASER)/13
[25] AGN:X←INPUTS 'Which version of Descriptions to use, (M)aster/(C)urrent or (
Q)uit?--C--'
[26] +(O=ρX)/NEXT ◇ +('C'≠1↑X)/DLC+1 ◇ →NEXT
[27] +('M'≠1↑X)/DLC+1 ◇ ΔSPEXPAR←'O SPDYESC' ΔFREAD F1 ◇ →NEXT
[28] +('Q'≠1↑X)/DLC+1 ◇ →0
[29] →AGN
[30] NEXT:
[31] EDIT 'ΔSPEXPAR'
[32] ('O SPDYESC';',≠F1)ΔFREPLACE ΔSPEXPAR
[33] DTCFF
[34]
[35] A ΔDATA←ΔSPEXPAR ◇ 0 0 ρS1 SINFLDS F1 ◇ ΔSPEXPAR←ΔDATA ◇ DTCFF
[36]
[37]
[38]
[39]
▽

```

```

      QVR 'DISFFILE'
      ▽ DISFFILE:FID;N;L;M;XYU;I
[1]  #Displays a graphic file using SPLOTc
[2]  'Drive number' 0 D+0
[3]  'Existing files:' 0 , 0 11 + 0 '1 #DFLIB#D
[4]  'File name?' 0 FID+0
[5]  →(0=ΔFEXIST FID+D,' ',FID)/END
[6]  'Component numbers ?' 0 M+0N+,0 0 1+1
[7]  L2:HOW SPLOTc XYU+FID ΔFREAD NCI]
[8]  L1:'Replot using new Plotting command ? Type plotcommand or E (End)'
[9]  HOW+0
[10] →('E'#HOW)/L3
[11] HOW SPLOTc XYU 0 →L1
[12] L3:→(M)I+1)/L2 0 →0
[13] END:'Non existent file' 0 'Press space bar' 0 0 0 #DINKEY
      ▽

      QVR 'DISLASSYSTEM'
      ▽ DISLASSYSTEM:CLOR
[1]  →(ΔWHICHLASER='C')/DLC+1 0 LASYSTEM='CW DYE LASER' 0 CLOR+4
[2]  →(ΔWHICHLASER='P')/DLC+1 0 LASYSTEM='PULSE DYE LASER' 0 CLOR+1
[3]  →(ΔWHICHLASER='S')/DLC+1 0 LASYSTEM='SPECTROMETER ' 0 CLOR+0
[4]  0 50 1 15 DMPUT LASYSTEM 0 0 50 1 15 DMPUT CLOR+8+7*16
      ▽

      QVR 'NORMSCR'
      ▽ NORMSCR
[1]  ΔATTRE1]DPOKE 161
[2]  DTCTFF
      ▽

      QVR 'SCANPARA'
      ▽ SCANPARA
[1]  →(ΔWHICHLASER='P')/FULSE
[2]  →(ΔWHICHLASER='C')/CW
[3]  →(ΔWHICHLASER='S')/SPEX
[4]  →'**** UNKNOWN LASER *****' 0 →0
[5]  SPEX:ΔCOMMD+ΔCOMMDSP
[6]  ΔSPEXPAR+ΔSPEXPARSP
[7]  'datain+datainSP
[8]  →0
[9]
[10] CW:
[11] ΔLMTMAX+ΔLMTMAXCW 0 ΔLMTMIN+ΔLMTMINCW
[12] ΔAADN+ΔAADNCW 0 ΔAAUP+ΔAAUPCW
[13] ΔDLPOS+ΔDLPOSCW 0 ΔAB+ΔABCW
[14] T12+ΔDUTYCW
[15] ΔBACKLASH+ΔBACKLASHCW
[16] ΔCAL+ΔCALCW 0 datain+datainCW
[17] ΔSPEXPAR+ΔSPEXPARCW
[18] →0

[19]
[20] FULSE:ΔDLPOS+ΔDLPOSPUL 0 ΔAB+ΔABPUL
[21] ΔLMTMAX+ΔLMTMAXPUL 0 ΔLMTMIN+ΔLMTMINPUL
[22] ΔAADN+ΔAADNPUL 0 ΔAAUP+ΔAAUPPUL
[23] T12+ΔDUTYPUL
[24] ΔBACKLASH+ΔBACKLASHPUL
[25] ΔCAL+ΔCALPUL 0 datain+datainPUL
[26] ΔSPEXPAR+ΔSPEXPARPUL
[27] →0
[28]
[29]
[30]
[31]
[32]
[33]
      ▽

```

Graphics Subsystem

```

DVR 'SPLOTc'
▽ HOW SPLOTc XY;S;N;I;XT;U;CMDS;M;NXY;C;DELX;XYU;△△A;A1;A4;CC;N1;SC;SCR;WIND
;A
[1] A DELX+DAVE[40],'....Illegal input...',DAVE[40],'+OUT'
[2] C+1 ◇ A SCR+(WIND+QWINDOW)QWGET 1
[3] +(Q#QNC 'HOW')/L15 ◇ HOW+'PD'
[4] L15:HOW+'/',HOW ◇ M+PDIM HOW
[5] +(82#QDR XY)/L9
[6] NXY+PDIM XY+'/',XY ◇ I+1 ◇ SC+4p 1 1 1 1 x1E20
[7] L10:△△A+±(I PIC XY)
[8] SCC[1]+SCC[1]LL/△△A[;1] ◇ SCC[2]+SCC[2]LL/, 0 1 ↓△△A
[9] SCC[3]+SCC[3]ΓΓ/△△A[;1] ◇ SCC[4]+SCC[4]ΓΓ/, 0 1 ↓△△A
[10] +(NXY2I+I+1)/L10 ◇ →L11
[11]
[12] L9:+(1#ppXY)/L5 ◇ XY+(1pXY),[1.1]XY
[13] L5:SC+L/XY[;1] ◇ SC+SC,L/, 0 1 ↓XY ◇ SC+SC,Γ/XY[;1] ◇ SC+SC,Γ/, 0 1 ↓XY
[14] L11:+(~v/HOW DSS 'SC')/L8
[15] SC+±',SC' PICARG HOW
[16]
[17] L8:△SCRSCA+ 2 2 pSC A Actual screen scale
[18] △MODE+△MTH
[19] +(~v/HOW DSS 'pTXT')/L7
[20] QEDIT 'scrTXT'
[21]
[22] L7:INIT ◇ 0 0 pQWINDOW △GWINDOW ◇ 0 0 pQVIEW △GVIEW
[23]
[24] 7 HNUMA SCC[1 3] ◇ △SPWC[1 2 4]VNUMA SCC[2 4],1
[25] I+1 ◇ S+ 2 2 p 0 0 1023 1023
[26] N+ 1+ 1+1pXY ◇ +(82#QDR XY)/L13 ◇ N+NXY
[27]
[28] L13:△SCOLL1]SFRAME △SPW
[29] (2 982 ,△SCOLL[2])GWRITE △FID,'#',±FCNUM
[30] △DATE QGWRITE(△SPW[3 4]- 300 150),△SCOLL[2]
[31] +(~v/HOW DSS 'TXT')/L1
[32]
[33] scrXY GWRITE scrTXT
[34] L1:+(82#QDR XY)/L12
[35] U+ 2 0 ↓△SPW SCA,△SCRSCA,[1]XY[;1,I+1] ◇ →L14
[36] L12:U+ 2 0 ↓△SPW SCA,△SCRSCA,[1]±I PIC XY
[37]
[38] L14:C+△COLL[1;1+16]I-1]
[39] CMDS+(NpCH)[I]PIC HOW
[40] A +(v/CMDS DSS 'SP')/L2
[41] L2:+(~v/CMDS DSS 'PD')/L3
[42] (CC+C)QGLINE(1,pU)pU
[43] L3:+(~v/CMDS DSS 'SMc')/L6
[44] C QGCIRCLE U,5
[45]
[46] L6:+(N(I+1+1)/DLC+1 ◇ QSOUND 2 2 p 5500 200 4400 200 ◇ 0 0 pQINKEY ◇ →L1
[47] 0 0 pQTYPE 2 ◇ 0 1023 TCKL2 XT ATick marks
[48] L66:QSOUND 2 2 p 5500 200 4400 200 ◇ N+QINKEY ◇ +(N='P')/DLC+1 ◇ +(N=' ')/L
4 ◇ →DLC

```

*continued - SPLOTc*

```

[49] ΔGPRSHC[1]+255 ◊ ΔGPRSHC[10]+,ΔSCOL,,ΔCOL[1;13]]+219 ◊ ΔGPRSHC[10]+,ΔMODE[5]]+
255
[50] (DAVC[10]+ΔGPRSHJ)DGPRINT 2+ΔGFR
[51] 0 0 ρ3 DINT 16
[52] MESSAGE+ '13;248' SUBSTR ΔSPEXPAR
[53] X+INPUTS 'MESSAGE TO PRINT (Y or N)+ ' ◊ +('Y'≠X)/OUT2 ◊ MESSAGE[1,ρΔDATE]+Δ
DATE ◊ DEDIT 'MESSAGE' ◊ ΔSPEXPAR+ '248;13' SUBSTR MESSAGE ◊ →OUT1
[54] OUT2:MESSAGE+ ' '
[55] OUT1:→(DPEEK 234)/L44 ◊ 0 0 ρ1 DPOKE 116 ◊ MESSAGE,DAVC[13] ◊ 0 DPOKE 116
[56] L4:
[57] CLOSE ◊ →OUT
[58]
[59] L44:
[60] N N+INPUTS ' Send the page to next one?'
[61] N→(0=ρN)/0
[62] N →(N≠'Y')/0
[63] 0 0 ρ1 DPOKE 116 ◊ DAVC[14 14 14] ◊ 0 0 ρ0 DPOKE 116 ◊ →OUT
[64]
[65] OUT: N WIND D WPUT SCR
[66]
[67]
[68]
[69]
▽
  DVR 'SFRAME'
  ▽ C SFRAME W
[1] →(0≠ρW)/L ◊ W+ΔGWINDOW
[2] L:C DGLINE 1 5 2 ρWC 1 2 3 2 3 4 1 4 1 2]
▽
  DVR 'HNUMA'
  ▽ N HNUMA U;Δ;X;X1
[1] Δ+N AUTOSC U
[2] X+(Δ-UC[1])×(-/ΔSPWC 3)÷-/U
[3] XT+X1+((A4+Δ SUBTCK U)-UC[1])×(-/ 0 1023)÷-/U
[4] (' ',ρΔ)HOCH X
▽
  DVR 'AUTOSC'
  ▽ R+N AUTOSC AB;M
[1] R+(-/φAB)÷N ◊ M+(10+L10*(R+1E-99×(R=0)))× 1 2 2.5 5 10
[2] R+1+(R≤M)/M ◊ M+R×[(1+AB)÷R ◊ R+M+R×-1+LN
[3] R+(ABC[2]≥R)/R
▽
  DVR 'HOCH'
  ▽ C HOCH X;Δ;I
[1] C[('0'=C)/1,ρ,C]+ '0' ◊ C[(' '=C)/1,ρ,C]+ '- '
[2] X+φ0,[1.1]10.5+X
[3] X+X+(ρX)ρ 0 0
[4] Δ+20-8×DIM C ◊ I+1
[5] NINIT ◊ 0 0 ρDGWINDOW ΔGWINDOW ◊ 1 SFRAME ΔGWINDOW ◊ 1 SFRAME ΔSPW
[6] L1:((56 72 +X[C1;]+Δ[C1],0),ΔSCOL[3])GWRITE I PIC C ◊ +((ρΔ)≥I+1)/L1
[7] ρ0 0 ρDINKEY ◊ CLOSE
▽

```

```

DVR 'INIT'
▽ INIT
[1]  INITIALIZE GRAPHICS FOR SINGLE MONITOR CONFIGURATION.
[2]  ΔSCREEN← 0 0 25 80 DWGET 3 ◇ ΔCURSOR←DCURSOR ◇ DELX←DALX←'CLOSE ◇ BDM'
[3]  DSEG←'' ◇ myorigin←256LDPEEK 177 176  a GET ORIGIN OF GRAPHICS CHARS
[4]  0 0 ρΔMODE DGINIT ΔCCARD

```

```

DVR 'CLOSE'
▽ CLOSE
[1]  ACLOSE GRAPHICS FOR SINGLE MONITOR CONFIGURATION.
[2]  3 DINT 16 ◇ DELX←DALX←'BDM'
[3]  (0,0,2↑ρΔSCREEN)DWPUP ΔSCREEN ◇ DCURSOR←ΔCURSOR
[4]
[5]
[6]

```

```

DVR 'SUBTCK'
▽ X←Δ SUBTCK U;Δ1;N;A
[1]  Δ1←1-/2↑Δ  aenumeration interval
[2]  A←Δ1×10+L10#Δ1  anormalize to 1-10 interval
[3]  N←5 ◇ +(A≠2)/L ◇ N←4  aadded number of ticks/interval
[4]  L:N1←5+N×1+ρΔ  anumber of ticks plus
[5]  X←(Δ[1]-Δ1)+(Δ1÷N)×-1+N1  anew tick coord.
[6]  X←((X2UC[1])ΔXUC[2])/X  aeliminate those out U range

```

```

DVR 'VECH'
▽ C VECH Y;Δ;I;N;XY
[1]  AC characters to be disp vert,CC[1]=delimiter
[2]  AY[1 2] origin of chars,Y[3]=0 to right,Y[3]=1 to left
[3]  CC['0'=C)/↑ρ,C]←'0' ◇ CC['1'=C)/↑ρ,C]←'-'
[4]  I←1 ◇ Δ←-↑/DIM C ◇ AΔ is max length of chars in C
[5]  XY←(2↑Y)+ 1 0 ×13×Δ×Y[3] ◇ Y←3↑Y ◇ N←ρY  aXY=coord of char origin
[6]  XY←(0 AND Y)+(N,2)ρXY  acoords of chars
[7]  L:(I PIC C)BGWRITE(XY[1];]- 0 44),ΔSCOL[3]  awrite chars in color ΔSCOL[3]
[8]  +(N≥I←I+1)/L

```

```

DVR 'VNUMA'
▽ XY VNUMA U;M;Y;Y1
[1]  AAutoscales and nubers UC[1 2] onto a vertical axis
[2]  aXY[1 2],XY[1 3] is the axis
[3]  AU[3]=0 to the right,1 to the left
[4]  M←7  amax number of numeration numbers
[5]  Y←M AUTOSC 2↑U  aenumeration digits
[6]  XYV←Y1+XY[2 3]SCA1 UC[1 2],Y  ascaled Y positions
[7]  (' ',≠Y)VECH A1←XY[1 2],UC[3],Y1

```



```

DVR 'TCKL2'
▽ SLT TCKL2 X;XO;N;XYT
[1] N←ρX ◊ +(X[N]≠X[N-1])/L2 ◊ X←1+X ◊ N←N-1
[2] L2:N←N-1 ◊ X←1+X ◊ XO←X,(Nρ0),X,[1.1](NρSLT[2])
[3] +(0 0.5 =1↑SLT)/LO,L1
[4] XO←(0 0 ,180×1↑SLT)ROT XO ◊ +LO
[5] L1:XO←ϕXO
[6] LO:XO←LO.5+,XO+(ρXO)ρ2↑ 0 0
[7] XYT←((LO.5×ρ,XO),2)ρXO
[8] XYT← 2 0 ↓ΔSPW SCA A←(2 2 ρ 0 0 1023 1023),[1]XYT
[9] XYT←LO.5+(N, 2 2)ρXYT
[10] (VGRID XYV)□GLINE XYT
▽

```

```

DVR 'VGRID'
▽ G←VGRID XYV;N;Δ
[1] N←ρXYV number of vert numeration pts
[2] Δ←0.5×--/2↑XYV agrid delta =half num delta
[3] G←XYV[1]+Δ×1+↑N×2 agrid points
[4] G←(G↓ΔSPW[4])/G eliminate those outside 0,YM
[5] G←G-ΔSPW[2] nconv to integer and scale to 0,
[6] G←LO.5+G×167÷-/ΔSPW[4 2]
[7] N←(168ρ0) ◊ N[G+1]←ΔSCOLI[4] ◊ G←N
▽

```

## Scanning Subsystem

```

DVR 'SETDYELAS'
▽ SETDYELAS;A;N
[1] +(ΔWHICHLASER≠'S')/DLC+1 ◊ 0ρSETPOS 0 ◊ +0
[2] A←,'F7.2' DFMT ΔDLPOS
[3] A←INPUTS 'SET POSITION of Dye laser-(mil)-now',A,'→→'
[4] +(0=ρA)/0 ◊ A←±A
[5] SETDYE A
▽

DVR 'SETPOS'
▽ R←SETPOS A;A;R
[1] R←' ' ◊ +(0≠ρA)/LO3 ◊ 'Set position to ?' ◊ A←□ ◊ A←(A≠' ')/A
[2] LO3:+(0=ρA)/0
[3]
[4] +((±A)≥8999)/DLC+1 ◊ +(unit='N')/DLC+1 ◊ unit←'N' ◊ CHANGEUNIT ◊ +DLC+2
[5] +(unit='W')/DLC+1 ◊ unit←'W' ◊ CHANGEUNIT
[6] □←Unit
[7] A[(' '=A)/↑ρA]←'- '
[8] 0 0 ρARBF
[9] R←ΔARB1 □ARBIN □←ΔSTX,'SE',(±A),ΔETX
[10] R←R,ΔARB2 □ARBIN ΔCAN,'F',ΔETX
▽

```

```

DVR 'SETDYE'
▽ SETDYE A;N;D;DPOS;AA
[11] →((A1ΔLMTMAX)^(A2ΔLMTMIN))/DLC+1 ◇ '!!!! out of limits. Stop at ',ΔDLPOS
    ◇ 0 0 ρDINKEY ◇ →0
[12]
[13]
[14] AA←((ΔDLPOS(A)×ΔAAUP)+(ΔDLPOS)A)×ΔAADN
[15] DPOS←ΔDLPOS ◇ N←NN←LAA+IΔCAL×(ΔDLPOS-A)÷8.4E-3 ◇ →(N=0)/0
[16] →(N132000)/DLC+1 ◇ NN←N+32000
[17] N←2ρ 65534 65334 τN ◇ N←PINT N
[18] D←,×A-ΔDLPOS ◇ DC(τ1=D)/τρD]←0
[19] →(ΔWHICHLASER≠'P')/DLC+1 ◇ →(D=1)/L1 ◇ 0 PULSE1 ΔBACKLASHPUL
[10] →(ΔWHICHLASER≠'C')/DLC+1 ◇ →(D=ΔDIRCW)/L1 ◇ D PULSE1 ΔBACKLASHCW ◇ ΔDIRCW←
    D
[11] L1:D PULSE1 NC2]
[12] →(NC1]=0)/L2
[13] I←1
[14] L:D PULSE1 PINT 65534
[15] →(NC1]≥I←I+1)/L
[16] L2:→(ΔWHICHLASER≠'P')/DLC+1 ◇ →(D=1)/L3 ◇ 1 PULSE1 ΔBACKLASHPUL
[17] L3:ΔDLPOS+DPOS+(×D-0.5)×(((NN-AA)÷ΔCAL)×8.4E-3)
[18]
▽

DVR 'SETDYELAS'
▽ SETDYELAS;A;N
[1] →(ΔWHICHLASER≠'S')/DLC+1 ◇ 0ρSETPOS 0 ◇ →0
[2] A←,'F7.2' DFMT ΔDLPOS
[3] A←INPUTS 'SET POSITION of Dye laser-(mil)-now',A,'→→→'
[4] →(0=ρA)/0 ◇ A←ΔA
[5] SETDYE A

DVR 'PULSE1'
▽ D PULSE1 N;N;D
[1] →(ΔWHICHLASER≠'C')/DLC+1 ◇ ρUSE THIS FOR WEDGE D←1-D
[2] 0 0 ρ((4,T12E1], 0 0 ,T12E2],N,D+2)DCALL MAPULS1)
▽

DVR 'SCANDL'
▽ SCANDL;X;Nmax;I;F;Rdata;A;A1;A4;D;XX;TCUR;INKY254;Y
[1] →(ΔWHICHLASER≠'S')/DLC+1 ◇ SCAN ◇ →0
[2] DCURSOR← 0 0
[3]
[4]
[5]
[6] A←INPUTS 'Sample name? (File name) was ',ΔFID,'-----'
[7] →(22ρA)/1+DLC ◇ ΔFID←A ◇ →(+/'01'εΔFIDC1])/DLC+1 ◇ ΔFID←'1 ',ΔFID
[8] →(0≠(ΔFEXIST ΔFID))/L7 ◇ '...File not exist,yet...',ΔFID ◇ ΔFCNUM←3 ◇ →L8
[9] L7:' '
[10] ΔFCNUM←1+ΔFSIZE ΔFID
[11] L8:

```

*continued - SCANDL*

```

[12]
[13] AGAIN:
[14] X+INPUTS 'SCAN START----', (≠ΔABC[2]), '----->'
[15] +(0=ρX)/DLC+1 ◇ ΔABC[2]≠±X
[16] X+INPUTS 'SCAN END ----', (≠ΔABC[3]), '----->'
[17] +(0=ρX)/DLC+1 ◇ ΔABC[3]≠±X
[18] X+INPUTS ' INCREMENT ----', (≠ΔABC[1]), '----->'
[19] +(0=ρX)/DLC+1 ◇ ΔABC[1]≠±X
[20] '*****DATA FETCH ROUTINE---now:' ◇ datain
[21] X+INPUTS '++++'
[22] +(0=ρX)/DLC+1 ◇ datain≠X
[23] F+datain
[24] '*****PLOTTING COMMANDS ---now:' ◇ ΔHOWPL
[25] X+INPUTS '++++'
[26] +(0=ρX)/DLC+1 ◇ ΔHOWPL≠X
[27] ΔABC[1]≠(X(ΔABC[3]-ΔABC[2]))×ΔABC[1] ◇ +(ΔABC[1]=0)/AGAIN
[28] +(ΔWHICHLASER≠'C')/NEXT
[29] a X+INPUTS '!!!! Do you change the position manually? Y/N--'
[30] a +(0=ρX)/DLC-1 ◇ +(X='Y')/DLC+1 ◇ +(X='N')/NEXT ◇ +DLC-1
[31] a X+INPUTS '---LAST SCAN DIRECTION was ', (10ρΔDIRC[10]+ΔDIRC[1]), '. N
eed to change?(0/Inc. 1/Dec.)---->' ◇ +(0=ρX)/DLC+1 ◇ ΔDIRC[1]≠±X
[32] NEXT:TCUR=DCURSOR
[33] DCURSOR+TCUR ◇ X+INPUTS '-----0. X. Y/N/Q' ◇ +(0=ρX)/DLC ◇ +(X='Y')/D
LC+1 ◇ +(X='Q')/0 ◇ +(X='N')/2
[34]
[35]
[36] Nmax+ρX+ΔABC[1]ΔARG ΔABC[2 3]
[37] I+1 ◇ 12 0 1 80 DWPUR '0' ◇ DCURSOR+ 12 10 ◇ ' Ctrl-C: Stop the scan, tem
porally. ' ◇ DWINDOW+ 13 0 12 80 ◇ DTCFF ◇ INKY254+0 DPOKE 254
[38] SETDYE XC[1] ◇ Rdata≠±F ◇ +(Δquitcode≠Rdata)/ΔOUT ◇ TEMPL+(1,ρ(Rdata))ρRdat
a ◇ Rdata+ρTEMPL ◇ Rdata[2]+Rdata[2]+1 ◇ I+I+1
[39] L:SETDYE XC[1] ◇ XX≠±F ◇ +(Δquitcode≠XX)/STOPS
[40] TEMPL+TEMPL, [1]XX ◇ XC[1], TEMPL[1;]
[41] +(17≠DAV[DINKEY])/STOPS
[42] L9:+(Nmax[1]+I+1)/L
[43] ΔOUTO:
[44] TEMPL+(((1+ρTEMPL), 1)ρX), TEMPL
[45] DWINDOW+ 0 0 25 80 ◇ 0ρINKY254 DPOKE 254
[46] MELODIE
[47] ΔFCNUM+1+ΔFSIZE ΔFID
[48] ΔHOWPL SPLOTc TEMPL
[49] '' DSAVE TEMPL
[50] ΔOUT: '
[51] DWINDOW+ 0 0 25 80 ◇ 0ρINKY254 DPOKE 254
[52] +0
[53]
[54] STOPS:
[55] Y+INPUTS '***Interrupt. Do you want to Continue/Quit[save]/Abort (C/Q/A)'
[56] +( 'CQA'≠1+Y)/L9, ΔOUTO, ΔOUT
[57] +L9

```

```

DVR 'SCAN'
▽ SCAN;B;D;S;M;A;S1;FID;HOW
[11] M+(40↑'Sample name? (File name) was '),20↑△FID,'-----' ◇ A+60↓M
[12] →(22ρA)/1+DLC ◇ △FID+A ◇ →(+/'01'ε△FID[1])/DLC+1 ◇ △FID+1 ' ',△FID
[13] →(0=△FEXIST △FID)/DLC+1 ◇ '...File not exist...yet...→+',△FID ◇ △FCNUM+3 ◇
→DLC+2
[14] △FCNUM+1+△FSIZE △FID
[15]
[16] RRewritten DEC. 1986
[17] M'M'Full screen editor will be used for description of file',DTCNL
[18] M'M,'CTRL E ends the editing session',DTCNL,'Press space bar to continue'
[19] L9:B+40ρ'>' M 'Enter B for a BURSTSCAN' ◇ ' T for a Triggered Scan'
[100] M L5:A+DINKEY ◇ →('BT'εA)/L5,L7 ◇ 'You typed ',A,' type a B or T' ◇ →L5
[111] M L6:ELT+SECS ◇ S+BURSTSCAN ◇ ELT+SECS-ELT ◇ MELODIE ◇ 1 SPLOT S ◇ →L8
[112] L7:ELT+SECS ◇ S+TRIGSCAN 1 ◇ →(ΔquitcodeεS)/0
[113] ELT+SECS-ELT ◇ ELT+SECS-ELT ◇ MELODIE
[114] 'Elapsed time : Total= ',(15 2 εELT),' Seconds' ◇ ' Scanning =
',(15 2 εELT),' Seconds'
[115] (ΔHOWPL)SPLOT S ◇ →L8 ◇ M →(2=1+ρS)/L8
[116] 'Second data set, press space bar' ◇ 0 0 ρDINKEY
[117] ΔHOWPL SPLOT S; 1 3]
[118] M 'First data set divided by normalised second data set'
[119] M 'Press space bar'
[120] M ΔHOWPL SPLOT S; 1]AND S; 2]÷S; 3]÷[ /S; 3]
[121] L8:
[122] M+40↑'Save on disk? (Y/N)',B ◇ A+40↓M ◇ →('N'εA)/L1
[123] L2:M+50↑'Drive number and File name were ',△FID,' -----'
[124] A+50↓M ◇ FID+△FID ◇ →(2)ρA)/DLC+1 ◇ FID+A
[125] →(0=△FEXIST FID)/L3 ◇ △FID+FID
[126] L4:M ◇ 0 0 ρDINKEY ◇ D+△SPEXPARG DC[20]+20ρ(ΔDATE),' ' ◇ DEDIT 'D' ◇ FID △
FAPPEND D ◇ △SPEXPARG+D ◇ M+△FCNUM+△FID △FAPPEND S ◇ →L1
[127] L3:'File ',FID,' does not exist yet'
[128] M+40↑'Do you want to create this file (Y/N)',B ◇ A+40↓M ◇ →('N'εA)/L2
[129] 'This description will be the general one for the complete file'
[130] M ◇ 0 0 ρDINKEY ◇ DEDIT 'D' ◇ FID △FAPPEND D ◇ D+''
[131] 'The next description concerns the particular spectral data just measured'
[132] →L4
[133]
[134] L1:
[135] MscrTXT+△SPEXPARG
[136] M ΔHOWPL SPLOT S; 1 2]
[137] M+40↑'Another SCAN (Y/N)',B ◇ A+40↓M ◇ →('Y'εA)/L9
[138]
[139]
[140]
[141]
▽

```

```

OVR 'TRIGSCAN'
▽ R=TRIGSCAN X;S;A;OU;LL;R1;U;NMAX;DELY;RS;ACNT;CNTBRK164;INKY254;INKY255;EN
DD;Y;X;R
[1]  *This version rewritten July 8/86
[2]  +(K=0)/L4
[3]  M+(40↑'Unit W(avenumber) or N(anometer) was '), (10↑unit), '-----'
[4]  A+55↓M ◊ +(0=ρA)/1+DLC ◊ A+1↑A ◊ +(unit=A)/DLC+1 ◊ unit+A ◊ CHANGEUNIT
[5]  Unit+'wavenumber' ◊ +(unit='W')/1+DLC ◊ Unit+'nanometer'
[6]
[7]  M+(40↑'Starting scan position in ',Unit,' was'), (10 2 ↯ΔSTART), '-----'
[8]  A+55↓M ◊ +(0=ρA)/1+DLC ◊ ΔSTART+ΔA ◊ S+ΔSTART
[9]  L1:M+(40↑'End position in ',Unit,' was'), (10 2 ↯ΔEND), '-----'
[10] A+55↓M ◊ +(0=ρA)/1+DLC ◊ ΔEND+ΔA
[11] M+(40↑'The ',Unit,' increment was'), (10 2 ↯ΔBURSTINC), '-----'
[12] A+55↓M ◊ +(0=ρA)/1+DLC ◊ ΔBURSTINC+ΔA
[13] M+(40↑'The MOTION ON+1 OFF+0'), (10 2 ↯ΔBUR), '-----'
[14] A+55↓M ◊ +(0=ρA)/1+DLC ◊ ΔBUR+ΔA
[15] M+(40↑'Maximum pulse counting time was'), (10 2 ↯ΔDWELL[1]), '-----'
[16] A+55↓M ◊ +(0=ρA)/1+DLC ◊ ΔDWELL[1]+ΔA
[17] M+(40↑'Number of repetitions of meas was'), (10 2 ↯ΔDWELL[2]), '-----'
[18] A+55↓M ◊ +(0=ρA)/1+DLC ◊ ΔDWELL[2]+ΔA
[19] M+(40↑'Maximum number of pulses was'), (10 2 ↯ΔPCNT), '-----'
[20] A+55↓M ◊ +(0=ρA)/1+DLC ◊ ΔPCNT+ΔA
[21] DTCLF, 'Measurement program was →→' ◊ dainSP ◊ 'Change to→'
[22] A+M ◊ +(0=ρA)/1+DLC ◊ dainSP+A
[23] 'How to plot string was→→' ◊ ΔHOWPL ◊ 'Change to→'
[24] A+M ◊ +(0=ρA)/1+DLC ◊ ΔHOWPL+A
[25] +( 'W'=unit)/1+DLC ◊ +(ΔSTART↯ΔEND)/L41 ◊ A+ΔSTART ◊ ΔSTART+ΔEND ◊ ΔEND+A ◊
  →L41
[26] +(ΔSTART)ΔEND)/L41 ◊ A+ΔSTART ◊ ΔSTART+ΔEND ◊ ΔEND+A ◊ →L41
[27]
[28] L41:ΔBURSTINC+(-xΔSTART-ΔEND)×1ΔBURSTINC
[29] Y=INPUTS '---0. K.? Y/N QUIT? Q[CR]' ◊ +(0=ρY)/DLC ◊ +( 'N'=1↑Y)/2 ◊ +(
  'Y'=1↑Y)/DLC+1 ◊ +( 'Q'≠1↑Y)/DLC+1 ◊ R+Δquitcode ◊ +0
[30]
[31] DTCBEL ◊ INSTR+ 2 4 ρ'16811403'
[32]
[33] ')>>>>>>Set the COM. SW to ',5ρINSTR[DIO+1x(unit='W');],'. '
[34] M+'#####)>>>>REMOTE ON?>>>>#####' ◊ DINKEY
[35] L4:
[36] SETTING:DTCLF ◊ 'SETTING PARAMETERS'
[37] +(ΔBUR≠0)/2+DLC ◊ R+ 0 0 ◊ 0 0 ρSETPOS ΔSTART
[38] +(1↯/A DSS unit, ↯ΔSTART)/L555 ◊ →L5
[39] R+ΔARB1 DARBIN ΔSTX, 'ST', (↯ΔSTART), ΔETX
[40] R+R, ΔARB1 DARBIN ΔSTX, 'EN', (↯ΔEND), ΔETX
[41] R+R, ΔARB1 DARBIN ΔSTX, 'BI', (↯ΔBURSTINC), ΔETX
[42] R+R, ΔARB1 DARBIN ΔSTX, 'DT', (↯ΔDWELL[1]), ΔETX
[43] R+R, ΔARB1 DARBIN ΔSTX, 'TYB', ΔETX
[44] A+ΔARB2 DARBIN ΔCAN, 'E', ΔETX
[45] A+ΔARB2 DARBIN ΔCAN, 'T', ΔETX
[46]
[47] S+ΔSTART
[48] L5:A+ΔARB2 DARBIN ''
[49] +(DAVE[130 132 136]ρA)/L555, L555, L555
[50] +(0=ρA DSS 'S', unit)/L5

```

*continued - TRIGSCAN*

```

[51] L555:NMAX*(ΔDWELL[1])*1+(ΔSTART-ΔEND)÷ΔBURSTINC
[52]
[53] ')>>>>>USE Control-C to interrupt the program....'
[54] DSOUND 3 2 ρ 500 300 1000 300 850 500 ρ INKY254+0 DPOKE 254 ρ INKY255+1 DP
OKE 255
[55] '... SETTING COMPLETE.. BEGIN DATA FETCH ....' ρ ACNT+0 ρ CNTBRK164+0 DP
OKE 164 ρ ELTO+SECS
[56] R+ΔdatainSP ρ R+(1,ρR)ρR ρ (12,M+1+~1↑ρ,R)≠(ΔSTART),R
[57] 0 0 ρ128 OUT ΔLABM+15
[58] +(ΔBUR≠0)/1+DLC ρ S+0 ρ DELY+÷/datainSP DSS 'PCOUNT' ρ →L5555
[59] TRIG
[60] L5555:LL+L8,L9,L7 ρ OU+DAV[110+ 238 203]
[61]
[62] L7:
[63] +(ΔBUR≠0)/LL77
[64] +(DELY≠0)/L8 ρ 0 0 ρDDL ΔDWELL[1] ρ →L8
[65]
[66] LL77:
[67] A+ΔARB2 DARBIN ' ' ρ →(DAV[130 132 136]≠A)/L8,L8,L8
[68] →(('BE'≠A),1)/LL
[69]
[70] L8:R+R,[1]ΔdatainSP ρ →(272=BINKEY)/QUITT
[71] +(ΔBUR≠0)/1+DLC ρ →((NMAX)ΔS+S+ΔDWELL[1])/L9 ρ (12,M)≠S,(~1,M-1)↑R ρ →L7
[72] (12,M)≠(S+S+ΔBURSTINC),(~1,M-1)↑R
[73] 0 0 ρ(0 0 0 ,ΔLABM+15)DCALL OU ρ 0 0 ρ(1 0 0 ,ΔLABM+15)DCALL OU ρ →L7
[74] L9:R+R,[1]ΔdatainSP
[75] ENDD+ΔSTART+ΔBURSTINC*1↑ρR
[76] R+((1↑ρR)ρ(ΔBURSTINC ΔARG≠≠ENDD,ΔSTART)),R
[77] +(ΔBUR≠0)/1+DLC ρ R[;1]←(ΔDWELL[1])*~1+ρR[;1]
[78] L91:TEMP+R ρ 0 0 ρCNTBRK164 DPOKE 164 ρ 0 0 ρINKY254 DPOKE 254 ρ 0 0 ρINKY2
55 DPOKE 255
[79] →0
[80]
[81] QUITT:Y+~1↑INPUTS '***** INTRUPT. Review,Continue, Kill OR Quit? R/C/K/Q →→
[82] 0 0 ρCNTBRK164 DPOKE 164 ρ 0 0 ρINKY254 DPOKE 254 ρ 0 0 ρINKY255 DPOKE 255
[83] →(O=ρY)/QUITT
[84] Y+1↑Y
[85] →(Y≠'Q')/DLC+1 ρ A+ΔARB2 DARBIN ΔCAN,'H',ΔETX ρ →L9
[86] →(Y≠'K')/DLC+1 ρ A+ΔARB2 DARBIN ΔCAN,'H',ΔETX ρ R+Δquitcode ρ →L91
[87] →(Y≠'C')/DLC+1 ρ 0 0 ρ0 DPOKE 164 ρ 0 0 ρ0 DPOKE 254 ρ 0 0 ρ1 DPOKE 255 ρ
→L8+1
[88] →(Y='R')/REVIEW
[89] →QUITT
[90]
[91] REVIEW:
[92] ENDD+ΔSTART+ΔBURSTINC*~1+1↑ρR
[93] X+(ΔBURSTINC ΔARG≠ENDD,ΔSTART)
[94] +(ΔBUR≠0)/1+DLC ρ X+(ΔDWELL[1])*~1+ρR[;1]
[95] 0 0 ρ1 DPOKE 254
[96] SPLOTc X,R
[97] 0 0 ρ0 DPOKE 254
[98] →QUITT
[99]

```

Data-Fetch Subsystem

```

DVR 'PCOUNT'
▽ R←T PCOUNT N;I;M;A;T
[1] →(I≠,ρT)/L1 ◇ T←T,1
[2] L1:M←TC[2] ◇ R←L0 ◇ I←I ◇ T←I↑T
[3] T←L0.5+100×TL70 ◇ T←DECBCD T
[4] N←L0.5+INL32000
[5] L:A←PINT(O,T,N)◇CALL M△PCOUNTM
[6] R←R,(AC[4])÷((0.01×BCDDEC AC[1])+(1E-6×BCDDEC AC[2]))
[7] →(M≥I←I+1)/L ◇
[8] R←(+/R)÷M
▽

```

```

DVR 'ADN'
▽ R←N ADN C
[1] aCC[2]=GAIN CC[1]=CH# N=number of readin averaged
[2] R←I↑((128+CC[2]),CC[1],N)◇CALL M△ADN
[3] R←(R×R(32767)+(R(32767)×R-65536
[4] R←(R-2048)÷2048 ◇ R←R×10× 1 0.1 0.01 2E-3 [1+CC[2]]
▽

```

```

DVR 'VOLTIN'
▽ R←GA VOLTIN CH;S
[1] 0 0 ρ((GA+128×△INCREN),CH,0)OUTN △LABM+ 4 5 6
[2] R←INN △LABM+ 4 5 6
[3] R←2561R[15 8]
[4] R←4.88281E-3×(R×R(32767)+(R(32767)×R-65536
[5] R←R× 1 0.1 0.01 2E-3 [1+GA]
▽

```

```

DVR 'PEAK'
▽ R←INP PEAK D; INP; D; X; D1; N; MODE; PKSZ; NMAX
[1] NMAX←INP[1]
[2] PKSZ←INP[2]
[3] MODE←O+2↓INP
[4] X←ρDC;2] ◇ R←DC[1↑X;] ◇ N←1
[5] LOOP:
[6] a 'SC 14150 0 14500 500,PD' GRAPH DC[X[4X];]
[7] D1←DC[X;1]
[8] D1←D1-1↑D1
[9] X←((1D1)≥PKSZ)/X
[10] →(NMAX≤N)/OUT
[11] →(O=ρX)/OUT
[12] R←R,[1]DC[1↑X;]
[13] N←N+1 ◇ →LOOP
[14] OUT:→(O=ρMODE)/DLC+2
[15] R←R,[1]DC[X[4X];]
[16]

```

```

DVR 'RAMANSCAN'
▽ R←RAMANSCAN P:SETP;OFFS;WIDTH;INC;R;P;A;NMAX;X;Window;CUR
[11] SETP←0.1×L100000000÷PC1] ◇ OFFS←PC2] ◇ WIDTH←PC3] ◇ INC←PC4] ◇ ΔDWELL[1]←P
[5]
[2] ΔPCNT←PC6]
[3] unit←'W'
[4] ΔSTART←SETP-OFFS
[5] ΔEND←ΔSTART-WIDTH-INC
[6] ΔBURSTINC←INC
[7] ΔBUR←1
[8] ΔDWELL[2]←1
[9] datainSP←'ΔDWELL PCOUNT ΔPCNT'
[10] →('W'=unit)/1+DLC ◇ →(ΔSTARTΔEND)/L4 ◇ A←ΔSTART ◇ ΔSTART←ΔEND ◇ ΔEND←A ◇
→L4
[11] →(ΔSTARTΔEND)/L4 ◇ A←ΔSTART ◇ ΔSTART←ΔEND ◇ ΔEND←A ◇ →L4
[12]
[13] L4:ΔBURSTINC+(-×ΔSTART-ΔEND)×1ΔBURSTINC
[14] A B←'SET AT',(≠ΔDLPOS),'mil'
[15] A D SOUND 10 2 ρ 5500 200 3300 200 ◇ N←DINKEY ◇ +(N=' ')/DLC+1 ◇ →DLC
[16]
[17]
[18] ΔFID ΔFAPPEND 'Exp..Set position(mil/nm)/Offset/width/inc/time/Nmax ----',
('F8.3 ' DFMT ΔDLPOS,5↑P),' ',(≠PC6]),'**',ΔDATE
[19]
[20] Window←DWINDOW ◇ CUR←DCURSOR- 1 0 ◇ DWINDOW← 13 50 11 30
[21] R←TRIGSCAN 0 ◇ →(1-Δquitcode÷R)/DLC+1 ◇ ΔFID ΔFAPPEND R ◇ →LO
[22] ΔFID ΔFAPPEND R
[23]
[24] NMAX←L1×1↑ρR
[25] R←NMAX RAMANPEAK R
[26] A R←, 1 1 PEAK R
[27]
[28] LO:DWINDOW←Window ◇ DCURSOR←CUR
[29]
[30]
[31]

```

## Function Tool Subsystem

```

DVR 'PIC'
▽ B←N PIC A;I
[11] A DICKS THE NTH RECORD OF A
[2] A A IS A CHARACTER STRING
[3] A THE FIRST CHARACTER OF A IS
[4] A THE DELIMITER WHICH
[5] A SEPARATES RECORDS
[6] I←(A=1↑A)/ρA←,A
[7] →(N≥ρI+1,1+ρA)/E
[8] B←I[NI]+ρ 1+I[CN+1]-I[CN]
[9] B←A[E]B
[10] →0
[11] E:'INDEX TOO LARGE IN PIC'
▽
DVR 'PICARG'
▽ R←CMD PICARG ΔA;I;ΔA;R
[11] A CMD[1]← end delimiter of arg
[2] A I←CMD command string
[3] I← 1+1↑(ΔA DSS 1+CMD)/ρΔA
[4] ΔA←(I+ 1+ρCMD)↓ΔA
[5] R←1 PIC CMD[1],ΔA
▽
DVR 'SIN'
▽ R←SIN X
[11] R←100X÷180
▽
DVR 'BCDDEC'
▽ R←BCDDEC A
[11] R←101(6ρ16)↑A
▽

```



```

      OVR 'AND'
      ▽ C←A AND B
[1] →(1←ρρB)/L ◊ B←(Φ1,ρB)ρB
[2] L:C←A, B
      ▽

      OVR 'MINMAX'
      ▽ R←MINMAX D
[1] R←(MIN D),(MAX D),(MAX D)-(MIN D)
[2]
      ▽

      OVR 'AUTOSC'
      ▽ R←N AUTOSC AB;M
[1] R←(-/ΦAB)÷N ◊ M←(10+L10*(R+1E-99*(R=0)))× 1 2 2.5 5 10
[2] R←1+(R≤M)/M ◊ M←R*(1↑AB)÷R ◊ R←M+R1+LN
[3] R←(ABC212R)/R
      ▽

      OVR 'DSAVE'
      ▽ P DSAVE DA;B;D;M;A;FID
[1] M←'Full screen editor will be used for description of file',DTCNL
[2] M←M,'CTRL E ends the editing session',DTCNL,'Press space bar to continue'
[3] B←40ρ''
[4] □←40↑'Save on disk? (Y/N)',B ◊ A←40+□ ◊ →('N'EA)/0
[5] L2:□←40↑'Drive number ',B ◊ FID←40+□ ◊ →(0≠ρFID)/DLC+1 ◊ FID←'1'
[6] DTCNL,'APL files on disk ',FID,DTCNL
[7] , 0 11 ↓ 0 '1 ↓DFLIB≡FID
[8] B←INPUTS 'File name is now---',ΔFID,'----'
[9]
[10]
[11] →(22ρB)/1+DLC ◊ ΔFID←B ◊ →(+/'01'EAΔFIDC11)/DLC+1 ◊ ΔFID←'1 ',ΔFID
[12] FID←ΔFID
[13] →(0=ΔFEXIST FID)/L3
[14] L4:'The next description concerns the particular data to be saved'
[15] M ◊ D←ΔSPEXPAR ◊ D[20]←20ρ(ΔDATE),' ' ◊ 0 0 ρDINKEY ◊ DEDIT 'D'
[16] FID ΔFAPPEND P,DTCNL,D ◊ FID ΔFAPPEND DA ◊ ΔSPEXPAR←D ◊ →
[17] L3:'File ',FID,' does not exist yet'
[18] □←40↑'Do you want to create this file (Y/N)',B ◊ A←40+□ ◊ →('N'EA)/L2
[19] 'This description will be the general one for the complete file'
[20] M ◊ 0 0 ρDINKEY ◊ DEDIT 'D' ◊ FID ΔFAPPEND D ◊ D←'
[21] →L4
      ▽

      OVR 'MAX'
      ▽ MX←MAX F;F;ΔXX;IMAX;I
[1] IMAX←ρF ◊ ΔXX←F
[2] →(12ρIMAX)/NEXT
[3] IMAX←IMAXC1]
[4] ΔXX←FC;2]
[5] NEXT:
[6] MX←ΔXXC(↑ΔXX)[1]]
      ▽

      OVR 'MIN'
      ▽ MX←MIN F;F;ΔXX;IMAX;I
[1] IMAX←ρF ◊ ΔXX←F
[2] →(12ρIMAX)/NEXT
[3] IMAX←IMAXC1]
[4] ΔXX←FC;2]
[5] NEXT:
[6] MX←ΔXXC(ΔΔXX)[1]]
      ▽

      OVR 'DIM'
      ▽ R←DIM A
[1] R←(A=1↑A)/1ρA←,A
[2] R←1+((1↑R),1+ρA)-R
      ▽

      OVR 'COS'
      ▽ R←COS X
[1] R←200X÷180
      ▽

```

```

      DVR 'ΔFAPPEND'
      ▽ R+FID ΔFAPPEND D;T
[11] T=DFNUMS Δ +(0=ρT)/L Δ T+1+f/T Δ +L+1 nTie numb of FID
[12] L:T+1
[13] +(1=ΔFEXIST FID)/L1 n L1 if file exists
[14] FID DFCREATE T Δ +L2 nElse create it
[15] L1:FID DFRTIE T
[16] L2:R+D DFAPPEND T Δ ΔFCNUM+R Δ DFUNRTIE T nNow append D and untie
[17]
      ▽

      DVR 'ΔFREAD'
      ▽ R+FID ΔFREAD N;T
[11] T=DFNUMS Δ +(0=ρT)/L Δ T+1+f/T Δ +L1
[12] L:T+1
[13] L1:FID DFRTIE T Δ S=DFSIZE T Δ +(N(S[2])/1+L1 Δ +L2
[14] R=DFREAD T,N Δ DFUNRTIE T Δ +0
[15] L2:R+0 Δ 'Component number ',(ΞN),' larger than ',(Ξ-1-S[2]),'the actual n
      umber'
      ▽

      DVR 'ΔFEXIST'
      ▽ R+ΔFEXIST FID;F;D
[11] D+Δ1 PIC ' ',FID Δ FID+2 PIC ' ',FID
[12] F=DFLIB D nNames of files in library in drive D
[13] +(0≠1↑ρF)/L Δ R+0 Δ +0 Δ n R=0 no filest exist on drive D
[14] L:F+ 0 11 ↓F nF now contains only file names,no lib. numbs
[15] R+√/F^.=11↑FID Δ nR=1 file exists, R=0 o/w
      ▽

      DVR 'ΔFREPLACE'
      ▽ Z+FN ΔFREPLACE R;T;N;A
[11] nReplaces component N in file F
[12] nFN is a list with first element the file name
[13] nThe second element is the component number
[14] FID+1 PIC ';',FN Δ N+Δ2 PIC ';',FN
[15] +(0=ΔFEXIST FID)/END
[16] T=ΔFTIE FID Δ +(NΔA+(DFSIZE T)[2])/L1
[17] R DFREPLACE T,N Δ DFUNRTIE T Δ ΔFCNUM+N Δ +0
[18] END:Z+'Nonexistent file' Δ +0
[19] L1:Z+'Component number larger than existing number=',Ξ~1+A
      ▽

      DVR 'ΔFSIZE'
      ▽ X+ΔFSIZE FID;T
[11] +(0<ΔFEXIST FID)/DLC+1 Δ X+0 Δ +0
[12] T=DFNUMS Δ +(0=ρT)/L Δ T+1+f/T Δ +L1
[13] L:T+1
[14] L1:FID DFRTIE T Δ S=DFSIZE T
[15] DFUNRTIE T
[16] X+S[2]
      ▽

```

```

      QVR '△FTIE'
    ▽ T+△FTIE FID
  [1] T+QNUMS ◊ +(Q=ρT)/L ◊ T+1+[/T ◊ +L1
  [2] L:T+1
  [3] FID QFTIE T
    ▽

      QVR '△NAPPEND'
    ▽ R+FID △NAPPEND D;T
  [1] T+QNUMS ◊ +(Q=ρT)/L ◊ T+1+L/T ◊ +L+1 nTie numb of FID
  [2] L:T+1
  [3] +(1=△NEXIST FID)/L1 n L1 if file exists
  [4] FID QNCREATE T ◊ +L2 nElse create it
  [5] L1:FID QNTIE T
  [6] L2:D QNAPPEND T ◊ QNUNTIE T nNow append D and untie
    ▽

      QVR '△NEXIST'
    ▽ R+△NEXIST FID;F;D
  [1] D+1↑FID ◊ D+(D='AB')/ 0 1
  [2] F+QLIB D nNames of files in library in drive D
  [3] +(Q≠1↑ρF)/L ◊ R+Q ◊ +Q ◊ R=0 no filest exist on drive D
  [4] nL:F+ 0 11 ↓F nF now contains only file names,no lib. numbs
  [5] L:R+√/F^.=14↑FID ◊ nR=1 file exists, R=0 o/w
    ▽

      QVR '△NREAD'
    ▽ R+FID △NREAD N;T
  [1] T+QNUMS ◊ +(Q=ρT)/L ◊ T+1+L/T ◊ +L1
  [2] L:T+1
  [3] L1:FID QNTIE T ◊ S+QNSIZE T ◊ N+n,S
  [4] R+QNREAD T,N ◊ QNUNTIE T ◊ +Q
  [5] L2:R+Q ◊ 'Component number ',(≠N),' larger than ',(≠S[2]),'the actual number'
    ▽

      QVR '△NTIE'
    ▽ T+△NTIE FID
  [1] T+QNUMS ◊ +(Q=ρT)/L ◊ T+1+[/T ◊ +L
  [2] L:T+1
  [3] FID QNTIE T
    ▽

      QVR 'DECBCD'
    ▽ R+DECBCD A
  [1] nConverts the binary coded digit A into a decimal digit.
  [2] R+16i(5ρ10)↑A
    ▽

```

## VITA

Pan Sang Jung  
Candidate for the Degree of  
Doctor of Philosophy

**THESIS:** OPTICAL PROPERTIES OF GaAs-Al<sub>x</sub>Ga<sub>1-x</sub>As SUPERLATTICES  
INVESTIGATED BY TUNABLE LASER SPECTROSCOPY

**MAJOR FIELD:** Electrical Engineering

### **BIOGRAPHICAL:**

**PERSONAL DATA:** Born in Busan, Korea, June 27, 1954, the first son of  
Soon Chang and Jong Sik Jung.

**EDUCATION:** Graduated from Busan High School, Busan, Korea, in Feb.  
1973; received Bachelor of Science Degree in Electronic  
Engineering from Seoul National University, in Aug., 1977;  
received Master of Science Degree in Electrical Science at Korea  
Advanced Institute of Science in Feb. 1980; completed  
requirements for the Doctor of Philosophy Degree at Oklahoma  
State University in December, 1989.

**PROFESSIONAL EXPERIENCE:** Researcher at Applied Optics Laboratory,  
*Korea Advanced Institute of Science and Technology*, March 1980  
to July 1983; Teaching Assistant at Department of Electrical  
Engineering and Research Assistant at Center for Laser Studies  
from January 1984 to June 1986, and Research Assistant,  
Department of Physics from July 1986 to December 1987 at  
*University of Southern California*, Los Angeles, Calif.; Research  
Assistant at Department of Physics, *Oklahoma State University*,  
January 1988 to December 1989.